SiHf(B)CN-based ultra-high temperature ceramic nanocomposites: Single-source precursor synthesis and behavior in hostile environments

A dissertation approved by the department of Material Science
In fulfillment of the requirements for the degree of Doktor-Ingenieur (Dr. Ing.)
M. Eng. Jia Yuan
Hubei, China
Matrikel-Nr. 1830415

TECHNISCHE
UNIVERSITÄT
DARMSTADT

Berichterstatter: Prof. Dr. Ralf Riedel
Mitberichterstatter: Prof. Dr. Zhaoju Yu

Fachbereich Material- und Geowissenschaften
Technische Universität Darmstadt

Date of submission: 28.08.2015
Date of oral examination: 12.10.2015

Darmstadt 2015
D17

ACKNOWLEGEMENT

I would like to appreciate those who have supported, accompanied and helped me during my PhD work; I would never have been able to finish my dissertation without the guidelines from our colleagues, as well as support from my family.

First and foremost, I would like to give thanks to Prof. Dr. Ralf Riedel, who has provided me with the opportunity to be a part of his group, offering me this interesting topic. Moreover his humorous remarks always lightened the tense atmosphere during discussions, he was always kind enough to ask whether any of his students are having problems in their work or everyday life, I would like to thank him very much for his caring, patience, and providing me with an excellent atmosphere.

I am very grateful to my sub-supervisor PD Dr. Emanuel Ionescu, who has always taken invaluable time to give me suggestions and inspire me whenever I ran into a tough phase of my PhD work, I felt lucky being one of people you supervised. I appreciate that you have contributed a great deal to my PhD work.

Many thanks to Dr. Xingang Luan for kindly supporting my work, especially in the preparation of CMCs. Moreover, he has shared his plentiful experience with me on material behavior in harsh environments (i.e. oxidation, corrosion), as well as his collaboration on hydrothermal corrosion of CMCs which has been published.

Thanks to Prof. Dr. Zhaoju Yu, for kind suggestions while writing the dissertations, for encouraging me and supporting me during my PhD work.

Thanks to Duan Li and Prof. Dr. Zhijian Shen (Stockholms Universitet) for productive collaboration in preparation of dense Hf-containing UHTC-NCs by spark plasma sintering (SPS), moreover for providing a valuable suggestion to me.

Thanks to Dr. Y Wang for fully edit my thesis and kind suggestion for high temperature oxidation part.

Thanks to Dr Yeping Xu and Dr. H Breitzke for NMR MAS measurements, to Dipl. S Hapis and Prof. Dr. H.-J. Kleebe for TEM measurement, to Dipl. Claudia Fasel for TGA-DTG measurements, to Dipl. Jean-Christophe Jaud for assisting in XRD measurements, to Dr. Kurt Johanns for microindentation and nanoindentation, and also J. Prof K. Webber for support in in four-point bending strength.

Thanks to my kind colleagues in our group: Apl. Prof. Dr. Norbert Nicoloso, Dr. Gabriela Mera, Dr. Magdalena Joanna Graczyk-Zajac, Dr. Isabel Gonzalo de Juan, Dr. Jan Kaspar, Dr. Pradeep Vallachira Sasikumar, M. Sc. Sarabjeet Kaur, M. Sc. Cristina Schitco, M. Sc. Dragoljub Vrankovic, M. Sc. Christina Stabler, Dipl.-Ing. Felix Roth, Dipl.-Ing. Alexander Uhl, Dipl.-Ing. Amon Klausmann. I appreciate all of you for providing a pleasant and harmonious atmosphere during my PhD.

Many thanks to Dr. Yan Gao, M. Sc. Wenjie Li, M. Eng. Qingbo Wen, M. Sc. Cong Zhou and M. Eng. Xingmin Liu. All of you are not only my dear colleagues, but you are also my partners in our daily life.

I would also like to acknowledge the financial support from the China Scholarship Council (CSC) for my PhD career. A deep thank you to my parents, my sister and relatives, their support has been unconditional all these years; they have given up much for me to be at TU Darmstadt; they always encouraged me with their best wishes and expectations.

Finally, the most important person in my life to whom I would like to express my best and special thanks are you, my wife, Yuqing Peng. She has always cheered me up and encouraged me during our very difficult time. Although we live separated in different countries, she has brought sunshine into my life, and I wish to dedicate my thesis to you.

Finally, I would like to share one famous Chinese paragraph which has inspired so many others following difficult paths.

路漫漫其修远兮，

吾将上下而求索

The journey is long,

but I’ll search up and down

TABLE OF CONTENTS

List of Figures

List of Tables

ABSTRACT

Hf-containing ultra-high-temperature ceramics (UHTCs) are being pursued for Thermal Protection Systems (TPSs) for high-temperature applications (i.e., future hypersonic vehicles) in harsh environments. Most of these ceramic composites have been prepared using traditional powder techniques; however, the grain sizes of the resulting composites are limited to the micrometer range. Furthermore, nano-sized Hf-containing materials have proven to exhibit tremendously improved structural/functional properties, even at elevated temperatures, compared with microcomposite ceramics. Single-source precursors (SSPs) have yielded promising results in the processing of ceramic nanocomposites; moreover, these composites exhibit unique properties, e.g., high-temperature stability and high-temperature oxidation and corrosion. The objective of this work was to synthesize new Hf-containing ultra-high-temperature ceramic nanocomposites (UHTC-NCs) using SSP-based methods and to investigate their behavior in harsh environments.

In the research presented in this PhD thesis, focus was first placed on the synthesis of novel Hf-containing SiHfCN and SiHfBCN amorphous UHTC-NCs derived from polysilazane. Amorphous SiHfCN and SiHfBCN ceramics were prepared from commercial polysilazane (HTT1800, AZ-EM), which was modified through reactions with $Hf(NEt_2)_4$ and $BH_3{\cdot}SMe_2$ and subsequently cross-linked and pyrolyzed. The prepared materials were investigated with respect to their chemical and phase compositions using spectroscopic techniques (FTIR, Raman, and MAS NMR spectroscopy) and via X-ray diffraction (XRD) and transmission electron microscopy (TEM). Annealing experiments on SiHfCN and SiHfBCN samples in inert gas atmospheres (Ar and N_2) at temperatures ranging from 1300 to 1700 °C revealed the conversion of the amorphous materials into nano-structured UHTC-NCs, whose high-temperature decomposition and crystallization were also investigated. It was found that β-SiC/HfC_xN_{1-x} nanocomposites were obtained from SiHfCN upon annealing at 1500 °C. Depending on the annealing atmosphere, HfC_xN_{1-x}/HfB_2/SiC (annealing in argon) and HfN_xC_{1-x}/Si_3N_4/SiBCN/C (annealing in nitrogen) nanocomposites were obtained from SiHfBCN annealed at 1700 °C. The results demonstrate that the conversion of single-phase SiHf(B)CN into UHTC-NCs is thermodynamically controlled and thus offer insight toward the development of nano-structured ultra-high-temperature stable materials with tunable compositions.

The second focus of the present study was the development of dense Hf-containing ceramic monoliths via pressureless sintering (PLS) or spark plasma sintering (SPS) and the development of ceramic matrix composites (CMCs) via polymer infiltration and pyrolysis (PIP) methods. Dense amorphous ceramic monoliths were prepared upon annealing pyrolytic ceramics in nitrogen at 1300 °C. Dense SiHfCN- and SiHfBCN-based UHTC-NCs were successfully prepared via SPS at 1850-1950 °C using high heating rates (~450 °C/min.) and high pressures ($\geq$ 100 MPa). The obtained UHTC-NCs were investigated via spectroscopic analyses (XRD and Raman spectroscopy) and electron microscopy (SEM and TEM) with regard to their phase evolution and microstructure. Despite the very high sintering temperatures, the microstructures of the prepared dense UHTC-NCs remained rather fine, with grain sizes varying from 165 nm down to a few tens of nm. The hardness and elastic modulus of the dense SiHfCN were found to be 26.8 and 367 GPa, respectively, whereas the SiHfBCN samples exhibited a hardness of 24.6 GPa and an elastic modulus of 284 GPa (measured by nanoindentation). Additionally, C_f/SiCN and C_f/SiHfBCN CMCs were fabricated via a simple and low-cost PIP route. C_f/SiC-SiCN and C_f/SiC-SiHfBCN materials with pyrolytic carbon coatings were synthesized using hybrid techniques (CVI and PIP). The bending strength of the prepared CMCs resulted in the observation of brittle fracture surfaces only in the C_f/SiHfBCN material, indicating strong interfacial bonding between the fibers and the matrix; the much higher values of bending strength observed for C_f/SiC-SiCN and C_f/SiC-SiHfBCN resulted from the fact that weak interfaces (pyrolytic carbon) lead to transfer loading. This finding of the present work suggests that a single-source precursor route is suitable for the preparation of a variety of (ultra)-high-temperature ceramics, such as amorphous ceramics, UHTC-NC monoliths, and CMCs.

Moreover, we explored the behavior of the prepared materials in harsh environments, e.g., their high-temperature stability with respect to decomposition and crystallization and their oxidation, corrosion and ablation behavior. High-temperature annealing experiments revealed that the SiHfCN and SiHfBCN materials exhibited improved high-temperature stability with respect to decomposition compared with non-modified SiCN. The oxidation behavior of the SiCN, SiHfCN and SiHfBCN ceramic powders was studied via thermogravimetric analysis (TGA) in air at 1200-1400 °C, revealing that the modified SiHfCN and SiHfBCN ceramics exhibited poorer oxidation resistance than that of SiCN. However, parabolic oxidation kinetics of SiHfCN and SiHfBCN were observed, wherein the parabolic rate (K_p) that was obtained from the equation $K_p = \left(\frac{\Delta m}{S_{BET} \times m}\right)^2 \times t^{-1}$ indicated that the amorphous SiHfBCN ceramic powder exhibited enhanced oxidation resistance compared with that of the SiHfCN. Furthermore, the oxidation behavior of SiHfBCN ceramic monoliths was investigated in a tube furnace (stagnant air, up to 100-200 h). The microstructure and phase composition of the monoliths' oxide scale was investigated via XRD and microscopy (SEM, BSE and EPMA). The results revealed that the oxidation of the SiHfBCN ceramic monoliths followed typical parabolic kinetics, indicating that the oxidation diffusion was controlled by a passive oxide layer. However, the microstructure and composition of the oxide scale were strongly dependent on temperature. A continuous oxide layer, consisting of cristobalite and hafnia (m- and t- HfO_2), was observed at 1200 °C; however, at 1400 °C, it became a discontinuous oxide layer and its composition changed to cristobalite, HfO_2 and $HfSiO_4$. Thus, the wide range of E_a values (174 and 140 KJ mol^{-1}, depending on the Hf content) obtained from the apparent or corrected oxidation kinetics indicate the complex nature of their oxidation process, which might be the result of a wide variety of oxygen-controlling mechanisms in both the inward oxygen transport into the oxide scale (borosilicate or silica, hafnia, or hafnium silicate) and the outward transport of gas produced by oxidation reactions. Additionally, an investigation of the oxidation of the prepared dense UHTC-NCs at high temperature revealed that both samples exhibited parabolic behavior. Interestingly, the parabolic oxidation rates of the SiHfCN were comparable to those of other UHTCs (e.g., HfC-20 vol% SiC), whereas the parabolic oxidation rates of the SiHfBCN were 3 to 4 orders of magnitude lower. The results obtained in this study indicate that amorphous Hf-containing Si(Hf)BCN ceramics nanocomposites and nanoscale Hf-containing UHTC-NCs are promising candidates for high-temperature applications in harsh environments.

The behavior of C_f/SiCN and C_f/SiHfBCN under subcritical hydrothermal conditions was also investigated at temperatures of 150-250 °C for exposure times of 48, 96 and 240 h. The effect of the ratio between the surface area of the sample and the volume of water used (S/V ratio) on the corrosion behavior of the prepared CMCs was analyzed. For S/V ratios greater than 0.18, the exposure of the CMCs to hydrothermal conditions led to a gain in mass, whereas at lower S/V ratios, a mass loss of the samples was recorded. Because the behavior of the studied samples was representative and reliable at small S/V ratios, both investigated CMC samples were concluded to exhibit active corrosion behavior in a subcritical hydrothermal corrosive environment. Based on the corrosion experiments performed at an S/V ratio of 0.075, the data for the mass loss as a function of the corrosion time and temperature were used to rationalize the corrosion kinetics of the C_f/SiCN and C_f/SiHfBCN samples. Both materials were shown to exhibit excellent stability under subcritical hydrothermal conditions. The corrosion rate of C_f/SiHfBCN was found to be lower than that of C_f/SiCN; furthermore, an SEM investigation indicated that spallation occurred in the C_f/SiCN samples, whereas the ceramic matrix remained attached to the individual carbon fibers in C_f/SiHfBCN. The results of the present study indicate that the incorporation of Hf and B into the SiCN matrix leads to significant improvement in its hydrothermal corrosion performance.

Finally, the ablation mechanism of the C_f/SiHfBCN ceramic composites after treatment in a laser ablation environment was investigated. The microstructure and ablation behavior of this composite were studied using SEM combined with EDS. The formation of porous HfO_2, molten HfO_2 and $Si_xO_yHf_z$ yielded fibers with good protection from oxidation and the laser beam. Three regions with different ablation behaviors are proposed based on the temperature distribution. The ablation center exhibited bubble-like structures, corresponding to the melting of HfO_2 and $SiHf_xO_y$ layers that covered the ends of the carbon fibers, and moreover, eroded carbon fibers that retained their original shape were also observed. In the transition region, carbon sheets and oxidation-product particles (HfC_xO_y and SiO_2) peeled off from the eroded fibers and the matrix because of the high vapor pressure. Additionally, the growth of SiC grains and glass with bubble structure, corresponding to SiO_2 with inclusions of B_2O_3 and SiO gas, was observed.

ZUSAMMENFASSUNG

Hf-enthaltende Ultra-Hochtemperatur-Keramiken (ultra-high-temperature ceramics, UHTCs) sind von Interesse für Temperaturschutzssysteme (thermal protection systems, TPSs) zur Anwendung unter hohen Temperaturen (z.B. zukünftige Überschall-Flugzeuge) in harsch Umgebungen. Die meisten solcher Keramik-Verbundwerkstoffe werden mit traditionelle Pulver-Verfahren hergestellt; allerdings beschränken sich die Korngrößen der entstehenden Verbundwerkstoffe auf den Mikrometer-Bereich. Darüber hinaus nanoskalige Hf-enthaltende Materialien weitreichend verbesserte strukturelle/funktionelle Eigenschaften auf, selbst bei erhöhten Temperaturen, im Vergleich zu den mikroskalige Verbundwerkstoffe. Einkomponentenvorstufen (single-source precursor, SSPs) lieferten vielversprechende Ergebnisse bei der Herstellung von Keramik-Nano-Verbundverkstoffen; jenseits dessen weisen diese komposite einzigartige Eigenschaften auf, z.B. Stabilität bei hohen Temperaturen sowie Oxidation und Korrosion bei hohen Temperaturen. Das Ziel dieser Arbeit war es, neue Hf-enthaltende Ultra-Hochtemperatur-Keramik-Nano-Verbundwerkstoffe (UHTC-NCs) mittels SSP-basierter Methoden herzustellen und ihr Verhalten in harsch Umgebungen zu untersuchen.

Der Schwerpunkt der Forschung, welche in dieser Dissertation vorgestellt wird, wurde zunächst auf die Synthese neuartiger Hf-enthaltender amorpher UHTC-NCs basieren (auf) SiHfCN und SiHfBCN gelegt, welche aus einem Polysilazan abgeleitet wurden. Amorphe SiHfCN- und SiHfBCN-Keramiken wurden aus kommerziellem Polysilazan (HTT1800, AZ-EM) synthetischer, welches mit $Hf(NEt_2)_4$ und $BH_3 \cdot SMe_2$ modifiziert und anschließend vernetzt und pyrolysiert wurde. Die hergestellten Materialien wurden auf ihre chemische und Phasenzusammensetzung mittels Spektroskopische verfahren (FTIR, Raman- und MAS-NMR-Spektroskopie) als auch mittels Röntgenbeugung (X-ray diffraction, XRD) und Transmissionselektronenmikroskopie (TEM) untersucht. Auslagerung Experimente der SiHfCN- und SiHfBCN-Proben in einer Inertgasatmosphäre (Ar und N_2) bei Temperaturen im Bereich von 1300 bis 1700 °C zeigten die Umwandlung der amorphen Materialien in nanostrukturierte UHTC-NCs, deren Zersetzung und Kristallisation bei hohen Temperaturen ebenfalls untersucht wurde. Es wurde festgestellt, dass β-SiC/HfC (N) Nanoverbundwerkstoffe beim Auslagerung bei 1500° C aus SiHfCN erhalt. Abhängig von der jeweiligen atmosphäre wurden, $HfC_xN_{1-x}/HfB_2/SiC$ (in Argon) und $HfN_xC_{1-x}/Si_3N_4/SiBCN/C$ (in Stickstoff), Nanoverbundwerkstoffe aus SiHfBCN durch Auslagerung bei 1700 °C erzeugt. Die Ergebnisse zeigen, dass die Umwandlung von einphasigem SiHf(B)CN in UHTC-NCs thermodynamisch kontrolliert abläuft und somit Erkenntnisse im Hinblick auf die Entwicklung nano-strukturierter, bei hoher Temperatur stabiler Materialien mit einstellbaren Zusammensetzungen liefert.

Der zweite Schwerpunkt der vorliegenden Studie war die Entwicklung sowohl von dichten Hf-enthaltenden Keramik-Monolithen durch druckloses Sintern (pressureless sintering, PLS) oder Spark Plasma Sintering (SPS) als auch Keramikmatrix-Verbundwerkstoffe (ceramic matrix composites, CMC) durch Polymer-Infiltration und Pyrolyse (PIP). Dichte amorphe Keramik-Monolithe wurden durch Auslagerung pyrolytischer Keramiken in Stickstoff bei 1300 °C erhalten. Dichte SiHfCN- und SiHfBCN-basierte UHTC-NCs wurden durch SPS bei 1850-1950 °C, hohen Heizraten (~450 °C/Min.) und hohen Drücken (≥ 100 MPa) erhalten. Die erzeugten UHTC-NCs wurden mittel Röntgenbeugung diffraktometrie und Raman-Spektroskopie und Elektronen-Mikroskopie (SEM und TEM) im Hinblick auf ihre Phasenentwicklung und Mikrostruktur untersucht. Trotz der sehr hohen Sintertemperaturen blieb die Mikrostruktur der dichten UHTC-NCs feinkörnig, mit Korngrößen von 165 nm bis zum niedrigen zweistelligen nm-Bereich. Die Härte-und Elastizitätsmodul des dichten SiHfCN lagen jeweils bei 26.8 und 367 GPa, während die SiHfBCN-Proben eine Härte von 24.6 GPa und einen Elastizitätsmodul von 284 GPa aufwiesen (durch Nanoindentierung gemessen). Weiterhin wurden C_f/SiCN- und C_f/SiHfBCN-CMCs über einen einfachen und kostengünstigen PIP-Weg erzeugt. C_f/SiC-SiCN- und C_f/SiC-SiHfBCN-Materialien mit pyrolytischer Kohlenstoffbeschichtung wurden mittels hybrider Methoden (CVI und PIP) hergestellt. Die Biegefestigkeit der hergestellten CMCs ergab, dass spröde Bruchoberflächen nur in dem C_f/SiHfBCN-Material festgestellt wurden, was auf eine starke Adhäsion zwischen den Fasern und der Matrix hinweist; die deutlich höheren Biegefestigkeitswerte für C_f/SiC-SiCN und C_f/SiC-SiHfBCN ergaben sich daraus, dass schwache Schnittstelle Faser-Matrix-Bindungen (pyrolytischer Kohlenstoff) zu einem Last-transfer führen. Die Erkenntnisse der vorliegende Arbeit legen nahe, dass sich die Route über Einkomponentenvorstufen für die Herstellung einer Bandbreite von (Ultra-)Hochtemperaturkeramiken eignet, wie z.B. amorphe Keramiken, UHTC-NC-Monolithe und CMCs.

Darüber hinaus erforschten wir das Verhalten der SiCN- basieren Materialien in harschen Umgebungen, z.B. ihre Stabilität bei hoher Temperatur bezüglich Zersetzung und Kristallisation als auch bezüglich Oxidations-, Korrosions- und Ablationsverhaltens. Hochtemperatur-Glüh-Experimente ergaben, dass SiHfCN- und SiHfBCN-Materialien gegenüber nicht-modifiziertem SiCN verbesserte Hochtemperatur-Stabilität bei der Zersetzung aufwiesen. Das Oxidations-Verhalten der SiCN-, SiHfCN- und SiHfBCN-Keramikpulver wurde durch thermogravimetrische Analyse (TGA) in Luft bei 1200-1400 °C untersucht, wobei es sich erwies, dass die modifizierten SiHfCN- und SiHfBCN-Keramiken schlechteren Oxidationswiderstand als SiCN aufwase. Allerdings wurde auch die parabolische Oxidationskinetik von SiHfCN und SiHfBCN beobachtet, wobei eine parabolische Rate (K_p), welche aus der Gleichung $K_p = (\frac{\Delta m}{S_{BET} \times m})^2 \times t^{-1}$ abgeleitet wurde, anzeigt, dass das amorphe SiHfBCN-Keramikpulver einen erhöhten Oxidationswiderstand im Vergleich zu SiHfCN aufwies. Weiterhin wurde das Oxidationsverhalten von SiHfBCN-Keramik-Monolithen in einem Röhrenofen (stehende Luft, bis zu 100-200 h) untersucht. Die Mikrostruktur und Phasen-Zusammensetzung der Oxidationsschicht der Monolithe wurde durch XRD und Mikroskopie (SEM, BSE und EPMA) untersuchen. Die Ergebnisse besagen, dass die Oxidation der SiHfBCN-Keramik-Monolithe der typischen parabolischen Kinetik folgt, was darauf hindeutet, dass die Diffusion der Oxidation von einer passivieren Oxidschicht kontrolliert wurde. Allerdings waren die Mikrostruktur und Zusammensetzung der Oxidschicht stark von der Temperatur abhängig. Eine durchgehende Oxidschicht, aus Cristobalit und Hafnien (m- und t-HfO_2), wurde bei 1200 °C analysiert; jedoch entstand bei 1400 °C eine brüchige Oxidschicht, und ihre Zusammensetzung wechselte zu Cristobalit, HfO_2 und $HfSiO_4$. Entsprechend kann die große Bandbreite an E_a-Werten (174 und 140 KJ mol^{-1}, abhängig von dem Hf-Anteil), auf komplexe Eigenschaften das Oxidationsprozesses hinweisen. Diese können sich aus einer großen Vielfalt sauerstoff-kontrollierender Mechanismen ergeben, sowohl bei dem Sauerstofftransport in die Oxidschicht hinein (Borosilicate oder Silica, Hafnia oder Hafnium-Silicate) als auch bei dem Transport von

Gasen, die durch Oxidationsreaktionen entstehen, nach außen. Zusätzlich hat eine Untersuchung der Oxidation der vorbereiteten dichten UHTC-NCs bei hohen Temperaturen gezeigt, dass die Proben parabolisches Verhalten aufweisen. Interessanterweise waren die parabolischen Oxidationsraten von SiHfCN mit denen anderer UHTCs (z.B. HfC-20 vol% SiC) vergleichbar, während die parabolischen Oxidationsraten von SiHfBCN 3 bis 4 Größenordnungen niedriger lagen. Die in dieser Studie gewonnenen Ergebnisse deuten darauf hin, dass amorphe Hf-enthaltende Si(Hf)BCN-Keramiken und nanogroße Hf-enthaltende UHTC-NCs vielversprechende Kandidaten für Hochtemperaturanwendungen in harschen Umgebungen sind.

Das Verhalten von C_f/SiCN und C_f/SiHfBCN unter subkritischen hydrothermalen Bedingungen wurde bei Temperaturen von 150-250 °C mit Expositionszeiten von 48, 96 und 240 h untersucht. Die Auswirkung des Verhältnisses zwischen der Oberfläche der Probe und des verwendeten Wasservolumens (S/V-Verhältnis) auf das Korrosionsverhalten der CMCs wurde analysiert. Bei S/V-Verhältnissen oberhalb von 0.18 führte die Exposition der CMCs bei hydrothermalen Bedingungen zu einer Zunahme der Masse, während ein Masseverlust der Proben bei niedrigeren S/V-Verhältnissen festgestellt wurde. Da das Verhalten der untersuchten Proben bei niedrigen S/V-Verhältnissen repräsentativ und verlässlich ist, wurde bei beiden untersuchten CMC-Proben darauf geschlossen, dass sie ein aktives Korrosionsverhalten in subkritischen hydrothermalen Korrosionsumgebungen aufwiesen. Auf Grundlage der Korrosionsexperimente, die bei einem S/V von 0.075 durchgeführt wurden, wurden die Daten des Masseverlusts als eine Funktion der Korrosionszeit und -Temperatur verwendet, um die Korrosionskinetik der C_f/SiCN- und C_f/SiHfBCN-Proben zu rationalisieren. Beide Materialien wiesen exzellente Stabilität bei subkritischen hydrothermalen Bedingungen auf. Die Korrosionsrate von C_f/SiHfBCN erwies sich als niedriger als die von C_f/SiCN; weiterhin legte eine SEM-Untersuchung nahe, dass es bei den C_f/SiCN-Proben zu einer Aufsplitterung kam, während die Keramikmatrix in C_f/SiHfBCN weiter mit den einzelnen Kohlenstofffasern verbunden blieb. Die Ergebnisse der vorliegenden Studie deuten darauf hin, dass die Einbindung von Hf und B in die SiCN-Matrix zu einer deutlichen Verbesserung ihres hydrothermalen Korrosionsverhalten führt.

Schließlich wurde der Ablationsmechanismus von C_f/SiHfBCN-Keramikverbundwerkstoffen in einer Laser-Ablations-Umgebung untersucht. Die Mikrostrukturen und das Ablationsverhalten dieser Verbundwerkstoffe wurden mittels SEM in Kombination mit EDS untersucht. Die Bildung von porösem HfO_2, geschmolzenen HfO_2 und $Si_xO_yHf_z$ gab den Fasern einen besseren Schutz vor oxidation und dem Laserstrahl. Drei Regionen mit verschiedenem Ablationsverhalten werden gemäß der Temperaturverteilung an der Probe vorgeschlagen. Das Ablationszentrum wies blasenähnliche Strukturen auf, die sowohl geschmolzenem HfO_2 entsprechen als auch den $SiHf_xO_y$-Schichten auf den Enden der Kohlenstofffasern; des Weiteren wurden erodierte Kohlenstofffasern gefunden, die ihre ursprüngliche Form beibehalten halten. In der Übergangsregion lösten sich Kohlenstoffschichten und die Partikel der Oxidierungsprodukte (HfC_xO_y und SiO_2) aufgrund des hohen Dampfdrucks von den erodierten Fasern und der Matrix. Weiterhin konnte das Wachstum von SiC-Körnern und Glas mit Blasenstruktur gefunden, welches SiO_2 mit Einschlüssen von B_2O_3- und SiO-Gas entspricht.

1. INTRODUCTION

1.1 Introduction and Motivation

When operated at (ultra) high temperatures and in harsh environments, structural parts and components are exposed to additional and more severe design constraints as compared to those used in service at or near ambient temperature. A fundamental property which is required in order to be able to operate materials at (ultra)high temperatures relates to their melting point. Naturally, (ultra)high melting points of the chosen materials are necessary, as usually the maximum operation temperature of a material is, with some exceptions, round half of its melting point.

Generally, high tolerance to thermal and mechanical stress is desirable in order to avoid catastrophic failure of the materials during operation. Thus, a high compliance to thermal stress can be provided by using highly thermoshock resistant materials. Additionally, suitable, optimized ductility of the materials or, in the case of brittle components, such as ceramic-based, improved fracture toughness are desirable in order to provide high tolerance to mechanical stresses. Finally, no phase transformation of the materials in the range from the ambient to the operation temperature may occur, as those processes usually are accompanied by significant volume changes which consequently might generate tremendous stresses and induce a catastrophic failure of the component. In the case of amorphous materials, an increased crystallization resistance may be beneficial for avoiding the generation of mechanical stress upon operation at (ultra)high temperatures.

Intense efforts have been made in the last decades in order to accommodate those requirements, which are often strongly conflicting. Thus, several types and classes of (ultra)high-temperature materials have been proposed and developed over the years, such as highly refractory metals, inter-metallic/alloys, metal matrix composites (MMCs) as well as UHTCs ceramic monoliths or ceramic matrix composites (CMCs).

Single-source-precursors synthesis approaches have been used in recent years to generate nanoscaled ceramic composites, which show excellent behavior at ultra-high temperatures and even in harsh environments. For instance, SiOC/t-HfO_2 [1, 2] , SiOC/t-ZrO_2 [3] ceramic nanocomposites were successfully synthesized, starting from a commercially available preceramic polymer, namely poly(siloxanes). These exhibited excellent high temperature stability, good high temperature oxidation and corrosion resistance under hydrothermal conditions [4]. However, the low melting points of oxygen-containing ceramic nanocomposites turn them into a bottleneck in high temperature engineer application due to their impaired high temperature mechanical properties. Therefore, it is necessary to investigate non-oxygen nanocomposites. Many non-oxygen silicon-based preceramic polymer are available commercially, such as SiC-based (SMP10) [5], Si_3N_4-based (PHPS) [6], SiCN-based (HTT1800) [7] polymer precursor, etc. Among these precursors, SiCN-based substances can be converted into amorphous SiCN or SiC/Si_3N_4 nanocomposites, which have been considered as combining the merits of SiC and Si_3N_4. Furthermore, this amorphous ceramic has been intensively investigated concerning its oxidation behavior, water vapor corrosion, and high temperature creep behavior. All of these behaviors in harsh environment proved to be outstanding. Additionally, researchers modified these materials by aluminum, boron, titanium and zirconium to yield SiAlCN [8], SiBCN [9], SiTiCN [6], or SiZrCN ceramics, allowing the creation of novel SiCN-based ceramic and its ceramic nanocomposites.

Among ultra-high temperature ceramics, Hf-containing ceramics (HfC, HfN and HfB_2) were considered as the most promising category based on their extremely high melting point, superior thermal conductivity and oxidation resistance compared to Ti, Zr-based UHTCs [10]. Furthermore, a great deal of research has presented the addition of silicon-based second phase into HfC or HfB_2 enable to significantly improve the oxidation resistance of silicon-free HfC or HfB_2, consisting of SiC/HfC, SiC/HfB_2 or SiC/HfC/HfB_2 composites [11-13].

Accordingly, we consider a novel SiHf(B)CN amorphous ceramic and its nanocomposites as promising candidate in (ultra)high temperature applications. Furthermore, these composites (i.e. HfC/SiC, HfB_2/SiC) are conventionally synthesized by using powder techniques. Moreover the grain size of these composites is in the micrometer range. To the best of our knowledge, no studies reported the synthesis of these ceramics composites via single-source-precursor so far. Hence, the present research is focused on the following topics:

- The essential key aspect of our study is to develop novel SiHf(B)CN ultra-high temperature ceramic composites with refined nanostructure via a single-source-precursor route, starting from the commercial precursor polysilazane HTT1800.
- Investigating the polymer-to-ceramic conversion
- Processing dense monolithic amorphous ceramics and ceramic nanocomposites and ceramic matrix composites (CMCs).
- Their response to harsh environments, i.e. high temperature stability with respect to decomposition and crystallization, high temperature oxidation, hydrothermal corrosion, ablation behavior etc., is studied.

1.2 Terms and definitions

1.2.1 Ceramic Nanocomposites

Nanocomposite materials can be defined as having more than one Gibbsian phase, where at least one dimension is in the nanoscale. Furthermore, phases can be amorphous, semi-crystalline or crystalline etc.; the state can be inorganic or organic, in any of their compositions. The nanocomposites theory is thought to also apply to biological systems, such as bones, teeth and shells, which can be considered as inorganic and organic, consisting of nanocomposites.

The synthesis of nanocomposites can be tracked back to work performed by Roy and Komarneni [14], who created heterogeneous rather than homogeneous materials using the sol-gel approach. Furthermore, the related work of H. Gleiter on nanocrystalline materials shows that a reduction in the size of the composites to the nanometer range can achieve a significant improvement in their structural (mechanical) and functional properties (electrical, optical etc.) [15]. Recent advances in producing nano-structured materials with novel properties have stimulated research to create multi-functionality by designing structures in the nanometer scale.

Nanocomposite materials can be classified as: (I) microstructure; (II) materials function, physical and chemical differences, formation of temperature. In the microstructure concept, R. E. Newnham *et al.* proposed the fascinating word “connectivity” for describing nanocomposites [16], as he illustrated that connectivity is a critical parameter in composites. It influences the properties of the multi-phase, because the properties can be tailored by many orders of magnitude through varying the connections. Thus, the relationship between structure and properties can be interpreted by connectivity providing a guideline for the materials design. However, some of the connectivity patterns applying classification (I) are difficult to implement in the ceramic-based nanocomposites. Roy and Komarneni *et al* identified nanocomposites as five major groups according to (II) [17]: (1) sol-gel nanocomposites, which are synthesized at temperatures below 100 °C; these nanocomposite precursors are converted into multiphasic crystalline ceramics nanocomposites upon high temperature heating; (2) intercalation-type nanocomposites, which are generally prepared at temperatures below 200 °C; compared to sol-gel nanocomposites, their synthesis temperature is relatively low (< 500 °C); (3) entrapment-type nanocomposites, which are converted from precursors with network structures (3D) at low temperatures (< 250 °C); (4) electroceramic nanocomposites, which can be prepared by incorporating nanophases of materials with electric properties (i.e. ferroelectric, dielectric, superconducting and ferroic) into a polymer matrix at temperatures below 200 °C; (5) structural ceramic nanocomposites, which are prepared by traditional ceramic processing at very high temperatures (1000 - 1800 °C). Furthermore, structural ceramic nanocomposites could be subdivided into four categories: intra- and intergranular nanocomposites, hybrid intra-intergranular nanocomposites, as well as nano/nano composites, where the latter can have any phase in the nano scale, and the other nanocomposites require only one nano-structured phase.

1.2.2 Ultra-high temperature ceramics

In order to define ultra-high temperature ceramics, it is necessary to understand the definition of (ultra)high temperature. One often used definition in materials science is that such a temperature reaches about two-thirds of the melting point of a solid [18]. Another definition, related to the alteration of a material’s properties, kinetics, and chemical behavior from room temperature to that high temperature, states that such chemical reactions in high temperature are highly different compared to those at room temperature and that this may depend on thermodynamic properties rather than kinetics in the high temperature range [19]. Additionally, the extrapolation of materials structure and properties from near room temperature are no longer valid, i.e. a solid solution’s range increases significantly due to the structure becomes more disordered with increasing temperature [18], or the physical properties of materials are unpredictable in the high temperature range [18]. Therefore, materials design has to combine the alteration of structure and properties with the dependence on high temperature, which is quite a challenge for its usefulness in (ultra)high temperatures.

As mentioned before, the melting point is a major and simple criterion for classification. Currently, there are more than 300 materials with melting points above 2000 °C, including SiC, refractory metals (Hf, Nb, Ir, Re, Ta, W), a variety of transition metal oxides, carbides, nitrides and borides etc. However, materials with melting temperatures over 3000 °C include only few elements (Carbon, W, Re) or compounds (TiC, TaC, TaN, TaB_2, ZrC, ZrN, ZrB_2, HfC, HfN, HfB_2, NbC, ThO_2, BN), which are called ultra-high temperature materials (UHTs) [10]. It should be noted though that the melting point is only one of the properties relevant for materials selection. Assessment materials still rely on their usefulness in a real structural application (i.e. leading edge, nozzle components) in very high temperature, where materials suffer from a complex steam atmosphere including O_2, NaCl, Na_2SiO_4 vapor etc. [20, 21]. Thus, those extreme conditions limit the number of suitable materials for defining UHTC material. Firstly, oxides are thought to be suitable for use in those environments (oxidizing), but their high thermal expansion and low thermal conductivity limit their use in high temperature applications, which might eliminate them from this discussion. Additionally, despite graphite being best known for its extremely high melting point, it starts to diminish at only 800 °C. Similarly, the other category may have a very high melting point, but they will undergo oxidation to form some liquid or gaseous reaction product, i.e. BN can only be used in air up to 900 °C due to the formation of boria (liquid phase) [22]; furthermore, oxidic products with low melting points are formed under exposure to an oxidizing environment, such as TiB_2 [23], TiC [24, 25] (TiO_2-T_m=1840 °C), NbB_2 [26] or NbC (Nb_2O_5-T_m=1485^{o}C) [27].

What we are left with are carbides, nitrides and borides of early transition metals (such as ZrC, ZrN and ZrB_2, HfC, HfN, and HfB_2.etc), which have been broadly termed Ultra High Temperature Ceramics (UHTCs). Since the 1960's, these materials have been investigated by ManLabs under a research program funded by the Air Force Materials Laboratory (AFML) [28]. The work on these materials was initiated to meet the need for the development of hypersonic flight vehicles with sharp leading edges [29]. Materials forming in the HfO_2 or ZrO_2 scale are an oxidation product derived from hafnium or zirconium carbide, nitride and boride in the oxidizing environment, which are considered as desirable candidate for short-term applications (>2000 °C) [20]. However, the unprotecting oxide scale (HfO_2 or ZrO_2) with porous structure generated from refractory carbide, nitride restricts their long-term applications. The better oxidation resistance of refractory diboride compounds was shown compared to other refractory compounds (carbide, nitride), as liquid B_2O_3 can be protective up to 1200 °C. However, it is known that B_2O_3 evaporates at higher temperatures and no longer provides a barrier to gas diffusion. Thus, the addition of a second phase into the refractory compound was found to improve oxidation behavior and its strength, typically, ZrB_2 or HfB_2 plus 20 vol% SiC, producing the highest oxidation resistance up to 2000 °C [30]. The other way to enhance the oxidation resistance is the formation of complex immiscible glasses as well as increasing the viscosity of glasses that can limit the permeation of molecular oxygen. The addition of 10 mol% TaB_2 into ZrB_2/SiC has been shown to significantly improve the oxidation resistance, as compared to pure ZrB_2 and ZrB_2/SiC [31].

Accordingly, the definitions of UHTCs need to be associated with the application, where applications include both short-term and long-term applications. In short-term applications, stability in shape is more important than the formed oxide scale, in contrast to dense, protective oxides that are needed in long-term applications (oxidizing/water vapor environment) at temperatures up to 1600 °C. For the latter, silicon-based ceramics (silicon carbide, silicon nitride or metal silicides) are materials with excellent environmental stability (oxidation resistance) at temperatures up to ca. 1600 °C, as they are able to generate a layer of dense silica glass at the surface that strongly inhibits the oxygen diffusion and reaction with the parent material by its parabolic oxidation behavior.

Therefore, we can summarize two terms for the definitions related to the aforementioned discussion:

1) A strict definition is determined by the melting point of the material over 3000 °C, encompassing materials thought to be operable at extremely high temperatures ($\geq$ 2000 °C) for a short time.

2) The other definition related to the present work is that the synthesized materials can withstand temperatures above 1600 °C, as well as being useful for long-term applications in harsh environments (oxygen or water vapor) and can thus also be considered as UHTC materials.

1.2.3 Polymer-derived ceramics (PDCs)

The polymer-derived ceramics (PDCs) are a new class of ceramics being prepared, without any additives, by thermal treatment in a controlled atmosphere, starting from a polymer precursor with a Si-containing molecular structure. Thus, PDCs are distinguished by following the chemical route rather than the traditional powder route, which can produce ceramic fibers, coatings, or ceramic matrix composites by polymer-forming techniques.

The synthesis of pre-ceramic precursors can be tracked back to the early 1960s when Chantrell and Poper [32] reported the synthesis of non-oxide ceramics from molecular precursors. However, the production of Si_3N_4/SiC ceramic fibers was achieved for the first time by the polymer to ceramic transformation of polysilazanes, polysiloxanes, and polycarbosilanes [33]. Furthermore, continuous SiC ceramic fibers have been created on a commercial scale by Yajima *et al* [34, 35], using the thermolysis of polycarbosilanes.

The molecular structures and types of preceramic polymer not only influence the composition and microstructure of the final ceramics, but also their crystallization and physical properties which can be varied by tailored chemical compositions and molecular precursors. Therefore, the synthesis of preceramic precursors is a critical step in the field of PDCs. The success of synthesizing silicon-containing PDCs such as Si-C, Si-N, and Si-C-N can be attributed to the strong bonding between silicon and carbon, nitrogen etc. Moreover, exceptional properties including high temperature stability (i.e. against crystallization, phase separation, decomposition), high temperature durability towards oxidation, corrosion and creep resistance have also been shown. R. Riedel *et al* have found that the high temperature stability of boron-containing SiCN ceramics with respect to decomposition could reach 2200 °C [9]. Currently, quaternary systems SiCNO, SiBCN, SiBCO, SiAlCN etc. have been synthesized; within the present work, quaternary and pentanary systems SiHf(B)CN will be reported, representing a novel ceramics at the nano scale, namely polymer-derived ceramic nanocomposites (PDC-NCs).

1.2.4 Extreme environments

Nature is rich with examples of phenomena and environments that we might consider extreme. For example, the regular temperature range on Earth where we live reaches from -50 to +50 °C. Moreover, various natural phenomena and environments (i.e. large fluxes of radiation and particles from the sun, volcanic eruptions that originate deep underground, extraordinary pressures and temperatures in the interiors of the planet, electromagnetic discharges etc.) are also considered extreme. Therefore, for the new materials, the response to the broad range of such extreme environments leads to new physical phenomena that have to be understood, which cannot occur under ordinary conditions. Considering the development of materials (i.e. a device's performance, extending its lifetime, the creation of new technologies), researchers not only need to understand how materials behave in such environments, but also to tailor and modify materials to satisfy demand [36].

Within this context, three major classes of extreme environments are discussed with the development of novel, suitable materials for usage in extreme conditions: energetic fluxes, thermomechanical forces, extreme chemistry.

Energetic fluxes represent crucial conditions in nuclear fission, fusion reactors and energy conversion. In those conditions, materials are exposed to energetic particles and intense radiation; obviously, it is necessary to know how materials behave in such extreme environments in order to optimize the performance of materials able to tolerate harsh fluxes. Furthermore, new materials need to be created for even harsher conditions, i.e. next generation fission reactors will suffer neutron fluxes an order of magnitude higher than current systems.

Besides the potential damage experienced from energetic fluxes, fluxes (i.e. irradiation) could also be used as effective tools in creating new materials and structures with more thermodynamic stability. For instance, shaped laser pulses can be used to anneal a material and produce specific microstructures or repair materials that have been damaged by prior irradiation.

Thermomechanical forces include high pressure and stress loading, high strain and strain rate as well as thermal stress (high and low temperature), and they can be found in high temperature turbines as well as heat exchangers in engines and electrical power plants, where temperatures and stresses reach 1030K and roughly 40MPa [37]. More importantly, an understanding on the original behavior of materials under those conditions enables the improvement of the material's performance and allows the origin of new materials to be recognized, i.e. the pronounced improvement in strength may contribute to internal structure with nanoscale architectures, compared to conventional materials with the same compositions [38]. Furthermore, the application of pressure has produced new super-hard materials, such as doped diamond, cubic carbon and boron-nitride.

Extreme chemistry is found in many advanced power systems such as fuel cells, nuclear reactors, and batteries. The performance is unreliable when the materials are exposed to reactive liquids (acids, ionic liquids, molten salts) or gas (steam, hydrogen, ammonia, NO_x etc.). Obviously, equilibrium and non-equilibrium thermodynamic and kinetics aspects have to be considered, in order to be able to develop monolithic or protective films with excellent resistance to an extreme chemical environment.

Studies of materials in extreme environments are essential for different applications, ranging from creating better turbines and reactors over improving energy storage to developing future energy systems. However, there are problems: In-situ characterization of the motion of atoms and defects in materials exposed to harsh environment might be particularly difficult.

1.3 A literature survey

1.3.1 Synthesis of ceramic nanocomposites

Introducing terms for ceramic nanocomposites within this context, Niihara and his colleagues have classified structural ceramic nanocomposites into four categories [39]: (a) intragranular, (b) intergranular, (c) hybrid intra/inter-granular, and (d) nano/nanocomposites. They distinguished between the intra-type and inter-type according to the dispersion of the nanometer-sized second phase within matrix ceramic materials or at the grain boundary of the matrix, respectively. Due to these exceptional structures, intra- and intergranular nanocomposites proved a tremendous improvement of mechanical properties even at elevated temperatures compared with those of microcomposite ceramics. Furthermore, the nano/nanocomposites provided new functions, such as machinability and super plasticity like metals.

In this section, we will discuss the synthesis of ceramic nanocomposites. Various techniques are utilized in this process [40], such as gas-phase reactions (chemical vapor deposition is used to prepare Si_3N_4) [41, 42], liquid-phase process (sol-gel process, intercalation, organometallic pyrolysis, combustion synthesis, and spray conversion), solid phase method (mechanical alloying).

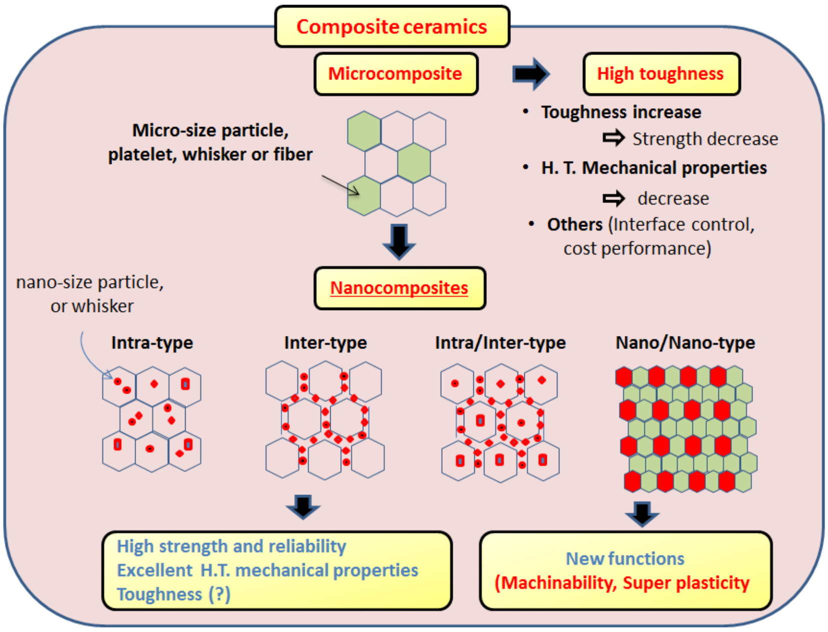

Figure 1.1. K. Niihara's concept of designing ceramic metal nanocomposites with inter- and intra-granular structure: the aim was to improve the mechanical properties compared to microcomposites (such as high strength and toughness) (adapted with permission from source **[43]**).

Gas-phase and solid-phase synthesis are beyond our scope, thus only the liquid-state process for preparation of ceramic nanocomposites will be presented in the following discussion, mainly focusing on sol-gel and pyrolysis of the polymeric precursor.

1.3.1.1 Sol-gel techniques

Sol-gel processing is commonly used in the synthesis of nanocomposites. Generally, ultra-homogeneous glasses and ceramics can be converted starting with a mixture solution, followed by gelation and then thermal treatment [44]. The sol-gel process was initially produced for oxide ceramics, involving three steps: i) mixing with metal organic precursors to form a solution; 2) forming sol and later gel during desiccation; iii) achieving the final product after gelation. Accordingly, this process involves the transformation from a homogeneous solution to a phase, which is irreversible, i.e. the gel to desired phase was shown to shrink. The pronounced advantage of the sol-gel process is to develop homogeneous ceramics at the beginning of research. However, in 1982, Roy *et al* have created “heterogeneous” materials in the nanometer range (nanocomposites), such as ceramic/metal nanocomposites [14] (Al_2O_3, SiO_2, ZrO_2 as oxides and Cu, Pt, Sn, and Ni as metals). Since alkoxide can react readily with water, the -OH band is attached to the silicon or metal atom after hydrolysis. Afterwards, polymerization occurs accompanied by the production of H-O-H and R-O-H species, leading to the formation of a network of M–O–M (M=metal or silicon) bonds. Thus, using metal alkoxide as starting materials is one of the most-promising techniques for fabrication of nanocomposites with a tailored structure, i.e. alkoxysilanes were commonly used to react with suitable metal alkoxide to generate SiO_2-TiO_2 [45], SiO_2-Al_2O_3 [46] etc. nanocomposites. However, the kinetics of the hydrolysis and polycondensation process during the formation of network structures (colloidal gels) are quite important, since these equilibrium reactions depend on a number of parameters (e.g. temperature, pH value, concentration of various compositions etc.). For example, acids or bases may be used to catalyze hydrolysis, the slowest rate is at approximately neutral pH (pH=7). Each change of pH by 1 pH unit in either the acid or basic direction produces a ten-fold acceleration in the hydrolysis rate. Polycondensation is also pH-dependent; if fast hydrolysis followed by slow condensation is desired, acidic catalysis is preferred and vice versa [47].

Nonoxide-based nanocomposites can also be synthesized by the sol-gel process [48]. P. R. Strutt *et al* [48] synthesized AlN/BN material using boric acid, urea and aluminum chloride (or aluminum lactate) as starting materials. The gel was achieved using the ammonolysis of the aqueous solution and subsequently converted into the AlN/BN nanocomposites by further heat treatment.

The advantages of the sol-gel techniques lie in synthesizing in a convenient process (low processing temperature) and of high-purity materials with a tailored phase (e.g. single phase nanocrystalline materials or nanocomposites). Furthermore, the compositions could be adapted to stoichiometry control, which allows suitable shaping/morphology of the end product (i.e. powders, thin films, or monoliths).

1.3.1.2 Synthesis from polymer-based single-source-precursor (SSPs)

The PDCs have attracted great attention in the last few decades, due to their advantages over traditional ceramic processing methods. For example, additives and very high sintering temperature (1700-2000 °C) are required for the preparation of SiC [49] or Si_3N_4 [50] using powder processing techniques; in comparison, relatively low processing temperature (1100-1300 °C) are used for the preparation of silicon-based ceramics and therefore of economic interest. Furthermore, PDCs offer an easier route to synthesizing ceramic fibers [51], coatings [52] or ceramic matrix composites [53], which in principle cannot be produced by the powder technique. The non-oxide ceramic ‘SiC’ via molecular organosilicon compounds was reported for the first time by Fritz and Raabe in 1956 [54], and then Verbeek and his colleagues presented the preparation of small-diameter SiC/Si_3N_4 ceramic fibers from a silicon-based polymer precursor [33]. And subsequently, in 1976, a significant breakthrough was made by Yajima *et al* [34] in the development of SiC-based ceramic fibers using polycarbosilane.

The molecular structure and the type of preceramic polymer have a significant effect on the composition and microstructure of the desired ceramic. In this way, the chemical and physical properties of PDCs can be varied and adjusted to a great extent by the design of the molecular precursor. Therefore, the synthesis of preceramic polymers is one of the key issues in the PDCs field [55]. Different classes of preceramic precursors (i.e. polysilanes, poly(carbonsilanes), poly(organosilazanes), poly(borosilazanes) etc.) which are generally used for the synthesis of PDCs are presented in Figure 1.2.

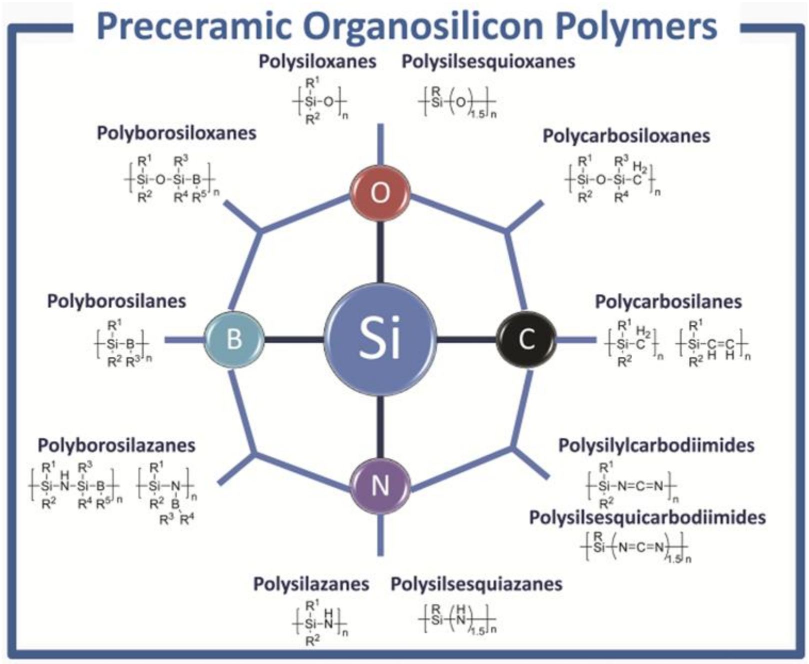

Figure 1.2. Main classes of Si-based preceramic precursors for the synthesis of PDCs: polysilazanes, polycarbosilanes, polyborosilazanes, polysiloxane, polysilylcarboiimides etc. (reproduced with the permission of literature **[55]**).

For the synthesis of polymer-derived ceramic nanocomposites (PDC-NCs), different silicon-based preceramic precursors (as the aforementioned polysiloxanes, polycarbosilanes or polysilazanes) have been chemically modified with organometallic compound, such as metal alkoxides, metal amido complexes, leading to single-source precursors which are subsequently converted into PDC-NCs upon pyrolysis. Preliminary work has been done by Interrante *et al*, using polycarbosilane mixed with $[R_2AlNH_2]_3$, which led to SiC/AlN nanocomposites [56]. Furthermore, it has also been noted that a combination of AlN with SiC provided solid solutions with fine grain sizes, high microstructure uniformity and improved mechanical properties of SiC ceramics. Some highlights of the recent progress in the synthesis of polymer-based precursor ceramic nanocomposites are summarized by Paine *et al* [57]: 1) In the first method, a polymeric precursor is incorporated with reactive filler particles; 2) in the second approach, two (or more) polymeric precursors are blended to form the desired ceramic compositions; 3) the synthesis of polymeric precursor compounds that contain all of the involved elements.

In the first approach, reactive metal particles are simply blended with the preceramic polymers and followed by cross-linking and pyrolysis. Seyferth and coworkers [58, 59] have utilized this approach to prepare several composites. Furthermore, the composition and crystallization of the resulted products depend on processing conditions, including pyrolysis temperature and gas (i.e. reactive ammonia or inert argon gas). For instance, a solution of $[(CH_3SiHNH)_{0.4}(CH_3SiN)_{0.6}]_n$ was ultrasonicated together with W powder (W: Si ratio 5: 3). The pyrolysis of the powder precursor was implemented in a stream of argon at 1500 °C after removing the solvent in a vacuum, leading to WC/W_5Si_3 nanocomposites. In contrast, polysilazane/W powder was pyrolyzed in a stream of dry ammonia at 800 °C, and followed by further heating to 1500 °C, yielding only one phase W_5Si_3. More interestingly, when the initial ratios of Si were adjusted higher (W: Si=1:2), additional ceramic phases (WSi_2, WC and SiC) were found. Greil *et al* [60] proposed the model of active-filler controlled pyrolysis of preceramic polymers (AFCOP) using a blending of preceramic polymers and active fillers (metallic, intermetallic). This concept aims to serve engineering application (such as bulk, coating, ceramic matrix composites etc.), demonstrating that the shrinkage and porosity generation might be alleviated by adding passive or active filler during the conversion from polymers to ceramics. Reactive filler particles (such as metallic: Ti, Cr, V, Mo and intermetallic: $CrSi_2$, $MoSi_2$ etc.) were used to react either with the decomposition products of the polymer phase or the gas atmosphere, not only compensating for the intrinsic shrinkage of polymer-to-ceramic conversion, but also preparing various ceramic composites, such as Si-O-C/TiC, Si-O-C-N/TiN, Si-O-C-N/Cr_3C_2/Si_3N_4 [60]. Obviously, these results will likely be practical and useful. Moreover, ceramic composites synthesized by AFCOP exhibit improved mechanical and functional properties (e.g. electric [61] and magnetic properties [62]) compared to equivalent ceramics without filler. For example, in the case of the SiOC-based composite, the SiOC/$MoSi_2$ ceramic composites can be prepared by ceramization of the polysiloxane/$MoSi_2$ blend. The obtained composite exhibited a remarkably lower electrical resistivity (10^{-2} Ω m) than that of pure SiOC prepared under the same conditions (10^9–10^{12} Ω cm) [61].

A second approach involves the blending of two (or more) precursors of the desired ceramic composites. Interrante and his colleagues have presented numerous works on this, as they synthesized Si_3N_4/AlN ceramic nanocomposites employing a blending of polysilane with $[Et_2AlNH_2]_3$, followed by pyrolysis under NH_3 [63]. Similarly, mixtures of polysilane (VPS) with polyborazinylamine (PBZA) produced the preceramic precursor, and then they were converted into Si_3N_4/BN nanocomposites through thermal pyrolysis [64]. Sneddon *et al* [65] synthesized boron-containing β-Si_3N_4/β-SiC composites starting from the reaction of liquid borazine with hydridopolysilazane (HPZ) and then pyrolyzing the resulted polymer. In contrast to the ceramic materials obtained from HPZ, a better retention of nitrogen and suppression of crystallization could be observed due to the presence of amorphous phase BCN.

A third approach regards the synthesis of single-source precursors (SSPs) containing all the elements of the desired composites. Within this work, SSPs mainly focus on the modification of silicon-based polymers with metal complexes. Depending on the types of silicon-based polymer precursors, the synthesis of SSPs will be described by various polymer precursors in the following.

Polycarbosilane (PCS) are often used to synthesize SiC-based ceramic nanocomposites. The chemical modification of PCS with transition metal complex were reported for the first time by Seyferth and coworkers [59]. Soraru *et al* synthesized a series of preceramic precursors using PCS modified with metal alkoxide, producing the single-source-precursor Si-M-C-O (M=Al, Zr, Ti) [66, 67] (Figure 1.3), while Ishikawa *et al* [68, 69] also synthesized SiC-based SSPs using metal acetylacetonate as the modification reagent. Depending on the metal precursor used, different reaction pathways of PCS with metal-organic precursors have been reported. The reaction with metal alkoxides involves the formation of Si-O-M units, accompanied by the generation of alkanes (Figure 1.3, (i)), whereas with metal acetylacetonate, metal directly bonded to Si releasing acetyl acetone, leading to the formation of Si-M (see Figure 1.3 (ii)). Although the interaction between PCS and metal alkoxide might be supported by FTIR and NMR [69], for both cases, there was no clear evidence for the formation of units of Si-O-M or Si-M. For instance, in the case of polycarbosilane reacting with zirconium (IV) acetylacetonate, the Si-Zr bond was indirectly predicted by the increase in the molecular weight during the cross-linking reaction and a significant decrease in the amount of Si-H. Furthermore, the ceramization of metal complex-modified PCS leads to Si-M-C-O ceramic fibers consisting of β-SiC/MC, which can also be considered as ceramic nanocomposites [70]. The other example is the synthesis of magnetic SiC nanowires, which involved the pyrolysis of an iron-containing polycarbosilane, in which SSPs were synthesized through the reaction of PCS and iron (III) acetylacetonate; XRD showed that β-SiC crystals were present together with diffraction lines related to Fe_5Si_3, Fe_3Si and FeC [71].

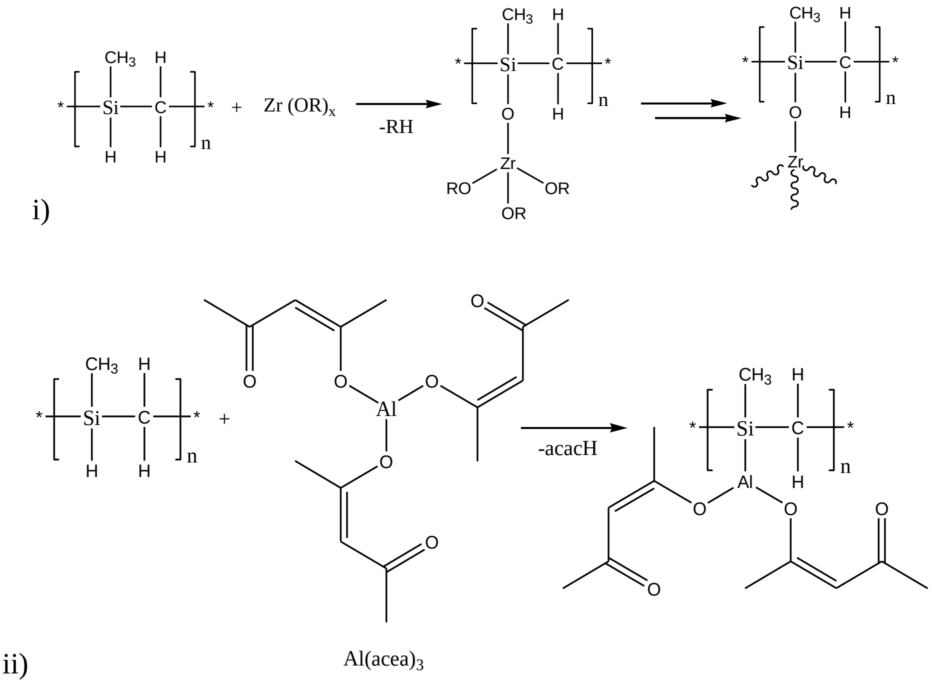

Figure 1.3. Chemical modification of PCS: (i) with metal alkoxies; ii) with metal acetyl acetonate.

Owing to polysiloxane having suitable functional groups (such as hydroxyl or alkoxy), they can be chemically modified with transition metal alkoxides. Ionescu *et al* [1-3] have intensively investigated the synthesis, ceramic conversion and microstructure evolution. They commonly used polysilsesquioxane and metal alkoxides (i.e., zirconium n-propoxide, hafnium butoxide) as starting materials. The reaction between polysilsesquioxane (PMS) with metal tetra(n-butoxide) is presented in Figure 1.4. In comparison to metal-containing free polysiloxane, it has showed a strong increase in the degree of cross-linking of the preceramic precursor due to the formation of Si-O-M (M=Hf, Zr). Furthermore, the phase and microstructure evolution within ceramic conversion and the subsequent annealing process were investigated. For instance, the hafnium alkoxide-modified precursor was shown to convert into an amorphous single phase $Si_xHf_yC_zO_w$ ceramic at temperature up to 800 °C. Subsequently, the amorphous ceramic pyrolyzed at 1100 °C in argon atmosphere, the metal oxide particles (size < 5 nm) precipitate (i.e. HfO_2 and ZrO_2) throughout the silicon oxycarbide matrix. By increasing the temperature up to 1600 °C, novel $HfSiO_4$/SiC/C ceramic nanocomposites can be generated, which showed excellent thermal stability compared to metal-free SiOC ceramics **[2]**.

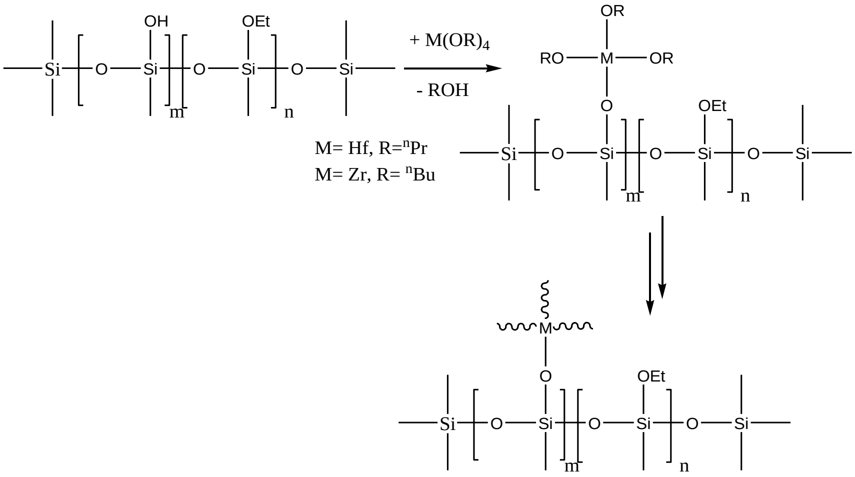

Figure 1.4. Chemical modification of a polysilsesquioxane with zirconium and hafnium alkoxides.

Among the various polysilazanes, perhydropolysilazanes (PHPS) are often used in the fabrication of Si_3N_4-based ceramics, due to them having some advantages in high purity and high ceramic yield. Iwamoto and his coworkers **[72]** synthesized poly-titanosilazanes by modifying commercial PHPS with TiX_4 ($X=N(CH_3)_2$, $OCH(CH_3)_2$), the prepared precursor was converted into Si_3N_4/TiN nanocomposites by pyrolysis at 1000 °C in NH_3. Furthermore, methlyl- and vinyl-substituted polysilazane (HTT1800) was also reacted with metal alkoxide, generating SiCN-based ceramic nanocomposites **[73]**. It is interesting, in the case of the synthesis of poly-titanosilazane, that the condensation reaction only occurs at the N-H groups, while the reaction of HTT1800 with hafnium n-butoxide takes place at both functional groups (N-H and Si-H) **[73]**. Additionally, cyclotrisilazane was also chemically modified with hafnium n-butoxide: The reaction only occurs at the N-H groups because no S-H bonds are present in this monomeric silazane. Furthermore, the microstructure and properties have a crucial connection to the architecture of polymer precursor. Both ceramic nanocomposites obtained from hafnium n-butoxide-modified CTS and HTT1800 were studied via microscopy (TEM and SEM, see Figure 1.5). As illustrated in the TEM image, both ceramics showed featureless amorphous structures confirmed by SAED. However, bright-field imaging in TEM typically reveals a dark contrast in regions where high atomic numbers are localized. Therefore, a local enrichment of hafnium was clearly observed in the HRTEM image of CTS. Moreover, thermal stability of both ceramics are shown to be highly different, the HTT1800-derived ceramic showed better high temperature stability with respect to decomposition at a temperature of 1600 °C, compared to CTS-based ceramics. The reason behind this is that hafnium dispersed homogeneously within the SiCN(O) matrix has a beneficial influence on the thermal stability, whereas the local enrichment of hafnium seems to separate from the SiCN(O) matrix **[73]**.

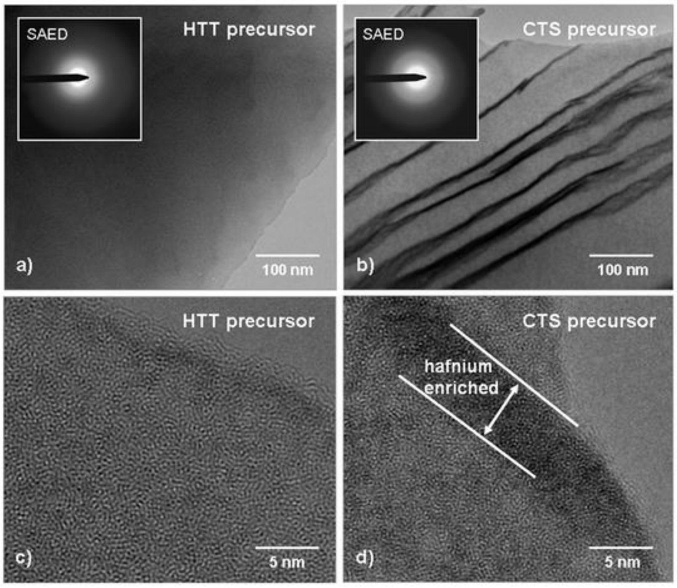

Figure 1.5. TEM bright-field images of the samples pyrolyzed at 1100 °C: (a and c) the HTT1800-based ceramic and (b and d) the CTS-based material (reproduced with the permission of Literature [73]).

Additionally, in the modification of polysilazane with early transition metal alkoxide or amido complex (M=Ti, Hf, Zr), it is interesting that only metal oxide or metal nitride/SiCN nanocomposites were generated. However, metals like Cu, Ni, Pd or Au lead to the formation of metal/SiCN or metal-silicide/SiCN nanocomposites [74, 75]. For instance, the aminopyridinato copper complex $[Cu_2(Ap^{TMS})_2]$ ($Ap^{TMS}H$=(4-methylpyridin-2-yl) trimethylsilanylamine) reacts with HTT1800 via aminopyridine elimination, ^{1} H and ^{13} C NMR studies of this reaction showed the liberation of protonated ligand $Ap^{TMS}H$ provide indirect evidence for the copper polycarbosilazane binding. Copper-coordinated polysilazane can be cross-linked and converted into copper-modified SiCN ceramics. SEM, EDS, and ^{65}Cu solid-state NMR confirmed the formation of crystallites and particles consisting of elemental copper [76]. R. Kempe *et al* synthesized palladium silicide nanoalloy particles/SiCN nanocomposites starting from HTT1800 chemically modified with a aminopyridinato complex [77].

1.3.2 Ultra-high temperature ceramics (UHTCs)

Within this section, a brief description of the state of the art concerning the research on UHTCs will be given. Among them, group IV transition carbide, nitride and borides and their properties are of particular importance and will be consequently emphasized.

1.3.2.1 UHTCs-Group IV transition metal carbides and nitrides

Transition metal carbides, nitrides and carbonitrides represent a class of materials with unusual combinations of outstanding structure properties, such as exceptional hardness, high melting points etc. (e.g. HfC having the highest melting points of all materials). Furthermore, the structure of this category is comprised of mixture of metallic, covalent and ionic bond, thus they exhibit a metallic character which shows high electrical and thermal conductivity [78].

Group IV transition metal carbides and nitrides have very broad ranges of composition which can be tailored by the C (or N)/M ratio of the upper maximum to 1. Moreover, their properties are influenced by the ratio of [C]/([C]+[N]), thus this behavior offers a large field for tailoring carbonitrides [78]. They also exhibit excellent thermal stability with respect to the decompositions, since it can be melted without decomposition.

Furthermore, since the density of state (DOS) of transition metal carbides at the Fermi level is lower than that of transition metal nitrides, the electrical properties of the carbides, such as electrical and thermal conductivity and the superconducting transition temperature, Tc, are lower than those of the nitrides. For instance, the DOS at E_F for HfN is higher than for HfC, which is corresponding well with observed electric resistivity (HfC: 67, HfN: 27 μΩ cm) as shown in Table 1.1.

Table 1.1. Physical properties of Transition Metal monocarbides and mononitrides

Material	Color	Lattice Parameter [nm]	Density [g/cm^3]	Hardness [GPa]	Young modulus [GPa]	Melting Point [°C]	Heat Conductivity [W/mK]	CTE [$\times 10^{-6}$/K]	Electric Resistivity [μΩ cm]
TiC	Gray	0.4327	4.93	28	450	3067	28.9	8.5	100
ZrC	Gray	0.4703	6.46	25	350	3420	24.6	7.5	75
HfC	Gray	0.4638	12.3	20	420	3930	25.1	6.1	67
TiN	Golden-yellow	0.4242	5.39	17	420	3050	29	9.9	27
ZrN	Pale-yellow	0.4570	7.32	15	460	3000	11	7.8	24
HfN	Greenish-yellow	0.4516	13.83	18	380	3330	11	8.5	27

Generally, transition metal carbides can be prepared from element or metal hydrides, at elevated temperatures (e.g. Ti + C = TiC). As the reaction between both elements is exothermal, such as with Ti and C, they can provide enough heating to keep up this reaction temperature. Accordingly, the reaction between the elements could be carried out in a self-propagating high temperature synthesis (SHS) [79]. However, the high cost of transition metal and metal hydride raw materials makes it disadvantageous for the synthesis of transition metal carbides. Thus, the carbothermal reduction of carbon and the corresponding metal oxides at low cost is suitable for the synthesis of transition metal carbides powders [80, 81]. However, in most cases, when starting from powder initially mixed together, the carbide-forming powders with relatively large particle size were obtained but did not prove suitable for further processing (e.g. hot pressing, spark plasma sintering). Accordingly, Sack *et al* synthesized a ZrC, HfC powder with fine-scale (nanometer size) by using solution-based processing;

moreover, the reduction reaction occurred at a relatively low temperature (<1500 °C), and the particle size of the resulting powder was estimated at 50~130 nm [80].

Transition metal nitrides can be prepared by a nitriding reaction between the metal or metal hydride and molecular or atomic nitrogen or flowing ammonia (e.g. $ZrH_2 + 4N_2 = ZrN + H_2$). During the nitriding process, the pressure of molecular nitrogen at a given temperature is necessary to obtain a specific nitride phase. Alternatively, the formation of nitrides from metal oxides can be performed by the presence of carbon as a reducing agent, such as $TiO_2 + 2C + ½ N_2 = TiN + 2CO$. Additionally, carbonitride powders are usually prepared by mixing carbide and nitride powders together, subsequently heating them to a high temperature [78].

Among the transition metal carbides and nitrides, carbide compounds are shown to have a higher melting point. One of the highest known melting temperatures of any material as shown in Table 1.1, HfC melts congruently at 3930 °C (see Table 1.1 for the melting temperatures of other carbide phases), while various nitrides also show extremely high melting point temperatures which can reach more than 3000 °C.

As discussed in the structure of metal carbides or nitrides, the mixing of metallic, covalent, ionic bonding is proposed, thus they exhibited good thermal conductivity (see Table 1.1). Furthermore, thermal conductivity increases with rising temperatures; however, it follows a non-linear relationship [82]. Moreover, the thermal conductivity of HfC exhibited strong stoichiometry dependence (Figure 1.6), which showed that the conductivity of the $HfC_{0.98}$ is two times that of the $HfC_{0.67}$. This decrease in the thermal conductivity can be attributed to increased phonon scattering from carbon vacancies in the sub-stoichiometric carbides [83].

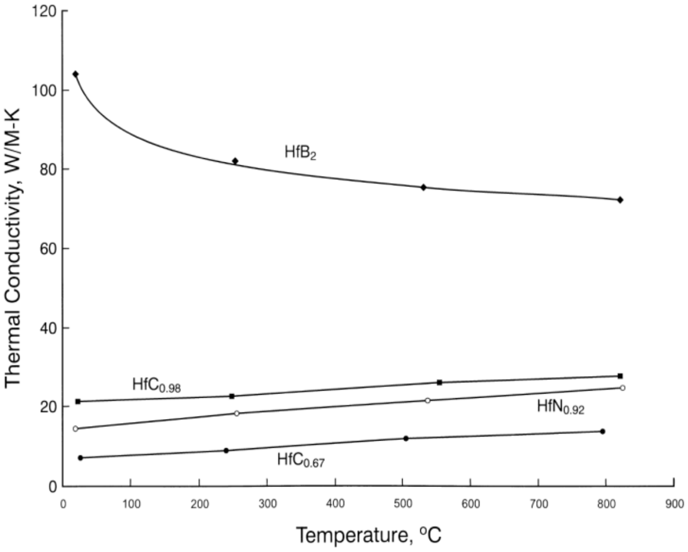

Figure 1.6. The thermal conductivity of hafnium carbides, nitrides and borides (reproduced with the permission of literature**[83]**).

Transition metal carbides, nitrides also exhibit excellent electric conductivity. Usually, the electrical resistivity of transition metal carbides is shown to be higher than that of corresponding transition metal nitrides (see Table 1.1). Furthermore, those electrical conductivities of each carbides or nitrides are greatly influenced by the ratio of nonmetal and metal, showing an increased trend with raising this ratio.

Thermal expansion is a very important property for transition metal carbides, nitrides and carbonitrides, because they are commonly used in combination with other materials (coated on the surface of metals, Si, SiC or Si_3N_4

etc.). The significant mismatch in thermal loading between carbide, nitrides phase and substrate might cause the spallation from the parent materials. Usually, the thermal expansion of this category is shown to be similar or higher than that of the corresponding metals (e.g. compared to the coefficient thermal expansion, 7.5×10^{-6}/K for ZrC to 5.7 $\times10^{-6}$/K for Zr). For the group IV carbonitrides, the thermal expansion can be expressed in a linear function with the temperature. Furthermore, the relationship illustrates that the CTE of Zr(C, N) has lower values among corresponding Ti(C, N) and Hf(C, N).

The Young's modulus of transition metal carbides, nitrides and carbonitrides generally exhibits higher values than that of the transition metals, e.g. Young's modulus of TiC and TiN shows around 450~460 GPa and 420 GPa, respectively, which is much higher than that of metallic Ti (110 GPa). Although a lot of information is available, the scattering of data is quite wide [84]; the elastic properties are shown to be affected by various conditions, such as compositions and types of samples. For instance, the E increased with raising the nitrogen content for the measured Young's modulus of nitrides (TiN_{1-x}, ZrN_{1-x} and HfN_{1-x}). Additionally, most of the thin film samples showed a higher Young's modulus than bulk samples. Also, there are large differences between the microhardness of bulk materials and thin films. This is probably due to different dislocation densities and grain sizes of both types of materials. Generally, transition metal carbides are very hard materials; moreover, the hardness rises with increasing carbon content for MC_{1-x} (e.g. TiC_{1-x}), which is probably related to the valence electron concentration (VEC) with a maximum stability at VEC=8. However, the opposite result is to be found in the microhardness of nitrides. They proposed that this behavior is a consequence of generating anti-bonding states which might cause lattice softening [78]. Additionally, the microhardness of the carbonitrides has an increasing trend with a rising [C] / ([C] + [N]) ratio.

1.3.2.2 UHTCs-Group IV transition metal diborides

Borides have exceptional properties due to a high amount of covalent bonding in combination with small band gaps or even metal-like transport properties [85]. This unique structure character results in a high melting point, along with high thermal and electrical conductivity. The crystal structure of group IV transition metal diborides is a primitive hexagonal (AlB_2-type), composed of layers of B atoms in a 2D graphite-like network alternating with hexagonally close-packed metal layers [86]. Thus, the unique combination of bonds (M-M, B-B and M-B) result in exceptional properties: For example, the strength of B-B and M-B bonds is responsible for hardness (23 GPa and 28 GPa for ZrB_2 and HfB_2 respectively, see Table 1.2). Moreover, Post. B *et al* proposed that the melting points of diboride is related to the strength of the Me-B bonds in these structures [87].

Table 1.2. Structural, physical, and mechanical properties of ZrB_2 and HfB_2.

Properties	ZrB_2	HfB_2
Crystal system space group	Hexagonal	Hexagonal
Prototype structure	P6/mmmAlB$_2$	P6/mmmAlB$_2$
Density (g/cm^3)	6.119	11.212
Melting temperature (°C)	3245	3380
Young's modulus (GPa)	489	480

Bulk modulus (GPa)	215	212
Hardness (GPa)	23	28
Coefficient of thermal expansion (K^{-1})	5.9×10^{-6}	6.3×10^{-6}
Electrical conductivity (S/m)	1.0×10^{7}	9.1×10^{6}
Thermal conductivity (W/mK)	60	104

Generally, reduction processes, reactive processes and chemical routes are commonly used to synthesize diboride powders [86]. In terms of reduction processes, carbothermal reduction is mostly used to produce ZrB_2 and HfB_2 on a commercial scale. These reactions are endothermic processes and strongly rely on a thermodynamically driving force: For instance, the formation of ZrB_2 generated from ZrO_2, B_2O_3 and reducing agent C has an enthalpy of reaction (ΔH) of 1475.6 KJ at 298K, thus a simultaneously reaction ($\Delta G < 0$) occurs when the temperature is above 1500 °C. Accordingly, the heating temperature was generally controlled at 2000 °C for the synthesis of ZrB_2 in this case [86]. In comparison with other reducing agents, the advantage of the reduction with B_4C mainly lies in decreasing the reaction temperature (e.g. a reaction temperature at 1200 °C for ZrB_2 and B_4C), and also reducing the amount of oxide impurities in non-oxide ceramics [88].

The diborides can also be produced by the simplest reaction between both elements (e.g. Hf and B). Since the reaction is exothermic and favorable at all temperatures, the reaction can be used to synthesize diboride by SHS [89]. In contrast to SHS, Fahrenholtz *et al* [90] produce nanosized ZrB_2 without igniting the SHS reaction using very fine powders of Zr (ca.10nm) and B; furthermore, the reaction temperature between Zr and B can be controlled as low as 600 °C.

Chemical routes used for the preparation of diborides are related to the thermal conversion of SSPs as well as the solution reaction between metal-containing powder and boron-containing polymers. The former illustrates the synthesis of titanium diboride ceramics which were converted from titanium borohydride ($Ti(BH_4)_3$) by thermal decomposition [91]. Moreover, the resulting powder was found to be fine crystalline at a nano-scale of 100-200 nm. The latter can produce much finer powder (nanocrystalline), nanocrystallines of ZrB_2 and HfB_2 have been prepared by the reaction between anhydrous chlorides (MCl_4) and sodium borohydride ($NaBH_4$) in the temperature range of 500-700 °C [92, 93]. Furthermore, the successful synthesis of diboride relies on the gas reaction between the decomposition product borane (BH_3), derived from $NaBH_4$ and gaseous chloride; the grain size of the final diboride was estimated at about 20 nm. L.G. Sneddon *et al* synthesized a series of MB_2 (M=Ti, Zr, Hf, Nb and Ta) by the latter route, a MB_2 powder was firstly achieved by dispersing metal oxides in the decaboranedicyanopentane polymer $(\text{-}B_{10}H_{12}NC\text{-}(CH_2)_5\text{-}CN\text{-})_x$, followed by pyrolysis of the precursor dispersions at above 1400 °C [94]. In the synthesis, the key requirements are *in-situ* generation of boron carbide and carbon within boron-containing polymers and the carbothermal reduction between metal oxide and that product [95].

The non-oxide ceramics with high thermal conductivity have been progressively used as structural components for engine-related material components. The thermal conductivities of ZrB_2 and HfB_2 showed the high values of 60 and 104 W/m·K respectively, facilitating heat-dissipating from substrates [83]. Previous studies have shown that the coefficients expansion in the c direction decreases with an increasing radius of the metal atoms [96], thus ZrB_2 and HfB_2 have lower coefficients of thermal expansion (CTE) of 5.9 and 6.3×10^{-6} K^{-1} respectively (Table 1.2) compared to those of TiB_2, TaB_2 and NbB_2. Additionally, the crack is commonly caused by the difference in the CTE between the matrix and the particulate, e.g. the CTE mismatch between SiC ($\sim 4 \times 10^{-6}$ K^{-1}) and HfB_2 (6.3×10^{-6} K^{-1}) produces microcracks at the HfB_2-SiC interface during the cooling process [97]. Generally, the secondary phase has the advantage of improving mechanical properties and reducing grain size of transition metal diboride matrix, due to the reinforced particles inhibiting the propagation of micro cracking or the nucleation of grain particles. However, the mechanical degradation might occur at the grain boundary with elevated temperature [98]. For example, in the case of HfB_2-20 vol% SiC prepared by hot pressing, some secondary phases containing oxygen-bearing phases with poor high temperature stability localized at triple points could impair the fracture strength of composites at higher temperatures. Additionally, some recent studies show that the Elastic modulus (E) and Hardness (H_v) of composites (e.g. ZrB_2-SiC) are dependent on the types of additives. For instance, additions of SiC ($H_v = 28$ GPa) to ZrB_2 result in a slight increase in hardness, while that of $MoSi_2$ (low hardness, $H_v = 9$ GPa) reduce the hardness of ZrB_2-based ceramic composites [99]. The fracture toughness of ZrB_2 and HfB_2 is generally at about 3.5 MPa $m^{1/2}$; basically, the higher fracture toughness can be achieved by incorporating the higher aspect ratio of additives (e.g. SiC platelets or rods/whiskers), Chamberlain *et al* reported that the significant increase in fracture toughness of ZrB_2-30 vol% SiC (5.3 MPa $m^{1/2}$) was compared to pure ZrB_2 [100].

1.3.3. Processing of PDCs and UHTCs

1.3.3.1 Ceramic Monoliths

The PDCs' route can be used to produce complex shaped monoliths by using the advantage of plastic forming technologies [55]. Generally, such a route includes tailored cross-linking of polymer precursors, followed by shaping and pyrolysis, high temperature annealing. The shaped polymer precursor at elevated temperature (e.g. warm pressing) is also considered as concurrent cross-linking. Moreover, the polymer precursors can be effectively bound together at lower temperature, thus making them easily being compacted before ceramization [101]. A cross-link treatment is necessary, not only to allow the ceramic yield to increase, but also to prevent micro cracks during pyrolysis. However, high cross-linking of the precursors has a negative effect on their potential in the shaping technique, this result in hindering plastic flow and creating residual porosity [102, 103]. Therefore, a suitable cross-linking parameter has a significant influence on the fabrication of dense monoliths. Furthermore, the shrinkage and *in-situ* formation of pores occur during the ceramization conversion due to oligomer, organic groups and gaseous products (CH_4, NH_3, H_2) released in the pyrolysis process, as shown in the flow chart of polymer to ceramic transformation presenting the evolution of polymer to crystalline ceramics in Figure 1.7. Obvious shrinkage could be observed. Hence, creating a monolithic that is crack-free and fully dense is one of the challenges in processing PDCs. Much effort has been devoted to obtaining dense monoliths ceramics, such as casting, injection molding and pressing. Pressing is the most commonly used technique in the preparation of monoliths, which includes cold isostatic pressing (CIP), uniaxial pressing (cold and warm), hot isostatic pressing, hot pressing, spark plasma sintering etc.

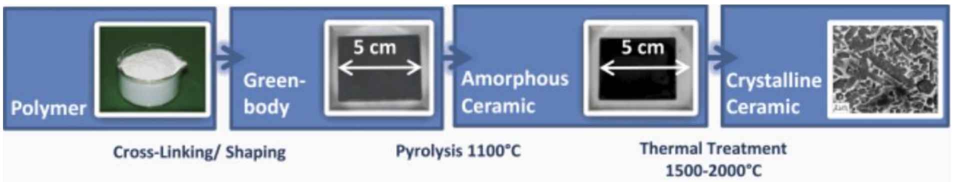

Figure 1.7. Polymer to ceramic transformation (reproduced with the permission of Literature **[55]**).

Accordingly, the infusible polymethylsilazane powders were shaped via CIP into green bodies which were converted into amorphous SiC_xN_y ceramics by subsequent pyrolysis under argon at 1000 °C. Thus, the relative density of 93% of the monolithic ceramic was achieved. The residual porosity is difficult to eliminate, because this porosity initially presented in the incomplete densification by CIP, or new pores were created during the pyrolysis process. Furthermore, comparing between cross-linked samples for 100min and 6h, it was found that highly cross-liked samples cannot be transformed into monoliths, due to their brittle nature [104]. In contrast, J. Bill *et al* [105] used warm pressing to shape SiCN monolithic ceramic based on a plastic-forming character of the polymer precursor. The results showed that a plastic-shaping polymer has a significantly lower porosity and a more homogenous microstructure [105]. Warm pressing has been proved effective route in processing of various precursor systems (e.g. SiCN [102, 103, 106, 107], SiOC [108], Si(Al)OC [109], SiBCN [110]. Moreover, optimal processing parameters rely on the type of precursor, as pressing temperatures usually vary from 120 °C to 350 °C for SiOC, SiC, SiCN etc. [102]

Fillers are added, mainly serving a role in reducing the shrinkage of the component by avoiding the micro cracks during ceramization. They can allow for different functions: Inert fillers do not react at all, such as SiC and Si_3N_4, they occupy space and reduce the volume fraction of polymer. Active fillers (metals or intermetallics, e.g. Al, Ti, Zr, B, Si) usually react with the decomposition products or in the pyrolysis atmosphere to form a new phase that retards the shrinkage of the original materials [60]. However, inert or active fillers prefer to form second phases, localized at the grain boundary, that commonly impair the mechanical and physical properties. Therefore, self-fillers pyrolyzed from the parent precursor can be a better choice; they can be obtained from complete or incomplete inorganic conversion. Self-fillers are considered as a "pure" system for matching the polymeric precursor, which can improve the ceramic yield and reduce the occasional formation of cracks.

The fabrication of UHTC monolithic materials has been traditionally accomplished by hot pressing (HP). High temperature and high pressure are required due to their strong covalent bonding and low self-diffusion. Hot pressing at temperatures ranging from 1700-1900 °C with higher pressures (800-1500 MPa) provides a means of preparing fine-grained dense monoliths without sinter additives [111]. Recent studies have found that reducing the particle size of starting materials can lower the HP temperature to achieve dense monolithic [100]. Additionally, the sinter additives were originally incorporated into pure diborides, carbides and nitrides to improve its strength, oxidation properties (e.g. SiC addition) and thermal stress resistance (e.g. C addition), rather than primarily considered as a potential advantage of fabrication. Interestingly, the hot pressing characteristics of pure HfB_2 and HfB_2-20 vol% were compared, clearly indicating that the SiC enhances the densification of HfB_2 by reducing the temperature and holding time required for a comparable density [29]. Spark Plasma Sintering (SPS) is similar to HP, in contrast, in that rapid heat rates (100-450 °C/min) supplied by direct heating through an electrical field facilitate rapid densification and hinder the growth of grains, leading to a much finer size. For example, in the case of ZrB_2-30 vol% ZrC-10 vol% SiC was fabricated by SPS and HP [112], the entire processing time took ~23min to obtain full density through SPS, which is much faster than the technique for HP (~140 min). Furthermore, refined and homogenous microstructures (grain size around 2 μm) were shown in SPS samples. Similar results were also observed in the comparison between HP and SPS for HfB_2-15 vol% $MoSi_2$ [113], HfB_2-30 vol% SiC-2 vol% $TaSi_2$ [114]. In contrast to HP and SPS, pressure-less sintering usually involves the shaping of starting powder under pressure, followed by sintering (densification without pressure), enabling the fabrication of complex or near-net shape monoliths. Moreover, the reduction of starting particle size and use of the sintering aids are effective methods for enhanced densification during pressure-less sintering [115].

1.3.3.2 Ceramic matrix composites (CMCs): polymer infiltration pyrolysis (PIP)

CMCs are promising candidates for the production of advanced high performance structures developed for applications in various fields like aerospace, energy, and the automobile industry [116], due to their outstanding properties (e.g. high fracture toughness [117], stability in aggressive chemical environments, high-temperature resistance, lightweight [118], etc.). They can be fabricated using different processing routes, such as chemical vapor infiltration (CVI) [119, 120], polymer infiltration pyrolysis (PIP, also called liquid polymer infiltration - LPI), as well as liquid silicon infiltration (LSI, also called melt infiltration), each of them with their own advantages and drawbacks. For instance, CVI offers high mechanical strength and strain capability of the obtained CMCs; however, the CVI preparation of CMCs is time consuming and expensive. Comparatively, the PIP/LPI methods can benefit from the low costs; furthermore, the PIP technique allows complex-shaped, large-scale components to be fabricated. Currently, commercial carbon fibers are generally used as reinforcements of CMCs; various C_f-based CMC systems were prepared using the PIP method, depending on the preceramic polymers used for infiltration. C_f/SiC CMCs can be obtained from poly(organosilanes) or poly(organocarbosilanes) [121], C_f/SiCN are prepared using poly(organosilazanes) for the PIP process [122]. Poly(organoborocarbosilazanes) are used for preparing C_f/SiBCN [123]. Due to the SiC fibers' excellent high temperature stability and oxidation resistance, SiC_f-based CMCs are known to be attractive materials for high-temperature structural applications (e.g. first wall and blanket components in fusion reactors) [124]. However, the use of SiC_f are expensive; few studies reported the fabrication of SiC_f-based CMCs by PIP, SiC_f/SiC [125], SiC_f/SiCN [126].

The properties of polymer precursors strongly influence the processing of CMC materials via the PIP methods. Especially the viscosity, the cross-linking behavior of the pre-ceramic polymer and the ceramic yield are important factors [127]. As mentioned before, during the transformation of the polymeric material to ceramic materials, volume shrinkage occurs along with the creation of porosity. The porosity can be reduced by repeating both the polymer infiltration (re-infiltration) and the pyrolysis several times. An increase in the ceramic yield of the preceramic precursors results in a lower number of infiltration cycles [55]. Nonetheless, porosity with a lower value (< 10%) could be quite difficult when the infiltration reaches its saturation degree. Moreover, the large inter-bundle voids and complete densification of fibrous preforms cannot be avoided via PIP methods. Almost eight or more cycles are necessary to reduce the porosity. The addition of inert or active fillers into matrix can reduce the cycles of infiltration and pyrolysis due to the excessive shrinkage of the ceramic matrix being limited by filler. Zhu *et al* [128] produced SiC_f/SiC composites by a modified polymer infiltration and pyrolysis process. The SiC and Al powders were introduced into large inter-bundle pores, resulting in a significant improvement of mechanical properties. Rak *et al* [129] employed a novel process to synthesize C_f/SiC, filling a 2D carbon fiber preform with a SiC powder by a pressure infiltration method before the infiltration of liquid preceramic polymers, leading to a highly shortened process time and equally lowered cost.

Additionally, many efforts focus on using hybrid processes to simplify the fabrication process and obtain dense C_f- or SiC_f-based CMCs with high mechanical and thermal properties, such as CVI+PIP [130-132], PIP+HP [125], PIP+LSI [133] etc. CVI is commonly used to deposit the interface (e.g. PyC and BN) or SiC-matrix, whereas LSI is utilized to fill the residual open porosity of composites prepared either by CVI or PIP.

1.3.4 Behavior of PDCs/UHTCs in harsh environments

PDCs and UHTCs are commonly used in harsh environments, e.g. exposure to high pressure in intermediate temperature (hydrothermal corrosion), oxidizing or steam corrosion environment in high temperatures, erosive conditions at extremely high temperatures (> 2000 °C). Thus, the properties assessment of the prepared materials (silicon-based ceramics, refractory carbides, nitrides or diborides composites etc.) is introduced briefly with respect to stability upon these harsh conditions.

1.3.4.1 High temperature oxidation behavior

The oxidation behavior of group IV transition metal carbides shows linear kinetics at low temperatures (up to 600 °C), because a porous HfO_2 scale is formed at such low temperature accompanying the evolution of CO_2 [134]. At higher temperature, the kinetics can be parabolic due to slower oxygen permeation into a dense scale. Shimada *et al* [134, 135] investigated more deeply, reporting that the oxide scale might consists of two regions in a temperature of 600 to 900 °C, zone 1 (HfC_xO_{1-x}) and zone 2 (HfO_2). HfC_xO_{1-x} locating at the interface between HfC and HfO_2 was found to be almost dense and pore-free phase. Thus, zone 1 seems to act as a diffusion barrier for oxygen permeation, leading to parabolic kinetics. Furthermore, experimental measurement and calculations indicate that the interlayer oxide is a better diffusion barrier for oxygen than either of the other layer based on the diffusion constants of oxygen in each of the three layers [136]. Additionally, the effect of carbide stoichiometry on oxidation behavior has also been studied [10]. $HfC_{0.67}$ had a thinner oxide scale than

$HfC_{0.98}$ in the identical oxidation test (< 1600 °C). The oxide on the subcarbide was also denser, with less porosity and cracking, than on the higher carbides.

The oxidation of group IV transition metal diborides have proved better resistance compared to those of carbides and nitrides. The pure diborides undergo stoichiometric oxidation to form the oxide product (e.g. ZrO_2, HfO_2) and boria (B_2O_3). Moreover, the mass gain of HfB_2 during oxidation has been shown to be significantly lower than ZrB_2 at all investigated temperatures [137]. At lower temperatures (< 1000 °C), a glassy B_2O_3 film is observed on top of the oxide scale (MO_2/B_2O_3) forming a continuous and dense layer, which can provide passive oxidation protection [138, 139]. Hence the mass gain or the thickness of the oxide layer for pure diborides show a parabolic behavior, indicating that the oxidation rate is limited by the transport of oxygen through B_2O_3 [140]. However, due to the evaporation of B_2O_3, liquid B_2O_3 starts to convert into a gaseous phase within the temperature range of 1000 and 1400 °C, leading to a loss of protection for diborides. Thus, the mass change is thought to be a combination of mass loss (evaporation of B_2O_3) and mass gain (ZrO_2, HfO_2); the oxidation kinetics is no longer parabolic. As the external layer B_2O_3 evaporated at higher temperatures, the oxide scale consists of residual B_2O_3 and porous ZrO_2, HfO_2, which is considered to weaken the protection for the matrix. When the oxidation temperature reaches above 1500 °C, the oxide layer no longer serves as a protective scale, resulting in the linear increase in the mass gain kinetics.

Silicon-based ceramics (e.g. SiC and Si_3N_4) are very important structural ceramic materials that show excellent stability for long-term, high temperature applications because oxygen permeation can be slowed by continuous oxide scale silica [141]. As shown before, PDCs exhibit good stability with respect to high temperature decomposition and creep resistance [142]. Oxidation property is alternative critical point for their considering as a structural ceramic in a high temperature application. There have been investigations of the oxidation behavior of PDCs with regard to the Si-C-N system [143, 144], Si-C-O [145], SiAlCN [8, 146], the Si-B-C-N [147, 148] and SiAlBCN [149] ceramic. They demonstrated excellent oxidation resistance compared to state-of-art CVD SiC and Si_3N_4 ceramics [150]. For instance, SiAlCN-based ceramics synthesized by SiCN polymer modified with Al-doped exhibited that the parabolic rate determined by the oxidation thickness for SiAlCN at 1200 °C is 10 times lower than the reported lowest values for CVD SiC and Si_3N_4 [8]. SiBCN ceramics have been considered as typically candidates for high temperature applications because their thermal stability in terms of decomposition up to 2000 °C [151]. Moreover, the *in-situ* formation of a thin amorphous dual layer oxide for $SiBN_3C$ ceramic fibers exposed under air limits oxidation diffusion in matrix [152]. Nickel *et al* [148, 153] studied that SiBCN ceramics have extremely thinner oxide scales than pure SiC or Si_3N_4 at 1500 °C in air exposure. However, gaseous silicon monoxide (SiO) formed at higher temperatures (depending on the oxygen partial pressure) is indicated, thus Si-based ceramics suffer primarily from active oxidation in this region [150, 154-156]. Thus, silicon-based ceramics cannot be fully taken into considerations when envisaging higher operational temperatures (≥ 1600 °C).

Due to the relatively poor oxidation resistance for pure diboride, the focus of research in the past few decades has been on improving their oxidation behavior, commonly using additives to pure diborides, most frequent here is SiC [157, 158]. Furthermore, the various compositions of SiC have been extensively investigated, indicating that 20 vol% addition exhibited the best oxidation behavior compared to counterpart compositions (10 vol and 30 vol%) [159]. Below 1100 °C, adherent borosilicate (SiO_2 plus B_2O_3) forms a continuous glass film, acting similar to B_2O_3(l) in controlling the oxidation diffusion, thus the oxidation rate is significantly decreased [160]. With higher temperatures (up to 1500 °C), the evaporation of boria probably increase the potential of internal oxygen. A porous oxide layer (HfO_2 or ZrO_2) however can be protected by a dense silica-rich layer; oxidation diffusion is still controlled by the oxygen through the silica layer [158, 161-163]. With the oxidation temperature beyond 1500 °C, the formation of a depleted SiC layer beneath a ZrO_2 (or HfO_2)-SiO_2 layer was found [164, 165]. Fahrenholtz [166] proposed a thermodynamic model to elucidate the development of SiC-depleted region that resulted from the active oxidation of SiC under the oxide scale. Furthermore, the outer SiO_2 is regained by the transport of SiO (g) which is derived from that SiC-depleted region. Hu *et al* [159, 167] recently found that the formation of the SiC-depleted layer significantly decreased the oxidation resistance of ZrB_2-SiC at temperatures above 1800 °C.

Besides, SiC additives, such as Si_3N_4, silicide ($MoSi_2$, Ta_5Si_3, $TaSi_2$) [168-171] and other diborides [12, 169], improve the oxidation resistance of diborides. Based on the purpose of stabilizing the oxide scale, the effective method to improve the oxidation behavior of UHTCs can be summarized as following:

i) The addition of a silicon-containing compound to the diborides leads to the formation a continuous and protective glass film (borosilicate), such as SiC, Si_3N_4, silicide etc.

ii) A Cr, Ta-containing compound induced immiscible glasses with higher viscosity, leading to a decrease in oxygen diffusivity and lower permeability to oxygen. Furthermore, doping the higher valence (i.e. $TaSi_2$ [171], Ta_2O_5 [31], TaB_2 [169]) into baseline materials ZrB_2-20 vol% exhibited improved oxidation resistance. This rely on the higher valence (i.e. Ta^{5+}) increases the scale adhesion by modifying the oxide scale with a cation that can insert into lattice. The lower concentration of oxygen vacancies decreases oxygen transport, which can lower the oxidation rate [170].

1.3.4.2 Corrosion behavior

In such an application (e.g. heat engine and heat exchanger structural components), these materials are not only exposed to an oxidized but also more severely corrosive environment (e.g. heat steam water vapor, CO_2, Na_2SiO_4 etc.), where silicon-based materials are mainly exposed to high-temperature water vapor [172]. The corrosion behavior under water vapor conditions generally involves the following: i) the formation of silica due to the oxidation reaction; ii) H_2O may alter transport properties through the silica scale, leading to an accelerated oxidation reaction. The formed silica occurs as degradation due to the formation of volatile products, such as $Si(OH)_4$. It is noted that reactions i) and ii) occur simultaneously [173].

Many studies have recognized the demand for studying the oxidation of SiC and Si_3N_4 in water-vapor-containing environments [174, 175]. The oxidation rate was shown that intrinsically increases in water vapor over oxygen atmosphere, resulting from the increased solubility of silica in the water vapor [175-177]. Furthermore, a bubble structure was observed in the silica scale, while the amount of bubbles and the oxidation kinetics increased along with the water vapor content [177]. The formation of bubbles in the silica scale was determined by various factors, such as temperature, the partial pressure of water vapor, crystalline or amorphous structure and the viscosity of silica etc. In the case of CVD SiC ceramics, the lack of bubbles in H_2O/O_2 (water vapor content < 90 vol%) mixtures at 1100 °C may contribute to an increase in the amorphous SiO_2 viscosity. Bubble formation seems to occur at 1200 and 1300 °C, while no bubbles were present in the silica scale at 1400 °C. The authors proposed that the higher solubility of gaseous products in crystalline SiO_2 supports the results [177]. However, the volatility of silica was attributed primarily to the formation of gaseous $Si(OH)_4$, leading to the degradation of silicon-based ceramics [156, 175, 178-180]. Opila *et al* employed paralinear kinetics to quantify the corrosion kinetics that included the water vapor-oxidized Si-based ceramics (e.g. SiC and Si_3N_4) and simultaneously volatilized the silica scale. Moreover, this paralinear kinetics can be monitored by weight changes (see Figure 1.8), oxide thickness, or material recession rates. A weight gain was observed within a short time due to the formation of a solid scale, changing to a weight loss after a short steady state with the prolonged soaking time concerning the volatile of the gaseous product ($Si(OH)_4$). Thus, the overall shape of the paralinear weight change curve is related to parabolic oxidation and linear volatility reactions.

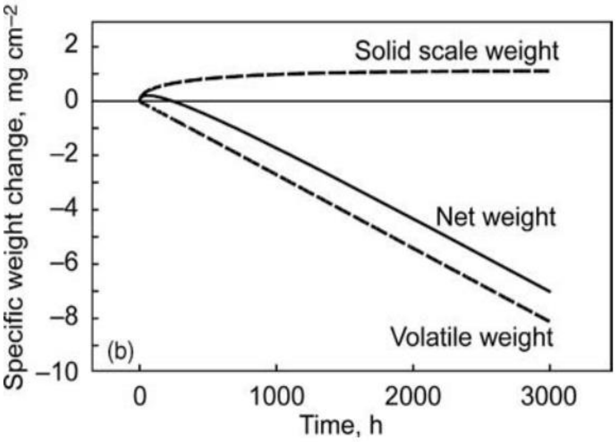

Figure 1.8. Paralinear oxidation kinetics in terms of weight change (Reproduced with permission from Literature**[178]**).

The corrosion behavior of PDCs in water vapor is also reported by An and co-workers, stating that polymer-derived SiAlCN ceramics exhibited much better oxidation and hot-corrosion resistance than other silicon-based ceramics at temperatures up to 1200 °C [173, 181]. The possible explanation for this result is that Al at the center of the six-member SiO_4 network within cristobalite is able to block the diffusion and strengthen the oxygen bond, leading to a lower corrosion rate.

Although a number of studies have reported on high-temperature oxidation and corrosion behavior of these materials exposed in air or combustion environments, there have been few reports concerning the corrosion behavior in intermediate temperatures and a high-pressure environment (e.g. hydrothermal conditions) for water nuclear reactor plants and petrochemical application.

The hydrothermal corrosion of SiC and Si_3N_4 has been summarized by the following reactions:

$Si_3N_4 + 6\ H_2O = 3\ SiO_2 + 4\ NH_3$; $SiC + 2\ H_2O = SiO_2 + CH_4$; $SiO_2 + 2H_2O = Si(OH)_4$

The corrosion behavior of Si-based ceramics generally exhibit active corrosion under hydrothermal conditions, thus, the dissolution of silica predominate in the corrosion behavior of SiC or Si_3N_4 without additives. Moreover, the solubility of Si_3N_4 under hydrothermal conditions show to be higher than that of SiC ceramics, leading to worse corrosion resistance for Si_3N_4 compared to SiC ceramics [182-184]. Previous studies reported that the grain-boundary would be easily attacked by corrosion at temperatures below 150-200 °C [183]. Therefore, the stability of the grain boundary phases determines the stability of the materials. Herrmann *et al* [185] investigated the hydrothermal corrosion behavior of Si_3N_4 with different additives at 210 °C. Materials with a low SiO_2 content in the grain boundary phase are more stable under hydrothermal conditions [185]. Moreover, the stability of silicon nitride materials under hydrothermal conditions strongly depends on the composition of the grain boundary. The Si_3N_4 with Al_2O_3/Y_2O_3 additives (YAl1) presented superior stability against corrosion, compared to that Si_3N_4 with other and without additives; it contributed to the formation of a passive layer (e.g. alumosilicate etc.). Based on the controlling interface, tailoring of the grain boundary composition of silicon nitride ceramics is necessary. Formation of rare earth-, Al- hydroxides may perhaps at least partially passivate the slow dissolution of grains [186].

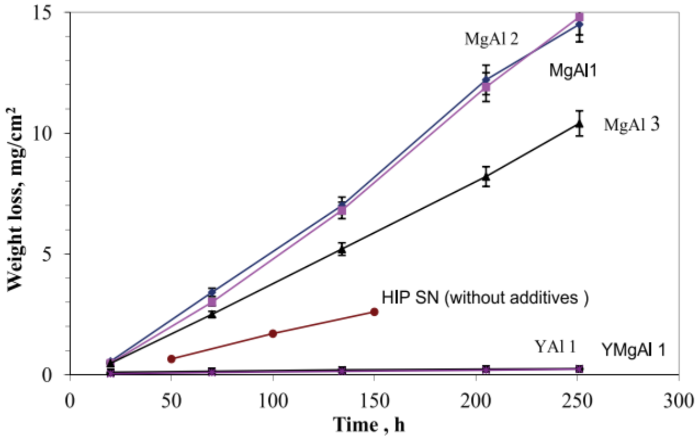

Figure 1.9. Hydrothermal corrosion of Si_3N_4 materials with different additive composition during corrosion at 210 °C.(Reproduced with the permission of Literature**[184]**).

At temperatures above 250 °C, as the higher solubility of SiO_2 occurred, the surface layer became less stable, which induced the pronounced dissolution rate of Si_3N_4 grains [185].

The corrosion behavior of SiOC-based ceramic nanocomposites (SiOC, SiZrOC and SiHfOC) under hydrothermal conditions was also investigated. The corrosion rates of SiOC derived from the SiOC polymer precursor were found to be much lower than typical SiC and Si_3N_4. Additionally, the incorporation of Hf and Zr into SiOC matrix can significantly improve the corrosion resistance under hydrothermal conditions. The possible reason for this result is that zirconia or hafnia precipitations act as “reinforcing” phases in improving the hydrothermal stability of SiOC matrix [4].

1.3.4.3 Ablation behavior

The increasing attention to UHTCs is driven by the need to develop reusable hot structures as thermal protection materials and systems (TPS) [187, 188]. Especially re-entry vehicles (e.g. crewed moon or Mars return missions) will be exposed to high velocity aero capture or extremely heated environments. Qualifying the limits of material performance, validating reliability and repeatability of performance are very important and necessary for evaluating the effects of material damage [189, 190]. Therefore, the re-entry environments need to be simulated and created for evaluating the materials' ablation behavior [191, 192].

Ablation is a very aggressive test because it involves high temperatures, high-velocity gas flows and oxidizing gases. Many testing techniques are available for evaluating the high-temperature ablation performance of UHTC materials, including oxyacetylene torch testing [193-198], plasma wind tunnel testing [199, 200], arc jet testing [192, 201-203] and laser ablation testing [204]. None of these test methods alone can reproduce all the conditions experienced during hypersonic flight. Wind tunnel tests can simulate the conditions of high enthalpy and strong gas flows, plasma art-jet ablation can partially simulate the re-entry environment. The parameters here may be simple, but they are costly. Oxyacetylene torch testing benefits from a quick and inexpensive technique, which has been usually considered as convenient tool for evaluating the ablation properties of materials. During the testing, an oxygen-rich flame used for testing needs to be tailored to stoichiometrically ratio between excess oxygen and acetylene, thus it is quite difficult to control the temperature and pressure more exactly. Laser has been commonly used for the development of materials in protecting against laser irradiation. Recently, the laser beam has also been used to evaluate the ablation behavior of C_f/SiC composites [204].

Ablation behavior is an alternative criterion for ceramic composites in aerospace applications, except for the oxidation/corrosion assessment. Moreover, the effective approach to improving the ablation resistance of ceramic composites (e.g. C/C, SiC) is incorporation of one or more ultra-high temperature ceramics (UHTCs) component into matrix. Tang *et al* [205] prepared a range of UHTC composites using five different mixes of aqueous UHTC powder slurries (ZrB_2, SiC, HfC and TaC). It was found that the addition of ZrB_2 showed a better ablation-resistive property compared to other additives under a high 3920 kW/m^2 heat flux. Furthermore, the effect of the gas ratios (different temperature and heat fluxes) on the ablation behavior was investigated. The composites containing SiC demonstrated the lowest erosion depth when the heat flux decreased down to 2380 KW/m^2 (1800 °C). A. Paul *et al* [206] also investigated the ablation behavior of five different composites including ZrB_2, ZrB_2-SiC, ZrB_2–SiC–LaB_6, HfB_2 or HfC. They found that Hf-based UHTC powders offered superior oxidation protection compared to Zr-based composites. Moreover, HfB_2 composites showed improved oxidation performance, only comparing two Hf-based composites of them.

1.4 Scope of the work

Many studies discussed how to synthesize ceramic nanocomposites by the sol-gel and polymer to ceramic transformation processes; however, the sol-gel route mainly focuses on the preparation of oxide-based ceramic composites, because it usually involves hydrolysis and a subsequent polycondensation process. The PDCs approach can yield non-oxide materials and include: i) incorporating reactive filler particles with a polymeric precursor; ii) blending two (or more) precursors of desired ceramic composites; and iii) synthesizing from polymer-based single-source precursors (SSPs). Among them, the SSPs approach exhibits a promising advantage in synthesis of nanocomposites, as novel ceramic nanocomposites can be easily synthesized by adjusting the compositions of SSPs, especially in transition IV metals and silica-formers polymer precursors.

UHTCs are those related to either very high melting point (above 3000 °C) or being used for long-term applications in harsh environments. Zr and Hf carbide, nitride, and boride are the most promising UHTCs. Furthermore, Hf-containing ceramics exhibit higher melting points, superior thermal conductivity, and better oxidation resistance than that of Zr-based ceramics. Based on these viewpoints, we focused on Hf-containing UHTC nanocomposites (UHTC-NCs) in our work. As adding a second phase (silicon-based ceramics) into the HfC, HfN, or HfB_2 ceramics can significantly enhance the mechanical properties and oxidation resistance, our synthesis of Hf-containing SSPs started from a silicon-based polymer precursor.

The formation of monoliths with a crack-free and dense microstructure is still a challenge in the processing of PDCs due to in-situ formation of pores. Optimizing the cross-linking and warm pressing conditions is essential for the synthesis of dense and crack-free PDCs. Additionally, silicon-based ceramic monoliths are difficult to densify, because of the low diffusion due to covalent bonding (Si-C, Si-N). Moreover, additional Hf composition makes them more difficult to consolidate because that increases the melting point. Therefore, developing dense Hf-containing UHTC-NCs is also a challenge, which requires understanding high-temperature decompositions and crystallization during annealing.

When considering real engineering applications at high temperatures**,** it is expected that components would inevitably be exposed to harsh (e.g., oxidizing/corrosive) environments. Thus, oxidation properties would be a primary consideration in material selection. Additionally, there is lack of related studies in the development of CMCs suitable for petrochemical applications characterized by moderate temperatures (several hundreds of °C) and high hydrothermal pressure. Fabrication of Hf-containing CMCs reinforced by carbon fibers by a low-cost and convenient approach might extend their application in high-temperature and high-pressure environments.

Accordingly, the objectives of our study are as follows:

i) To develop new Hf-containing UHTC-NCs with unique structure (HfC/SiC/HfB_2 or HfC/SiC/SiBCN);

ii) To obtain dense amorphous ceramic and UHTC-NCs ceramic monoliths;

iii) To evaluate the high-temperature stability (decompositions, crystallization), oxidation, hydrothermal corrosion, and ablation behaviors of those UHTC-NCs in harsh environments.

2. EXPERIMENTAL PROCEDURES

This chapter presents the experimental and characterization methods within this work. Section 2.1 illustrates the synthesis of single-source precursors SiHfCN and SiHfBCN as well as the polymer to ceramic conversion. Section 2.2 introduces the process for obtaining monoliths via warm pressing and SPS route, ceramic matrix composites (CMCs) via polymer infiltration pyrolysis (PIP). Section 2.3 summarizes the characterization methods which will be applied. Section 2.4 systematically investigates the behaviors of materials in harsh environments, including high temperature decomposition and crystallization, high temperature oxidation, hydrothermal corrosion as well as laser ablation.

2.1 Materials Synthesis

The synthesis of the polymeric SSPs SiHfCN and SiHfBCN was carried out in a purified argon atmosphere using the Schlenk technique. In contrast to the synthesis of SiHfCN, one additional reaction needs to be carried out for SiHfBCN, namely hydroboration. Thus, the SSPs SiHfCN can also be considered as an intermediate product during the synthesis of SiHfBCN.

i) 10.8 ml of polysilazane HTT 1800 (Clariant, Sulzbach am Taunus, Germany) were dissolved in anhydrous toluene in a 250 ml three-necked Schlenk flask equipped with inlet connection and magnetic stirrer. 1.2 ml or 4.8 ml (10 vol% and 30 vol% with respect to HTT1800) of tetrakis(diethylamido)hafnium ($Hf(N(Et)_2)_4$, Sigma, Aldrich), were dissolved in 20 ml toluene and added dropwise to the solution of HTT1800, and then stirred for 2 h at ambient temperature. The resulting solution was labeled as M1 and used for the synthesis of SiHfBCN. The liquid with high viscosity was achieved after removing the toluene in a vacuum at 50-60 °C (single-source precursor SiHfCN).

ii) The mixture obtained from M1 was cooled down to -50 °C by using isopropanol and dry ice. 2.4 ml or 0.6 ml of borane dimethyl sulfide complex ($BH_3.(CH_3)_2S$, Sigma Aldrich) were dissolved in 10 ml toluene and added dropwise to the mixture solution which was subsequently stirred for 2 h at -50 °C, then allowed to reach room temperature and stirred for 24 h. After the removal of the solvent in a vacuum at 50-60 °C, a viscous liquid was obtained (single-source precursor SiHfBCN).

iii) The obtained single-source precursors were cross-linked at 200-250 °C (heating rate 50 °C/h, dwelling time 3 h, different cross-linked temperature were shown in different precursors, see Section 2.2 on yielding yellow solids which were warm-pressed (P/O Weber, Remshalden, Germany, Mold diameter 10mm). The obtained green bodies were pyrolyzed at 1100 °C (heating rate 25-50 °C/h, dwell time 2 h, pyrolysis program see Section 2.2) to obtain the amorphous SiHf(B)CN ceramic monoliths.

2.2 Processing

2.2.1 Ceramic monoliths

Figure 2.1 presents two process routes to synthesizing ceramic monoliths: i) pressure-less sintering (PLS) and ii) pressure-assisted sintering (PAS). In the first route, the cross-linked polymer was firstly obtained after heating to 200-250 °C during 3 h in argon flow (horizontal furnace, GERO-furnaces, Germany). As the samples were still sensitive to air or moisture after cross-linking, thus the cross-linked powder had to be ground finely in a glove box. Approximate 0.25 g of fine powder were filled into the pressing mold and then consolidated by warm pressing apparatus to form a green body (Ø 10 mm, thickness of 3mm). Subsequently, the green body was transferred into a Schlenk tube in a glove box and then pyrolyzed up to 1100 °C. The parameters used for cross-linking, warm pressing and pyrolysis are given in Table 2.1. Additionally, the pyrolyzed monoliths were put in the graphite mold for annealing in the Graphite-furnace (GT&AT, Advanced technology, USA). Their behavior upon annealing is to be discussed in Chapter 3.3.

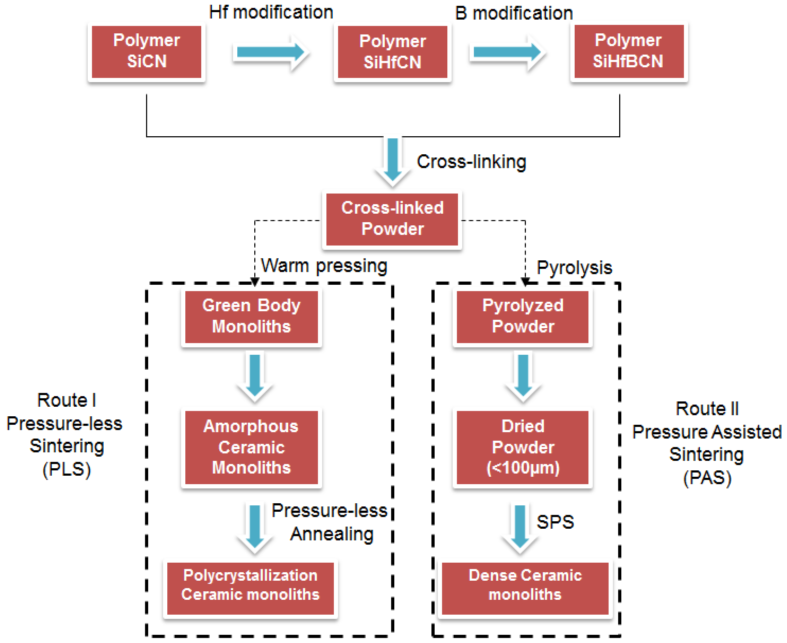

Figure 2.1. Processing route to preparing ceramic monoliths.

Table 2.1. Optimized parameters for cross-linking, warm pressing and pyrolysis.

Pre-ceramic precursor	Sample names	Cross-linking temperature/ Dwelling time	Warm pressing temperature/ Dwelling time, pressure	Pyrolysis program
SiCN	SiCN	250 °C/3 h	180-190 °C/1 h, 30MPa	RT–100 °C/h-300 °C-50 °C/h-400 °C-25°C/h-600 °C-50 °C/h-1100 °C

SiHfCN	SiHfCN1	250 °C /3 h	300 °C /1 h, 30MPa	RT–100 °C/h-300 °C-50 °C/h-400 °C-25^{o}C/h-600 °C-50 °C/h-1100 °C
	SiHfCN2	200 °C / 3 h	280 °C /1 h, 30MPa	RT–100 °C/h-300 °C-50 °C/h-400 °C-25^{o}C/h-600 °C-50 °C/h-1100 °C
SiHfBCN	SiHfBCN1	200 °C/3 h	240-260 °C/1 h, 30MPa	RT–100 °C/h-300 °C-50 °C/h-400 °C-25^{o}C/h-600 °C-50 °C/h-1100 °C
	SiHfBCN2	200 °C/3 h	280 °C/1 h, 30MPa	RT–100 °C/h-300 °C-50 °C/h-400 °C-25^{o}C/h-600 °C-50 °C/h-1100 °C

For the PAS route, the SSPs SiHfCN2 and SiHfBCN2 were cross-linked at 250 °C for 3 h and afterwards ground to fine powder respectively. The cross-linked powders were then pyrolyzed at 900 °C to deliver ceramic powders. As the smaller particle size provided high surface area energy, prior to densification, the pyrolyzed powders were suspended in *n*-hexane and wet milled in planetary ball mill using a Si_3N_4 ball (180 rpm, 18 h). The particle size after solvent removal in a rotation evaporator and drying was minimized below 100 μm.

The spark plasma sintering of these ceramic powders was conducted in vacuum in a SPS apparatus (Dr. Sinter 2050, Sumitomo Coal Mining Co. Ltd., Tokyo, Japan). For each test, ~1.2 g of ceramic powders were packed into a cylindrical graphite die with an inner diameter of 12 mm. A radiation pyrometer focused on a 5 mm drilled hole in the outer wall of the die was employed for controlling the temperature (Figure 2.2). The temperature was automatically raised to 600 °C over a period of 3 min, after which different sintering regimes were performed varying the sintering temperature (1850 or 1950 °C, as for SiHfCN and SiHfBCN, respectively), dwell time (1, 10, or 15 min) and uniaxially applied pressure (55~120 MPa). For all cases, a high heating rate of 450 °C/min was applied (unless specified) with a default on: off=12:2 pulse sequences.

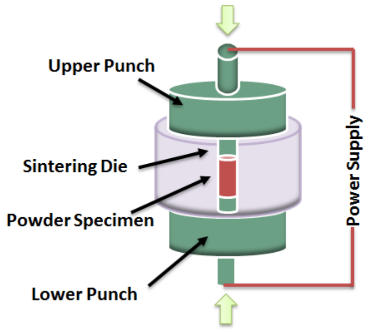

Figure 2.2. SPS schematics.

2.2.2 Ceramic matrix composites (CMCs)

2.2.2.1 Preparation of C_f/SiCN and C_f/SiHfBCN

A 2D carbon fabric (T300, manufactured by Toray) was used for the preparation of the carbon-fiber-reinforced CMCs. Polysilazane (HTT1800, AZ-EM, Wiesbaden, Germany) and a polysilazane-based SiHfBCN precursor were considered as pre-ceramic precursors for the PIP fabrication of the composites. The carbon fabric was cut into rectangular pieces with dimensions of 44 mm ×16 mm. After the infiltration with the pre-ceramic precursor, 16 pieces of carbon preforms were stacked onto each other within a Teflon mold (Figure 2.3 a) in a manual layering process in order to provide the fiber preform with ca. 3.5 mm thickness. After a curing step, the composites were pyrolyzed in a tube furnace (1100 °C, Ar) to furnish C_f/SiCN and C_f/SiHfBCN-based CMCs (Figure 2.3 b). The obtained samples were re-infiltrated and pyrolyzed up to 7 times. The specimens were cut and machined into rectangular coupons with dimensions of 44 mm × 3 mm × 3 mm. In order to reduce the open porosity, the specimens were re-infiltrated with HTT1800 or SiHfBCN precursors by using one more infiltration prior to the hydrothermal corrosion experiments.

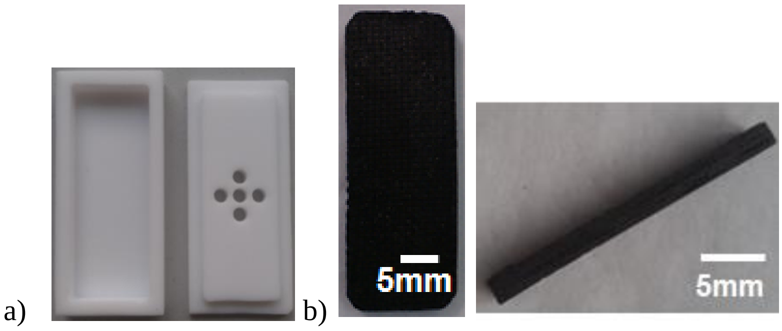

Figure 2.3. Photographs of the Teflon mold used for the manual layering process (a) and of the prepared C_f/SiHfBCN CMCs (b).

2.2.2.2 Preparation of C_f/SiC-SiCN and C_f/SiC-SiHfBCN

The C_f/SiC composites with the dimensions 40 × 5 × 3.5 mm fabricated by CVI (chemical vapor infiltration) with 4 times infiltration are provided by Northwestern Polytechnical University. The density, open porosity and bending strength of the C_f/SiC samples initially prepared by the CVI technique are presented in Table 2.2. The carbon preforms were prepared by stacking plain weave carbon cloths (T-300). Prior to depositing the SiC matrix, a thin pyrolytic carbon layer was deposited on the surface of each carbon fiber by the CVI process (960 °C). The preforms were treated with a graphitization process at 1800 °C for 2 h. Subsequently the SiC matrix was deposited in the preforms by CVI. This was on the one hand done in order to increase the stiffness and prevent damage during the machined process of C_f/SiC. On the other hand, the samples treated after CVI should provide enough space for infiltration of pre-ceramic precursor SiCN and SiHfBCN. Thus, the numbers of re-infiltration SiC matrix samples treated by CVI might be controlled within 4 times, the open porosity of the obtained C_f/SiC composites was estimated at 27.5 %, which is suitable for further infiltration. The C_f/SiC-SiCN and C_f/SiC-SiHfBCN were obtained by re-infiltration and pyrolysis of C_f/SiC up to 7 times.

Table 2.2. Physical properties and bending strength of C_f/SiC used for the infiltration of polymer precursor SiCN and SiHfBCN.

Ceramic matrix composites	Density [g·cm^{-3}]	Open porosity [%]	Bending strength [MPa]
C_f/SiC	1.52	27.5	187±43.31

2.3 Characterization

2.3.1 Attenuated total reflection FTIR (ATR-FTIR) and FTIR

The synthesized single-source precursors were analyzed by means of attenuated total reflection FTIR spectroscopy (ATR FTIR) on a Bruker Vertex 70 FT-IR instrument (Bruker, USA). The spectra of the cross-linked and ceramic powders were recorded by the same machine in transmission geometry, using KBr pellets.

2.3.2 Raman spectroscopy

Raman spectra (5 scans, each lasting 10 s) were recorded from 200 to 4000 cm^{-1} on a confocal Horiba HR800 micro-Raman spectrometer (Horiba Jobin Yvon, Germany) equipped with an excitation Ar laser in this work, the laser wavelengths of 514 and 633 nm were used.

2.3.3 Nuclear magnetic resonance (NMR) spectroscopy

The ^{1}H, ^{29}Si of liquid SSPs SiHfCN1 and non-modification SiCN was characterized using a 500 MHz Bruker DRX 500 spectrometer. It has to be noted that the quality of the measurement depends on the solubility of the samples in the solvent. The SSPs SiHfCN1 and SiCN with their low viscosity are only suitable for standardized characterization. The C_6D_6 was used as a solvent, and the spectra of tetramethylsilane (TMS) ($Si(CH_3)_4$) as an external reference.

All MAS NMR experiments were performed on a Bruker AVANCE II+ spectrometer at 400 MHz proton resonance frequency, employing a Bruker 4 mm double resonance MAS probe at spinning rates of 12 kHz at room temperature. Single pulse (SP) ^{29}Si NMR spectra were recorded using a 90^{o} pulse of 9 µs and recycle delays of 120 s. In contrast to SP ^{13}C NMR spectra, a 90^{o} pulse of 4µs and recycle delays of 20 s were adopted. ^{29}Si and ^{13}C NMR chemical shifts were externally referenced to ($Si(CH_3)_4$). In the case of ^{11}B NMR, chemical shifts were referenced with respect to trimethyl borate.

2.3.4 Simultaneous thermal analysis (STA)

Thermogravimetry coupled with evolved gas analysis (EGA, i.e. in situ mass spectrometry, QMS 403C Aëolos, IPI and FTIR Tensor 27, Bruker Optics) was performed in argon and synthetic air atmospheres (STA 449C Jupiter, Netzsch Gerätebau GmbH). For investigations of in-situ high temperature decomposition at up to 1900 °C, thermogravimetry was performed in helium and nitrogen (STA 409 CD/7/G So, Netzsch Gerätebau GmbH, Selb). Oxidation experiments performing both non-isothermal and isothermal progress in synthetic air were performed by simultaneous thermal analysis (TG-DTA, STA 429, Netzsch Gerätebau GmbH, Selb).

2.3.5 Elemental analysis (EA)

For elemental analysis, a carbon analyzer Leco C-200 (Leco Corporation, USA) was used to determine the carbon content and an N/O analyzer Leco TC-436 (Leco Corporation, USA) to determine the oxygen and nitrogen content in the samples. The content of hafnium was estimated by energy-dispersive X-ray spectroscopy (EDS) which was performed with an EDAX Genesis spectrometer (FEI, Eindhoven, Netherlands) attached to a high-resolution scanning electron microscope (HR-SEM, Philipps, Netherlands). The samples were sputtered with a gold layer prior to investigation.

2.3.6 X-ray diffraction (XRD)

X-ray powder diffraction was obtained in flat-sample transmission geometry on a STOE STAD1 P (STOE & Cie. GmbH, Germany) equipped with monochromatic Mo Kα radiation at a scan speed of 1°/min in the 2theta range of 5-45°, and the monolithic samples were analyzed using D8 Advance diffractometer (Bruker, USA) with Cu Kα radiation in a reflection mode. The scan step size was 0.05°, and in the reflection range of 10-80°. The identification of the phase was analyzed using the program STOE WinXPOW. Phase fraction and lattice constants were obtained upon Rietveld refinement of the powder XRD patterns (software: Fullprof_suite).

2.3.7 Scanning electron microscopy (SEM)

Scan electron microscopy (SEM) was performed using FEI Quanta 600 instrument (FEI, Eindhoven, and The Netherlands). The specific samples with transition metal phases were identified using a FEI Quanta 600 instrument equipped with a back scatter affiliate (BSE). The samples used for SEM were sputtered with a gold layer (5-10 nm).

2.3.8 Transmission electron microscopy (TEM)

Transmission electron microscopy (TEM) measurements were performed using a JEM2100F (JEOL, Tokyo, Japan) operating at 200 kV equipped with the X-MAX 80 EDX system (SDD detector, Oxford Instruments, Oxford, UK). The powder samples were pulverized and dropped on a carbon-coated copper grid followed by light carbon coating to minimize charging under the incident electron beam. The ceramic monoliths samples were cut, polished by both sides until a thickness of maximum 10μm was reached and mounted on a molybdenum grid, followed by ion milling for electron transparency. To minimize charging under the incident electron beam, a light carbon coating was used.

2.3.9 Specific surface area measurement

The specific surface area (S_{BET}) values were calculated by the Brunauer, Emmett and Teller (BET) method, the BET surface area of pyrolyzed ceramic powders (SiCN, SiHfCN and SiHfBCN) and monoliths were measured by N_2 sorption analysis (Quantachrome Autosorb-3B, Quantachrome, USA).

2.3.10 Microindentation and nanoindentation

The hardness and elastic modulus was measured using a Micro Hardness Control unit (Fischer Scope H100, Germany) and Nanoindentation with a standard Berkovich indenter (iNano from Nanomechanics Inc. Oak Ridge, TN, USA). The samples were mounted in epoxy, ground using diamond-grinding 220, 600 and 1200, and then polished (largo 9 μm, DUR 6 μm and MOL 3 μm, each polishing step took 2 min), after fine polishing by OPS for 2 min. Single indentation load-displacement responses were measured using loads of 50 mN and 1000 mN (microindentation) as well as 45mN (nanoindentation).

2.3.11 Three point and four point bending strength

The fracture strength of the samples prepared by hybrid techniques were measured using a three-point bending test with a span of 30 mm (Sanscmt 4304, Shenzhen, China), that of the samples prepared by PIP were analyzed by four-point bending test with a lower span of 20 mm, an upper span of 10 mm and a crosshead speed of 0.5 mm/min at room temperature (Z010, Zwick/Roell, Germany).

2.4 Behavior of as-prepared materials in hostile environments

The prepared ceramics materials (e.g. powder, monoliths and ceramic matrix composites) are selected and used for properties assessment, i.e. powder and monoliths for the analysis of the oxidation properties, hydrothermal corrosion and laser ablation were assessed for CMC materials. These are presented in Figure 2.4.

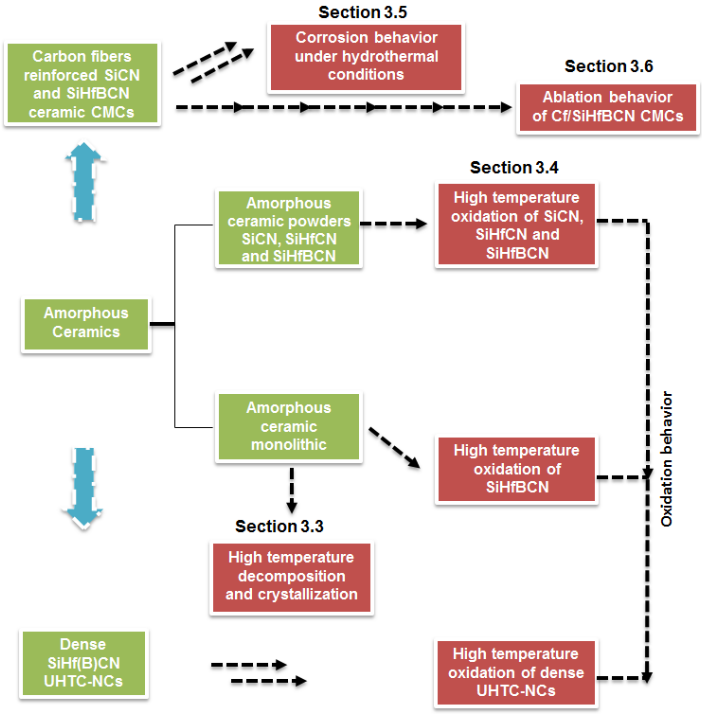

Figure 2.4. Flow chart of the studied properties and processing of the synthesized amorphous and UHTC-NCs ceramics.

2.4.1 High temperature crystallization and decomposition

In order to investigate the high temperature behavior with regard to decomposition and crystallization, the amorphous ceramic monoliths were annealed in a high-temperature graphite furnace at 1300, 1500 and 1700 °C in an argon or nitrogen atmosphere. In the subsequent discussion, a nomenclature code for the prepared SiHfCN and SiHfBCN ceramics will be used as described in Table 2.3. Polysilazane (HTT1800) was also cross-linked, warm pressed, pyrolyzed and further annealed at up to 1700 °C for comparison.

Table 2.3. SiHf(B)CN-based samples prepared within the present study.

No	Sample name	HTT1800 : $Hf(NEt_2)_4$ volume ratio	Annealing temperature	Annealing atmosphere
1	SiHf(B)CN1a_1300	90 : 10	1300 °C	Ar
	SiHf(B)CN1a_1500		1500 °C	
	SiHf(B)CN1a_1700		1700 °C	
2	SiHf(B)CN1b_1300		1300 °C	N_2
	SiHf(B)CN1b_1500		1500 °C	
	SiHf(B)CN1b_1700		1700 °C	
3	SiHf(B)CN2a_1300	70 : 30	1300 °C	Ar
	SiHf(B)CN2a_1500		1500 °C	
	SiHf(B)CN2a_1700		1700 °C	
4	SiHf(B)CN2b_1300		1300 °C	N_2
	SiHf(B)CN2b_1500		1500 °C	
	SiHf(B)CN2b_1700		1700 °C	

2.4.2 Oxidation Experiments

2.4.2.1 Oxidation testing of amorphous materials

The oxidation experiments of powder samples were performed using a Thermogravimetric (TG-DTA, STA 429, Netzsch Gerätebau GmbH, Selb, Germany). Ceramic powders used for oxidation testing pyrolyzed at 1100 °C were firstly suspended in *n*-hexane and subsequently wet milled using Si_3N_4 balls (180 rpm, 18 h). The average particle size after solvent removal and drying was ca. 7 μm. The characterization of samples including SiCN, SiHfCN and SiHfBCN are listed afterwards in the Table 2.4. ~80 mg of sieved powder was placed in the Al_2O_3 crucible and then transferred into the balance located in the furnace chamber of the TGA machine, where the empty Al_2O_3 crucible was also put on the other side of the balance for reference. Oxidation tests were performed at temperature from 1200, 1300 to 1400 °C for 5 h at a heating rate of 5K/min in synthetic air with a gas flow of 75 ml/min. The mass change was recorded *in-situ* and used for calculating the oxidation kinetics.

For the oxidation studies of amorphous ceramic monoliths, the surface to test specimens with a diameter of 7.5 mm and thickness of 2.2 mm were ground and polished with diamond paste up to 1 μm. Subsequently, the polished samples were cleaned in acetone using ultrasound and dried at 100 °C in the oven. The oxidation test of the monoliths was performed in the alumina furnace at the same simulated temperature as that of powder. In any designed temperature, the samples were performed for 100~200 h and the weight changes were recorded at the interval time in the analytical balance with an accuracy of ± 0.01 mg.

Table 2.4. Characterization of SiCN, SiHfCN and SiHfBCN ceramic powders pyrolyzed at 1100 °C.

Sample	Average size [μm]	specific surface area [$m^2 \cdot g^{-1}$]	Element composition						
			C	O	N	Hf	Si*	B*	Empirical Formula
SiCN	7	6.64	19.5	4.3	21.5	-	54.7	-	$SiC_{0.83}N_{0.79}O_{0.14}$
SiHfCN	7	2.40	10.7	3.2	18.8	21.0	46.3	-	$Si\ Hf_{0.07}C_{0.54}N_{0.81}O_{0.12}$
SiHfBCN	7	4.71	12.7	2.4	18.4	22.5	38.2	5.8	$SiHf_{0.09}B_{0.4}C_{0.78}N_{0.97}O_{0.11}$

* The silicon fraction of SiCN, SiHfCN were calculated as the difference to 100 wt-% of the sum of the wt-% values of carbon, nitrogen, oxygen or hafnium (for SiHfCN), assuming that no other elements are present in the samples. The silicon and hafnium fraction of SiHfBCN was estimated using quantitative electron Dispersive Spectroscopy (EDS), the boron fraction of SiHfBCN were calculated according to the difference method.

2.4.2.2 High temperature oxidation of SiHf(B)CN-based SPS UHTC-NCs

The oxidation behavior of dense SiHfCN- and SiHfBCN-based monolithic samples having dimensions of 3.7 mm × 3.85 mm × 2.2 mm and 3.35 mm × 4 mm × 2 mm respectively, were evaluated by means of TGA in air atmosphere, at 1400 and 1500 °C. Two different heating regimes were applied, namely T-1 and T-2. (T-1): non-isothermal run up to 1500° C in flowing dry air (75 cm^3/min), heating rate of 5 °C/min and then an isothermal run at 1500° C for 10h; (T-2): non-isothermal run in flowing argon, and then an isothermal run at 1400° C for 5 h in flowing dry air (75 cm^3/min), with subsequent free cooling. T1 was performed on a simultaneous thermal analysis device (STA 429, Netzsch Gerätebau GmbH, Selb), while T2 was performed on STA 449C Jupiter® (Netzsch Gerätebau GmbH, Selb).

2.4.3 Hydrothermal Corrosion

The hydrothermal corrosion experiments were carried out in closed steel autoclaves with a Teflon inlet (Figure 2.5) at temperatures of 150, 200 and 250 °C for 48, 96 and 240 h. The hydrothermal pressure within the autoclaves at the mentioned temperatures was 0.5, 1.5 and 4 MPa, respectively. Prior to the hydrothermal corrosion, the Teflon inlet of the autoclaves and the samples were cleaned in acetone using ultrasonic and then dried at 80 °C for 12 h. In order to vary the S/V ratio, different surface areas of the specimens were used in a defined deionized water volume (6.5 ml); the detailed information is available in Table 2.5. After the tests, the samples were removed from the autoclaves, rinsed with distilled water and then dried and weighted. Moreover, the pH value of the corrosion medium was determined. Each corrosion experiment was repeated three times in order to ensure the reproducibility of the corrosion results.

Figure 2.5. Photograph of autoclave and Teflon inlet used for hydrothermal corrosion experiment.

Table 2.5. S/V ratios of the hydrothermal experiments performed with the CMCs.

Sample dimensions W × T × L [mm × mm × mm]	Sample Surface [cm^2]	S/V ratio
3×3×20	2.5 ± 0.1	0.4
3×3×8.5	1.2 ± 0.1	0.18
3×3×2.5	0.45 ± 0.05	0.075

2.4.4 Laser Ablation

The ablation test was carried out by applying a continuous CO_2 laser beam (wavelength: 10.6 µm) of 1000 W. The targeted a circular spot (TEM00 Gaussian Beam) with a diameter of 3 mm at the center of the specimens which were recorded as having the dimensions of 10 × 4.5 × 3.5 mm. The 2D C_f/SiHfBCN was exposed under laser for 0.2, 0.5 and 1 second in air conditions.

3. RESULTS AND DISCUSSIONS

3.1. Materials synthesis

The synthesis of SiHf(B)CN-based UHTC-NCs first requires the synthesis of the SSPs, namely, SiHfCN and boron-containing SiHfBCN, via thermal conversion during the pyrolysis of a cross-linked precursor followed by further annealing at high temperatures (> 1400 °C). In this section, the focus will be placed on the characterization of the SiHfCN and SiHfBCN SSPs as well as their structural evolution during thermal pyrolysis. Because of the influence of the atmosphere on decomposition and crystallization, Hf-containing UHTC-NCs were synthesized in a subsequent annealing process, which will be discussed in Section 3.3 along with their high-temperature behavior.

3.1.1 Synthesis of SSPs for SiHf(B)CN

Novel Hf-containing polymeric SSPs for the synthesis of SiHf(B)CN ceramics were successfully prepared starting from a commercially available polysilazane containing Si-H and Si-vinyl groups (HTT1800). In the first step, the polymer was chemically modified via a reaction with a tetrakis (diethylamido) hafnium complex. In the second step, the hafnium-containing polymer was reacted with a borane-dimethyl sulfide complex, yielding the single-source precursor for the SiHfBCN ceramics.

The chemical modification of the polysilazane HTT1800 with $Hf(NEt_2)_4$ was investigated using FTIR spectroscopy and liquid NMR (Figure 3.1 and Figure 3.2). The FTIR spectrum of HTT1800 exhibits the typical absorption bands for the N-H (3378 cm^{-1}), C-H (2960 and 2965 cm^{-1}), Si-H (2124 cm^{-1}), C=C (1560 cm^{-1}), Si-CH_3 (1256 cm^{-1}), Si-N-H (1160 cm^{-1}) and Si-N (930 cm^{-1}) groups (Figure 3.1 (i)). The N-H, Si-H, and vinyl (C=C) groups are the active groups in HTT1800. Upon modification with the Hf complex $Hf(NEt_2)_4$, the intensities of the N-H and Si-H absorption bands in SiHfCN decreased compared with their counterparts in pure HTT1800 (Figure 3.1 (i) and (ii)). Moreover, the intensities of the N-H and Si-H groups in SiHfCN2 were found to be lower than those in SiHfCN1, indicating a higher content of $Hf(NEt_2)_4$, facilitating the reactions between Si-H/N-H and Hf-$N(Et)_2$. After the cross-linking of the SiHfCN1/2 polymer precursors at 250 °C, the N-H and Si-H intensities were further reduced. A stronger decrease was observed in the cross-linked SiHfCN2 (Figure 3.1 (v)), suggesting that a higher degree of cross-linking was achieved with higher content modification. Additionally, the intensity of the vinyl group remained unchanged among (i) and (ii), (iii), suggesting that no reaction with the vinyl group occurred during the modification with $Hf(NEt_2)_4$. However, a decreased intensity of the vinyl group (C=C) was observed in (iv) and (v), suggesting that the vinyl group was involved in the cross-linking reactions (e.g., polycondensation and hydrosilylation).

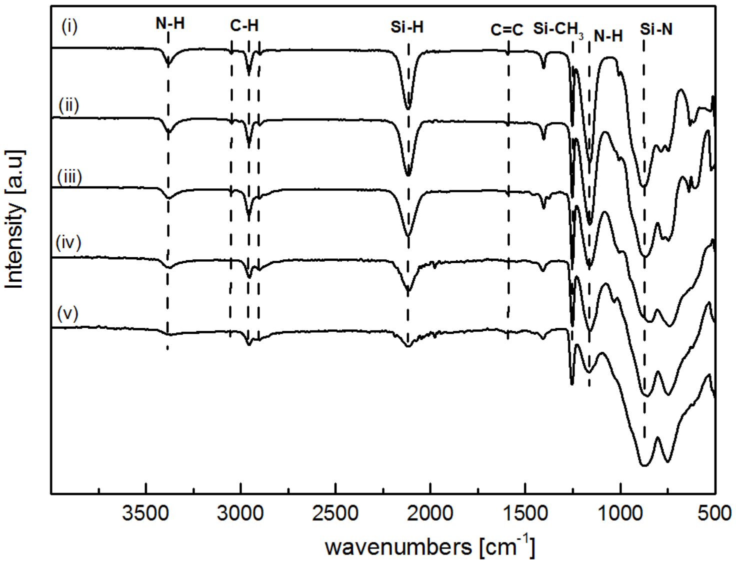

Figure 3.1. FTIR spectra of i) HTT1800, ii) HTT1800 modified with 10 vol% $Hf(NEt_2)_4$ (SiHfCN1), iii) HTT1800 modified with 30 vol% $Hf(NEt_2)_4$ (SiHfCN2), iv) HTT1800 modified with 10 vol% $Hf(NEt_2)_4$ and cross-linked at 250 °C and v) HTT1800 modified with 30 vol% $Hf(NEt_2)_4$ and cross-linked at 250 °C.

The liquid ^1H NMR spectra of HTT1800 and SiHfCN1 are presented in Figure 3.2a, exhibiting peaks with chemical shifts at 0.15-0.4, 0.5-1.1 and 4.4-5.0 ppm, which are associated with the $\equiv Si-CH_3$, Si-NH-Si and Si-H environments, respectively. The signals of the vinyl group ($\equiv Si-CH=CH_2$) are located at 5.5-6.3 ppm. In addition to these peaks, which are observed in both spectra, new signals located at 0.8 and 1.8 ppm are present in the spectrum of SiHfCN1; these signals are associated with the ethyl group in $Hf(NEt_2)_4$. Obviously, the peaks with decreasing intensity correspond to the Si-H and N-H groups, and the lack of variations in the vinyl-group signals confirms the FTIR results.

The ^{29}Si spectrum (Figure 3.2b) exhibits an evident peak with a chemical shift of -23.8 ppm, which is ascribed to $SiHC(sp^3)N_2$ and is observed in both the HTT1800 and SiHfCN1 spectra. Furthermore, weak signals at -33.5 ppm, which are associated with silicon in the $(N)_3SiVi$ (vinyl group) environment, are present in the liquid spectra of both precursors. The shoulder at -25.8 ppm beyond the $SiHC(sp^3)N_2$ environment, associated with the $SiN_3C(sp^3)$ group, is evident only in the SiHfCN1 spectrum, indicating that Hf may have bonded to Si-N through an Hf-N-Si linkage. However, the signal of the SiN_3C group seems to be largely subsumed by that of SiN_2C, indicating a fairly low SiN_3C content [207].

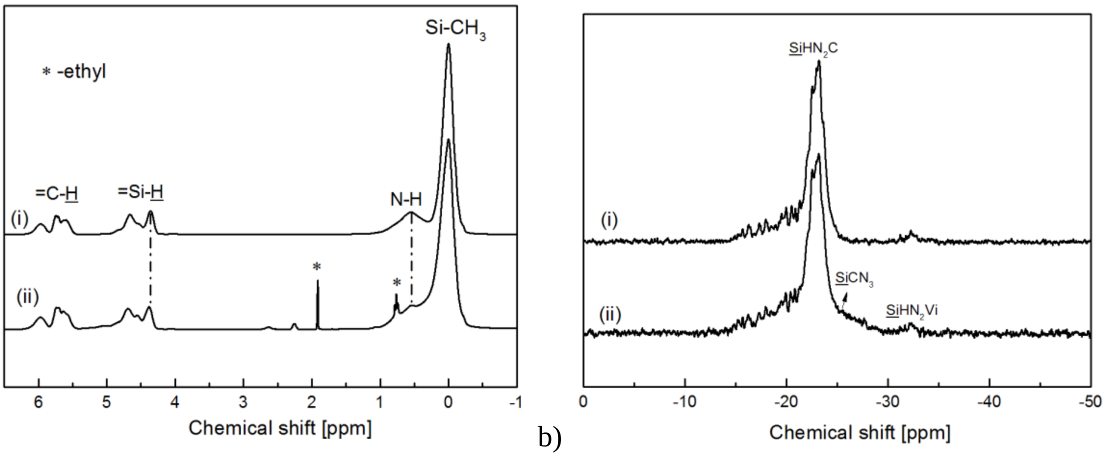

a) b)

Figure 3.2. Liquid NMR spectra of HTT1800 (i) and SiHfCN1 (ii): a) ^{1}H and b) ^{29}Si.

The chemical modification of the polysilazane HTT1800 with $Hf(NEt_2)_4$ and $BH_3{\cdot}SMe_2$ was also investigated using FTIR spectroscopy. In Figure 3.3a, the FTIR spectra of the pure polysilazane and of the polysilazane after its reaction with $Hf(NEt_2)_4$ and subsequent modification with $BH_3{\cdot}SMe_2$ are shown. In the FT-IR spectrum of HTT1800, typical absorption bands related to the C-H (2960 and 2965 cm^{-1}), N-H (3378 cm^{-1}), Si-H (2124 cm^{-1}), Si-N-H (1160 cm^{-1}) and Si-N (930 cm^{-1}) groups are observed.

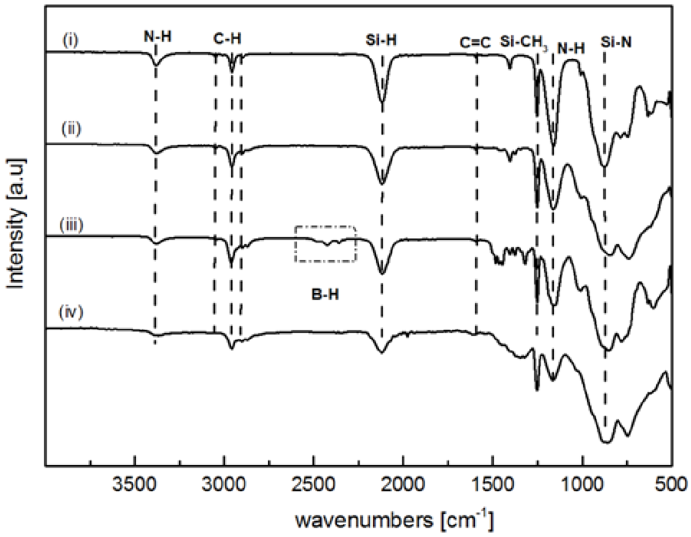

a)

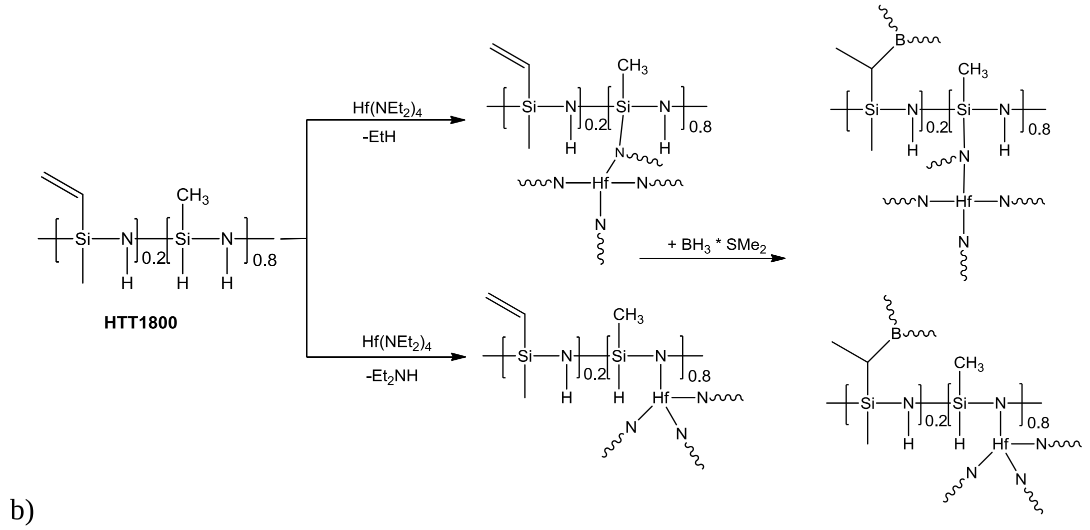

Figure 3.3. a) FTIR spectra of HTT1800 (i), Hf(NEt$_2$)$_4$-modified HTT1800 (ii) and HTT1800 modified with both (iii) as well as HTT1800 modified with Hf(NEt$_2$)$_4$/BH$_3$.SMe$_2$ and cross-linked at 250 °C (iv); b) Proposed reaction pathway of HTT1800 with Hf(NEt$_2$)$_4$ and BH$_3$.SMe$_2$.

The chemical modification of HTT1800 with Hf(NEt$_2$)$_4$ caused the intensities of the absorption bands related to the N-H and Si-H groups to decrease, indicating that the reaction occurred at the Si-H/N-H substituents of HTT1800 (see Figure 3.3b), whereas the vinyl groups in HTT1800 (absorption bands at 3053 and 1598 cm^{-1}) were not affected by the reaction with the hafnium amido complex (Figure 3.1 and Figure 3.3a). HTT1800 also exhibits a similar chemical reactivity, i.e., a reaction with both the Si-H and N-H groups of the polymers, in the case of the reaction of HTT1800 with a hafnium alkoxide [73]. Upon the addition of BH$_3$.SMe$_2$, hydroboration of the vinyl groups of HTT1800 occurred (Figure 3.3b). The presence of the absorption bands related to the vinyl groups (3053 cm^{-1}(=C-H) and 1598 cm^{-1}(C=C)) and to B-H bonds (2477 cm^{-1}) in the Hf- and B-containing single-source precursor illustrates, however, that not all vinyl groups of the polysilazane were involved in the reaction. This may be related to steric hindrance effects on the chemical modification of the polysilazane [208].

The FTIR spectrum of the polymer precursor cross-linked at 200 °C (Figure 3.3a) shows the disappearance of the B-H bands and thus indicates the occurrence of cross-linking reactions relying on hydroboration and dehydrocoupling within the polymeric backbone.

The ^{29}Si spectrum of the cross-linked polymer cured at 200 °C (Figure 3.4) exhibits a signal at -24 ppm, associated with the SiHC(sp^3)N$_2$ sites (compared to -35 ppm for SiHC(sp^2)N$_2$, see [207]). Furthermore, a signal at -31 ppm corresponds to the SiC(sp^3)N$_3$ sites, and a third signal at -3.5 ppm has been attributed to the SiC(sp^3)$_2$N$_2$ sites [207] (see Table 3.1). Thus, the ^{29}Si NMR data of the cross-linked single-source precursor indicate that the hydroboration and vinyl polymerization reactions occurring under those conditions led to the transformation of the sp^2 hybridized carbons of the vinyl groups into sp^3 carbon sites[207]. Moreover, all three signals show a low-field shift as compared to other SiCN-based materials[207] , which may be due to Hf being bonded to the SiC$_x$N$_{4-x}$ tetrahedra and thus decreasing the electron density at the Si sites (see also the discussion below on the NMR data of the obtained ceramic nanocomposites). This indicates consequently that the chemical modification of HTT1800 leads to the formation of a single-source precursor for SiHfBCN.

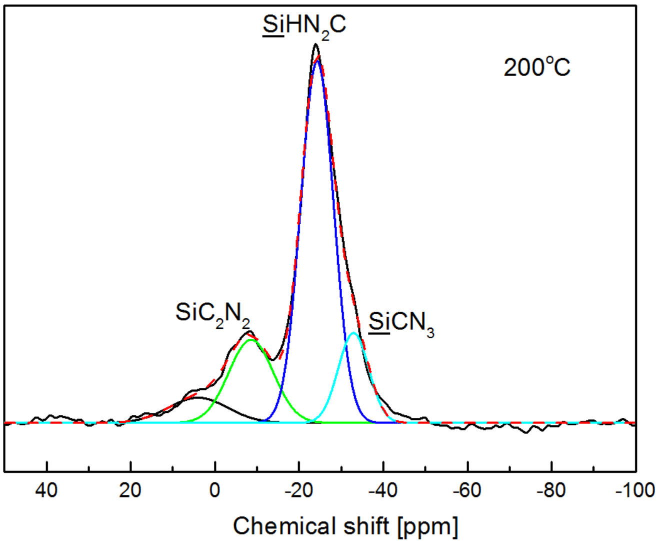

Figure 3.4. ^{29}Si MAS NMR spectrum of HTT1800 modified with Hf(NEt$_2$)$_4$ and BH$_3$·SMe$_2$ and cross-linked at 200 °C.

Table 3.1. Chemical shifts and site fractions of SiC$_2$N$_2$, SiHCN$_2$, and SiCN$_3$ sites derived from Gaussian line fitting of the ^{29}Si NMR spectrum in Figure 3.4.

	SiC$_2$N$_2$		SiHCN$_2$		SiCN$_3$	
	δ (ppm)	Site fraction (%)	δ (ppm)	Site fraction (%)	δ (ppm)	Site fraction (%)
200	-3.5	26.2	-24	60.0	-31	13.8

3.1.2 Polymer-to-ceramic conversion

The thermal conversion of the Hf- and B-containing single-source precursor into amorphous SiHfBCN was investigated via TGA coupled with evolved gas analysis (EGA) and was found to be quite similar to that of an Hf-containing polymer into amorphous SiHfCN, as shown in Figure 3.5, with the polymer-to-ceramic conversion proceeding in three main steps (as seen from the DTG curve) and resulting in a ceramic yield of approximately 80 wt %. This is significantly higher than the ceramic yield of HTT1800 (approximately 65 wt %) and is also considered to be a consequence of the strong increase in the cross-linking degree of the polymer upon its modification with Hf(NEt$_2$)$_4$ or with Hf(NEt$_2$)$_4$ and BH$_3$.SMe$_2$. At temperatures beyond 800 °C, no mass loss was recorded; thus, the polymer-to-ceramic transformation was concluded to be complete at this temperature. The cross-linking of the hafnium-containing polymeric precursor primarily relies on hydrosilylation and vinyl polymerization processes, as has also been reported for other Si-H- and Si-vinyl-substituted polysilazane-based polymers [209-212]. These processes occur without mass loss and contribute to a significant increase in the ceramic yield of the single-source precursor compared with that of the Hf- and B-free polysilazane. Additionally, transamination processes between the ≡Si-N=/≡Si-N and ≡Si-N=/≡Hf-N= groups occur, releasing amine fragments, as indicated by mass spectrometry data collected during EGA (see Figure 3.5). Thus, during the decomposition stage at temperatures beyond 400 °C, the mass loss is related to the evolution of hydrogen and methane as well as to ethane and diethylamino fragments. The hydrogen release is attributed to dehydrocoupling reactions occurring between Si-H and N-H groups or B-H and N-H groups, leading to the formation of ≡Si-N= and =B-N= linkages (for SiHfBCN materials), respectively [208, 212]. The release of methane and ethane occurs due to the decomposition of the organic substituents of the single-source precursor, whereas the development of the diethylamino fragments is attributed to the decomposition of the -NEt_2 end groups of the precursor or to transamination processes between ≡Si-N= and ≡Hf-N= groups.

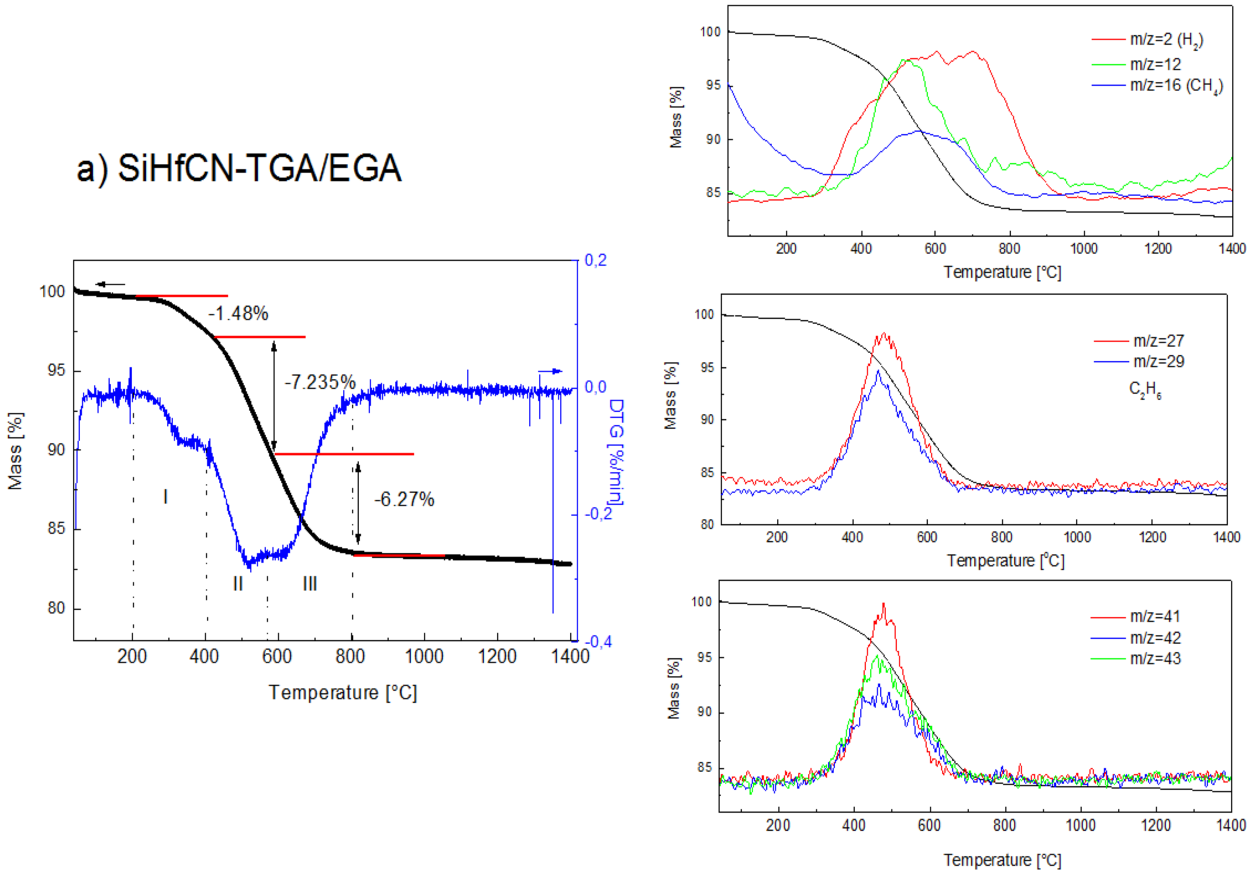

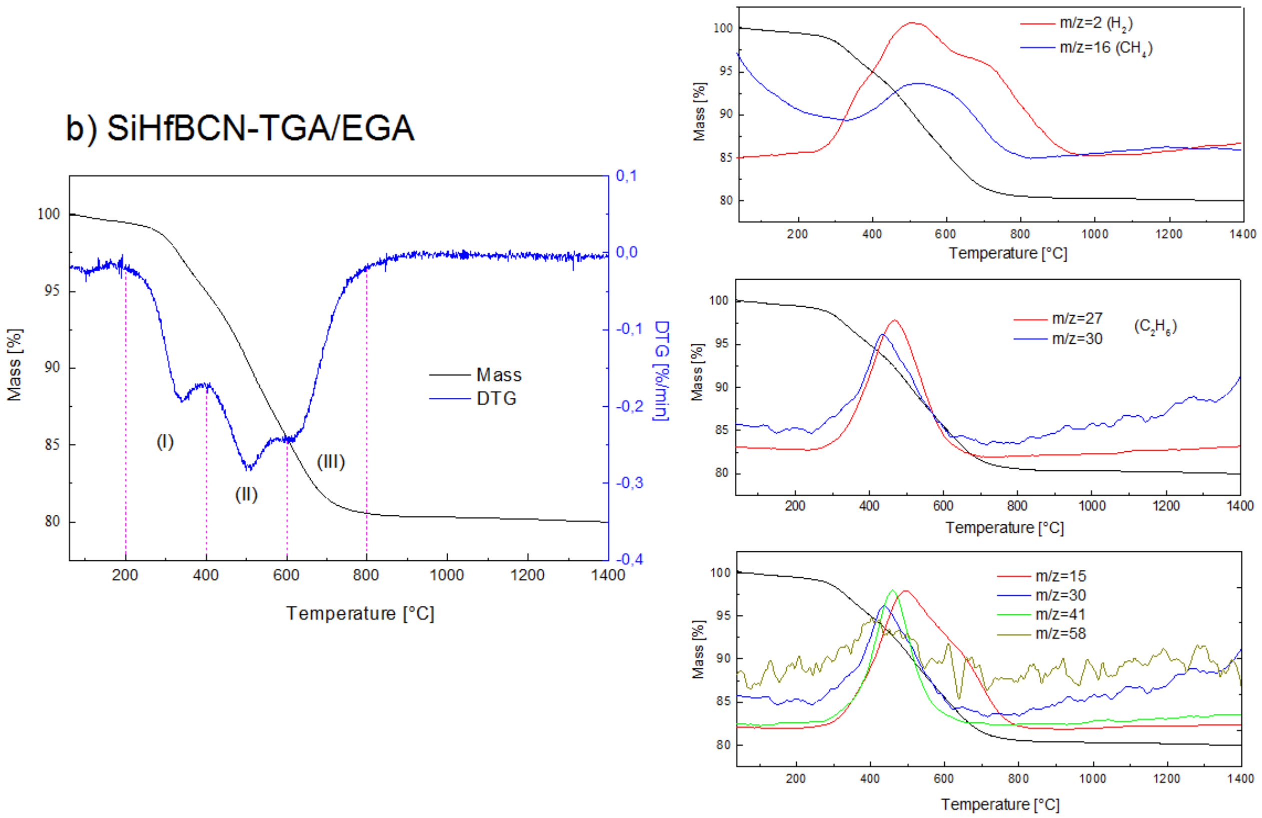

Figure 3.5. Thermogravimetric analysis and mass spectrometry QMID ion current curves (QMID—quasi multiple ion detection) of cross-linked a) SiHfCN2 and b) SiHfBCN2 showing the release of hydrogen (m/z=1, 2), methane (m/z=16), and ethane (m/z=27. 30) and diethylamido fragment (e, m/z= 41, 42 43 and 58) during the polymer to ceramic conversion.

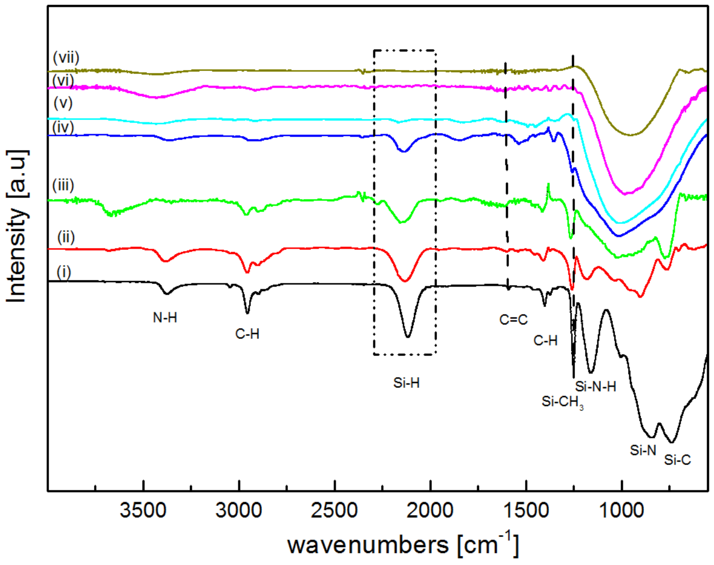

Figure 3.6. FTIR spectra of SiHfCN2 after the cross-linking of the precursor and subsequent pyrolysis in flowing argon from 200 to 1300 °C: i) polymer, ii) 200 °C, iii) 400 °C, iv) 600 °C, v)800 °C, vi) 1100 °C, and vii) 1300 °C.

The FTIR spectra of polymeric and pyrolytic SiHfCN2 products obtained at various temperatures from 200 to 1300 °C are presented in Figure 3.6. When the IR spectrum of cross-linked SiHfCN2 at 200 °C is compared with that of the polymer, it is evident that the intensities of the absorption signals ascribed to C-H, Si-H, the vinyl group and Si-N-H are significantly reduced, suggesting that hydrosilylation, and vinyl polymerization occurred during the cross-linking step. Upon an increase in temperature to 400 °C, the intensities of these bands continue to follow a decreasing trend; the vinyl group even disappears, representing an end to the process of vinyl polymerization. The IR spectra of samples exposed at higher temperatures, between 400 and 600 °C, indicate that the significant decrease in intensity of the Si-CH_3 band and the Si-H/N-H band can be explained by the evaporation of methane and hydrogen and also confirm the observation of hydrogen and methane as detected via EGA (Figure 3.5). At temperatures beyond 800 °C, the major change is that the signals corresponding to Si-H, Si-CH_3 and N-H, C-H vibration disappear completely, indicating the elimination of any residual hydrogen from the precursor. Accordingly, the inorganic conversion can be considered to be complete at this temperature. Additionally, the peaks at 840 and 730 cm^{-1}, attributed to Si-N and Si-C, shift toward a higher wavenumber range. Furthermore, the formation of a broad peak is observed in the spectrum of the sample pyrolyzed at 1100 °C, indicating the emergence of an amorphous phase structure consisting of a mixture of the bands between Si-C and Si-N.

In addition to the TGA/EGA *in situ* investigation, *ex situ* MAS NMR spectroscopy was performed to obtain more information about the polymer-to-ceramic process. Thus, ^{13}C, ^{29}Si and ^{11}B MAS NMR spectra of samples obtained upon the thermal treatment of the single-source precursor at 400, 800 and 1100 °C were collected.

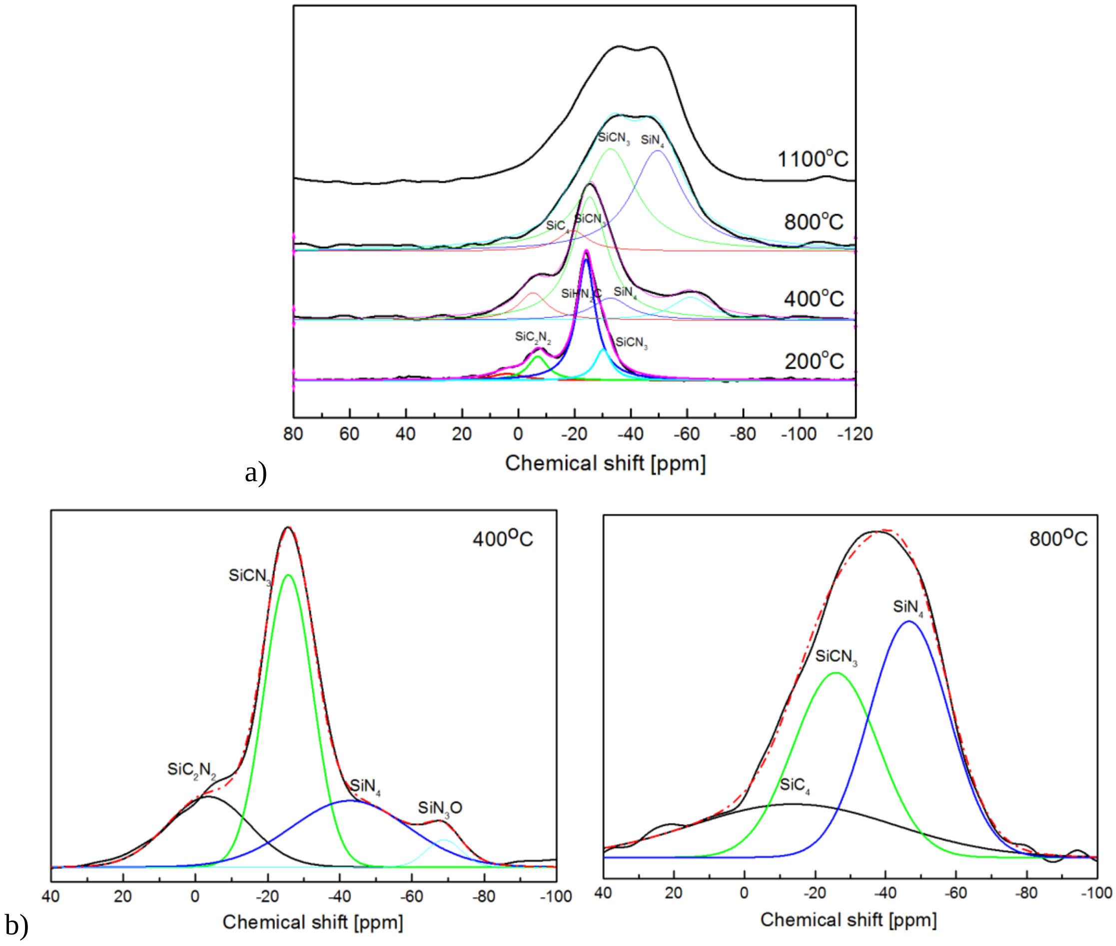

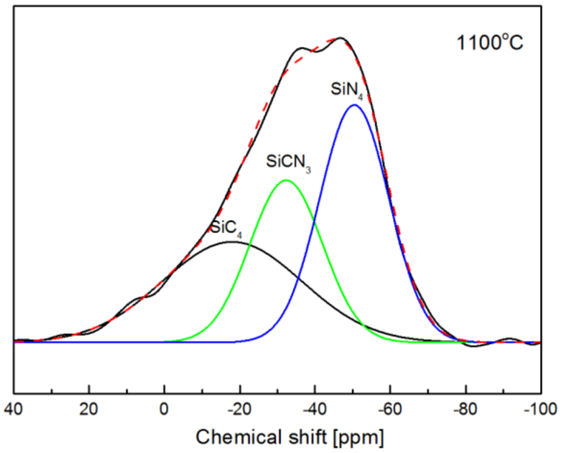

Figure 3.7. ^{29}Si MAS NMR spectra of a) SiHfCN2 and b) SiHfBCN2 pyrolyzed at different temperatures.

The ^{29}Si NMR spectra (Figure 3.7) exhibit signals for silicon sites with bonds to carbon and nitrogen, i.e., tetrahedral SiC_xN_{4-x} ($0 \leqq x \leqq 4$)[213]. The chemical shifts and the fractions of the different silicon sites were evaluated by deconvolving the ^{29}Si NMR spectra and are summarized in Table 3.2. In the case of SiHfCN, the ^{29}Si NMR spectrum at 200 °C exhibits three peaks, similar to that of SiHfBCN under identical conditions: the strong peak at a chemical shift of -23.5 ppm is attributed to $SiHC(sp^3)N_2$ (53.1 %), the shoulder at a chemical shift of -30.7 ppm is assigned to $SiC(sp^3)N_3$ (28.6 %), and a low-field chemical shift of -8.9 ppm corresponds to $SiC(sp^3)_2N_2$ (18.3 %) indicating crosslinking via hydrosilylation and/or polymerisation of the vinyl groups. This supports the finding that the reported transamination reaction induces the generation of $SiCN_3$ from $SiHN_2C$ or SiC_2N_2 [212]. When the pyrolysis temperature was increased to 400 °C, the signal ascribed to $SiHC(sp^3)N_2$ disappeared, suggesting a significant decrease in Si-H/N-H, as indicated by the FT-IR results (Figure 3.6). The number of $SiC(sp^3)_2N_2$ sites also decreased (13.1%), which is attributed to the transamination reaction. Additionally, the signals associated with these sites disappeared in the spectra collected at higher pyrolysis temperatures of 800 and 1100 °C because of the release of the methyl group, as observed in the FT-IR results (Figure 3.6 (v)). The ^{29}Si NMR spectra of the samples pyrolyzed at 800 and 1100 °C exhibit very broad resonances, corresponding to the presence of tetrahedrally bonded SiC_xN_{4-x} ($0 \leq x \leq 4$). In general, in the chemical shift range from -15 to -50 ppm, the mixed-bond environment with a chemical shift of -49 ppm is attributed to SiN_4, because hafnium generally serves an attractive role in determining the electron density in a silicon environment. Thus, modification with a hafnium complex leads to a lower field shift than that of the SiCN ceramics (approximately -50 ppm), with the peak associated with $SiCN_3$ located close to the SiN_4 peak at -33 ppm and the lower-field-shift peak attributed to SiC_4 located at -19 ppm. As observed in Table 3.2, the fraction of $SiCN_3$ sites decreases (from approximately 47.9 to 31.3 %), whereas that of SiC_4 sites increases (from 5.7 to 25.1 %), indicating a de-mixing conversion from $SiCN_3$ to SiC_4 (800-1100 °C).

The ^{29}Si NMR spectrum of the sample SiHfBCN pyrolyzed at 400 °C exhibits one peak at -26 ppm which was attributed to the $SiCN_3$ sites (site fraction 49.8%). Additionally, two signals at -4 and -43 ppm were attributed to the $SiC_2(sp^3)N_2$ (20.1%) and SiN_4 (26.8%) sites, respectively. Upon increasing the pyrolysis temperature to

800 °C, the amount of $SiC_2(sp^3)N_2$ sites decreased as a result of transamination reactions and methane release, as has also been reported for a hafnium-alkoxide-modified polysilazane [212]. This is in good agreement with the EGA data indicating the evolution of methane and amino fragments in the same temperature range (see Figure 3.5). The ^{29}Si NMR spectra of the samples pyrolyzed at 800 °C and 1100 °C exhibit a new signal with a chemical shift around -14 ppm, which has been assigned to the SiC_4 sites and is also found in the SiHfCN samples, indicating that de-mixing/partitioning processes occurred in the SiHf(B)CN samples, cf. $SiC_xN_{4-x} = SiN_4 + SiC_4$. This is rather intriguing, as at these temperatures, SiCN/SiBCN-based ceramics are typically assumed to be single-phasic and the intensity of the SiC_4 signal is usually very low. Interestingly, there was a high-field shift of the $SiCN_3$ and SiN_4 signals as the heat treatment temperature increases. Thus, the signal of the $SiCN_3$ sites shifted from -26 ppm (400 and 800 °C) to -32 ppm (at 1100 °C), indicating the presence of Hf in the secondary coordination sphere of the Si sites at temperatures up to 800 °C. As the pyrolysis temperature increased to 1100 °C, the signal shifted towards the high field, indicating Hf being released from the secondary coordination sphere of the silicon sites at the mentioned temperature. In the case of the SiN_4 signal, this effect was even stronger: the chemical shift of the signal was -43, -47 and -48 ppm upon pyrolysis at 400, 800 and 1100 °C, respectively. Thus, it seems that Hf is released first from the coordination sphere of the SiN_4 sites, as compared to the $SiCN_3$ sites. Thus, the NMR data indicate that the phase separation processes probably start in SiHf(B)CN at temperatures as low as 800 °C. Currently, it is assumed that the modification of the polysilazane with hafnium might be responsible for this behavior. This effect (viz. de-mixing of mixed-bond SiC_xN_{4-x} tetrahedra) was also reported for a hafnium-alkoxide-modified polysilazane [212]. However, whereas in the case of the reported SiHfCNO, the hafnium incorporation induces a partitioning process, cf. $SiC_xN_{4-x} = SiN_4 + C$ [212] (as known from silicon carbodiimide-derived SiCN materials) [214], in the present case, the partitioning of SiC_xN_{4-x} tetrahedra generates amorphous SiC in addition to Si_3N_4 [215-218]. This finding clearly emphasizes that the chemical composition and molecular architecture of the single-source precursor has a crucial effect on the phase composition of the resulting nanocomposite material [73].

Table 3.2. Fraction of SiC_2N_2, SiC_4, and $SiCN_3$ and SiN_4 sites derived from Gaussian line fitting of the ^{29}Si NMR spectra in Figure 3.7.

		$SiHN_2C$		SiC_4		SiC_2N_2		$SiCN_3$		SiN_4	
		δ (ppm)	Site fraction (%)	δ (ppm)	Site fraction (%)	δ (ppm)	Site fraction (%)	δ (ppm)	Site fraction (%)	δ (ppm)	Site fraction (%)
SiHfCN	200	-23.5	53.1			-8.9	18.3	-30.7	28.6		
	400					-5	13.1	-25	72.7	-33	14.1
	800			-19	5.7			-33	47.9	-49	46.4
	1100			-19	25.1			-33	31.3	-49	43.6
SiHfBCN	400					-4	20.1	-26	49.8	-43	26.8
	800			-14	23.8			-26	34.6	-47	41.6
	1100			-18	33.2			-32	27.8	-48	39.0

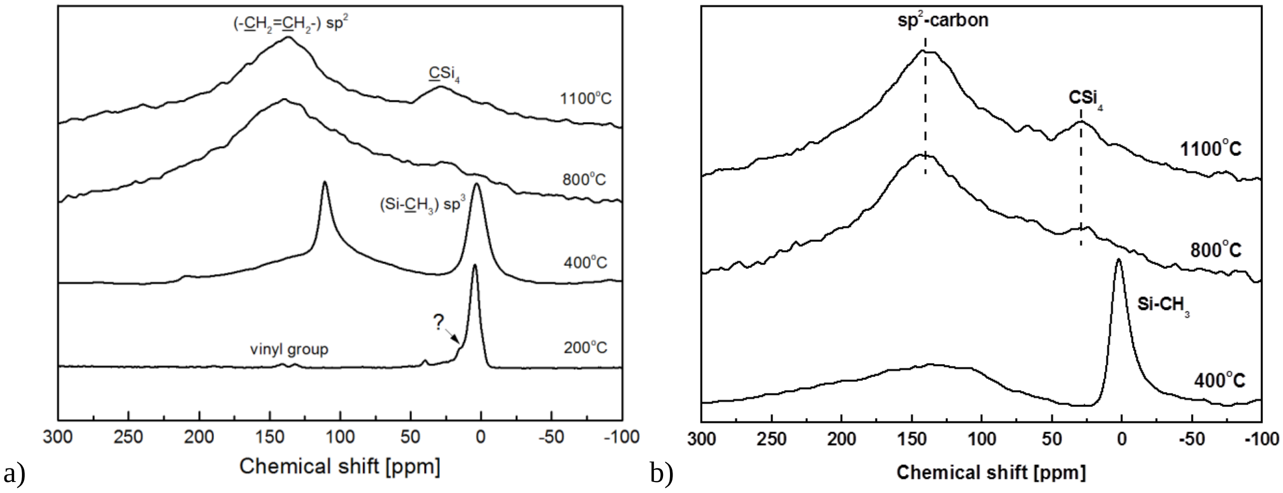

Figure 3.8. ^{13}C MAS NMR spectra of the a) SiHfCN2 and b) SiHfBCN2 samples prepared upon pyrolysis of the single-source precursor at 400, 800 and 1100 °C.

The ^{13}C NMR spectra of the cross-linked SiHfCN precursor (200 °C) and ceramic pyrolyzed at various temperatures (400-1100 °C) were shown in Figure 3.8a. The ^{13}C spectrum at 200 °C shows, in addition to the peaks corresponding to methyl- (~3.8-4.2 ppm) and the vinyl-group (132, 141 ppm), a broad signal at 26 ppm and a shoulder at 14 ppm; however, these cannot be identified. The methyl groups still presents at 400 °C, but disappears at 800 and 1100 °C. The ^{13}C MAS NMR spectra of SiHfBCN ceramic behaved similar. The sample prepared at 400 °C exhibits a signal at 2 ppm which was assigned to the Si-CH_3 groups (Figure 3.8)[74]. This signal was not found in the samples prepared at 800 and 1100 °C; as the pyrolysis of the polymeric precursor at those temperatures induces a drastic release of the methyl groups [74, 219], (e.g. CH_4 evolution, as detected by EGA) and the segregation of carbon, leading to the appearance of new signals in the ^{13}C NMR spectra (Figure 3.8). Thus, the ^{13}C spectrum of the sample pyrolyzed at 1100 °C indicates the presence of a sp^2 C network, which is however thought to contain large amounts of C-N/C-B bonds (as indicated by the shifting of the signal from usually ca. 130 ppm in sp^2-carbon to ca. 145 ppm). This has already been reported in the literature for polymer-derived SiBCN ceramics, which also contain a segregated sp^2 C phase with C-N and C-B bondings as interfaces between the carbon phase and the SiN_x- and BN_x-based domains, respectively [220, 221]. Additionally, the spectra of the samples pyrolyzed at 800 and 1100 °C exhibit a signal at 28 ppm which was assigned to the CSi_4 sites and thus supports the findings of the ^{29}Si NMR data revealing a strong phase separation of the samples (which was not observed in the case of ternary SiCN ceramics [222, 223]); obviously, the simultaneous incorporation of Hf and B into the preceramic polysilazane fundamentally affects its ceramization behavior.

The ^{11}B MAS NMR spectra of SiHfBCN samples showed two main signals at 40 and 30 ppm, which were assigned to BCN_2 (major) and BN_3 (minor) sites, respectively (Figure 3.9) [221]. Please note that after the hydroboration process of the hafnium-modified polysilazane, BC_3 sites are expected first, which obviously undergo rearrangement reactions already at temperatures as low as 400 °C, converting into BCN_2 and BN_3. Considering the evolution of the Si sites with temperature (SiC_2N_2 sites are consumed, and the amount of $SiCN_3$

decreases as the synthesis temperature rises; see Table 3.2 and Figure 3.7). We assume that the BC_3 units undergo exchange reactions with the SiC_2N_2 and $SiCN_3$ sites to generate BCN_2 and SiC_4 units as follows: $BC_3 + SiC_2N_2 = BCN_2 + SiC_4$ and $BC_3 + 2\ SiCN_3 = BCN_2 + 2\ SiC_4$, respectively [213]. Similarly, the formation of BN_3 can be explained as $2\ BC_3 + 3\ SiC_2N_2 = 2\ BN_3 + 3\ SiC_4$ and $BC_3 + SiCN_3 = BN_3 + SiC_4$.

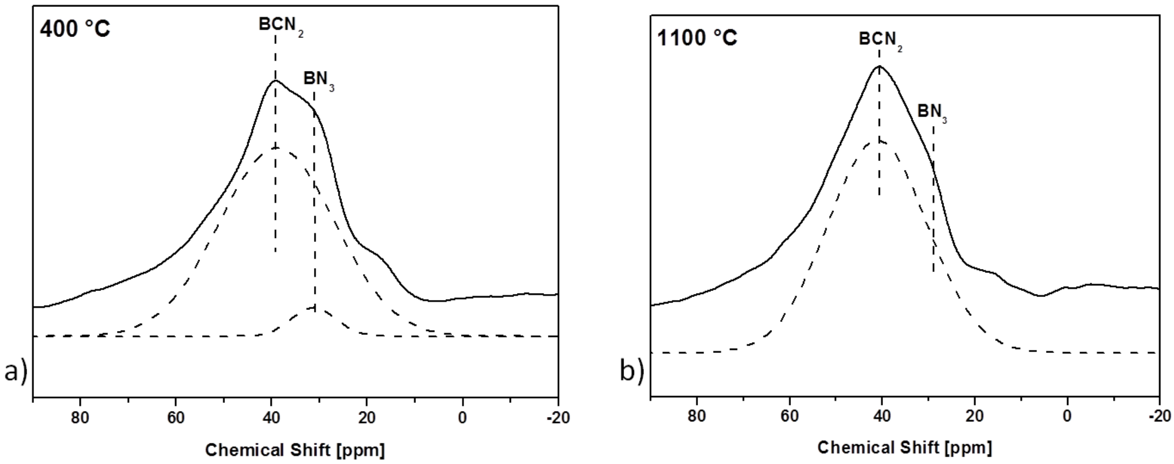

Figure 3.9. ^{11}B MAS NMR spectra recorded for the samples prepared at 400 (a) and 1100 °C (b).

High-resolution transmission electron microscopy (HR-TEM) of both samples prepared at 1100 °C indicates an amorphous, featureless and homogeneous microstructure (Figure 3.10). However, based on the MAS NMR data, the sample is highly nano-heterogeneous, thus having a complex phase composition, consisting of amorphous Si_3N_4, SiC, sp^2-C, HfN and BN (only for amorphous SiHfBCN ceramics) phases showing mixed bonds at their interfaces (e.g., C-N/C-B bondings and BC_2N sites at the interface between C and BN). The conversion from polymer to ceramic can be summarized in Scheme 3.1 and Scheme 3.2.

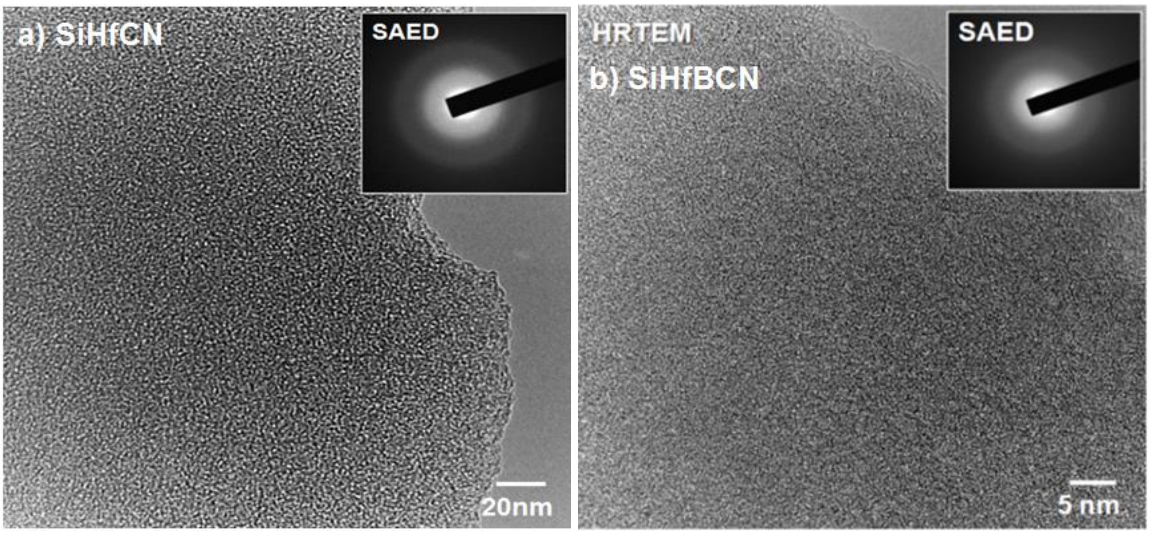

Figure 3.10. HR-TEM micrograph of a) SiHfCN2a and b) SiHfBCN2a powder sample prepared with pyrolysis at 1100 °C indicating a homogeneous microstructure. The selected area electron diffraction (SAED, see inset) clearly shows the amorphous nature of the sample.

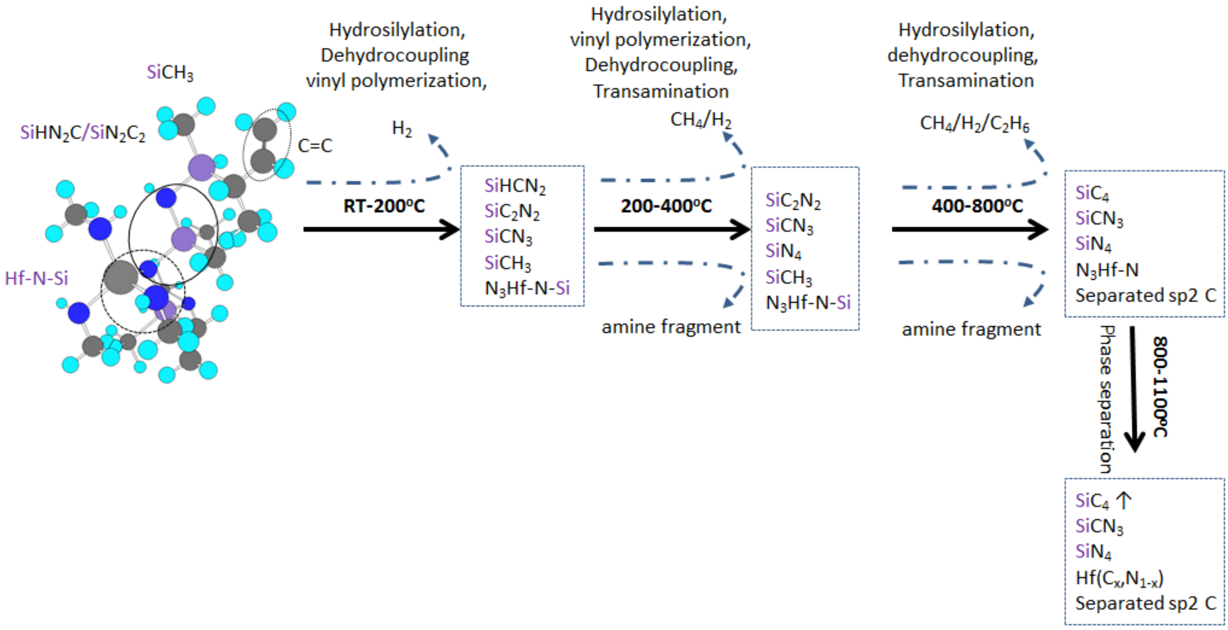

Scheme 3.1. Experimentally observed chemical pathways for the pyrolytic decomposition of single-source precursor into amorphous SiHfCN. Here, the scheme shows the evolution of tetrahedrally bonded $SiHC_xN_{4-x}$, the separation of HfC_xN_{1-x} from N_3Hf-N-Si, and the development of segregated free carbon during cross-linking and thermal pyrolysis.

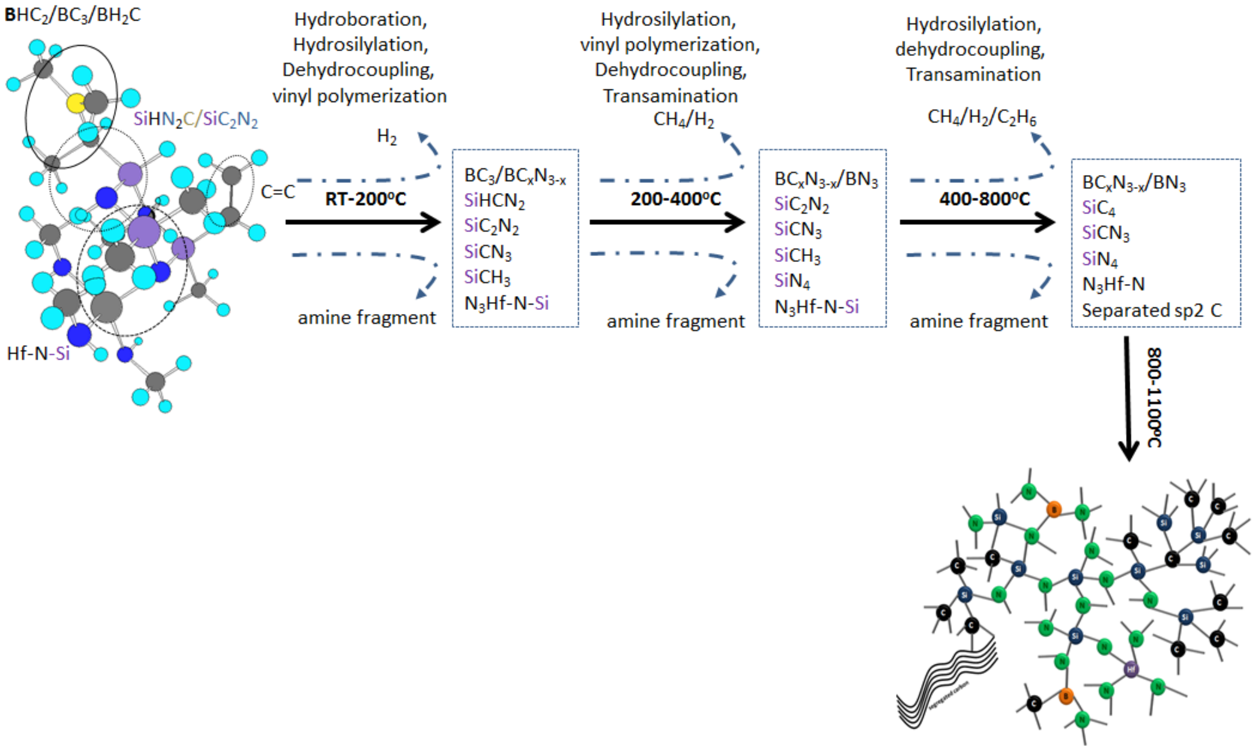

Scheme 3.2. Experimentally observed chemical pathways for the pyrolytic decomposition of a single-source precursor into amorphous SiHfBCN and the proposed amorphous structure for SiHfBCN. This scheme shows the evolution of tetrahedrally bonded $SiHC_xN_{4-x}$ and tricoordinated boron atoms linked to carbon and nitrogen (BC_xN_{3-x}), the separation of HfC_xN_{1-x} from N_3Hf-N-Si, and the development of segregated free carbon during cross-linking and thermal pyrolysis.

3.1.3 Summary

The single-source precursors SiHfCN and SiHfBCN were successfully synthesized. Moreover, spectroscopy (i.e., FTIR and NMR) was able to reveal the structures of the SSPs and all relevant elements of the desired composites. The observation of a decreasing intensity of N-H/Si-H indicated that the formation of Hf-N-Si linkages and vinyl groups in HTT1800 is not affected by the reaction with the hafnium complex in the synthesis of SiHfCN. However, the vinyl groups do react with the B-H group in BH_3 SMe_2 during the hydroboration reaction yielding the SiHfBCN SSP. Additionally, ^{29}Si NMR of cross-linked SiHfBCN at 200 °C revealed that all signals (i.e., $SiHC(sp^3)N_2$, $SiC(sp^3)_2N_2$, and $SiC(sp^3)N_3$) were shifted toward lower field shifts compared with those observed in the SiCN-based materials. This finding reflects the effect of Hf on the electron density of Si sites in tetrahedral SiC_xN_{4-x}, which is consistent with the formation of Hf-N bonded to Si sites (Hf-N-Si).

A single-source precursor could be successfully converted into amorphous ceramics, as verified by TEM, and their thermal transformation was studied using a combination of *in situ* thermal analysis, such as thermogravimetric analysis (TGA) coupled with evolved gas analysis (EGA), and *ex situ* analytical experiments, i.e., ^{13}C, ^{29}Si and ^{11}B (for SiHfBCN) MAS NMR investigations and FTIR spectroscopy. It was found that the ceramic yields of SiHfCN and SiHfBCN (approximately 80 wt%) are significantly higher than that of HTT1800 (approximately 65 wt %), which is regarded as a consequence of the strong increase in the cross-linking degree of the polymer upon modification with an Hf or Hf/B complex. Both materials exhibit a similar inorganic mechanism between 200 and 800 °C (see Scheme 3.1 and Scheme 3.2). The ceramic conversion predominantly occurs in a temperature range of 400-800 °C as a result of the evolution of hydrogen and methane as well as the release of amine fragments, which correspond to dehydrocoupling (i.e., Si-H and N-H in both ceramics, or B-H and N-H in the case of SiHfBCN) and transamination reactions (≡Si-N, ≡Si-N=/≡Hf-N=, etc.), respectively. The transformation of the SSPs into the amorphous ceramics SiHfCN and SiHfBCN are almost complete at 800 °C. Furthermore, the phase separation processes begins in SiHf(B)CN at temperatures as low as 800 °C, generating a complex structure. In the case of amorphous SiHfCN ceramics, this structure consists of SiC_xN_{4-x} (i.e., SiC_4, $SiCN_3$ and SiN_4), HfN, and separated carbon, whereas additional BCN_2 and BN_3 are observed in the structure of SiHfBCN. In conclusion, the presented investigations of the complex, Hf- and B-containing, modified samples reveal that the molecular structure has a significant effect on the phase composition of polysilazane-derived SiCN ceramics, such as SiC_4 and SiN_4, which are partitioned from tetrahedral SiC_xN_{4-x} when the pyrolysis temperature reaches 800 °C (which is not typically observed in the case of SiCN-based ceramics).

3.2. Processing

The category of processing has been introduced in Chapter 2 (experimental part), including monoliths and CMCs. The aim of this study in the processing of monoliths is to develop such ceramic monoliths with a low porosity and a crack-free or dense condition (open porosity is almost zero). PLS and PAS were applied to process the monoliths; the former focused on reducing porosity by optimizing the parameters concerning warm pressing, pyrolysis and annealing. While that section of PAS will consider the densification process and phase, the microstructure evolution will be emphasized in the latter. Additionally, since the SSPs method is beneficial to infiltrating fiber preforms, SiHfBCN might be a promising candidate among CMCs. In the present study, C_f/SiCN, C_f/SiC-SiCN and C_f/SiHfBCN, C_f/SiC-SiHfBCN CMCs are fabricated.

3.2.1 Ceramic Monoliths

3.2.1.1 Pressure-less sintering (PLS)

Cross-linked SiHfCN and SiHfBCN SSPs were shaped via warm pressing and then converted into amorphous ceramics by thermal pyrolysis at 1100 °C. The ceramic yield as well as the shrinkage and open porosity of the SSPs pyrolyzed at 1100 °C are presented in Table 3.3. It can be clearly seen that the ceramic yield of SiCN ceramic is significantly improved by the incorporation of Hf and B. This is a consequence of high cross-linking structures. Furthermore, the relationship between degree of cross-linking and the warm pressing parameters of these ceramics was shown in Table 2.1. The warm pressing temperature (T_{wm}) is shown to be 180-190 °C for SiCN ceramic, while that of SiHfCN1 is much higher (ca. 300 °C) at identical temperatures (T_{cs}) at 250 °C. This indicates that the SiHfCN1 with a high degree of cross-linking exhibit lower fluidity compared to that of SiCN. Since there is a limitation in the device at which a maximum of T_{wm} is 300 °C, the T_{cs} for highly cross-linked SiHfCN2, SiHfBCN1 and SiHfBCN2 have to be controlled to below 200 °C. Otherwise, as above, samples cannot be compacted into bulk at a limited temperature (up to 300 °C). It was also found that the T_{wm} of SiHfBCN2 (280 °C) is higher than that of SiHfBCN1 (260 °C, see Table 2.1), indicating a higher degree of cross-linkage along with the increasing Hf and B content. However, since worse fluidity is indicative of lower mobility for higher compositions (SiHfCN2 and SiHfBCN2), the SiHfCN2 and SiHfBCN2 present a higher open porosity, as shown in Table 3.3, while SiHfCN1 and SiHfBCN1 have a relatively lower open porosity. Furthermore, it was reported previously that the addition of boron can enhance the densification of SiCN[110]. Accordingly, the open porosity of SiHfBCN1 is lowest (7.9 %) in ceramic samples pyrolyzed at 1100 °C among all of them (see Table 3.3).

Table 3.3. Ceramic yield, shrinkage and open porosity after pyrolysis temperature at 1100 °C.

Ceramic	Density $[g{\cdot}cm^{-3}]$	Porosity [vol%]	Shrinkage [%]	Ceramic Yield [%]
SiCN	-	-	-	65
SiHfCN1	2.3	10.2	42.3	83
SiHfCN2	2.5	19.2	-	82.5
SiHfBCN1	2.4	7.9	54.3	81
SiHfBCN2	2.8	12.0	48.1	80

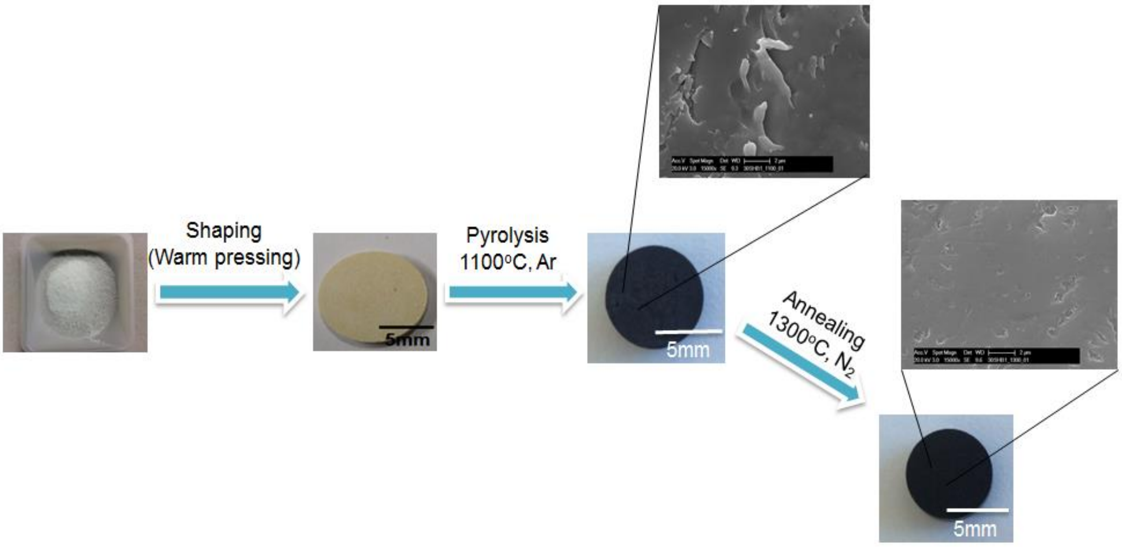

Figure 3.11. Overall process for preparing dense SiHfBCN2 ceramic monoliths, microscopy of samples showing denser and crack-free features can be achieved in annealed samples at 1300 °C compared to pyrolyzed samples at 1100 °C.

The pyrolyzed samples were annealed in argon and nitrogen atmospheres. The shrinkage, open porosity and density of the annealed SiHfBCN ceramics at different temperatures (1300, 1500, 1700 °C) are presented in Table 3.4. The sample annealed at 1300 °C in nitrogen shows a lower open porosity than samples pyrolyzed at 1100 °C, while the porosity of SiHfBCN1b-1300 and 2b-1300 amount 5.9 and 10.4 %, respectively. This is in agreement with the microscopy of samples pyrolyzed at 1100 °C and annealed at 1300 °C in nitrogen, which show that denser and crack-free features can be achieved in samples annealed at 1300 °C (see Figure 3.11). The high temperature stability of those ceramics with respect to decomposition is observed upon annealing at 1300 °C in nitrogen, indicating no decomposition occurs within this process (Figure 3.26). Because the volumes of samples annealed at 1300 °C are shown shrinkage as compared to that of samples pyrolyzed at 1100 °C (see Table 3.4). Thus, this decreasing in open porosity might results from the fact that is a contribution of molecular diffusion with the increasing temperature. Furthermore, In order to understand the evolution of the physical properties (which include shrinkage, open porosity and density), these will be described more details in association with crystallization and decomposition (see Section 3.3).

Table 3.4. Shrinkage, open porosity and density of SiHfBCN ceramic annealed at different temperatures.

Ceramic	Volume Shrinkage [%]	Open porosity [%]	Density [g·cm^{-3}]
SiHfBCN1a-1300	7.2	nd	nd
SiHfBCN1a-1500	15.4	nd	nd
SiHfBCN1a-1700	19.2	43.9	1.9
SiHfBCN1b-1300	10.5	5.9	2.46
SiHfBCN1b-1500	12.0	13.5	2.53
SiHfBCN1b-1700	13.7	14.9	2.68
SiHfBCN2a-1300	5.3	nd	nd
SiHfBCN2a-1500	10.7	nd	nd
SiHfBCN2a-1700	27.2	52.4	1.9
SiHfBCN2b-1300	3.9	10.4	2.68
SiHfBCN2b-1500	8.5	19.6	2.74
SiHfBCN2b-1700	14.5	21.2	2.80

*nd- not determined

3.2.1.2 Pressure-assisted sintering (PAS)

Sintering is an essential process for obtaining UHTCs with good mechanical strength, hardness, thermal stability and oxidation resistance [224]. However, this is rather a challenging task due to the fact that they have strong covalent bonding and low self-diffusion coefficients that significantly restrict their sinterability [225-227]. Within this context, the consolidation of UHTCs by using spark plasma sintering (SPS) technique was reported [225-230]. HfB_2-SiC [225], $SiB_{0.5}C_{1.5}N_{0.5}$ [226], ZrB_2-ZrC [227] and TaC-HfC [228] systems were well densified by SPS at moderate temperatures within minutes. High heating rate (up to ~1000 °C/min) and high external pressure (>100 MPa) renders SPS superior to the conventional approaches [231-235]. Both thermal and non-thermal effects contribute to its unique features [233, 234].

In this section, dense UHTC-NCs derived from SiHf(B)CN-based ceramics were successfully prepared by SPS, and their densification mechanism, phase identifications and microstructures are analyzed. Additionally, their mechanical properties of both dense ceramic materials were also evaluated.

3.2.1.2 .1 High temperature behavior of amorphous SiHfBCN ceramic

The crystallization and decomposition behavior of SiHf(B)CN during the annealing process will be addressed in Section 3.3 (the discussed temperature is up to 1700 °C), however the decomposition cannot be studied *in-situ* in the annealing experiment. Thus it is highly necessary to understand the thermal stability of the pyrolyzed ceramic samples, regarding whether simultaneous decomposition probably occurs during the densification process. Additionally, the sintering process is performed in vacuum within a few minutes by applying a very fast heating rate (450 °C) in our study. Thus, it is extremely difficult to match similar conditions as in

TGA/DTG. Nevertheless, the thermal behavior of SiHfBCN could be related to thermodynamic data in other atmosphere like helium.

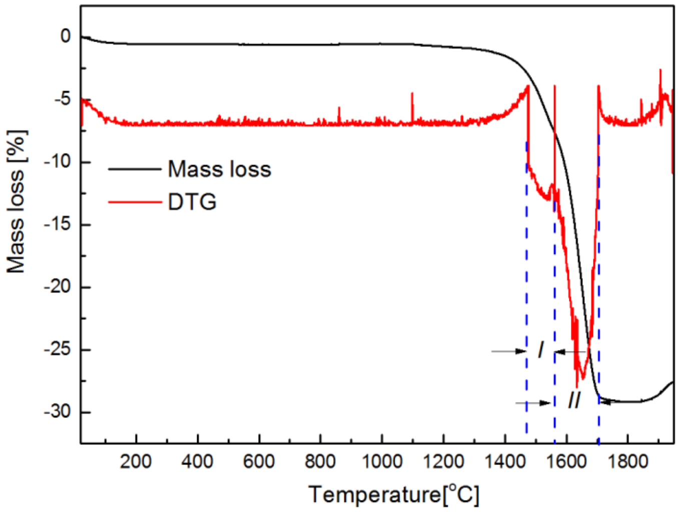

Figure 3.12. High temperature TGA (HT-TGA) of SiHfBCN samples pyrolyzed at 900 °C.

The evident mass loss can be found (ca. 30 %), which is in agreement with the recorded decomposition of SiHfBCN annealed in argon up to 1700 °C (see Section 3.3). Clearly, two decomposition stages can be distinguished: The first step ranges from 1470 to 1560 °C, with a comparable lower mass loss of the 5.6 %, which is attributed to the carbothermal reaction between Si_3N_4 and free carbon. However, in the samples annealed at 1500 °C in an argon atmosphere which recorded a mass loss of ca. 10 wt% (see Figure 3.26), the difference in mass loss is probably due to the partial decomposition with a continuous process in TGA. Further degradation causes the highest mass loss, ending at ca.1700 °C, which can be assumed to be either the contribution of residual decomposition of Si_3N_4 and the free carbon or the formation of the HfC phase from the HfN phase with the release of N_2. Accordingly, two-stage (from 1470-1700 °C) thermal decompositions might occurs simultaneously during consolidation of SiHf(B)CN ceramics, which may serve as a guideline for SPS process.

3.2.1.2 .2 Densification behavior and phase/microstructure evolution

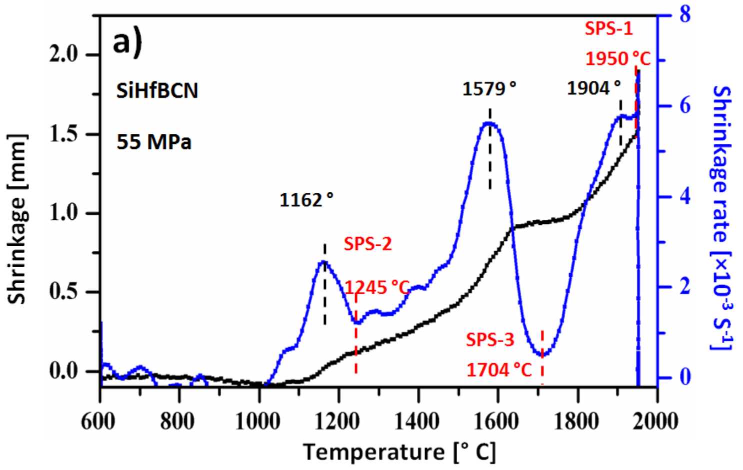

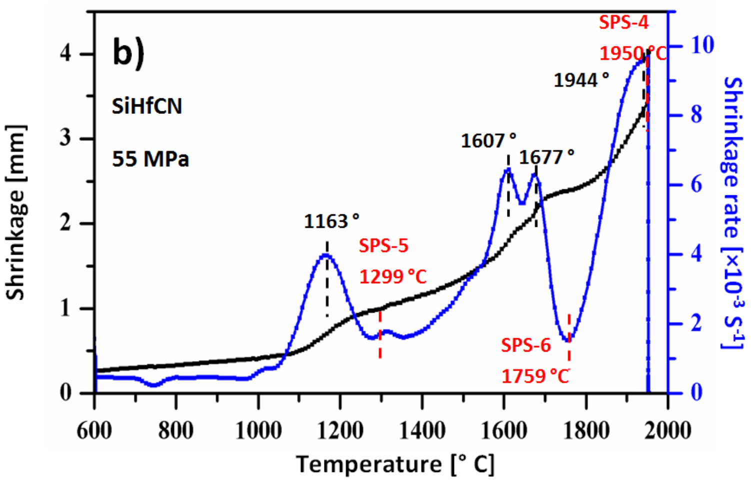

Figure 3.13. Shrinkage and shrinkage rate curves for SiHfBCN (a) and SiHfCN (b) ceramics as functions of the temperature. The red dashed lines show at which temperatures the sintering processes were interrupted.

In order to investigate the densification behavior of SiHfCN and SiHfBCN ceramics, two sintering regimes (corresponding to samples SiHfCN_04 and SiHfBCN_04 in Table 3.5) were applied to rapidly densify SiHfCN and SiHfBCN ceramics.

The shrinkage (ΔL) and the linear shrinkage rate (defined as -d(ΔL/Lo)/dt, with Lo being the thickness of the green body at room temperature) were recorded in intervals of one second in real time (the background was deducted) and the corresponding curves are shown in Figure 3.13. For all samples, the plots of the *shrinkage rate vs. T* curves display three evident peaks during the entire sintering process, indicating three individual densification steps. The temperatures at each peak (in black) correspond to the maximum shrinkage rate achieved at this temperature. Both SiHfCN and SiHfBCN samples behaved similarly. Appreciable shrinkage occurred from ~1100 °C and lasted until the end of the sintering circles. The three upward peak regions which appeared in the shrinkage rate curves during the entire processes (this densification behavior is different from the common cases in which only one peak is observed [236]) may relate to densification as well as to decomposition, phase transformation or other structural/chemical developments in the samples, as shown by the *in-situ* HT-TGA in Figure 3.12, a number of chemical reactions (including decomposition) were simultaneously involved in the densification processes. In order to attain more information about the individual processes occurring during these three stages, further sintering regimes were performed, e.g. upon interrupting the sintering regimes at different temperatures (samples SiHfCN_01, SiHfCN_02, SiHfBCN_01 and SiHfBCN_02 in Table 3.5) in Figure 3.13, the temperatures at which the sintering procedures were interrupted are marked in red. Regarding the SiHfBCN samples (see Figure 3.13a), the peaks for the highest shrinkage rates were located at 1162 °C, 1579 °C and 1904 °C. The sintering procedure was correspondingly interrupted at 1245 °C (SiHfBCN_01) and 1704 °C (SiHfBCN_02), i.e. shortly after the maxima of the shrinkage rate peaks. The SiHfCN samples (see Figure 3.13b) also show three densification processes at 1163 °C, 1607/1677 °C and 1944 °C, respectively. Note that the splitting of the peak at 1607/1677 °C does not imply two densification steps of the sample, but probably relates to pressure fluctuations or other extrinsic effects. The sintering cycles were interrupted at 1299 °C (SiHfCN_01) and 1759 °C (SiHfCN_02).

The samples obtained from the different sintering procedures shown in Figure 3.13 and Table 3.5 were investigated by XRD concerning their crystalline phase composition (XRD patterns in Figure 3.14). The samples for which the sintering process was stopped shortly after the maximum of the first densification peak (i.e. SiHfCN_01 and SiHfBCN_01) were shown to be X-ray amorphous. Furthermore, the density was relatively low (1.9 and 1.99 g/cm^3 for SiHfCN_01 and SiHfBCN_01, respectively), indicating only a slight densification. The samples for which the sintering procedure was interrupted after the second shrinkage rate peak (i.e. SiHfCN at 1299 °C and SiHfBCN at 1245 °C) showed an improved density (2.31 and 2.55 for SiHfCN_02 and SiHfBCN_02, respectively) and the presence of crystalline HfC$_x$N$_{1-x}$ and β-SiC. The increase of the sintering temperature to 1950 °C (as for SiHfCN_04 and SiHfBCN_04) led to a good compaction and very low porosity values. Thus, for SiHfCN the density was 3.65 g/cm^3 and the open porosity value was as low as 0.15 vol% (see Table 3.5). The same case also happened in the densification of the SiHfBCN system.

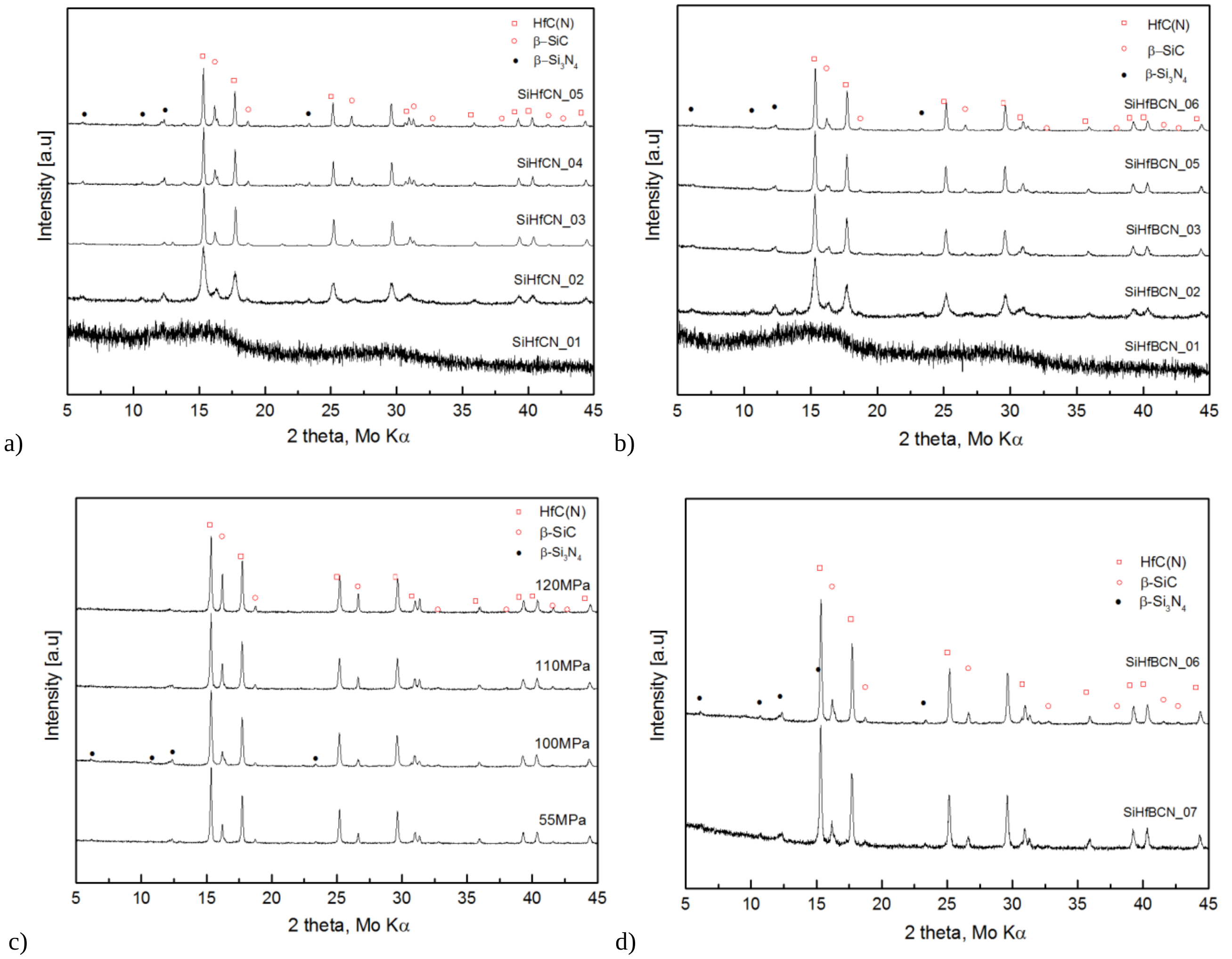

Figure 3.14. Crystallization behavior of SiHfCN and SiHfBCN upon SPS with different sintering parameters: (a) SiHfCN samples and (b) SiHfBCN samples; (c) SiHfBCN with different sintering pressure; (d) SiHfBCN with one-step and two-step sintering.

Table 3.5. The effect of sintering parameters on the crystallite size, phase composition, density and porosity of densified SiHfCN- and SiHfBCN-based ceramics.

	Sample label	Sintering parameters	Mean crystallite size			Phase fraction			HfC_xN_{1-x}	Density	Open porosity
		[^{o}C/min/MPa]	[nm]			[wt %]				[g·cm^{-3}]	[%]
			HfC_xN_{1-x}	β-SiC	β-Si_3N_4	HfC_xN_{1-x}	β-SiC	β-Si_3N_4			
SiHfCN	SiHfCN_01	1299/1/55 (SPS-5)								1.90	38.1
	SiHfCN_02	1759/1/55 (SPS-6)								2.31	35.5
	SiHfCN_03	1850/1/120	49.4	18.6	17.5	30.4	30.4	29.4	$HfC_{0.56}N_{0.44}$	3.03	16.1
	SiHfCN_04	1950/1/105 (SPS-4)	130.2	36.1	29.5	17.5	32.6	49.9	$HfC_{0.62}N_{0.38}$	3.65	0.15
	SiHfCN_05	1950/15/105	165.9	53.4	34.9	19.0	40.5	40.5	$HfC_{0.65}N_{0.35}$	3.68	0.12
SiHfBCN	SiHfBCN_01	1245/1/55 (SPS-2)								1.99	33.2
	SiHfBCN_02	1704/1/55 (SPS-3)								2.55	26.3
	SiHfBCN_03	1850/4/125	32.5	34.8	15.3	76.3	17.7	6.0	$HfC_{0.68}N_{0.32}$	3.34	9.1
	SiHfBCN_04	1950/1/55 (SPS-1)	69.1	75.3	18.6	31.6	41.0	27.4	$HfC_{0.61}N_{0.39}$	3.40	6.2
	SiHfBCN_05	1950/10/100	61.7	17.5	19.6	26.8	17.8	55.4	$HfC_{0.66}N_{0.33}$	3.67	0.3
	SiHfBCN_06	1950/15/100	64.4	32.7	21.7	28.5	31.4	40.1	$HfC_{0.66}N_{0.33}$	3.69	0.2
	SiHfBCN_07	1950/1/1850/15/100	45.8	35.6	13.9	30.2	29.5	40.3	$HfC_{0.67}N_{0.33}$	3.59	1.0
	SiHfBCN_08	1950/15/110	46.4	72.7	7.0	27.0	42.6	30.4	$HfC_{0.61}N_{0.39}$	3.69	0.4
	SiHfBCN_09	1950/15/120	45.6	119.8	<1.0	28.8	62.5	8.7	$HfC_{0.57}N_{0.43}$	3.68	0.3

In Figure 3.15, SEM micrographs of the fracture surfaces of SiHfCN and SiHfBCN sintered upon using different parameters are shown and obviously confirm the fact that their densification is achieved at temperatures as high as 1950 °C. The temperature facilitate densification for both ceramics, i.e. for the samples sintered at 1850 °C (Figure 3.15 a and d), a dense area is obviously observed; however, a softer surface or porous structures are also found, indicating insufficient densification. This finding also corresponds to the high open porosity (SiHfCN_03: 16.1%, SiHfBCN_03: 9.1%) seen in Table 3.5. Furthermore, there is no significant effect of the holding time on the densification of the samples. Thus, SiHfCN was consolidated at 1950 °C at a pressure of 105 MPa with holding times of 1 and 15 min (i.e., SiHfCN_04 and SiHfCN_05 respectively) and showed a rather comparable densities of 3.65 (SiHfCN_04) and 3.68 g/cm^3 (SiHfCN_05). On the other hand, the applied loading has been shown to have a significant effect on the densification [233], Hence, SiHfBCN samples sintered at 1950 °C upon using a pressure of 100 Mpa were found to have a markedly increased density (3.69 g/cm^3) as compared to that of the samples sintered at 1950 °C and 55 Mpa (3.40 g/cm^3) (see Table 3.5). Open porosity can be found in the lower loading samples, which seems to have disappeared by applying higher loading (100 MPa) at the given temperature of 1950 °C (see Figure 3.15 e and f).

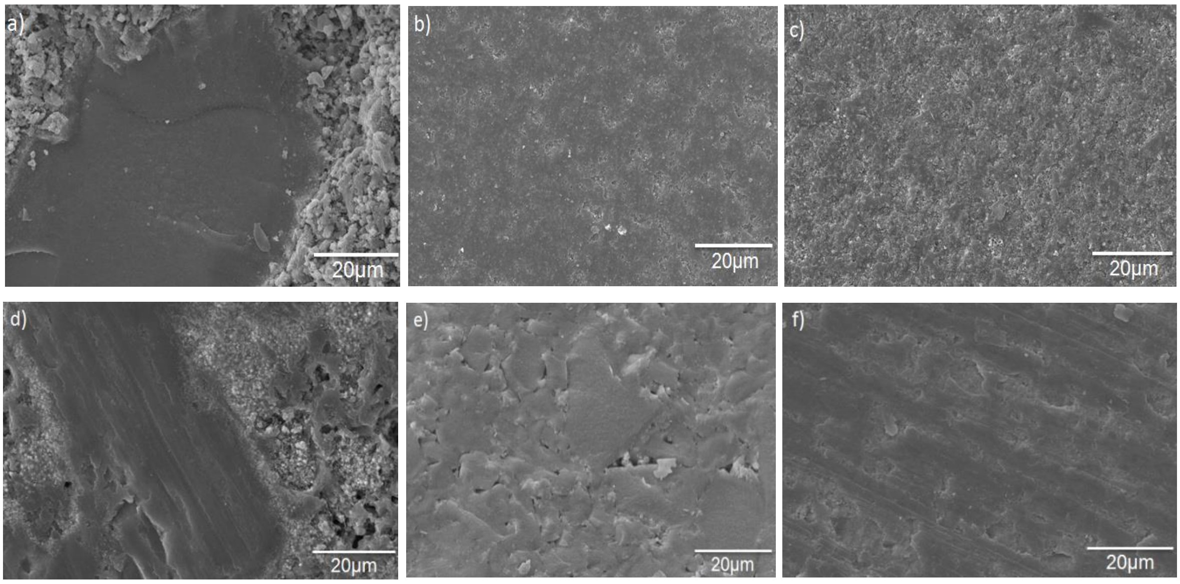

Figure 3.15. SEM micrographs of the sintered SiHfCN- and SiHfBCN-based SPS samples, a)-c) SiHfCN_03 to _05; d)-f) SiHfBCN_03, 04 and 06.

The effects of the sintering parameters on crystallization behavior were also investigated based on the presented sintering runs. Table 3.5 also summarizes the related parameters for the microstructure features of various phases, in which the phase fractions (relative to the crystalline content of the investigated samples) and crystallite sizes of the as-densified samples are determined from the Rietveld refinement of the XRD data. The XRD analysis of the as-sintered SiHfCN_01 and SiHfBCN_01 identified them as amorphous structures; all other sintered ceramics contain crystallization phases which are ascribed to HfC_xN_{1-x}, β-SiC and β-Si_3N_4. The presence of β-Si_3N_4 is somehow surprising (please note that the sintering process were performed in vacuum), as it is known that at high temperatures silicon nitride decomposes into elements (at temperatures beyond

1850 °C in nitrogen atmosphere, cf. $Si_3N_4 = 3\ Si + 2\ N_2$) or reacts with segregated carbon to generate β-SiC (at temperatures beyond 1450-1500 °C in nitrogen atmosphere, cf. $Si_3N_4 + C = 3\ \beta\text{-}SiC + 2\ N_2$). Since no elemental silicon was identified in the samples, it is concluded that the silicon nitride phase is consumed mainly via carbothermal reaction. Moreover, we assume that the very fast heating rate used for the densification as well as the rather short holding times were effective in suppressing the mentioned decomposition process and thus the silicon nitride phase was still present in the sintered samples.

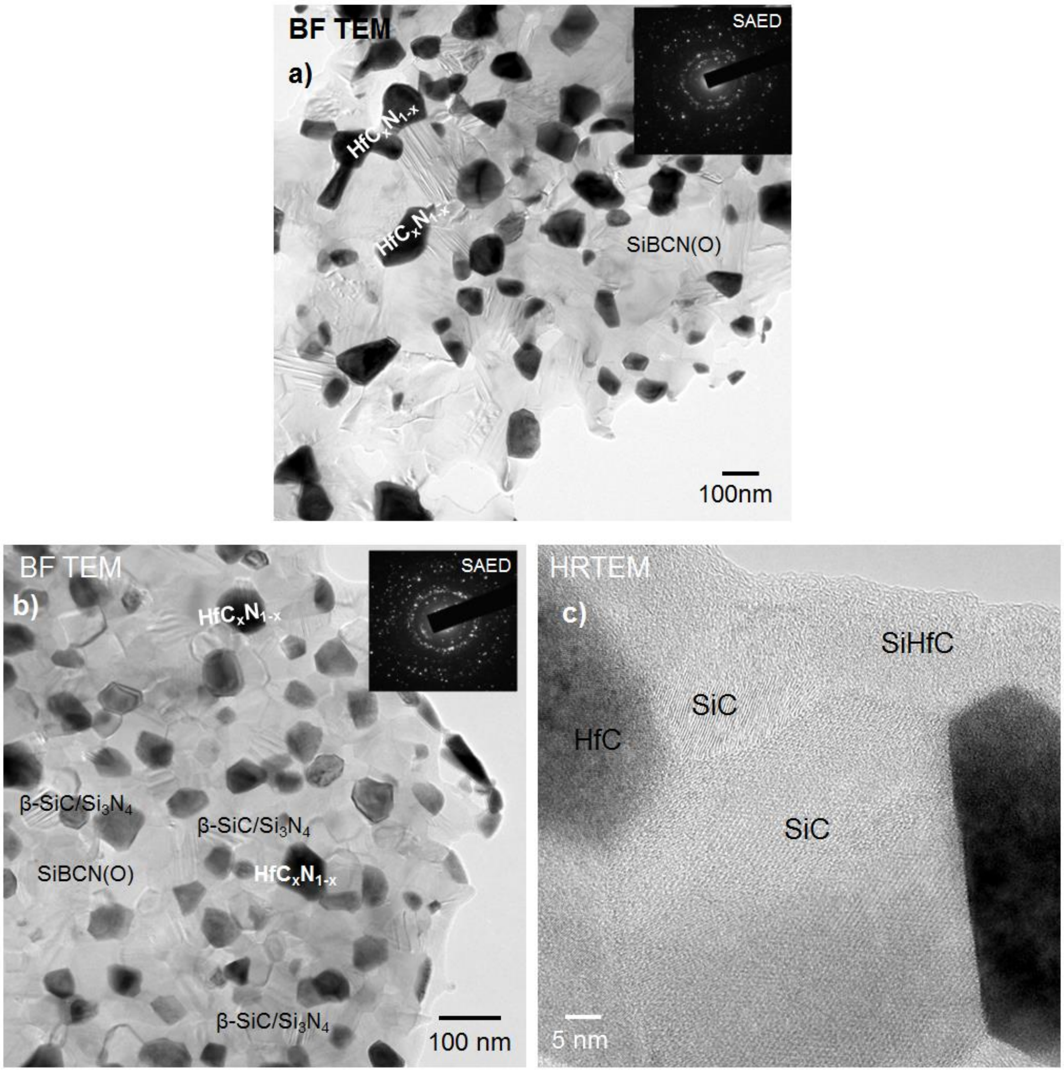

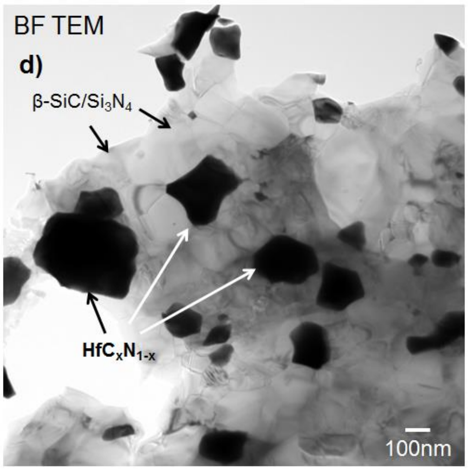

Figure 3.16. TEM micrographs of dense UHTC-NCs: a) SiHfBCN_06, b) SiHfBCN_07 and c) high solution image of SiHfBCN_07, d) SiHfCN_05

For as-sintered SiHfCN ceramics, the grain size of inside HfC_xN_{1-x} phase was beyond 100nm (i.e.130 and 166 nm, as determined from as determined from Rietveld refinement of the XRD patterns), whereas β-SiC and β-Si_3N_4 exhibit grain sizes below 100 nm(see Table 3.5). This is in good agreement with the TEM data (Figure 3.16d), which indicate a grain size of ca. 150nm for the HfC_xN_{1-x} phase. In contrast, the growth of the HfC_xN_{1-x} grains seems to be hindered in SiHfBCN, as in SiHfBCN_06 a significantly lower grain size (ca. 65nm) is found (Figure 3.16a).This might rely on the effect of boron, which is present in the matrix as BC_xN_y phase encapsulating the crystalline grains and thus providing a diffusion barrier against the crystal growth of HfC_xN_{1-x} phase. Additionally, this phase can also kinetically suppress the reaction between silicon nitride and segregated carbon, as reported earlier in the literature [237]. TEM micrograph of SiHfBCN_06 and SiHfBCN_07 (Figure 3.16a and b, respectively) illustrates the presence of nanocrystalline HfC_xN_{1-x} precipitations homogeneously distributed through an amorphous Si(B)CN(O) matrix. Interestingly, the average grain size of HfC_xN_{1-x} in SiHfBCN_06 (65 nm) was found to be higher than that in SiHfBCN_07 (40 nm), indicating that a two-step sintering process (as used for the densification of SiHfBCN_07) provides finer microstructures as compared to those obtained via one-step sintering (used for SiHfBCN-06). Moreover grains growth of HfC_xN_{1-x} tends to be inhibited, SiC grain adjacent to two HfC grains is found in high solution TEM (Figure 3.16c), which plays a role in isolating coarsening since grain to grain contacts of the same phase is minimized.

The comparison in the average size of the HfC_xN_{1-x} precipitations in the SiHfCN ceramics sintered with different dwelling times (see Table 3.5) indicate a strong effect of the dwelling time on the grain growth. As the pore-pinning which limits the growth of the grain size does not have any effect, the grain growth could not be avoided [238]. Thus, the increase of the sintering time from 1 to 15 min at 1950 °C and 105 MPa induces an increase of the grain size of HfC_xN_{1-x} from ca. 130 to ca. 166 nm. Additionally, the increase of the applied pressure during sintering has been shown to suppress the grain growth of HfC_xN_{1-x}, as the applied pressure rose from 55 MPa to 120 MPa, the grain size of HfC_xN_{1-x} significantly decreased from 69.1 to 45.6 nm respectively. This effect was shown also during sintering of other ceramic materials such as titania or tungsten carbide and relies on the fact that the increase in pressure slows down diffusion processes [239].

Furthermore, the peak corresponding to β-SiC is evidently increasing in dependence on pressure, whereas β - Si_3N_4 seems to have disappeared after sintering at 120 MPa (Figure 3.14c). Applying higher pressure seems to enhance the reaction between α-Si_3N_4 and free carbon by a higher driving force. In other words, the decomposition of α -Si_3N_4 seems to be accelerated, leading to an enhanced formation of β-SiC, i.e. the grain size as well as the content of β-SiC increased dramatically (i.e. from 31.4 wt% at 100 MPa to 62.5 wt% at 120 MPa, see Table 3.5). Thus, the conversion from α-Si_3N_4 to β-Si_3N_4 becomes less possible, and the content of β-Si_3N_4 is found to significantly decrease from 40.1 wt% to 8.7 wt%. Nonetheless, it is intriguing that the generation of more β-SiC is observed along with rising pressure. When the release of the N_2 is prevented by pressure, this reaction between SiN_x and free carbon is considered as a limitation. Thus, the opposite phenomenon would have been expected; however, the higher pressure applied in our study might promote the heating transfer for a thermodynamic reaction. That could be a plausible reason for this observation, but more experiments are needed to clarify this and is beyond the scope of our present study.

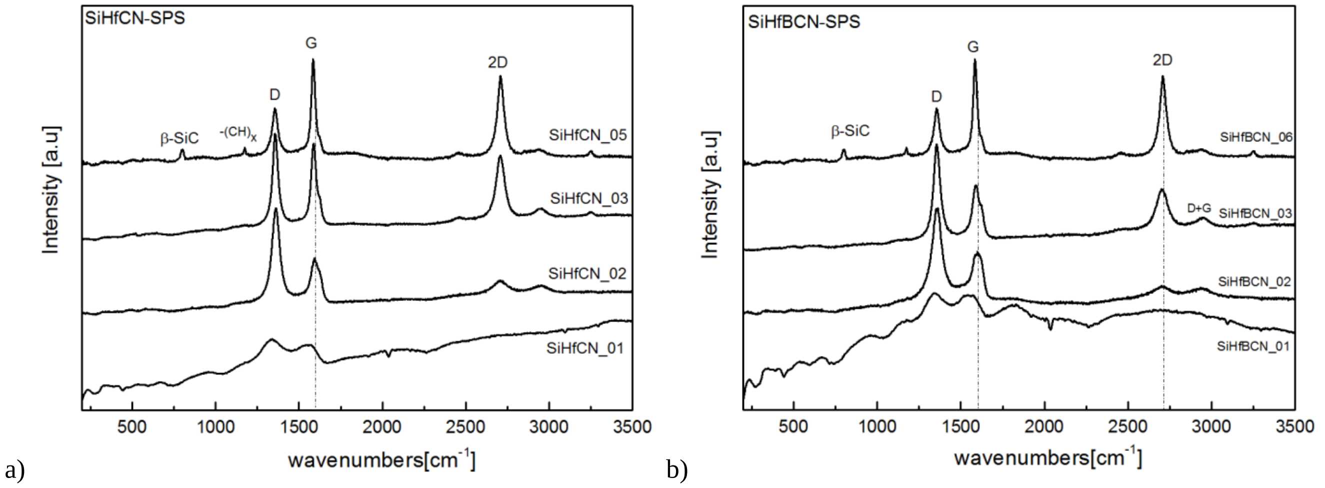

Figure 3.17. Raman spectra of the SiHfCN- and SiHfBCN-based SPS samples: (a) SiHfCN-based SPS samples; (b) SiHfBCN-based SPS samples.

Table 3.6. Peak positions, integral area ratios A_D/A_G and A_{2D}/A_D, crystallite lateral size (La, Leq) and full width at the half maximum of the D and G modes for the segregated carbon phase are present in SiHfCN and SiHfBCN sintered by SPS at different parameters (for more information on samples labels, see Table 3.6).

Samples label	A_D/A_G	A_D	A_G	A_{2D}	$FWHM_D$ [cm^{-1}]	ω_D [cm^{-1}]	$FWHM_G$ [cm^{-1}]	ω_G [cm^{-1}]	A_{2D}/A_D	La [nm]	Leq [nm]
SiHfCN_01	3,64	10156	2790	2046	220	1336	104	1547	0.20	1.21	1.77
SiHfCN_02	2,05	7865	3829	2374	56	1361	60	1597	0.30	2.14	2.66
SiHfCN_03	0,99	6617	6697	4983	54	1371	57	1598	0.75	4.45	6.63
SiHfCN_05	0,73	2896	3980	5588	42	1356	29	1585	1.93	6.05	16.98
SiHfBCN_01	5,15	10205	1983	2101	168	1341	82	1581	0.34	0.85	3.02
SiHfBCN_02	1,58	8238	5223	2201	65	1357	72	1598	0.27	2.79	2.35
SiHfBCN_03	1,53	6726	4405	5096	47	1356	56	1593	0.76	2.88	6.67
SiHfBCN_06	0,70	2757	3933	5396	40	1356	28	1586	1.96	6.28	17.22

Besides crystalline phases present in both sintering samples, the segregated carbon present in the SPS specimens were found to be highly disordered; the Raman spectra (Figure 3.17) exhibit the G and D modes at 1580 and 1350 cm^{-1}, respectively, which are typical for carbon materials. Furthermore, the overtone bands at 2700 and 2950 cm^{-1} (2D and D + G modes, respectively) were found in some spectra.

In order to rationalize the evolution of segregated carbon occurring during the SPS process, the change in the ratios of the integral area of D and G was assessed (Table 3.6): a) the ratio of A_D and A_G decreased with the temperature increasing for both ceramics, suggesting that the nano crystallization of free carbon becomes better organized. This indication is supported by being narrower across the full width at half maximum (FWMH) of the D and G-band, as well as by increasing the 2D modes. Furthermore, increasing the L_a and L_{eq} parameters which defined the average graphene length described the same trend; b) interestingly, the value of A_D is significantly larger than that of A_G when the sintering temperature is lower than 1850 °C, indicating the high degree of disorder in the carbon cluster. However, the ratio of A_D and A_G is found to be lower than 1.0 for both ceramics sintered at 1950 °C, suggesting that graphitization may be taking place; c) the parameter of L_{eq} is much higher than L_a, which means tortuosity is present and that small planar graphene units may be well connected [240].

3.2.1.2 .4 Mechanical properties of dense materials

The dense SiHfCN- and SiHfBCN-based ceramics are frequently prepared via the PLS and PAS methods, in which the almost fully dense materials can be achieved by using the SPS technique. This section will only present the mechanical properties of dense SiHfCN and SiHfBCN ceramic materials. Since the effect of porosity on the mechanical properties (i.e. elastic modulus, hardness) is quite complex and controversial, it is eliminated in later discussion. Thus, the mechanical properties of the dense samples prepared by SPS are only discussed.

Load-displacement (P-h) curves obtained from micro- and nano-indentation are presented in Figure 3.18, indicating that the stiffness of the SiHfCN_05 is higher than the corresponding SiHfBCN-based SPS samples (i.e., SiHfBCN_06 and SiHfBCN_09). The hardness and elastic modulus of materials are calculated from the load and unload curve and derived from Oliver-Pharr measurements by using the following Eqs 3.1-3.3 [241].

$$H = \frac{P_{max}}{A_{c,max}} \qquad \text{(Eq.3.1)}$$

$$E_r = \frac{S\sqrt{\pi}}{2\sqrt{Ac}} \qquad \text{(Eq.3.2)}$$

$$\left(\frac{1-\nu^2}{E}\right) = \frac{1}{Er} - \left(\frac{1-\nu i^2}{E_i}\right) \qquad \text{(Eq.3.3)}$$

With H being the hardness, A_c is the area of the indentation under load, E, E_r and E_i (E_i = 1147GPa for diamond) are the elastic, reduced elastic and indenter elastic moduli, S is the unloading stiffness (S) ν and ν_i are Poisson's ratio of the sample and of the indenter (ν_i = 0.07). Here, the Poisson's ratio of both SiHfCN and SiHfBCN was estimated with a value of 0.14-0.17, which corresponds to both β-SiC and HfC phases [242-244]**.** The values of the hardness (H) and elastic modulus (E) for both ceramics are listed in Table 3.7 and were found to be significantly higher than those of other Si-based ceramics derived from single-source precursors (e.g., SiOC, SiC, SiCN etc.). The primary reason for the higher elastic modulus probably relates to the crystallinity of the samples in the present study, as the elastic modulus is closely related to the force between atoms and increases along with the increase of the atomic force [245]. The reason why the elastic moduli of the SiHfBCN-based samples are smaller than those measured for SiHfCN most probably also rely on the different extent of crystallinity in the samples; thus, the samples with higher crystallinity (i.e., SiHfCN samples) have higher elastic moduli than their SiHfBCN counterparts (see Figure 3.18, i.e. the E of the SiHfCN-based after sintering at 1950 °C by SPS was determined to be 271 GPa, which is higher than that of SiHfBCN (207 and 245 GPa for SiHfBCN_06 and SiHfBCN_09, respectively).

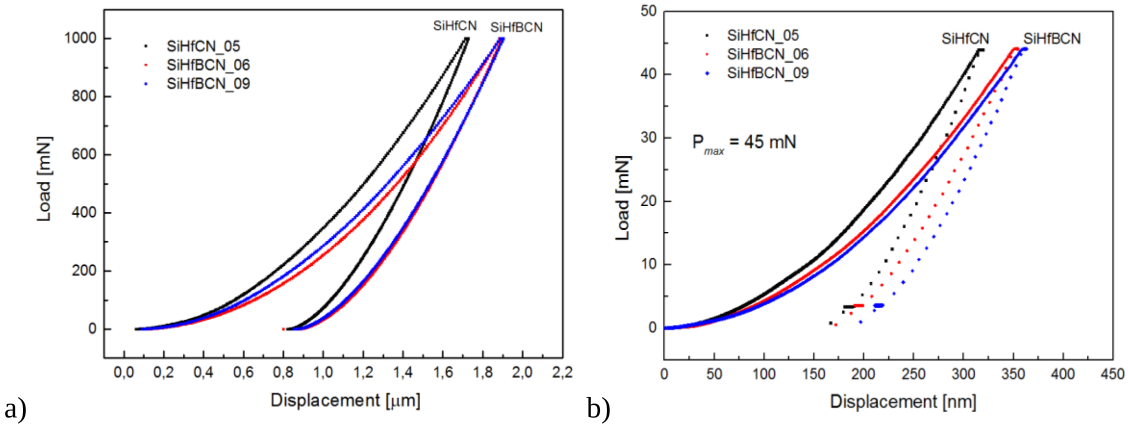

Figure 3.18. A comparison of load versus indenter displacement data of dense SiHfCN- and SiHfBCN-based samples. Data were obtained from (a) microindentation and (b) nanoindentation experiments.

Table 3.7. Mechanical properties of SiHfCN, SiHfBCN-based SPS ceramics and their counterparts derived from the SSPs SiOC, SiC and SiCN etc.

Materials	Load applied	Hardness [GPa]	Elastic modulus [GPa]	Processing route	Reference
SiC	10N	~7.9-12.8	-	Cold pressed and thermolyzed	[246]
SiOC	0.5-20N	~5.5-8.6	66	Photo crosslink and pyrolysis	[247]
SiCN	50-250mN	~13±2	121±10	Warm pressed and thermolyzed	[248]
SiCN	25-500mN	~15.7	-	Cast and pyrolyzed	[249]
SiCN	250 mN-50N	~8.3-11.3	82-140	Casting technique	[250]
SiCN	2-10N	~25-27	155±10	Cast and pyrolyzed	[107]
SiCN	0.98-98N	~6.1-12	105	Cold-pressed and thermolyzed	[245]
SiCN (with CNTs)	---	9.4-14.3	74-118	Pressure-assisted pyrolysis	[251]
SiTiN	10N/2mN*	25.1±4	183.3±25.9	Warm pressed and thermolyzed	[252]
SiBCN	20N	~0.7-5.4	48-102	PDC + SPS	[253]
SiHfCN_05	50mN, 1N/45mN*	23.1±1/26.8±3.4*	271±8/367±30*	PDC + SPS	Present work
SiHfBCN_06	50mN, 1N/45mN*	22.5±2.3/24.6±3.6*	245±18/284±44*	PDC + SPS	Present work
SiHfBCN_09	50mN, 1N/45mN*	19.5±1/20.8±3.7*	207±11/266±40*	PDC + SPS	Present work

* These values were measured by nanoindentation

3.2.2 Ceramic matrix composites (CMCs)

3.2.2.1 Preparation of C_f/SiCN and C_f/SiHfBCN CMCs via PIP technique

Since the polymer-to-ceramic conversion occurs upon the release of a low molecular weight species as well as with increasing density, the formation of porosity in the resulting ceramic is a natural consequence[60]. Therefore, for the fabrication of CMCs via the PIP technique, repeated infiltration-pyrolysis cycles are necessary in order to improve the densification and decrease the porosity. The development of the density and open porosity in the prepared CMCs as functions of the number of infiltration-pyrolysis cycles is shown in Figure 3.19. The results show that the open porosity decreases and the density increases as the number of infiltration-pyrolysis cycles increase [5].

As the ceramic yield directly correlates with the porosity of the obtained ceramics, it is expected that high ceramic yields will allow for the preparation of ceramics with low porosity values. The preceramic polymers used within the present study, i.e. polysilazane and a Hf-/B-modified single-source precursor, exhibit upon pyrolysis at 1100 °C ceramic yields of ca. 65 and 80 wt%, respectively [254]. Consequently, the residual open porosity of SiHfBCN was expected to be lower than that of SiCN. Indeed, the C_f/SiHfBCN obtained from applying three PIP cycles showed a residual porosity of ca. 17 vol%, whereas the C_f/SiCN prepared in the same way had a residual porosity of ca. 24 vol%. However, as the number of PIP cycles was increased to five, similar porosity values were obtained in both materials (i.e. 14.2 and 14.7 vol% for C_f/SiCN and C_f/SiHfBCN). As the number of infiltration-pyrolysis cycles was further increased, only a slight increase of the density and decrease of the porosity were observed. Considering the evolution of the porosity and density in the prepared CMCs (see Figure 3.19), a number of 8 PIP cycles was selected to prepare the CMC samples to be studied concerning their behavior in hydrothermal corrosion conditions (see Section 3.5). Thus, the studied CMCs exhibited porosity values of 7.3 and 9.2 vol% (for C_f/SiCN and C_f/SiHfBCN, respectively) and densities of 1.69 and 1.88, respectively.

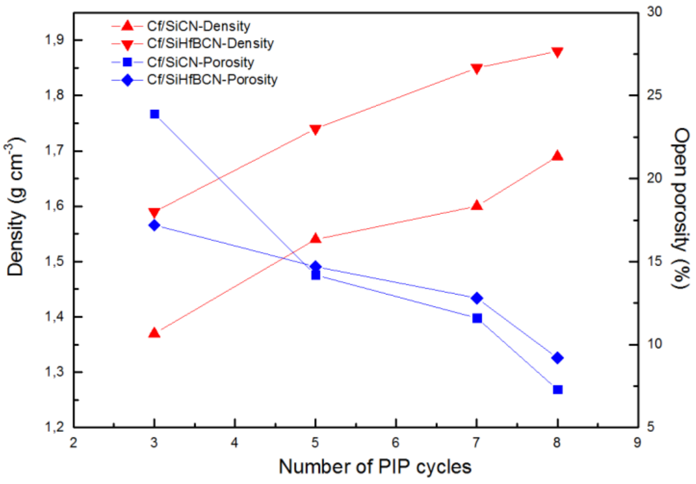

Figure 3.19. Density and porosity values for the as-prepared C_f/SiCN and C_f/SiHfBCN CMCs (as functions of the used number of infiltration-pyrolysis cycles).

The microstructure of the obtained CMCs was investigated by SEM (Figure 3.20). The micrographs of the cross-sections of C_f/SiCN and C_f/SiHfBCN indicate that the use of 8 PIP cycles produced low-porosity CMCs. Three regions have been distinguished: I) areas of longitudinal crossing between the individual carbon fibers, which were filled with the dense SiCN/SiHfBCN ceramic matrix; II) areas between transverse carbon fibers which were also shown to be effectively infiltrated by the pre-ceramic precursor; and III) areas between the layers, which consisted only of SiCN/SiHfBCN.

As shown in Figure 3.20b, the presence of some cracks and porosity was observed at the interface between the carbon fibers and the ceramic matrix, which may have been caused by the processing of the CMCs (e.g. evaporation of the solvent [121]) or the mismatch between the coefficients of thermal expansion of the fibers and of the ceramic matrix [122], [123].

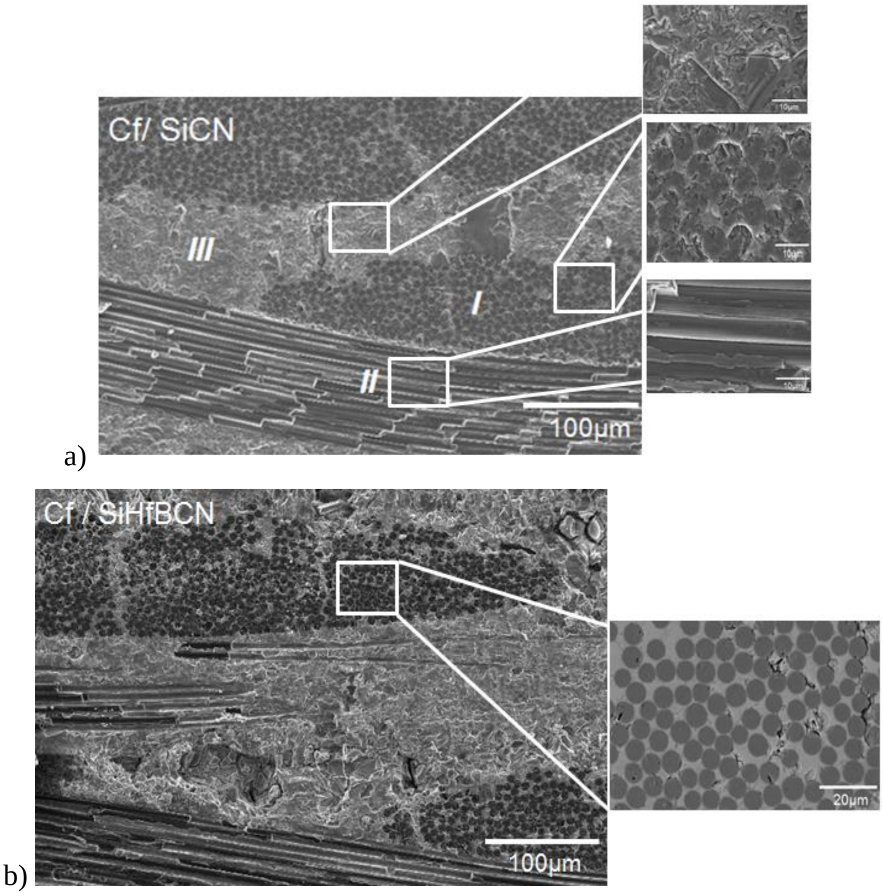

a)

b)

Figure 3.20. SEM micrographs of the prepared CMCs: a) cross-section surface of C_f/SiCN; b) cross-section surface of C_f/SiHfBCN.

The bending strength of the prepared CMCs was measured, and the corresponding stress–strain curves are presented in Figure 3.21. The C_f/SiCN composites show a ductile fracture behavior, with the displacement increasing at the beginning linearly along with the applied load, until hitting a sudden yield point and then gently increasing up to the peak of strength; whereas C_f/SiHfBCN shows a brittle behavior. The average strength of the as-fabricated C_f/SiCN and C_f/SiHfBCN was ca. 124.7 and 70.2 MPa, respectively. This is in agreement with the SEM micrographs of the fractured surfaces of the studied CMCs. Thus, C_f/SiHfBCN exhibits a brittle fracture behavior; whereas the C_f/SiCN sample clearly shows a fiber pull-out mechanism (Figure 3.22). Obviously, the interface between C_f and SiHfBCN is significantly stronger than that between C_f and SiCN [255]. However, the reason why the incorporation of Hf and B into SiCN leads to a strong improvement of the Cf-ceramic interface it is not clear.

Within this context, one should note that the requirements for an improved fracture behavior (i.e. ductile fracture) and hydrothermal corrosion performance are rather conflicting. Thus, a weak interface is needed for a good mechanical behavior, whereas a tight C_f-ceramic matrix interface is beneficial for good hydrothermal corrosion behavior, as discussed below in Section 3.5.

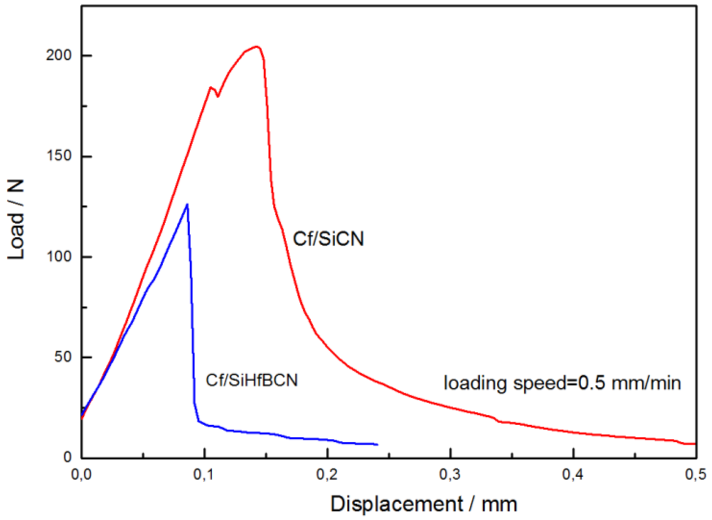

Figure 3.21. Typical load-displacement curves of C_f/SiCN and C_f/SiHfBCN.

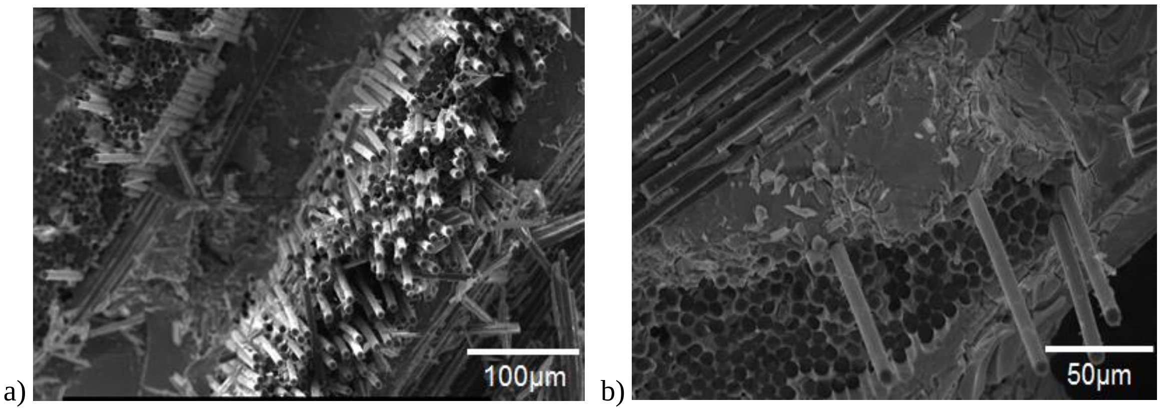

Figure 3.22. Fracture surface of C_f/SiCN and C_f/SiHfBCN composites, the C_f/SiCN sample fiber pull-out shows this clearly, whereas the brittle fractures can be observed for C_f/SiHfBCN.

3.2.2.2 Improvement of mechanical properties of CMCs via combined CVI and PIP technique

The C_f/SiHfBCN CMC only prepared by the PIP method has shown higher failure stress since the fiber-matrix (FM) bonding is too strong (Figure 3.22). Thus, decreasing FM-bonding is beneficial to improving mechanical properties, usually through a thin layer of an interfacial material referred to as the interface (e.g., pyrolytic carbon as interface in C_f/SiC) [120]. The CVI technique is commonly utilized for depositing pyrolytic carbon or another interface (i.e. BN); however, the CVI preparation of CMCs is time consuming and expensive. By comparison, the PIP/LPI methods can benefit from the low costs; furthermore, the PIP technique allows for fabricating complex-shaped, large-scale components. In this section, a hybrid combined CVI and PIP process, the elemental processes of which compensate for mutual weak points, is carried out.

The weight gain after each infiltration used to evaluate the degree of densification is shown in Figure 3.23. Compared with the composites C_f/SiC densified by the SiCN polymer precursor, the fraction of weight gain obtained by infiltration of SiHfBCN is shown to be higher. From this effect, it can be clearly seen that the higher ceramic yield induced more efficiency in the densification at the initial infiltration. Additionally, their variation trends versus the numbers of PIP cycles are similar for infiltration with SiCN and SiHfBCN, which shows that the fraction of weight gain increases linearly within 4 PIP cycles, before converting into a saturation situation in subsequent infiltrations. These interesting aspects could also be found in the evolution of density and porosity, as shown in Figure 3.24: As the number of PIP cycles increases, an increase in density and a decrease in porosity were observed. Once the number of PIP cycles exceeds 5 times, the efficiency in the infiltration sinks, resulting in a lower porosity decrease and density increase. Thus, the open porosity below 10 % was usually considered as a target in an effective impregnation. The CMCs C_f/SiC-SiCN and C_f/SiC-SiHfBCN prepared by the hybrid technique (CVI-PIP) show the value of open porosity at 7.7 and 9.2 %, respectively (see Figure 3.24).

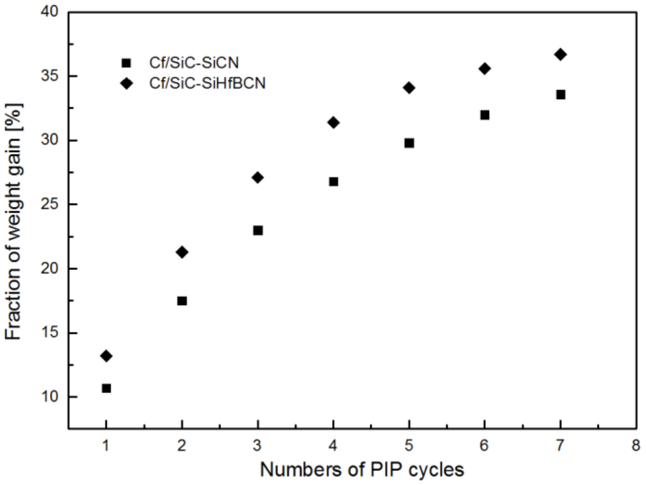

Figure 3.23. Fraction of weight gain of Cf/SiC prepared by CVI in 4 times that obtained after each infiltration; the polymer precursor (SiCN and SiHfBCN) is representative of the function of the number of PIP cycles.

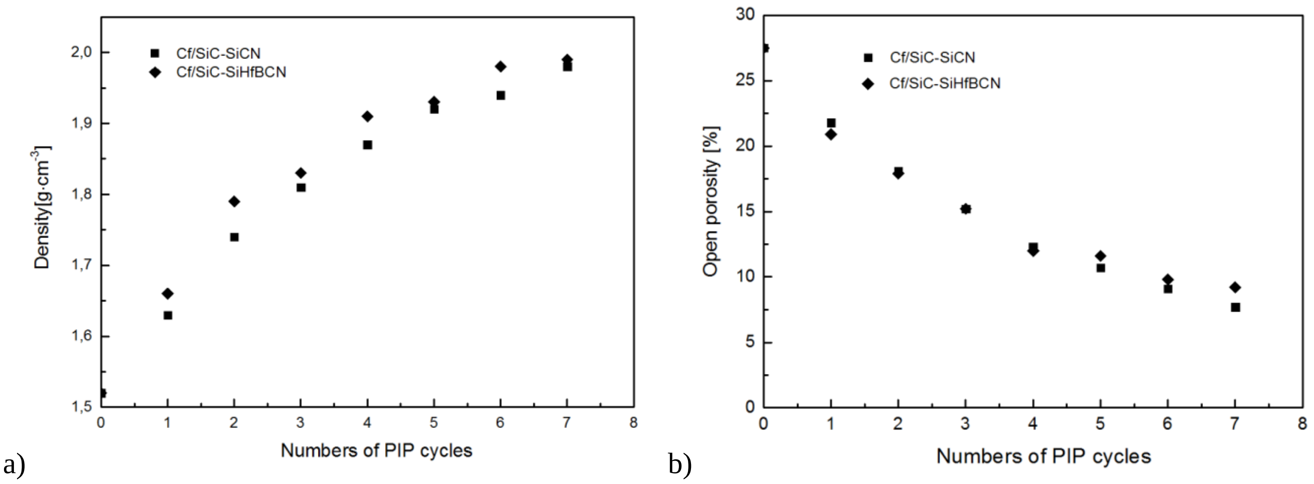

Figure 3.24. Density and open porosity trend for the as-prepared C_f/SiC-SiCN and C_f/SiC-SiHfBCN CMCs (as functions of the number of infiltration-pyrolysis cycles).

Typical stress-displacement curves of as-prepared CMCs by hybrid techniques (CVI-PIP) are presented in Figure 3.25a. For all the specimens, the curves show initial quasi-linear elastic behavior, followed by an increasing non-linear stress up to a maximum fracture stress, which reflects the ductile fracture behavior. After reaching the maximum value, the failure stress gradually decreases, which probably results from the additional SiC matrix initially deposited by the CVI technique, while the SiC matrix also acts as reinforcement and is furthermore responsible for loading transfer and better fracture toughness. Compared with non-interface composites C_f/SiHfBCN densified only by the PIP process, the pyrolytic carbon coating on the carbon fibers provides a weak fiber-matrix bonding [256]. As a result, the cracks slide along the debonded interface, causing fibers to debond from the matrix: Accordingly, fiber pull-out was observed at the surface (see Figure 3.25b-c), which is expected to improve the mechanical properties of the C_f/SiCN and C_f/SiHfBCN composites. However, the worse performance in strength for C_f/SiC-SiHfBCN (316.1 MPa) as compared to that of C_f/SiC-SiCN (474.5 MPa) might be attributed to the formation of cracks which originated from large differences in the CTE between SiC and SiHfBCN.

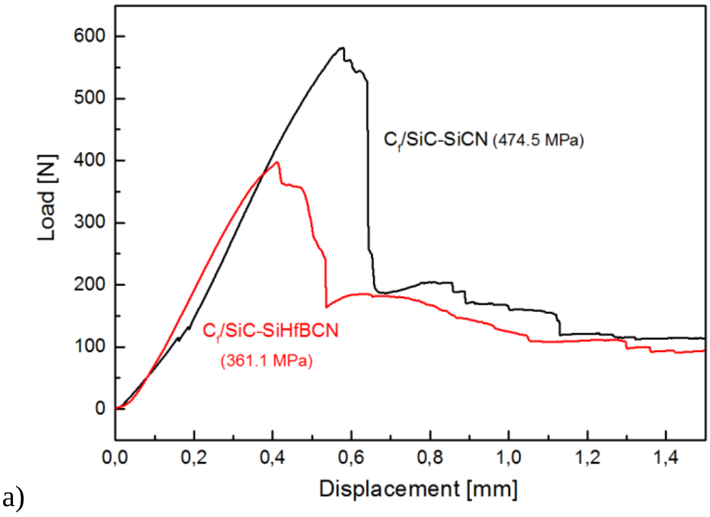

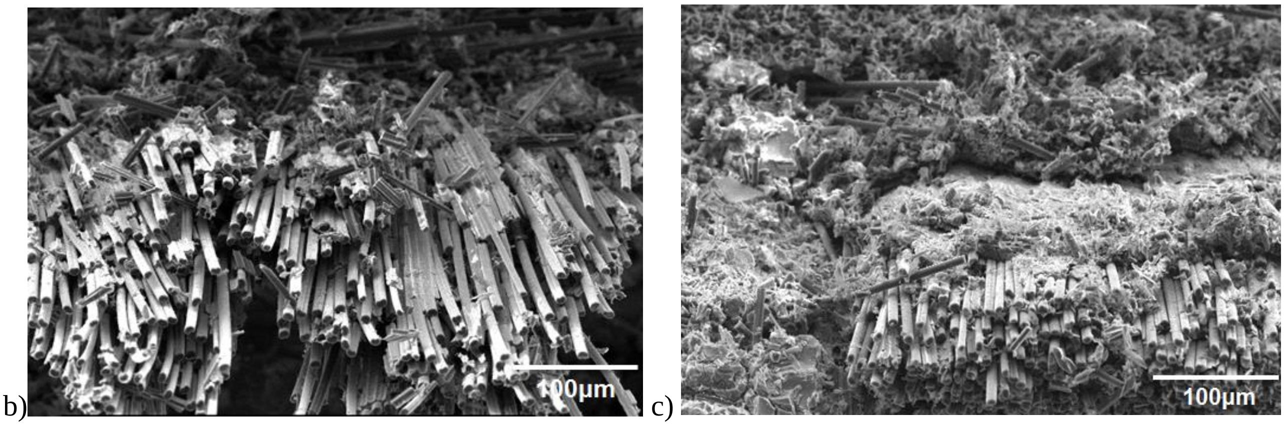

Figure 3.25. a) Stree-displacement curves of the obtained matrix composites C_f/SiC-SiCN and C_f/SiC-SiHfBCN; b) and c) Fracture surfaces of C_f/SiC-SiCN and C_f/ SiC-SiHfBCN composites, both cases show typical fiber pull-out.

3.2.3 Summary

Within this work, Hf-containing SSPs serve as a novel precursor, which is expected to convert into amorphous ceramic and its UHTC-NCs. Furthermore, SSPs allows for the fabrication of complex-shaped components. This makes SSPs SiHfBCN potentially more favorable for the preparation of ceramic monoliths and ceramic matrix composites (CMCs). For both ceramic composites, materials with low porosity and high densification provide a requirement for the novel class of SiHfBCN-based ceramics and their use in a variety of applications. Two techniques are used for the densification of ceramic monoliths: The PLS approach shows that the porosity of the amorphous ceramics annealed at 1300 °C in nitrogen can be controlled to 5.9 %; however, these are quite difficult to be prepared to full density due to their extremely low diffusion and simultaneous decomposition, while SPS facilitates a very fast heating rate (~450 °C/min) and high pressure (≥ 100 MPa), consolidating SiHfCN and SiHfBCN in a very high densification (Pop~0.1-0.2 %). Furthermore, ultra-high temperature ceramic nanocomposites (HfC(N)/β-SiC/β-Si_3N_4/C/Si(B)CN) can be tailored from SPS samples, which are promising to generate UHTC-NCs with good high temperature behavior at high or ultra-high temperatures, even in harsh environments.

Additionally, the synthesis of C_f/SiCN and C_f/SiHfBCN composites has been achieved through a simple and low cost PIP approach. However, C_f/SiHfBCN exhibits a brittle fracture behavior due to its strong interface between matrix and fibers. The mechanical properties can be improved through a hybrid technique consisting of CVI and PIP, leading to the synthesis of new composite CMCs (C_f/SiC-SiCN, C_f/SiC-SiHfBCN).

3.3 High temperature decomposition and crystallization

This chapter discusses the successful preparation of novel Hf-containing ceramic nanocomposites from a suitable single-source precursor at temperatures up to 1800 °C and the assessment of their behavior (i.e., thermal stability with regard to decomposition and crystallization behavior), which was shown to be thermodynamically controlled. Furthermore, the high-temperature stability of SiCN with respect to decomposition and crystallization is considered as a reference and compared with that of Hf-containing SiHf(B)CN ceramics.

3.3.1 High temperature decomposition

The SiHfCN and SiHfBCN samples prepared with pyrolysis at 1100 °C were annealed at 1300-1700 °C for 5 h in argon as well as in a nitrogen atmosphere. Figure 3.26 presents the mass loss upon annealing at different temperatures and atmospheres. The SiHfCN and SiHfBCN samples did not exhibit any mass change after annealing at 1300 °C in argon atmosphere. Moreover, there was little change in the volume shrinkage of samples annealed at 1300 °C (7.2 and 5.3 % for SiHfBCN1a and SiHfBCN2a respectively, see Table 3.4), which supports the results of mass change. Annealing at 1500 °C in an argon atmosphere on the other hand induced a mass loss of ca.15 wt% in SiHfCN2, ca. 10 wt % in SiHfCN1 and SiHfBCN1 and ca. 6 wt % in SiHfBCN2 (ca. 24 wt% Hf). Similarly, the development in the volume shrinkage of samples treated after 1500 °C was found to be greater than samples annealed at 1300 °C. Interestingly, the Hf- and B-free sample, SiCN, showed a significantly higher mass loss upon annealing under identical conditions, i.e. ca. 25 wt% (Figure 3.26a).

The development of the SiCN ternary system can be described as consisting of three possible processes: i) phase separation of the single-phase SiCN materials into a multi-phasic material consisting of SiC_x and SiN_x nanodomains as well as excess C (no mass loss); ii) carbothermal decomposition of the amorphous silicon nitride-rich regions, $SiN_x + C = \beta\text{-}SiC + N_2$ (accompanied by mass loss); iii) decomposition of the amorphous silicon-nitride-rich regions into elements, $SiN_x = Si + N_2$ (mass loss). In our case, mainly processes i) and ii) contributed to the mass loss of SiCN upon annealing at high temperatures [257]. The significant improvement of the stability of SiCN concerning decomposition by means of Hf alone (SiHfCN) or Hf and B (SiHfBCN) together is obvious. There are numerous studies in the literature concerning the HT behavior of SiBCN ceramics. In the case of SiBCN, the improvement of the stability has been related to the presence of BC_xN_y phase which separates SiN_x-rich regions from excess carbon and thus kinetically inhibits the carbothermal decomposition of the materials. Additionally, as the BC_xN_y phase is considered to encapsulate the SiN_x-rich regions, their decomposition into elements is also suppressed in SiBCN [258].

In the case of our SiHfBCN samples, we similarly assume a kinetic stabilization of the materials upon incorporation of Hf and B. The incorporation of Hf significantly increases the thermal stability of the ceramic system (SiHfCN samples show lower mass loss upon annealing at 1500 °C if compared to SiCN, see Figure 3.26a). This is thought to be due to the presence of HfN-rich regions which are significantly more stable concerning their carbothermal decomposition than the SiN_x regions. Furthermore, boron is considered to have a similar effect as that in the previously mentioned SiBCN ceramics [259]. This is supported by our NMR findings, which indicate the presence of BCN_2 structural units which might be located at the interface between carbon and BN-rich regions (i.e. in our case, carbon and SiN_x regions are also separated, and thus the carbothermal reaction is suppressed). The difference in the thermal stability of SiCN and SiHfBCN after annealing at 1700 °C in Ar was even larger: Thus, SiCN lost almost 50 wt% of its mass upon annealing at 1700 °C for 5 h; whereas the SiHfBCN samples exhibited mass losses of ca. 30 wt% (Figure 3.26).

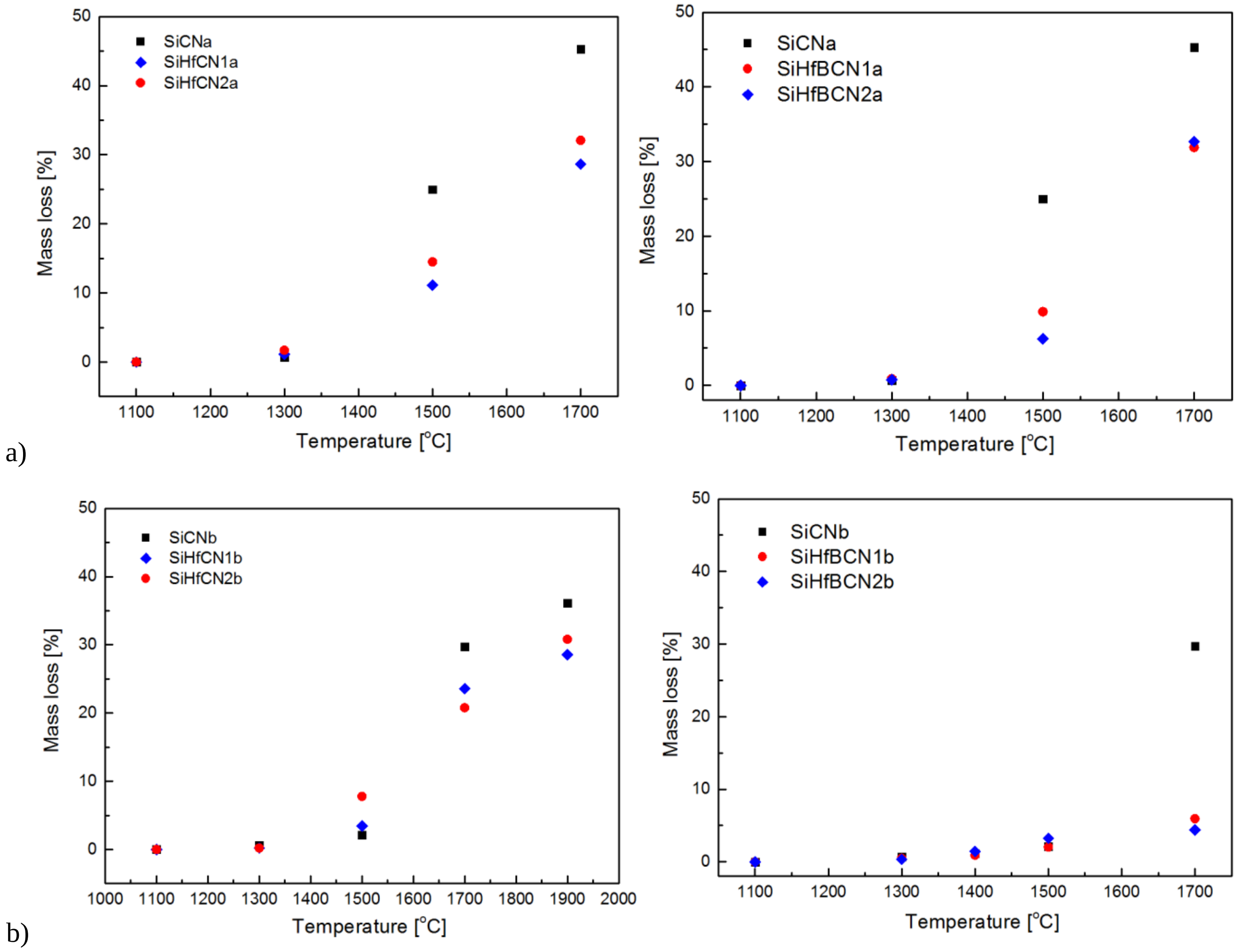

Figure 3.26. Mass loss of SiHfCN, SiHfBCN and SiCN ceramics as a function of the annealing temperature: a) annealing experiments in Ar atmosphere; b) annealing in N_2 atmosphere.

The elemental analysis data shown in Table 3.8 and Table 3.9 clearly emphasize the effect of the carbothermal decomposition of SiN_x upon nitrogen release on the chemical composition of the samples (occurring at 1480 °C; it should be noted that at 1700 °C, the decomposition of SiN_x into elements should also be taken into account): The nitrogen content of SiHfCN2a decreased significantly at 1500 °C (from 16.48 to 6.7 wt%), supporting the relatively higher mass loss upon annealing beyond 1500 °C. However, the nitrogen content of SiHfBCN2a stays constant upon annealing at 1500 °C; whereas annealing the sample at 1700 °C induces a strong depletion of nitrogen.

Table 3.8. Chemical composition of SiHfCN samples after annealing at different temperatures in argon.

Sample	N [wt%]	O [wt%]	C [wt%]
SiHfCN2a_1100	18.8	3.2	10.7
SiHfCN2a_1300	16.5	4.7	10.8
SiHfCN2a_1500	6.7	1.9	12.0
SiHfCN2a_1700	2.7	0.3	17.2

Table 3.9. Chemical composition of SiHfBCN samples after annealing at 1500 and 1700 °C.

Sample	Mass loss [wt%]	Shrinkage [vol%]	C [wt%]	O [wt%]	N [wt %]	Hf [wt%]*
SiHfBCN2a-1100			12.7	2.4	18.4	22.5
SiHfBCN2a-1500	6.3	10.7	16.4	1.7	19.1	25.2
SiHfBCN2a-1700	35.0	27.2	20.7	0.9	0.4	20.8.6
SiHfBCN2b-1500	3.1	8.5	11.4	2.4	23.8	27.3
SiHfBCN2b-1700	4.4	14.5	12.3	1.6	20.7	23.3

* - Hafnium content was measured by EDS

Annealing the SiHfCN samples in a nitrogen atmosphere showed similar mass loss as annealing in an argon atmosphere, whereas annealing the SiHfBCN samples in a nitrogen atmosphere obviously showed significantly lower mass losses compared to the annealing experiments performed in an argon atmosphere. This indicates that the effect of the atmosphere on the thermal stability is only of concern in the case of SiHfBCN. This is probably due to the formation of amorphous phase SiBCN by additional boron. Thus, the SiCN sample annealed at 1700 °C in nitrogen exhibited a mass loss of ca. 30 wt%; the relatively lower mass loss (ca. 20 wt%) is found in SiHfCN samples, whereas the SiHfBCN samples showed an excellent behavior, with mass losses below 5 wt% (see Figure 3.26b and Table 3.9). This finding clearly correlates with the nitrogen content of the SiHfBCN samples, which does not significantly change after the HT annealing, indicating that both the carbothermal decomposition of SiN_x as well as its decomposition into elements are effectively suppressed.

3.3.2 High temperature crystallization

The crystallization behavior of SiCN ceramics upon annealing from 1100-1700 °C in different atmospheres (Ar and N_2) is presented in Figure 3.27, which shows that no crystalline phase could be observed (i.e., the samples were amorphous) at temperatures up to 1300 °C in both atmospheres. The β-SiC began to crystallize upon annealing at 1500 °C in the argon atmosphere (see Figure 3.27a), while an amorphous (or nanocrystalline) phase is clearly observed in the samples annealed at identical temperatures (1500 °C) in nitrogen (see Figure 3.27b). A pronounced crystallization of β-SiC was found in samples after annealing at 1700 °C in an argon atmosphere, indicating that the decomposition of Si_3N_4 induces a very high mass loss (ca. 45 wt%, see Figure 3.26), whereas the partial crystallization of β-SiC in samples treated in nitrogen contributed to a lower mass loss of 30 wt%.

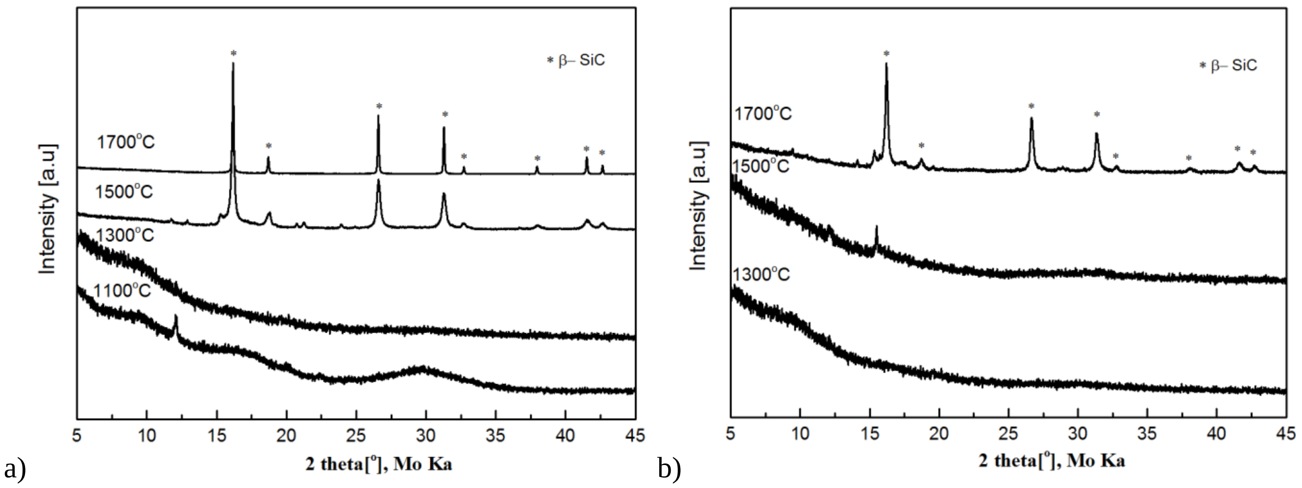

Figure 3.27. Crystallization behavior of SiCN upon annealing at temperatures from 1100 to 1700 °C in Ar (a) and N_2 (b).

Accordingly, the crystallization of the annealed samples of SiHfCN (both compositions: SiHfCN1 and SiHfCN2) in argon and nitrogen were studied via XRD. The findings regarding the crystalline structures of SiHfCN samples annealed at 1300 °C were similar to those for the SiCN samples, both revealing an amorphous phase. Upon annealing at 1500 °C in an argon atmosphere, two phases, assigned to Hf(C_x, N_{1-x}) and β-SiC, began to crystallize; interestingly, the formation of β-SiC seems to have been suppressed in SiHfCN2a (high Hf content), as indicated by the much lower intensity of β-SiC compared with SiHfCN1a. The SiHfCN sample annealed at 1700 °C in argon exhibited enhanced growth of β-SiC due to the carbothermal decomposition of Si_3N_4, in which the β-SiC phase was predominant among the crystalline phases of SiHfCN1. However, the samples annealed in a nitrogen atmosphere exhibited a different effect of the Hf content on the crystallization behavior: SiHfCN1 demonstrated a tendency toward retarded crystallization and retained an amorphous structure at temperatures up to 1500 °C, whereas in contrast, Hf(C_x, N_{1-x}) formed in SiHfCN2 (with a higher Hf content) annealed at 1500 °C, suggesting that the crystallization was facilitated by the formation of a solid solution phase of Hf(C_x, N_{1-x}). Upon annealing at 1700 and 1900 °C, the intensity of the β-SiC phase in the SiHfCN samples decreased with increasing Hf content. These results reveal no difference in the crystal structure for different annealing atmospheres; in both cases, the β-SiC and Hf(C_x, N_{1-x}) phases were the main crystalline phases to precipitate. To further understand the crystallization behavior, the results of Rietveld refinement of SiHfCN1 and SiHfCN2 annealed in argon at 1500 and 1700 °C are presented in Figure 3.29 and Table 3.10, showing that Hf(C_x, N_{1-x}) became enriched in the carbon with increasing temperature. When the weight fractions and crystallite sizes of the phases were estimated using the same methods, it was found that the weight fraction of β-SiC decreased from 89 to 71.2 wt% as the Hf content was increased. Although the crystallite sizes of SiHfCN2a-1700 (604.8 and 127.9 nm for Hf(C_x, N_{1-x}) and β-SiC, respectively) were much larger than those of SiHfCN1a-1700 (164.9 and 54.7 nm, see Table 3.10), the samples annealed at 1500 °C revealed crystallite sizes for SiHfCN1a-1500 and SiHfCN2a-1500 of below 100 nm.

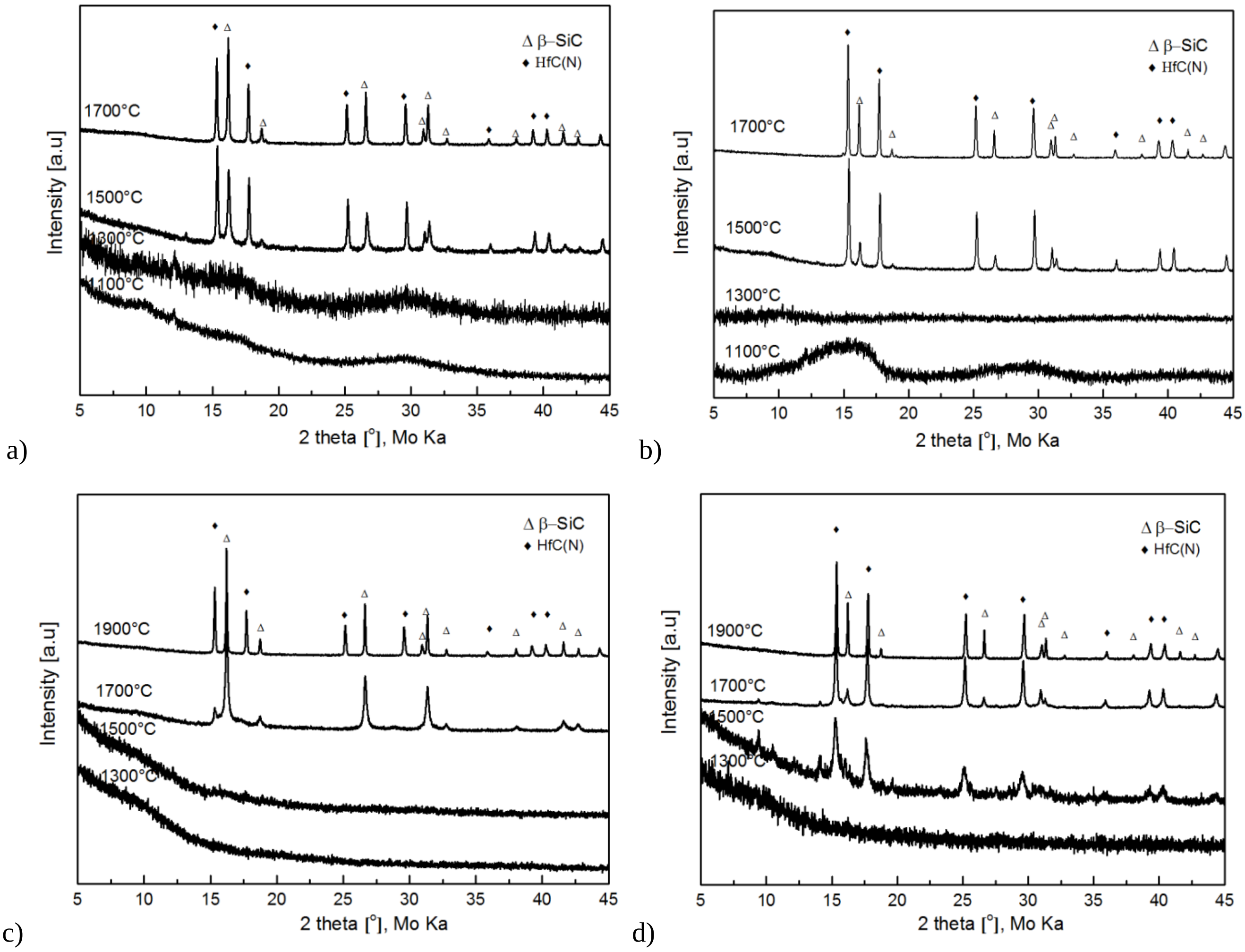

Figure 3.28. Crystallization behavior of SiHfCN upon heat treatment at temperatures from 1100 to 1700 °C in Ar and from 1300-1900 °C in N_2: (a) SiHfCN1a and (b) SiHfCN2a (argon atmosphere); (c) SiHfCN1b and (d) SiHfCN2b (nitrogen atmosphere).

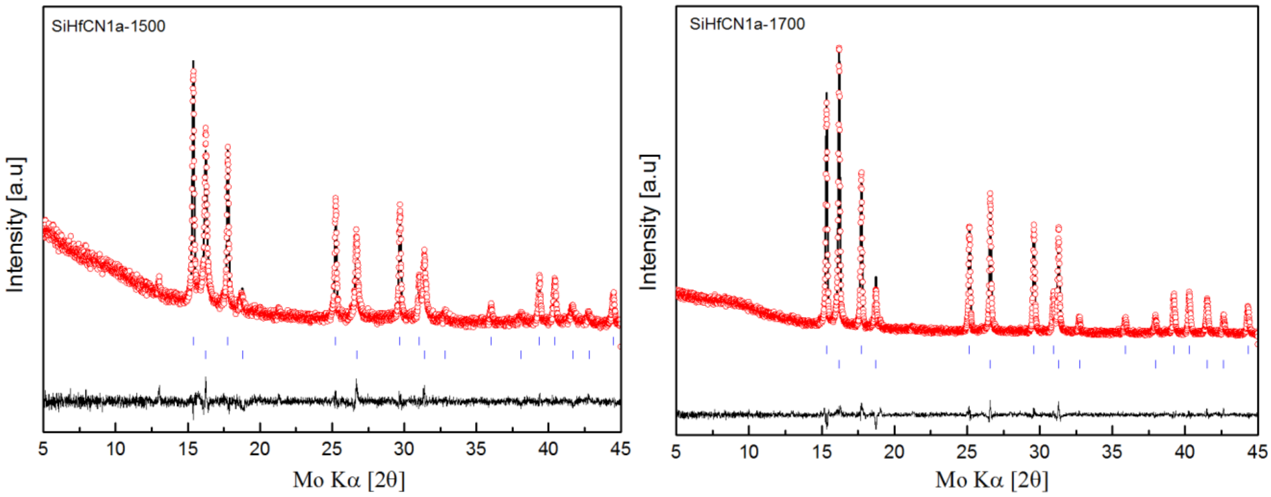

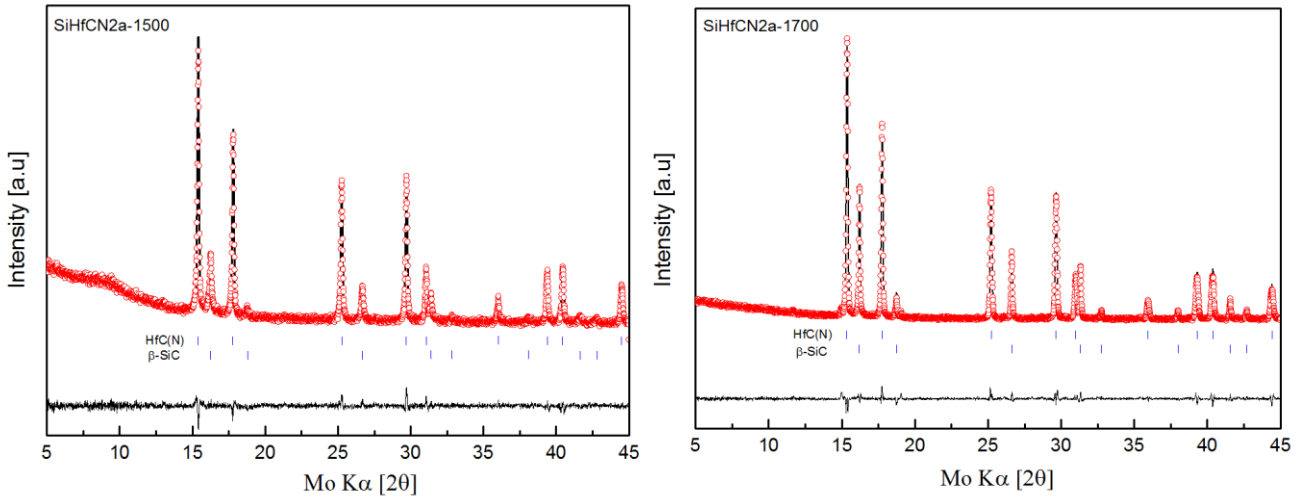

Figure 3.29. Results of Rietveld refinement of SiHfCN1 and SiHfCN2 annealed in argon at 1500 and 1700 °C. The positions of the Bragg reflections are indicated by vertical bars (|). The difference curve between the experimental intensities and those calculated from the refined model is shown in the lower part of the diagram.

Table 3.10. The lattice constant, weight fractions (relative to the crystalline content of the investigated samples) and crystallite sizes of HfC(N) and SiC for SiHfCN1a and SiHfCN2a annealed at 1500 °C and 1700 °C in Ar, as determined via the Rietveld refinement of the XRD data.

Ceramic	Lattice constant		HfC(N)		SiC	
	Cell parameter	HfC_xN_{1-x}	Fraction [wt%]	Size [nm]	Fraction [wt%]	Size [nm]
SiHfCN1a-1500	4.58983	$HfC_{0.58}N_{0.42}$	11.0	47.2	89.0	13.5
SiHfCN1a-1700	4.60496	$HfC_{0.71}N_{0.29}$	10.9	164.9	89.1	54.7
SiHfCN2a-1500	4.58831	$HfC_{0.56}N_{0.44}$	32.9	73.9	67.1	19.5
SiHfCN2a-1700	4.59698	$HfC_{0.64}N_{0.36}$	28.8	604.8	71.2	127.9

A TEM micrograph of an SiHfCN sample annealed at 1500 °C in argon reveals the crystalline phases β-SiC and Hf(C_x, N_{1-x}), which can be observed based on contrast variations (Figure 3.30). Additionally, the Hf(C_x, N_{1-x}) crystallite size is estimated from this image to be approximately 50-75 nm, which is consistent with the XRD results (Table 3.10).

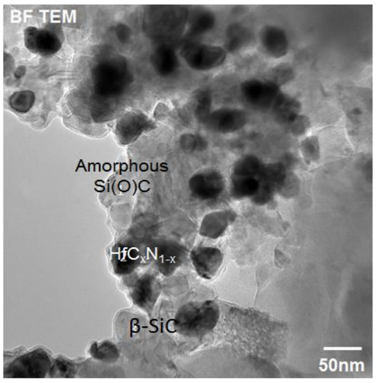

Figure 3.30. TEM micrographs of SiHfCN2a annealed at 1500 °C in an argon atmosphere showing HfC_xN_{1-x} homogenously dispersed through amorphous matrix Si(O)C.

The annealed SiHfBCN samples in argon were also investigated concerning their phase composition and microstructure by X-ray diffraction and TEM. The as-prepared samples (pyrolysis at 1100 °C) were shown to be X-ray amorphous (Figure 3.10 and Figure 3.31). The samples did not crystallize upon annealing at 1300 °C in argon atmosphere, whereas after annealing at 1500 °C, Hf(C_x, N_{1-x}) and β-SiC did crystallize. Upon annealing at 1700 °C, HfB_2 was identified as an additional crystalline phase (Figure 3.31a, b). The composition of Hf(C_x, N_{1-x}) was estimated from the position of the reflections upon using the Vegard's rule and Rietveld refinement of the XRD data (see Table 3.10), showing it to be $HfC_{0.77}N_{0.23}$.

The crystallization processes occurring in SiHfBCN upon annealing at 1500-1700 °C in an argon atmosphere can be rationalized as follows:

i) Based on the MAS NMR data, the as-prepared material is phase-separated and consists of SiN_x, SiC_x, excess carbon, BN and HfN amorphous phases (although this description does not take into account mixed bondings at the interfaces between the different phases).

ii) The amorphous SiN_x-rich regions can undergo a crystallization process to β-Si_3N_4 (detected in small amounts in the XRD patterns of the samples annealed at 1500 °C) as well as a carbothermal decomposition, cf. SiN_x + C = β-SiC + N_2, which induces the crystallization of the silicon carbide. As previously mentioned, the incorporation of Hf and B suppresses the formation of β-SiC. This is clearly shown in the samples annealed at 1500 and 1700 °C, as the amount of β-SiC is reduced with an increasing amount of Hf and B, as revealed by the Rietveld refinement of the X-ray diffraction patterns of the samples annealed in argon at 1700 °C (see Figure 3.32 and Table 3.11).Thus, the weight fraction of β-SiC (related to the crystalline content of the samples) decreases from 88% in SiHfBCN1a to 72% in SiHfBCN2a. Also, the crystallite size of β-SiC is shown to decrease from ca. 112 nm in SiHfBCN1a to ca. 50 nm in SiHfBCN2a (Table 3.11). Furthermore, the size of β-SiC in the case of SiHfBCN2a-1700 (ca. 50 nm) is much lower than that of the corresponding SiHfCN2a-1700 (127.9 nm, see Table 3.10), suggesting that the growth of β-SiC is suppressed by the incorporation of both Hf and B. This finding can emphasize the effect of boron on the crystallization behavior, which is distinct from that of Hf alone which shows that the growth of β-SiC is facilitated with an increasing Hf content.

iii) The presence of $HfC_{0.77}N_{0.23}$ (crystallite size of ca. 40 and 63 nm for SiHfBCN1a and SiHfBCN2a, respectively; see Table 3.11) can be explained as a result of the reaction of HfN with the excess carbon. In a subsequent step (annealing at 1700 °C), $HfC_{0.77}N_{0.23}$ reacts with the BN phase to generate free carbon and HfB_2 (and some nitrogen is probably released), as it is known from the reactions of metal carbides with boron nitride [260]. The size of the HfB_2 precipitation is significantly larger than those of β-SiC and $HfC_{0.77}N_{0.23}$ (200 and 330 nm for SiHfBCN1a and SiHfBCN2a, respectively; see Table 3.11).

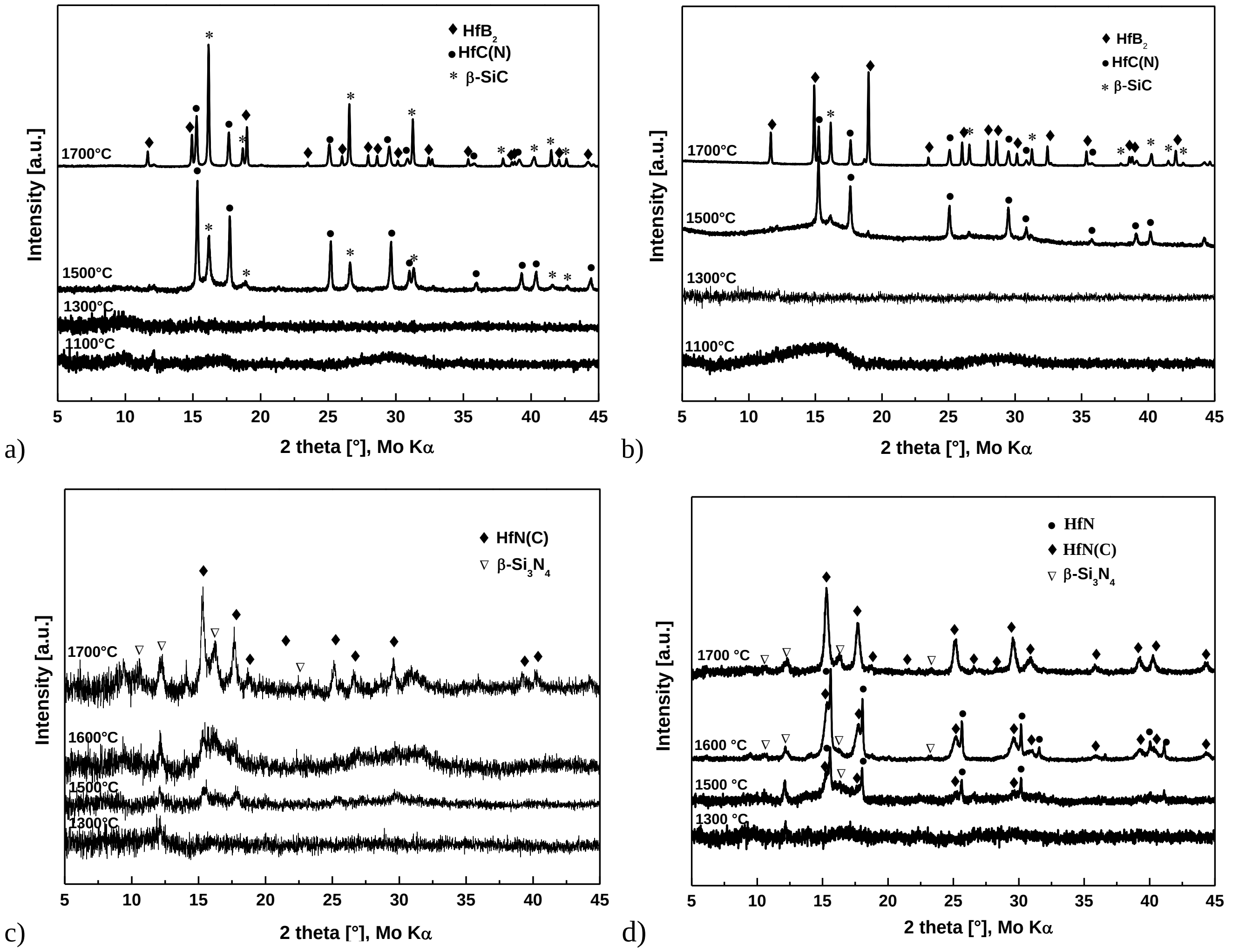

Figure 3.31. Crystallization behavior of SiHfBCN upon heat treatment at temperatures from 1300 to 1700 °C in Ar and N_2: (a) SiHfBCN1a and (b) SiHfBCN2a (argon atmosphere); (c) SiHfBCN1b and (d) SiHfBCN2b (nitrogen atmosphere).

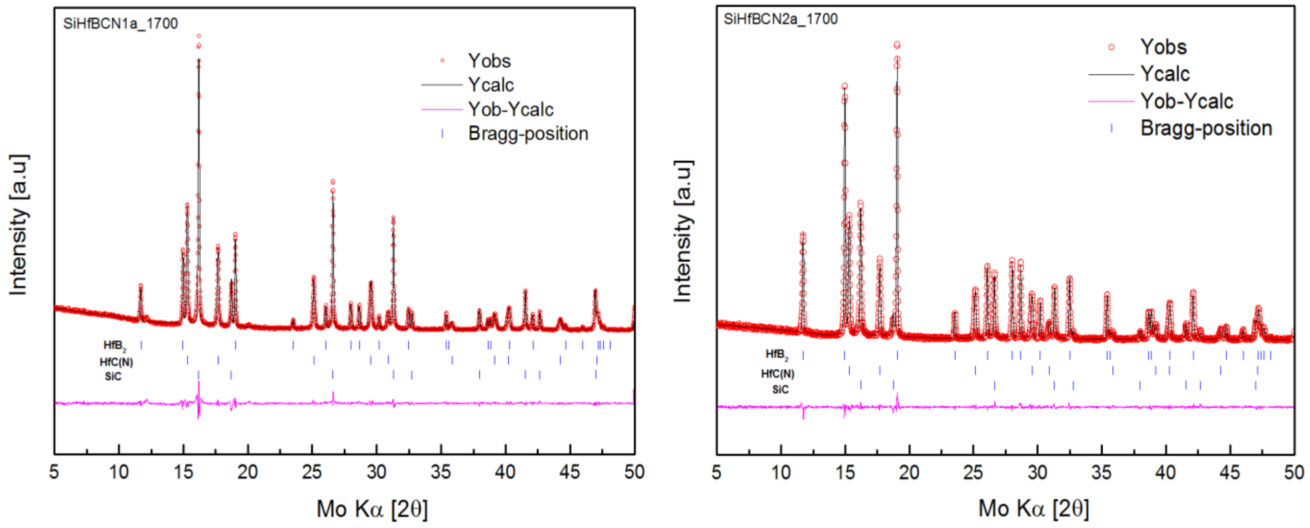

Figure 3.32. Result of the Rietveld refinement of the SiHfBCN1 and SiHfBCN2 annealed in argon at 1700 °C. The positions of the Bragg reflections are indicated by vertical bars (|). The difference curve between the experimental and the calculated intensities from the refined model is shown in the lower part of the diagram.

Table 3.11. The weight fractions (relative to the crystalline content of the investigated samples) and crystallite sizes of HfB_2, HfC_xN_{1-x} and SiC for SiHfBCN1a and SiHfBCN2a annealed at 1700 °C in Ar, as determined from the Rietveld refinement of the XRD data.

	Lattice constant		HfB_2		HfC_xN_{1-x}		SiC	
Ceramic	Cell parameter	$Hf(C_x,N_{1-x})$	Fraction [wt%]	Size [nm]	Fraction [wt%]	Size [nm]	Fraction [wt%]	Size [nm]
SiHfBCN1a	4.61200	$HfC_{0.77}N_{0.23}$	4.4	200.2	7.3	39.3	88.3	112.1
SiHfBCN2a	4.61102	$HfC_{0.77}N_{0.23}$	18.8	330.3	9.4	63.5	71.8	48.7

The information on the crystallization behavior of SiHfBCN obtained from the XRD data have been supported by the TEM investigation. In Figure 3.33, the microstructure of SiHfBCN2a is shown, indicating the presence of an amorphous SiC(N,O)-based matrix and of β-SiC as well as $Hf(C_x, N_{1-x})$ and HfB_2 nano-precipitations. The size of the β-SiC nano-particles is ca. 30 - 50 nm; whereas the $Hf(C_x, N_{1-x})$ and HfB_2 precipitations were significantly larger (ca. 100 - 200 nm). Thus, the TEM results agree very well with the values obtained from the Rietveld refinement of the XRD data (Table 3.11).

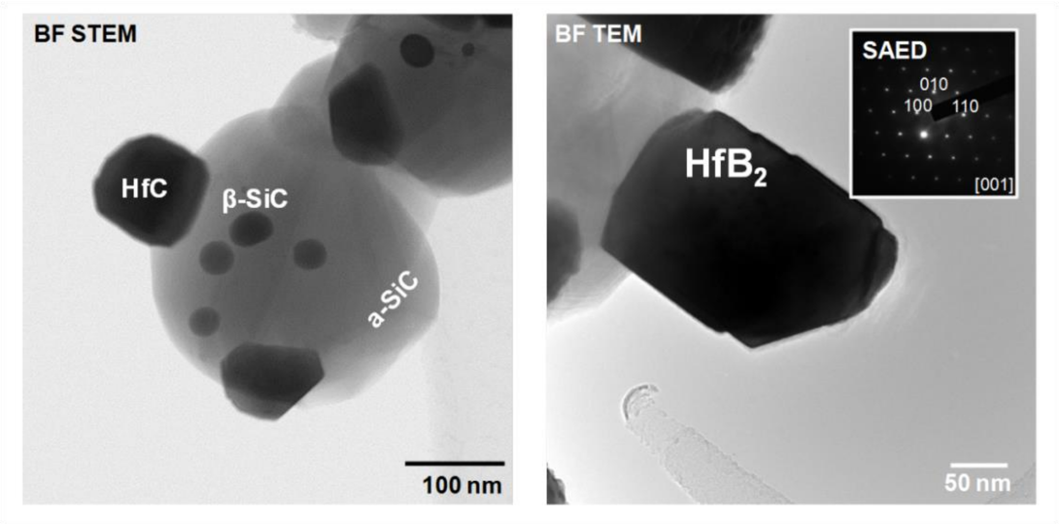

Figure 3.33. TEM micrographs of SiHfBCN2a annealed at 1700 °C in an argon atmosphere. In the left micrograph, HfC and β-SiC crystallites are shown; the matrix is SiC-based and amorphous; the micrograph on the right shows a HfB2 crystallite, as identified by means of electron diffraction (see SAED inset).

The samples annealed in a nitrogen atmosphere showed a significant effect of the Hf and B content on their crystallization behavior which is different from that of additional Hf alone. Thus, the sample with low Hf and B content (SiHfBCN1) remains mainly X-ray amorphous even up to 1600 °C, whereas SiHfBCN2 shows crystallization of β-Si_3N_4 and HfN upon annealing at 1500 °C. The crystalline HfN phase is shown to be consumed as the annealing temperature is raised to 1700 °C, and instead an N-rich HfN_xC_{1-x} (i.e., $HfN_{0.52}C_{0.48}$) is generated (Figure 3.31c and d). This clearly supports the assumption that HfN-rich regions react with excess carbon to yield $HfN_{0.52}C_{0.48}$ (as it is also known from titanium carbonitrides [6]).

The TEM micrographs of the SiHfBCN2b sample annealed at 1700 °C indicate the presence of the HfN_xC_{1-x} nanocrystallites with sizes of ca. 50 nm embedded within an amorphous SiBCN-based matrix (Figure 3.34). As it is known that HfN and SiBCN are materials which can withstand ultra-high temperatures (i.e. beyond

2000 °C), the nanocomposite obtained upon nitrogen annealing of SiHfBCN2b is considered to be a UHTC-NC with promising behavior at ultra-high temperatures and, due to the SiBCN matrix, even in harsh environments.

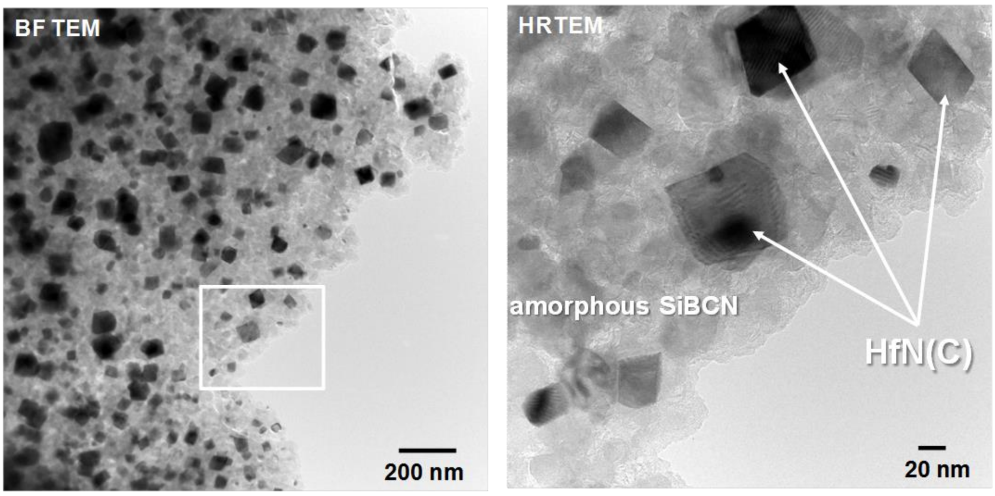

Figure 3.34. TEM micrographs of the SiHfBCN2b sample annealed at 1700 °C in a nitrogen atmosphere showing HfN(C) nano-precipitates embedded within an amorphous SiBCN matrix.

In order to clarify the development of the structures in samples annealed in nitrogen, the ^{29}Si MAS NMR spectra of SiHfBCN2b annealed at 1300, 1500 and 1700 °C in a nitrogen atmosphere are shown in Figure 3.35. The chemical shift of the SiN_4 sites in the sample annealed at 1300 °C was -49 ppm (Table 3.12), indicating that at this temperature, HfN already phase-separates (however as an amorphous phase, see Figure 3.31d). Annealing of the sample at higher temperatures leads to a partitioning of the Si(B)CN phase; thus, the $SiCN_3$ sites (mixed-bond tetrahedral) disappear, and instead SiC_4 and SiN_4 sites are present, showing the phase separation of the matrix into SiC and Si_3N_4 (Table 3.12), as also indicated by the XRD and TEM results.

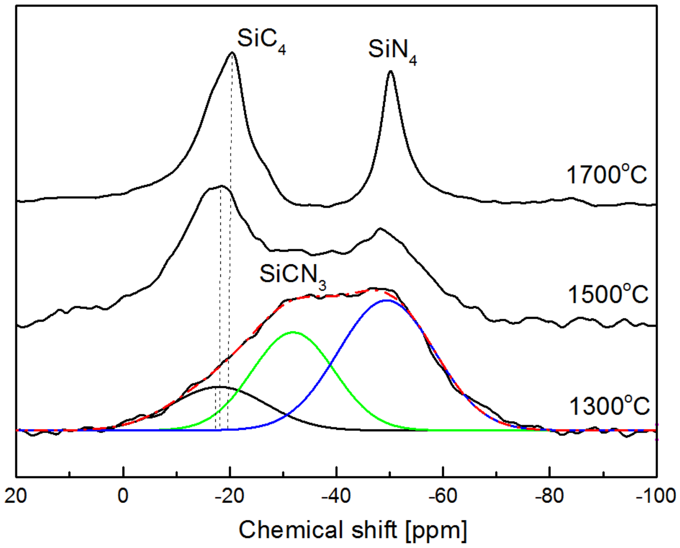

Figure 3.35. ^{29}Si MAS NMR spectra of SiHfBCN2b annealed in a nitrogen atmosphere at different temperatures.

Table 3.12. Fraction of SiC_2N_2, SiC_4, and $SiCN_3$ and SiN_4 sites of SiHfBCN2b, as derived from a Gaussian line fitting of the ^{29}Si NMR spectra from Figure 3.36.

	SiC_4		SiC_2N_2		$SiCN_3$		SiN_4	
	δ [ppm]	Site fraction [%]	δ [ppm]	Site fraction [%]	δ [ppm]	Site fraction [%]	δ [ppm]	Site fraction [%]
1300	-19	20.1			-31	20.1	-49	59.7
1500	-18	55.3			-35	10.1	-50	34.6
1700	-19	67.5					-50	32.5

To rationalize the different processes occurring upon HT annealing of SiHf(B)CN in Ar and N_2 atmospheres, the change of the Gibbs free energy for some possible reactions was assessed (see the Ellingham diagram in Figure 3.36). The Gibbs free energy (ΔG) shows as negative in the temperature range of 1000 to 1500 °C for the elementary reaction to B-containing (BN, B_4C) and Hf-containing (HfC, HfN and HfB_2), indicating that HfC, HfN and HfB_2 directly interact among Hf and C, N, B. On the basis of these ΔG values [261], the potential conversion between HfC and HfN is possible; the negative value shows that the generation of HfN from a reaction between HfC and N_2 is favorable at a lower temperature (< 1500 °C). However, this reaction is very slow at this temperature (1500 °C). Therefore, we can conclude that HfN is much more stable than SiN_x at the boundary temperature of 1500 °C. Furthermore, this can be confirmed by X-ray diffraction that showed the presence of a solid solution of HfC_xN_{1-x} as well as mass loss that is much lower than that of the SiCN ceramic derived from pure HTT1800 (Figure 3.26).

The thermodynamic data presented in Figure 3.36 indicate that the HfN phase, which is supposed to partition and crystallize from the single-phase SiHfBCN upon HT annealing, can react with segregated carbon to form HfC at temperatures beyond 1500 °C. This is indeed supported by the XRD data of the SiHfBCN2a sample annealed at 1700 °C, which clearly show the presence of HfC. As nitrogen is released during the conversion of HfN into HfC, it is obvious that this reaction is suppressed in a nitrogen atmosphere; thus, no HfC has been detected in the HT annealed SiHfBCN2b samples.

The data from Figure 3.36 also explains the formation of HfB_2 upon annealing in an Ar atmosphere and indicates that it can be generated from either HfN (or HfCN) and BCN (the BCN phase was stated to be present as the phase-separated phase in the microstructure of SiBCN and has been approximated in the present assessment as a mixture of BN and B_4C). Thus, the formation of HfB_2 from HfN has been shown to be favorable within the whole investigated temperature range; whereas the conversion of HfCN into HfB_2 becomes favorable at temperatures beyond 1300 °C. Gaseous N_2 is released as a side product in both processes. Accordingly, the nitrogen partial pressure was unfavorable for the HfB_2 formation during the annealing experiments, and thus no HfB_2 was detected in the samples annealed in a N_2 atmosphere.

Considering the discussed data from the Ellingham diagram in Figure 3.36, there is clearly a thermodynamic control of the high-temperature evolution of single-phase SiHfCN and SiHfBCN, indicating the phase composition of the resulting UHTC-NCs upon HT annealing, which allows for preparing materials with tailored phase compositions.

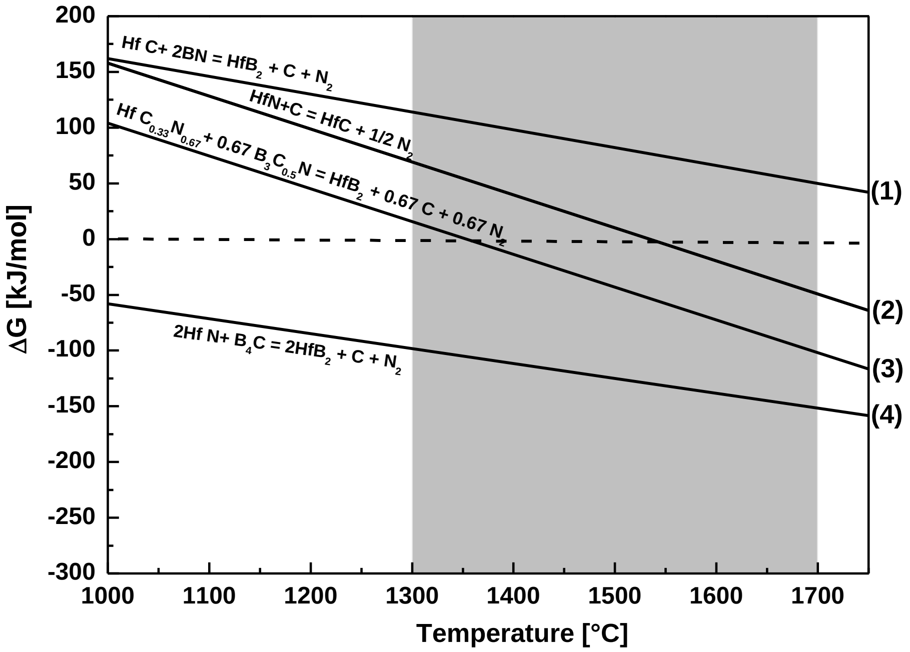

Figure 3.36. Temperature dependence of the change in the Gibbs free energy (Ellingham diagram) of different possible reactions occurring during HT annealing of SiHfBCN (data taken from [261]). ΔG for the reaction (3) has been estimated upon combining the reactions (1) and (4) (cf. (3) = 0.67 x (1) + 0.33 x (4)). The grayish area indicates the temperature range of the high-temperature annealing experiments.

Accordingly, the SiHfCN and SiHfBCN ceramics annealed at temperatures from 1300 to 1700 °C in argon and nitrogen atmospheres were studied by means of Raman spectroscopy. Both ceramics annealed in an argon atmosphere at 1300 and 1500 °C showed the presence of excess, free carbon (Figure 3.37 a and c). On the other hand, the sample annealed in Ar at 1700 °C did not contain any free carbon; instead, the presence of β-SiC has been shown in both ceramics; additional separation of Si from SiHfCN ceramics matrix could also be detected (Figure 3.37 a). The samples annealed in a nitrogen atmosphere exhibited the presence of segregated carbon independent of the annealing temperature, as shown in Figure 3.37b. This is in agreement with the XRD, elemental analysis and thermodynamic data, which show that annealing SiHf(B)CN in an Ar atmosphere leads to the consumption of segregated carbon at temperatures > 1500 °C, cf. $Si_3N_4 + 3\ C = \beta\text{-}SiC + 2\ N_2$. This reaction is suppressed in a nitrogen atmosphere, and thus the segregated carbon phase is still present in SiHfCN2b and SiHfBCN2b annealed at 1700 °C.

As discussed, there is a similar case in the separation of free carbon (see Chapter 3.2.1.2, Figure 3.17). The Raman spectra exhibit the G and D modes at 1580 cm^{-1} and 1350 cm^{-1} respectively, which are typical for carbon materials. Furthermore, overtone bands were found in some spectra at 2700 and 2950 cm^{-1} (2D and D+G modes, respectively). In all spectra, the integral area of the D-band (A_D) is significantly larger than that of the G-band (A_G), indicating the disordered feature of the segregated carbon [240]. Furthermore, the degree of disorder was also rationalized on the basis of the parameter L_D (inter-defect distance), which has been defined, cf. $\frac{\mathrm{ID}}{\mathrm{IG}} = \frac{\mathrm{C}(\lambda)}{\mathrm{LD}^2}$[262]. Thus, L_D becomes smaller as the annealing temperature increases (i.e. SiHfBCN2b_1300: 8.47 nm, SiHfBCN2b_1700: 6.73 nm), illustrating that the structural organization of the carbon phase increases. This conclusion is supported by the decrease of the FWHM of the bands as well as by the increase of the intensity of the G' band (see Figure 3.37 and Table 3.13)[240]. Moreover, the evolution of the parameter Leq (the lateral cluster size, which however takes into account the tortuosity of the graphene sheets, cf. $L_{eq} = 8.8 \left(\frac{A_{2D}}{A_D}\right)$ nm [240]), indicates the same trend as previously described (see Table 3.13), i.e. an increase of the ordering of carbon as the annealing temperature increases.

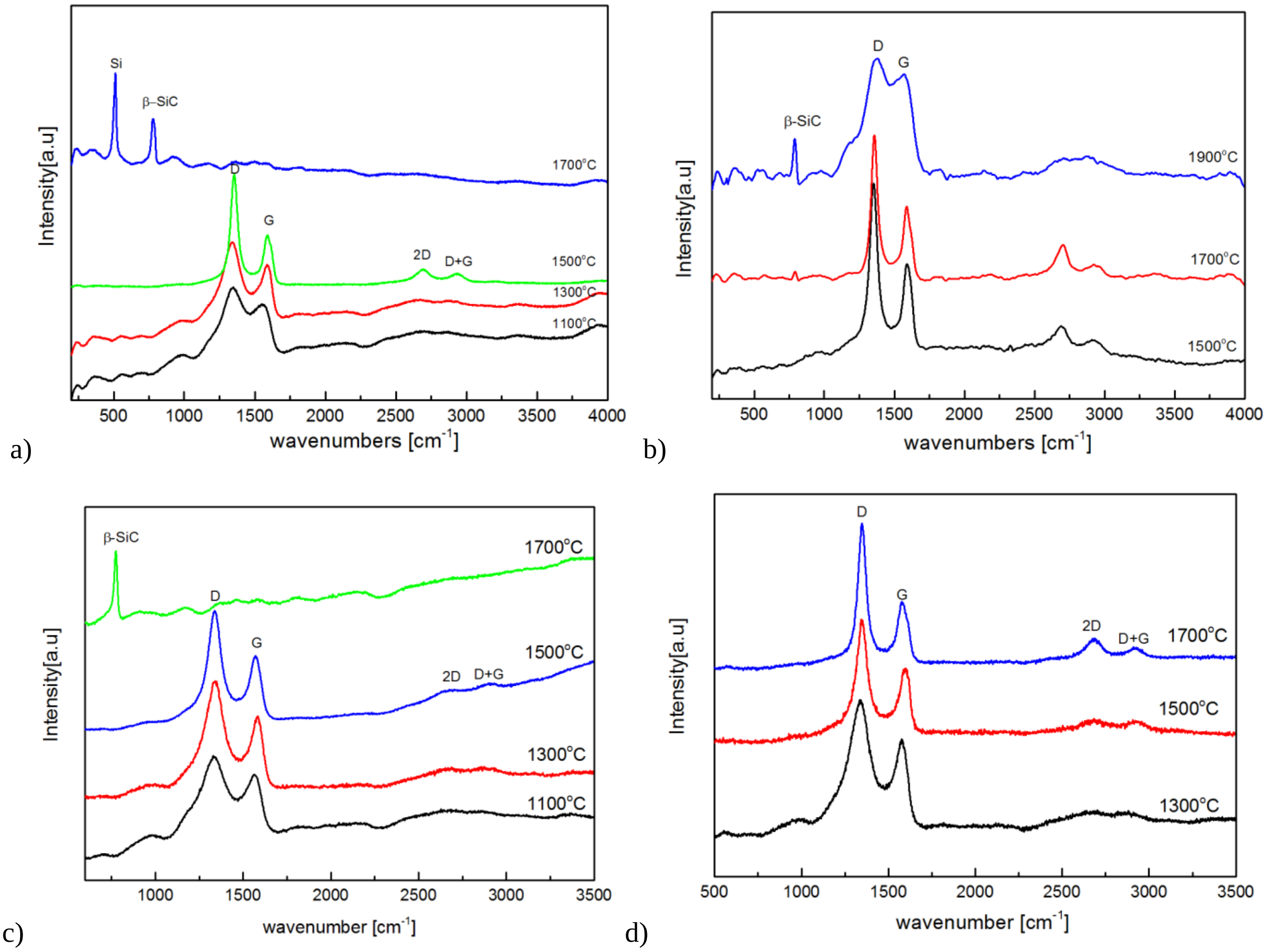

Figure 3.37. Raman spectra of the SiHfCN- and SiHfBCN-based samples annealed at different temperatures: (a) SiHfCN2a (annealing in an argon atmosphere); (b) SiHfCN2b (nitrogen atmosphere); (c) SiHfBCN2a (argon atmosphere); (d) SiHfBCN2b (nitrogen atmosphere).

Table 3.13. Peak positions, integral area ratios A_D/A_G and A_{2D}/A_D, crystallite lateral size (La, Leq) and full width at the half maximum of the D and G modes for the segregated carbon phase present in SiHfCN and SiHfBCN annealed in Ar and N_2 at different temperatures.

Sample	A_D/A_G	FWHMD [cm^{-1}]	ω_D [cm^{-1}]	FWHMG [cm^{-1}]	ω_G [cm^{-1}]	A_{2D}/A_D	La [nm]	Leq [nm]
sihfcn2a-1100	3,56	209	1345	102	1551	0,31	1,24	2,73
sihfcn2a-1300	3,75	170	1335	72	1582	0,08	1,17	0,76
sihfcn2a-1500	2,12	92	1354	62	1591	0,25	2,07	2,16

sihfcn2b-1500	2,04	69	1351	65	1592	0,21	2,16	1,89
sifhcn2b-1700	1,76	56	1358	63	1589	0,50	2,50	4,38

Sample	A_D/A_G	ω_D [cm^{-1}]	FWHMD [cm^{-1}]	ω_G [cm^{-1}]	A_{2D}/A_D	L_{eq} [nm]	L_D [nm]
SiHfBCN2a-1100	3.35	1335	155	1565	0.10	0.88	7.91
SiHfBCN2a-1300	6.10	1342	113	1587	0.20	1.74	8.45
SiHfBCN2a-1500	7.35	1337	89	1583	0.05	0.44	7.63
SiHfBCN2b-1300	5.31	1338	136	1584	0.11	0.96	8.47
SiHfBCN2b-1500	2.18	1347	80	1592	0.18	1.59	8.36
SiHfBCN2b-1700	2.11	1348	55	1581	0.23	2.02	6.73

Considering the obtained results, the SiHf(B)CN-based material prepared upon pyrolysis of the Hf- and B-modified polysilazane is greatly versatile concerning its crystallization behavior and evolution of the phase composition at high temperatures. In both argon and nitrogen atmospheres, the high temperature annealing of SiHfCN at 1500 °C leads to β-SiC and HfC_xN_{1-x} phases at the nanoscale (below 100 nm) as the main crystalline phases; whereas that of SiHfBCN contributes to ceramic nanocomposites with interesting phase compositions (i.e. SiC/HfC(N)/HfB_2 in argon and Si_3N_4/HfNC/SiBCN in nitrogen), which are expected to be promising candidates for applications at (ultra-)high temperatures and under extreme environmental conditions.

In comparison with the crystal structure of SiHfCN (Figure 3.38a), that of SiHfBCN proved to be much more complex. Figure 3.39 summarizes the conversion of SiHfBCN into UHTC-NCs upon annealing at high temperatures in argon (Figure 3.39a) and nitrogen atmospheres (Figure 3.39b). Interestingly, the SiHfBCN-based materials prepared via the pyrolysis of the Hf- and B-modified polysilazane were found to be highly versatile with regard to their crystallization behavior and the development of their phase compositions at high temperatures. In argon and nitrogen atmospheres, the high-temperature annealing of SiHfBCN yields ceramic nanocomposites with interesting phase compositions (i.e., SiC/HfC_xN_{1-x}/HfB_2 in argon and Si_3N_4/HfN_xC_{1-x}/SiBCN in nitrogen), which are expected to be promising candidates for use in ultra-high-temperature applications even under extreme conditions.

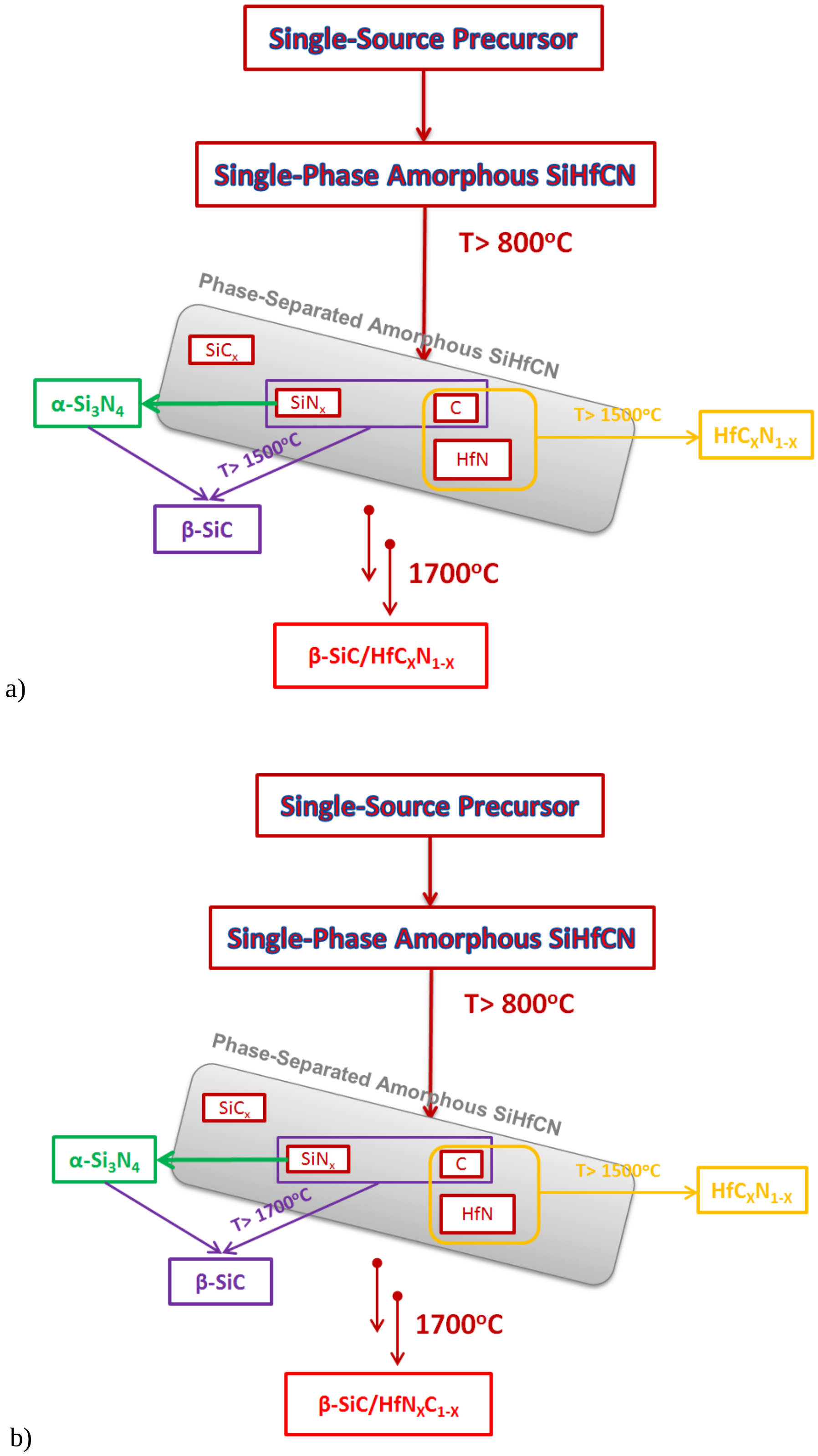

Figure 3.38. Proposed crystallization pathways for the high-temperature annealing of SiHfCN in argon (a) and nitrogen (b) atmospheres.

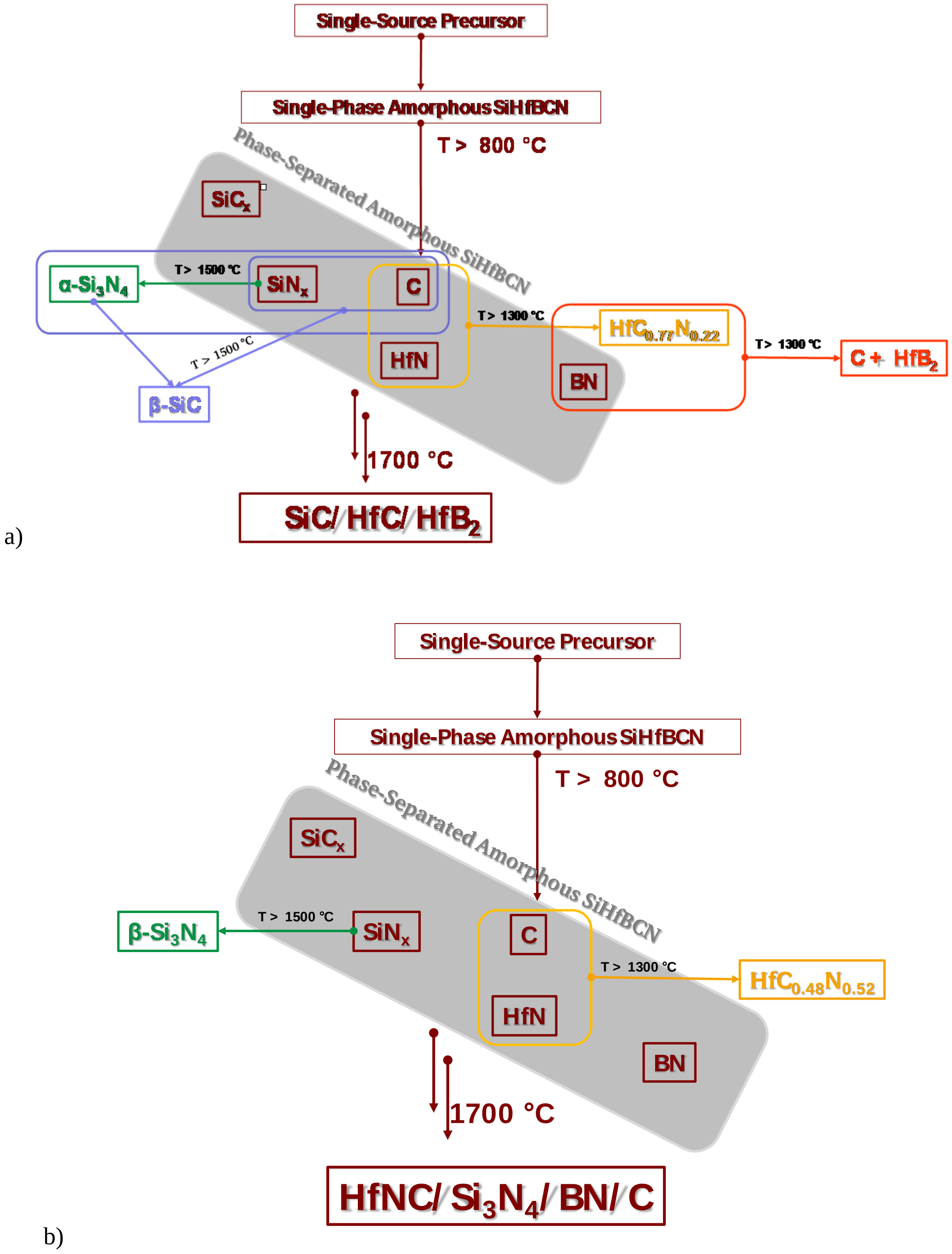

Figure 3.39. Proposed crystallization pathways for the high-temperature annealing of SiHfBCN in argon (a) and nitrogen (b) atmospheres.

3.3.3. Summary

In this study, the high-temperature decomposition and crystallization of Hf-containing UHTC-NCs was investigated. The presence of either Hf alone or of both Hf and B within the molecular structure of the single-source precursor leads to low-temperature phase separation processes, as described in the previous chapter (see

3.1 Material synthesis), within the resulting SiHfCN and SiHfBCN, and these processes are thermodynamically controlled. The resulting materials also exhibit superior high-temperature stability with respect to decomposition compared with non-modified SiCN ceramics. This stability facilitates the crystallization of such samples upon annealing at higher temperatures and thus enables the preparation of UHTC-NCs with phase compositions suitable for applications at ultra-high temperatures and under harsh conditions. The presented single-source precursor synthesis method is believed to be applicable for the preparation of other phase compositions consisting of a UHTC phase (e.g., group IV transition metal borides, carbides, and nitrides) dispersed within a silica-former matrix (e.g., SiC, Si_3N_4, SiCN, or SiBCN).

3.4 High temperature oxidation properties

The utilization of Si-based ceramics in high-temperature applications (≥ 1600 °C) has been limited because such materials are commonly susceptible to active oxidation, accompanied by the presence of a depletion layer. UHTCs represent a class of ceramics that can withstand use temperatures in excess of those for which Si-based ceramics are suitable (≥ 1500 °C), but this category of ceramics generally oxidizes more rapidly than Si-based ceramics. For instance, in the oxidation of single-composition UHTCs (transition metal carbides and nitrides, M=Zr, Hf, etc.), the formation of an oxygen-vacancy-containing scale (porous HfO_2 or ZrO_2) facilitates the inward diffusion of oxygen, resulting in linear behavior at high temperatures. Attempts to improve the oxidation properties of HfB_2, ZrB_2, HfC and ZrC have been made by incorporating these materials with 20-30 vol% SiC [11, 158, 263]. Furthermore, coating systems consisting of an HfB_2/SiC composite (20 wt% SiC) [264] and HfC/SiC [265, 266] have been considered for oxidation protection on CMC composites. The incorporation of refractory elements (Zr and Hf) into the silicon-based matrix was found to have a synergistic effect that could increase the resilience of Si-based ceramics at ultra-high temperatures and improve the oxidation behavior of UHTC components [4, 74, 212, 267].

This section presents an evaluation of the oxidation behavior of amorphous SiHf(B)CN polymer-derived ceramic powders and monoliths at high temperatures of 1200 to 1400 °C. Additionally, the oxidation behavior of dense SiHf(B)CN-based UHTC-NC ceramic materials was also studied at 1400 and 1500 °C with regard to their oxidation kinetics, microstructural development, etc. This investigation of the oxidation of the prepared materials at high temperatures revealed that all samples exhibited parabolic behavior, indicating that oxygen permeation was limited by a passive oxide scale. Interestingly, superior oxidation resistance was observed in SiHfBCN compared with SiHfCN ceramic materials. The present work demonstrates that SiHf(B)CN-based ceramic materials could be promising candidates for high-temperature applications in harsh environments (i.e., oxidizing gas).

3.4.1 Oxidation properties of amorphous SiHf(B)CN polymer-derived ceramics

3.4.1.1 Oxidation behavior of amorphous ceramic powder

The SiCN, SiHfCN and SiHfBCN ceramic powders were oxidized in synthetic air at temperatures of 1200, 1300 and 1400 °C, and the oxidation behavior was investigated by means of TGA (Figure 3.40). The results indicated that the weight curves of all samples followed a parabolic form. Moreover, an increase in the weight gain for each type of samples was observed with an increase in the oxidation temperature. This investigation clearly revealed that the weight gain of SiHfCN during oxidation was much higher than that of SiCN at all temperatures. The oxidation behavior of SiHfCN was found to be improved by the incorporation of B into the SiHfCN (Figure 3.40): the weight gain of SiHfBCN oxidized at 1300 °C was approximately 1.84 wt %, much lower than that of SiHfCN (2.97 wt %).

Additionally, previous studies on the oxidation behavior of PDCs have revealed that SiCN ceramics with amorphous structures demonstrate excellent oxidation resistance compared with typical SiC and Si_3N_4 ceramics. This improved performance is attributed to their lack of grain boundaries and segregated impurities that hinder oxidation resistance [143]. We can assume that similar oxidation behavior could be expected based on the amorphous nature of SiHfBCN ceramic powder. Indeed, the weight gain of approximately 1.84 wt% determined via TGA for oxidation at 1300 °C is much lower than that of micro-SiC (8.5 wt%) [268, 269].

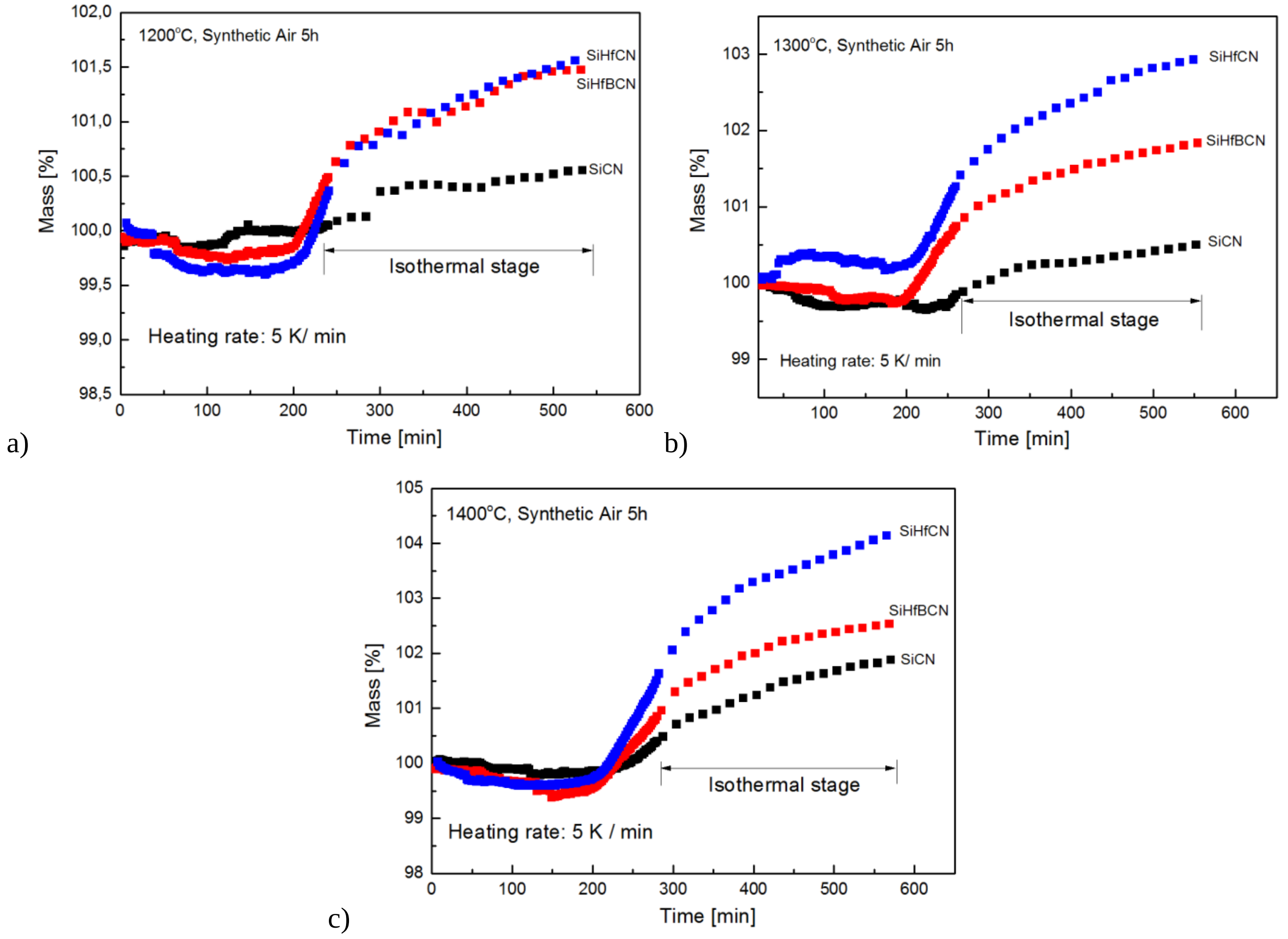

Figure 3.40. Weight gain as a function of oxidation time for amorphous SiCN, SiHfCN and SiHfBCN ceramic powders exposed to synthetic air at different temperatures: (a) 1200 °C, b) 1300 °C, and c) 1400 °C.

To quantifiably compare oxidation behavior among these ceramics, under the assumption that all elements or phases (e.g., SiC_xN_{4-x}, HfC_xN_{1-x} and BCN) are completely oxidized (converted into the products SiO_2, HfO_2 or B_2O_3, respectively), i.e., the oxidation of SiC results in a weight gain due to silicon oxidation and a weight loss due to carbon oxidation (as CO or CO_2), the oxidation of 1 mol of SiC yields a mass increase of 20 g. Using this approach, the weight gain observed in each phase in our study can be calculated as follows:

$$\Delta W = \frac{W \times \Delta m}{M}, \qquad \text{(Eq.3.4)}$$

Here, ΔW represents the weight gain in the phase in question after oxidation; W is the weight fraction of the element being investigated in the ceramic (e.g., the weight fractions of Si are 54.7, 46.3 and 38.2 % in SiCN, SiHfCN and SiHfBCN, respectively); and Δm and M are the weight gain after the oxidation of 1 mol of each phase and the corresponding element's molecular weight, respectively, e.g., the Δm values for the oxidation of SiC, HfC and BN into SiO_2, HfO_2 and B_2O_3 are approximately 20, 20 and 6 g, respectively.

The apparent weight gains (Δm1) can be obtained directly from TGA to estimate the fraction of apparent weight gain during the oxidation reaction at a given oxidation temperature based on the above equation *(Δm1/∑(ΔW))*; the results of such an analysis are shown in Table 3.14. The fraction of apparent weight gain was higher for SiHfCN (i.e., 11.9 wt% at 1400 °C) than for SiCN and SiHfBCN, for which lower values of 4.8 and 7.7 wt%, respectively, were found; this is consistent with the fact that the oxidation of SiHfCN more favorable compared with the other two ceramics (SiCN and SiHfBCN).

Table 3.14. Estimates of the apparent weight gain fractions of SiCN, SiHfCN and SiHfBCN amorphous ceramics.

Ceramic	Oxidation temperature [°C]	W*[wt%]			ΔW [wt%]			Δm1** [%]	Δm2 [%]
		Si	Hf	B	SiO_2	HfO_2	B_2O_3		
SiCN	1200	54.7	-	-	39.1	-	-	0.55	1.4
	1300							0.52	1.3
	1400							1.87	4.8
SiHfCN	1200	46.3	21.0	-	33.1	2.4	-	1.59	4.5
	1300							2.97	8.4
	1400							4.23	11.9
SiHfBCN	1200	38.2	22.5	5.8	27.3	2.5	3.2	1.47	4.4
	1300							1.84	5.6
	1400							2.54	7.7

* * These values were obtained from the elemental analysis summarized in Table 2.4

** These values were obtained from the TGA results shown in Figure 3.40

The oxidation curves of the samples measured under isothermal conditions for 5 h (Figure 3.41) indicate that the weight gain of each sample during this stage followed a parabolic relation, indicating that a passive oxidation layer limited the diffusion of oxygen in the matrix. Thus, an empirical equation can be written in terms of the parabolic constant K_p based on passive oxidation kinetics [270], K_p being defined as follows:

$$\left(\frac{\Delta m}{S}\right)^2 = \mathrm{K}_p \times \mathrm{t} + \mathrm{c} \qquad \text{(Eq.3.5)}$$

Where Δm/S is the surface-specific weight gain (mg cm^{-2}), K_p is the parabolic rate constant and c is constant. The specific surface area of the powder sample was determined to be 4.71 $m^2 \cdot g^{-1}$ and was used to determine the parabolic oxidation rate, cf. Eq. 3.6. The parabolic oxidation rate K_p is defined as a function of the surface-specific weight gain (as for considering the BET specific surface area of the powder) and the oxidation time:

$$\mathrm{K}_p = \left(\frac{\Delta \mathrm{m}}{\mathrm{S_{BET}} \times \mathrm{m_0}}\right)^2 \times \mathrm{t}^{-1} \qquad \text{(Eq.3.6)}$$

With S_{BET} being the SSA m_0 is the weight after oxidation at a given oxidation time and temperature. In Figure 3.41, the surface-specific mass gain of the samples is shown as function of the oxidation time; whereas in Figure 3.42, the linear relationship between $(\Delta m/(S_{BET} \times m))^2$ *vs. T* (oxidation time) confirms the parabolic nature of the oxidation process; the slopes give the values of the parabolic constant rate K_p at different temperatures, as summarized in Table 3.15. Interesting, the obtained values of K_p for SiHfCN powders are several orders of magnitude lower than those reported for micro- and nano-sized SiC at 1200 °C (9.65×10^{-6} and 13.2×10^{-6} $mg^2 \cdot mm^{-4} \cdot min^{-1}$, respectively), although they are also one order of magnitude higher than that of SiCN [268], which exhibits good oxidation resistance under such harsh environments. Furthermore, SiHfBCN exhibits lower oxidation rates than does SiHfCN: the K_p of SiHfBCN is 5-10 times lower than that of SiHfCN, and an oxidation rate of 8.19×10^{-9} $mg \cdot cm^{-2} \cdot h^{-1}$was calculated for SiHfBCN at 1200 °C, which is lower than the value of 4.85×10^{-8} $mg \cdot cm^{-2} \cdot h^{-1}$ calculated for SiHfCN at the same temperature. With increasing temperature, the oxidation rates of both samples increase to 2.5×10^{-8} and 2.24×10^{-7} $mg \cdot cm^{-2} \cdot h^{-1}$ for SiHfBCN and SiHfCN, respectively, oxidized at 1400 °C.

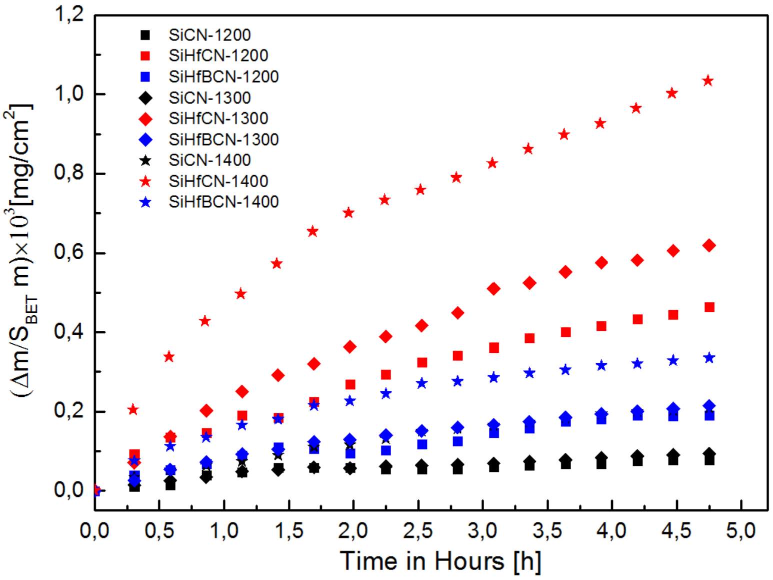

Figure 3.41. Surface-specific weight gain as a function of oxidation time for SiCN, SiHfCN and SiHfBCN ceramic powders in air at temperatures from 1200 to 1400 °C, determined on the basis of the mass change obtained directly via TGA.

Nevertheless, a meaningful comparison of the oxidation rates of our samples with those of typical ceramics (e.g., SiC/Si_3N_4) is very difficult because of the lack of a generalized standard. Furthermore, many factors could influence the oxidation rate of a ceramic powder, such as particle size, experimental conditions (ratio of air to H_2O, gas pressure, etc.). Thus, in this case, the K_p values of the SiCN, SiHfCN and SiHfBCN amorphous ceramic powders are assessed only in direct comparison with each other.

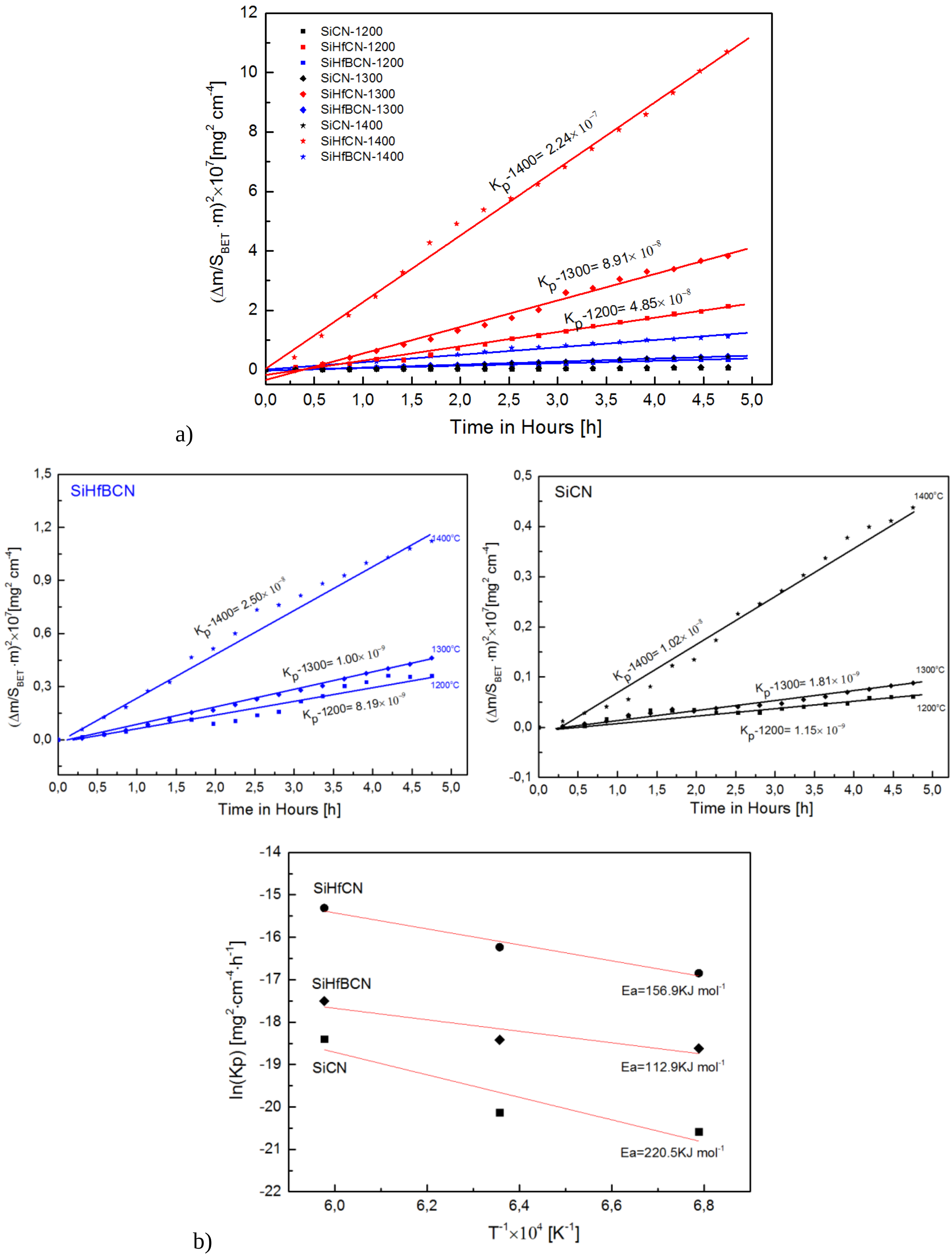

a)

b)

Figure 3.42. a) Relationship between the square of the weight gain per specific surface area and the isothermal oxidation time for SiHfCN (left) and SiHfBCN (right) ceramic powders at 1200, 1300, and 1400 °C (Fitted line). b) Arrhenius plot for the oxidation process.

Table 3.15. Parabolic oxidation rates K_p and activation energy as for SiCN, SiHfCN and SiHfBCN powders.

Ceramics	Temp. [°C]	Parabolic rate [$mg \cdot cm^{-2} \cdot h^{-1}$]	Activation energy [$kJ\ mol^{-1}$]
Micron sized SiCN powder	1200	1.15×10^{-9}	220.5±83.5
	1300	1.81×10^{-9}	
	1400	1.02×10^{-8}	
Micron sized SiHfCN powder	1200	4.82×10^{-8}	156.5±23.9
	1300	8.91×10^{-8}	
	1400	2.24×10^{-7}	
Micron sized SiHfBCN powder	1200	8.19×10^{-9}	112.9±46.5
	1300	1.00×10^{-8}	
	1400	2.50×10^{-8}	

Furthermore, the value of the activation energy E_a was determined cf. Eq.3.7:

$$K_p = A_0 e^{\left(-\frac{E_a}{RT}\right)} \qquad \text{(Eq.3.7)}$$

The linear slopes obtained from the relationships between $ln(K_p)$ and $1/T$ yield the corresponding values of E_a, which are presented in Table 3.15. The E_a value for SiCN (approximately 220.5 kJ mol^{-1}) is higher than those for SiHfCN and SiHfBCN (156.5 and 112.9 kJ mol^{-}1, respectively). This result is likely analogous to the high E_a value reported for Si_3N_4 (466 kJ mol^{-1}), which was attributed to oxygen permeation into the bilayer (SiO_2, Si_2N_2O) [271]. Furthermore, the E_a value for the oxidation of SiHfBCN (112.9 kJ mol^{-1}) correspond to those determined for the oxidation of Si and SiC [272], suggesting that the permeation of molecular oxygen through the oxidized silica scale controls further oxidation. To understand the crystalline phase compositions of the oxidation scale, the samples (SiCN and SiHfBCN) were characterized using XRD (Figure 3.43). The results revealed that the oxide scale that formed on SiCN below 1300 °C was amorphous, possibly indicating the formation of amorphous glass (e.g., silica and Si_2N_2O). XRD analysis of SiCN oxidized at 1400 °C suggested the sample began to convert into a cristobalite phase, which has proven to play a barrier role in the oxygen mechanism similar to that of amorphous silica glass [273]. By contrast, the oxide scale that formed on SiHfBCN at 1200 °C contained crystalline phases assigned only to HfO_2 (t-HfO_2 and m-HfO_2). As the temperature was increased to 1300 °C, crystalline phases in the oxide scale on SiHfBCN that corresponded to cristobalite and HfO_2 were observed. Upon oxidation at 1400 °C, the amount of the m-HfO_2 phase increased strongly, possibly indicating a phase transition between t and m-HfO_2.

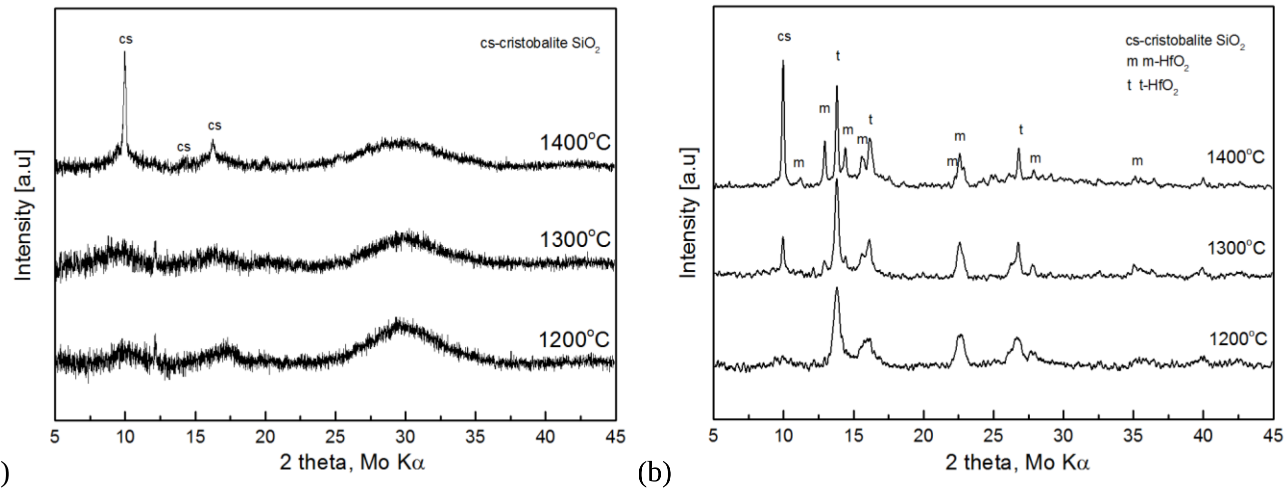

(a) (b)

Figure 3.43. XRD spectra of ceramic powders oxidized at 1200, 1300 and 1400 °C: (a) SiCN and (b) SiHfBCN.

3.4.1.2 Oxidation behavior of amorphous SiHfBCN ceramic monoliths

Although the oxidation rate of amorphous SiHfCN ceramic powder was found to be faster than that of SiCN ceramic powders, the results for the SiHfBCN ceramics also showed that the oxidation rate can be reduced once again via boron doping. Thus, for the further development of Hf-containing amorphous ceramics, SiHfBCN ceramic monoliths with improved anti-oxidation behavior prepared via PLS require further investigation.

Ceramic monoliths with low porosity were used for the oxidation investigation. As shown in Table 3.4, the open porosity of the samples was found to be lowest after annealing in N_2 at 1300 °C (the apparent density and open porosity of the monoliths were determined using the Archimedes method). Thus, SiHfBCN ceramic monoliths pyrolyzed at 1100 °C and then annealed at 1300 °C in N_2 were selected for the oxidation test. Here, in addition to the SiHfBCN2 (with 30 vol% $Hf((Et)_2)_4$ complex), a composition with lower Hf content (denoted SiHfBCN1, see Table 2.3) was also studied in order to elucidate the effect of Hf on the oxidation behavior of SiHfBCN.

The surface-specific weight gains as a function of the oxidation time for SiHfBCN ceramic monoliths oxidized at temperatures ranging from 1200 to 1400 °C are shown in Figure 3.44. The observed oxidation behavior of SiHfBCN1/2 also shows that they follow a parabolic law. Furthermore, at the temperatures of 1200 and 1300 °C, it was found that the specific weight gain of SiHfBCN2 exhibited a linearly increasing trend over short oxidation times (i.e., oxidation soaking times below 5 h) because of the strong affinity of Hf-containing phases with oxygen. However, the weight gain rate of SiHfBCN1 and SiHfBCN2 seems to slow down with increasing the exposure time (above 5 h); this probably relies on the formation of a silica-based dense oxide scale.

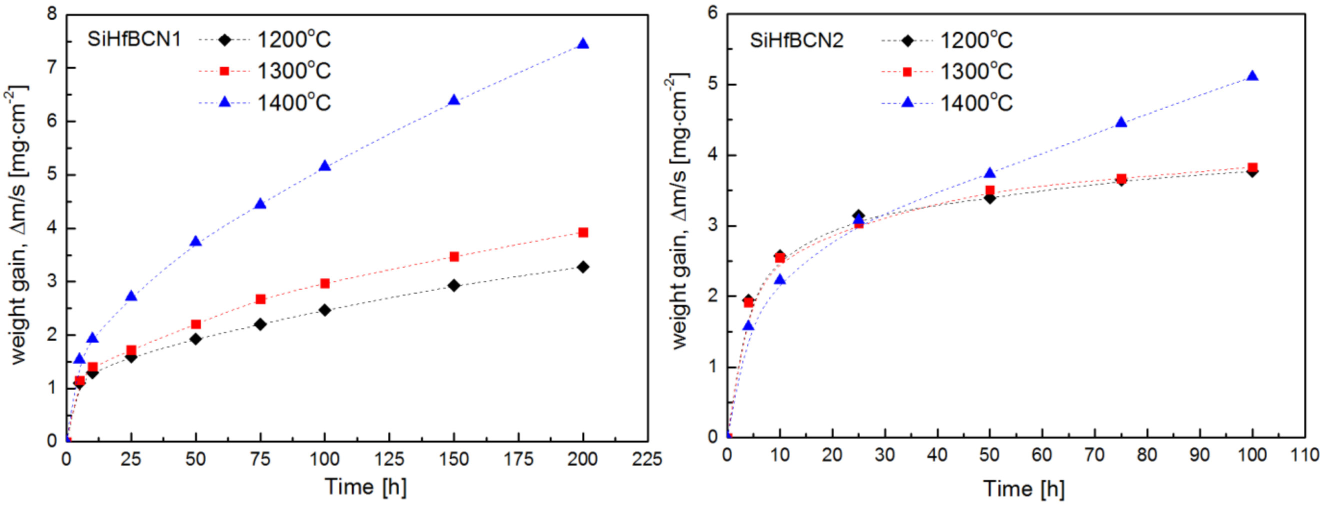

Figure 3.44. Surface-specific weight gain as a function of exposure time for SiHfBCN ceramic monoliths (SiHfBCN1 and SiHfBCN2) in stagnant air at temperatures of 1200 to 1400 °C.

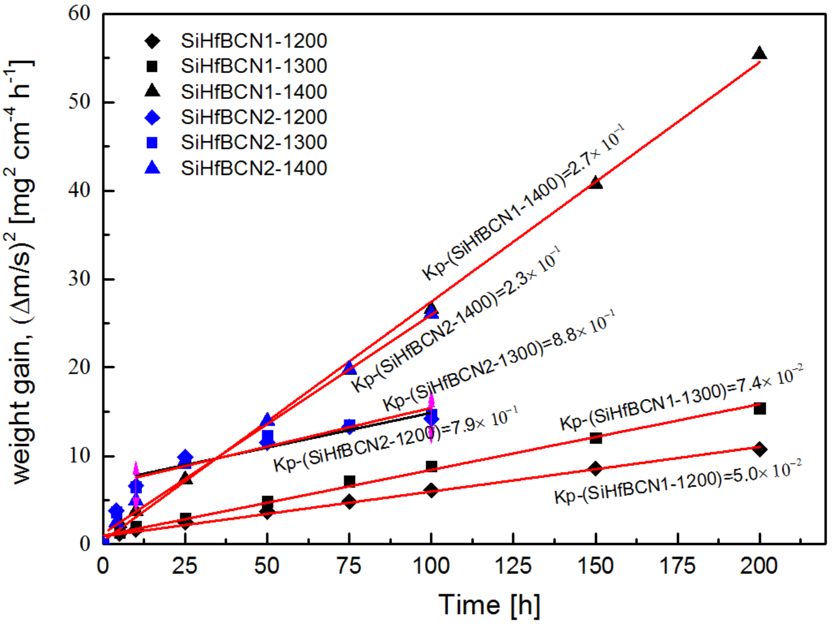

Figure 3.45. Plots of the parabolic rate constant as a function of the exposure time for SiHfBCN1 ceramics in stagnant air at temperatures of 1200 to 1400 °C.

To quantify the oxidation rates of the SiHfBCN1/2 ceramic monoliths, their K_p values were calculated from the slopes of the straight lines in Figure 3.45 using Eq. 3.5, assuming that the surface of the sample corresponds to their geometric surface. The values of the apparent parabolic rate (K_p) and E_a are summarized in Table 3.16. The K_p values of SiHfBCN1 and SiHfBCN2 were found to be 2.7×10^{-1} and 2.3 ×10^{-1} mg·cm^{-2}·h^{-1}, respectively, at 1400 °C; these values are two orders of magnitude higher than that reported for CVD SiC (1.3×10^{-3} mg·cm^{-2}·h^{-1}, 1400 °C) [150]. This relies on the presence of open porosity in the studied monolithic samples (i.e. 5.8 and 10.4 vol% for SiHfBCN1 and SiHfBCN2, respectively); in this case, it would not be possible to accurately determine the intrinsic parabolic rate in terms of the specific weight gain (considering geometric surface area). PDCs with full density are extremely difficult to obtain via pressureless methods, despite the reports of L.N. An *et al.*

describing the oxidation behavior of fully dense polymer-derived amorphous SiCN [144] and SiAlCN [8]; fully dense samples are limited to being very thin. The purpose of this investigation was simply to characterize the oxidation behavior of this novel PDC SiHfBCN material. For an oxidation temperature below 1400 °C, the SiHfBCN1 monolith (having lower Hf and B contents than that of SiHfBCN2) shows better oxidation resistance than SiHfBCN2. This finding can most likely be attributed to the lower porosity of SiHfBCN1 (P_{op} = 5.8 %). The higher open porosity of SiHfBCN2 (P_{op}=10.4 %) could result in many more channels being available for oxygen transport, leading to a higher oxidation rate. Furthermore, we consider that the oxidation of SiHfBCN1 and SiHfBCN2 leads to the formation of boron-containing silica scale (borosilicate). As borosilicate glasses show higher viscosities at lower boron contents [274], lower diffusion rates of molecular oxygen through the passivation scale of SiHfBCN1 can be expected. Thus, lower oxidation rate is observed in SiHfBCN1 at temperatures below 1400 °C. However, the oxidation kinetics is strongly influenced by the evaporation of boria when the oxidation temperature rises to 1400 °C, as the vapor pressure of B_2O_3 increases substantially at temperatures beyond 1300 °C [275], Thus, similar parabolic rates were found in both SiHfBCN1 and SiHfBCN2 exposed to oxidation conditions at 1400 °C. Furthermore, the K_p values of both compositions are much higher at a temperature of 1400 °C compared with those at 1200 and 1300 °C.

Table 3.16. Apparent parabolic rates and corrected parabolic rates of SiHfBCN amorphous ceramics.

Ceramic	BET surface [$m^2 \cdot g^{-1}$]	Temp. [^{o} C]	Apparent parabolic rate [$mg \cdot cm^{-2} \cdot h^{-1}$]	Corrected parabolic rate (SSA) [$mg \cdot cm^{-2} \cdot h^{-1}$]	Apparent activation energy (Ea) [$kJ\ mol^{-1}$]
SiHfBCN1	3.26	1200	5.0×10^{-2}	1.5×10^{-9}	174±57.7
		1300	7.4×10^{-2}	2.3×10^{-9}	
		1400	2.7×10^{-1}	8.4×10^{-9}	
SiHfBCN2	3.34	1200	7.9×10^{-2}	1.4×10^{-9}	139.7±39
		1300	8.8×10^{-2}	4.0×10^{-9}	
		1400	2.3×10^{-1}	5.4×10^{-9}	

The as-determined, apparent values of the oxidation rate were adjusted upon considering the specific surface area of the monoliths instead of their geometric surface area (see Eq. 3.6). Thus, the corrected parabolic rates are 6~7 orders and 5~6 orders of magnitude lower than the apparent parabolic rates K_p and that of reported CVD SiC ceramics. Additionally, the Ea of 174±57.7 and 139.7±39 kJ mol^{-1} for SiHfBCN1 and SiHfBCN2 were calculated from the apparent parabolic rate. As can be found in Table 3.17, the E_a values of the oxidation process for the monolithic SiHfBCN samples are listed in comparison to activation energies for the oxidation of other silicon-based ceramics as well as of borosilicate and HfC. We consider the oxidation process of SiHfBCN samples as being of parabolic nature but rather complex, i.e. occurring with the formation of silica, boria and HfO_2, as well as of borosilicate and $HfSiO_4$, as discussed below. This makes an interpretation of the activation energy of their oxidation rather difficult.

Table 3.17. Comparison of activation energies for the oxidation of SiHfBCN, other Si-containing materials and HfC.

Ceramic	Temp. [° C]	Activation energy [kJ mol^{-1}]	Reference
Si_3N_4 in dry air	1065-1340	285	[276]
Si in dry O_2	1000-1200	126	[277]
CVD SiC	1200-1600	125	[278]
Monolithic SiCN	900-1200	120	[144]
Borosilicate	700-800	138	[279]
HfC	480-600	197	[134]
SiHfBCN2 powder	1200-1400	112.9	Present work
Monolithic SiHfBCN	1200-1400	174±57.7 ; 139.7±39	Present work

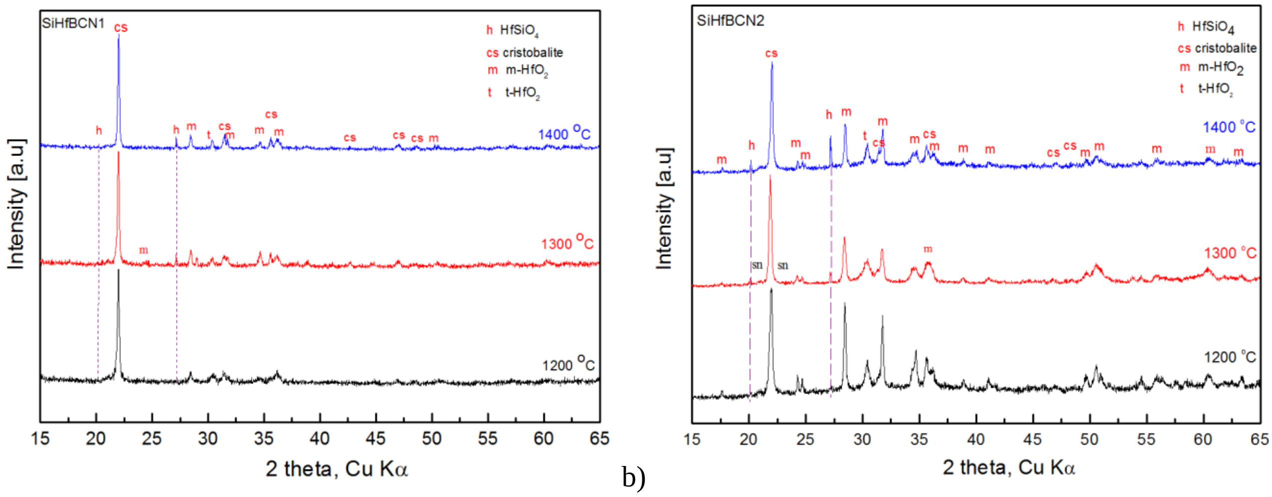

Figure 3.46. XRD spectra of the SiHfBCN samples oxidized at 1200, 1300 and 1400 °C: (a) SiHfBCN1; (b) SiHfBCN2 amorphous ceramic monoliths.

To attain more insights into the formation of the oxide scale, the SiHfBCN monoliths oxidized at 1200, 1300 and 1400 °C were performed by XRD, SEM and EPMA. XRD patterns of the oxidized SiHfBCN1 and SiHfBCN2 samples are presented in Figure 3.46. For the monoliths oxidized at 1200 °C, reflections corresponding to SiO_2 (cristobalite, major) and HfO_2 (monoclinic and tetragonal) are found in the XRD patterns of both compositions. In addition, borosilicate glass is expected to be formed and is considered to be beneficial for the oxidation resistance of the samples, as it is a more effective diffusion barrier for oxygen than silica. Upon oxidation at 1300 °C, a significant amount of crystalline HfO_2 precipitates at the outer surface of the scale which is observed in the SEM image (Figure 3.47, 1300 °C). A new peak ascribed to hafnon ($HfSiO_4$) appeared in the SiHfBCN1/2 spectra once the oxidation temperature reached to 1400 °C, consistent with the results of SEM microscopy (Figure 3.47, a 1400°C), which revealed dendrites and elongated precipitations corresponding to $HfSiO_4$. Because the consumption of the acicular crystal corresponding to m-HfO_2 induced the formation of $HfSiO_4$ at 1400 °C, less precipitation of m-HfO_2 was observed. This finding is attributed to the reaction between hafnia nanoparticles and silica, leading to an increasing intensity of the $HfSiO_4$ signal and a decreasing intensity of the m-HfO_2 peak with increasing temperature. A similar result has been shown by a study in the Y_2O_3-containing Si_3N_4 oxidized at 100 h, which showed the formation of yttrium silicate in its oxide scale [280].

As cristobalite has a different coefficient of thermal expansion (2.6×10^{-6}/ °C) from those of the silicon-based ceramic matrices (i.e., SiC: 4×10^{-6}/ °C, Si_3N_4: 3.3×10^{-6}/ °C), cracking of the scale has been observed (Figure 3.47), particularly at higher oxidation temperatures of 1300 and 1400 °C, thus favoring oxygen to permeate into the interior of the monoliths. Accordingly, the weight gain increased significantly at 1400 °C compared with the weight gain at temperatures of 1200 and 1300 °C. However, the formation of hafnon, $HfSiO_4$, is believed to be beneficial for the oxidation resistance of the SiHfBCN samples, as it has a significant lower oxygen diffusivity that that of silica or borosilicate glass. [281]. Moreover, $HfSiO_4$ promotes the formation of immiscible glasses, resulting in a higher viscosity and a higher melting temperature. Therefore, the presence of immiscible glass might retard oxygen diffusion at 1400 °C or even higher temperatures, at which silicon-based materials might melt.

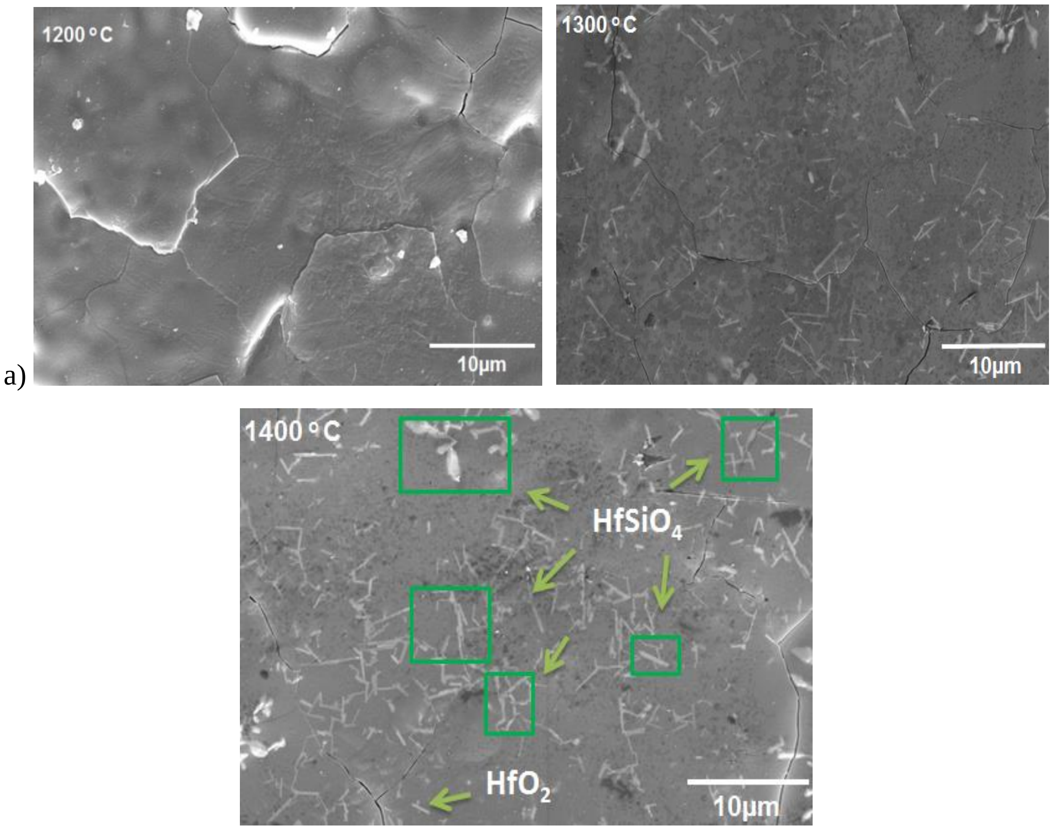

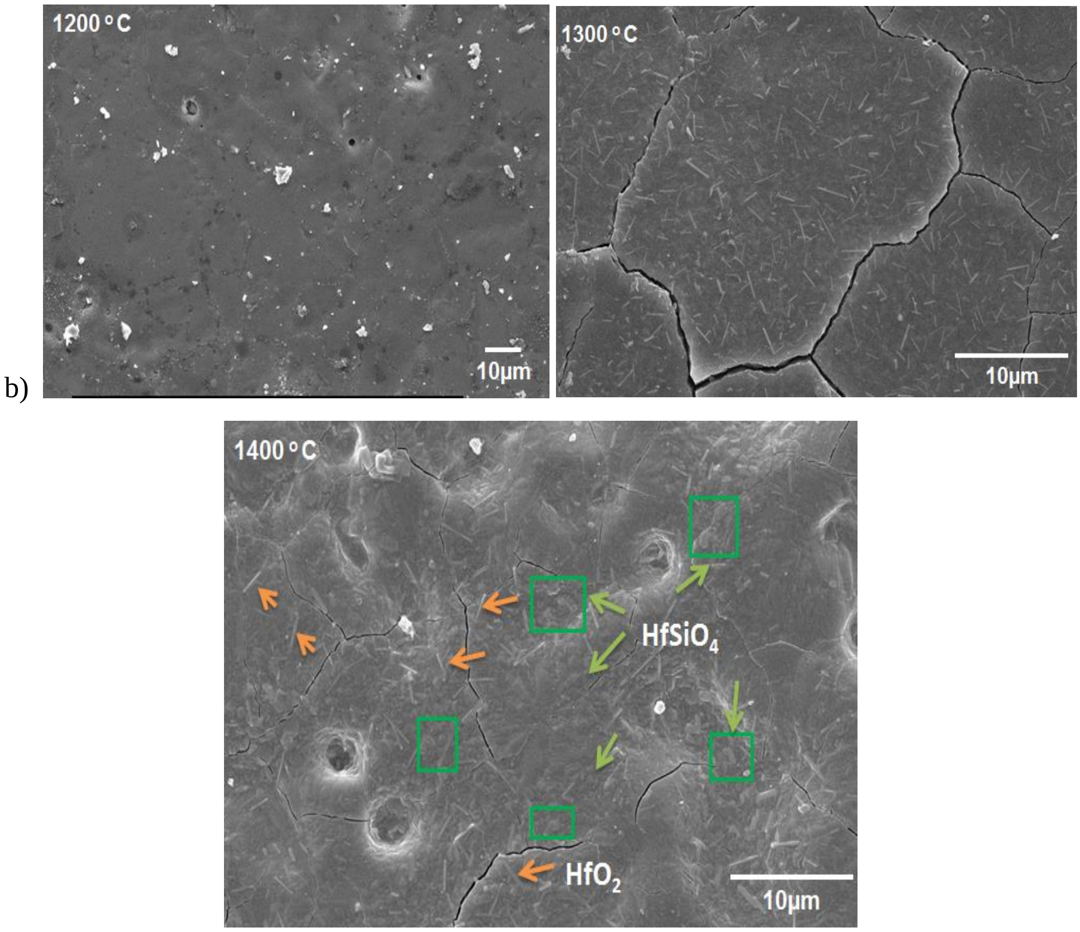

Figure 3.47. SEM micrographs of the oxidized surfaces of the PDCs: (a) SiHfBCN1 and (b) SiHfBCN2. The green arrows and rectangles indicate the formation of $HfSiO_4$, whereas the orange arrows indicate the precipitation of hafnia. The cracking can likely be attributed to the mismatch in the coefficient of thermal expansion between the silica scale and the Si-based matrix.

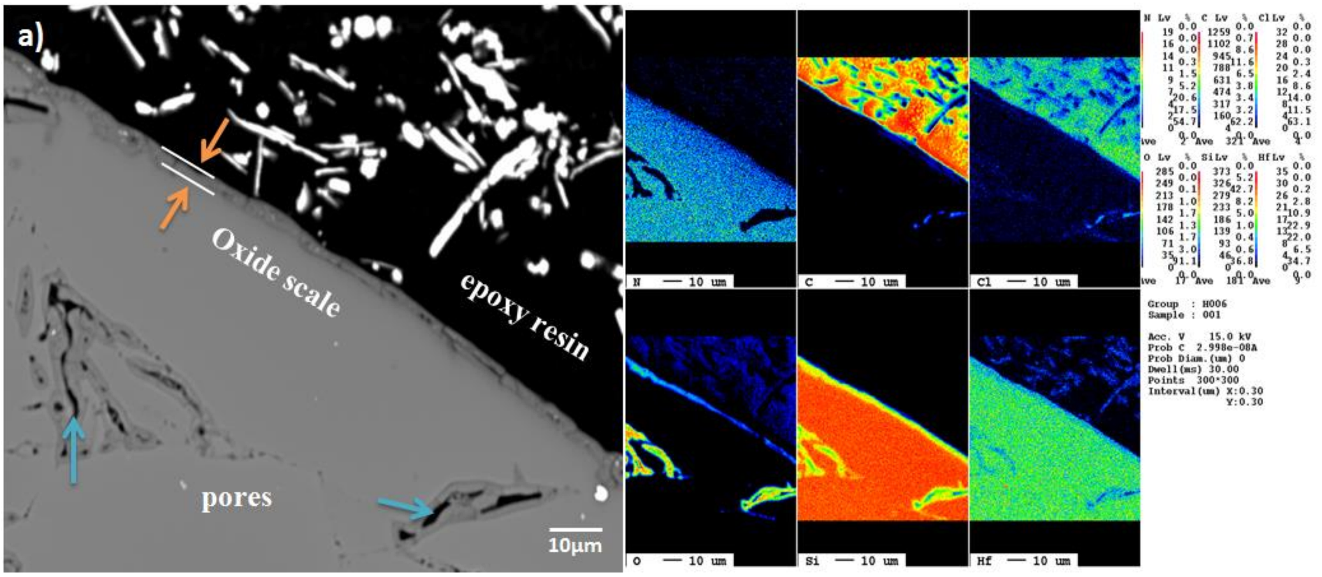

```
Group  : H006
Sample : 001

Acc. V     15.0 kV
Prob C   2.998e-08A
Prob Diam.(um) 0
Dwell(ms) 30.00
Points   300*300
Interval(um) X:0.30
             Y:0.30
```

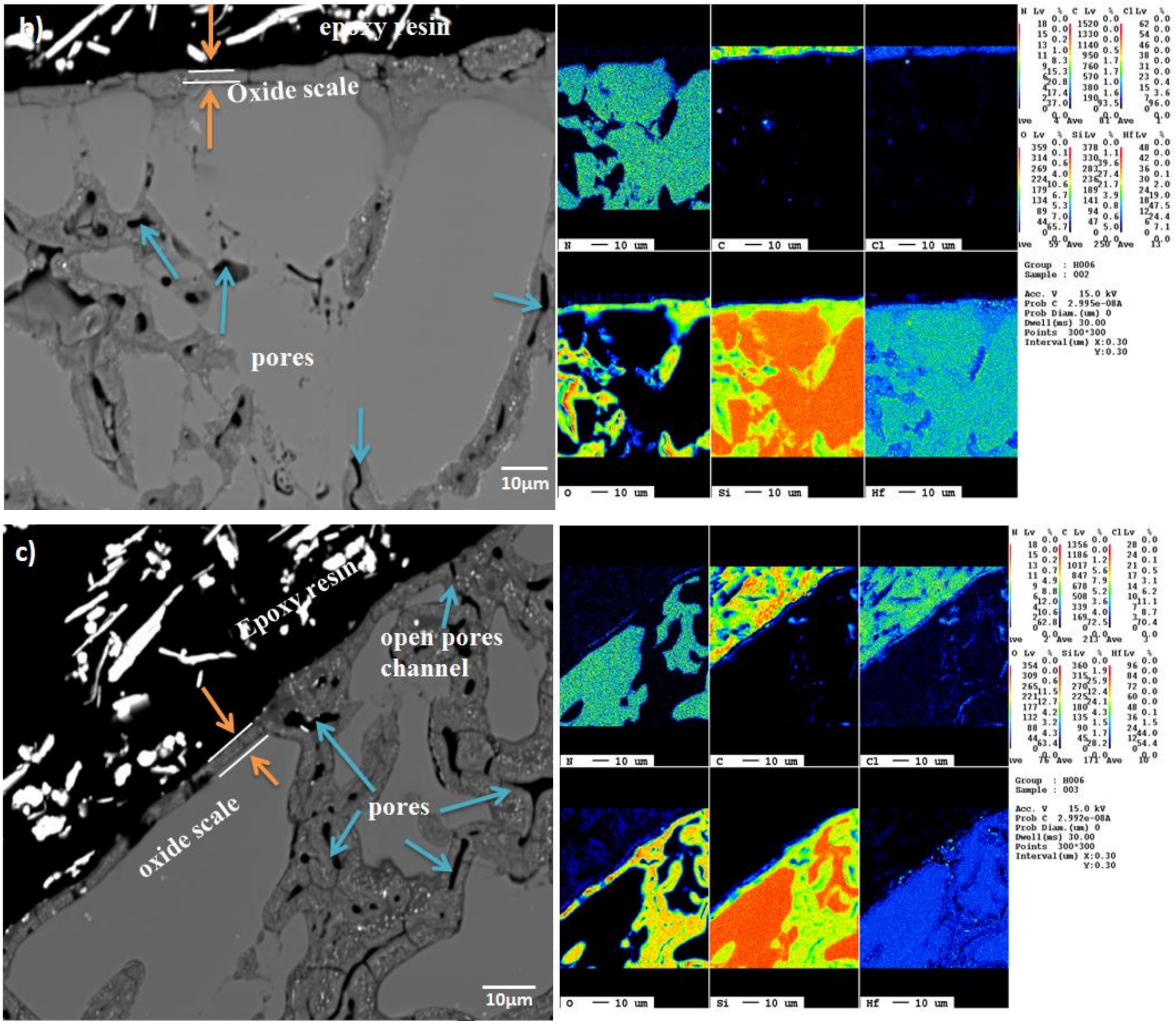

Figure 3.48. BSE micrographs and EPMA analyses of the fracture surfaces of SiHfBCN1 ceramics oxidized at 1200 (a), 1300 (b) and 1400 °C (c). The orange arrows and solid lines indicate the outermost oxide scale. The blue arrows indicate the intrinsic pores and the pores created by the evaporation of boria or the outward diffusion of decomposition species.

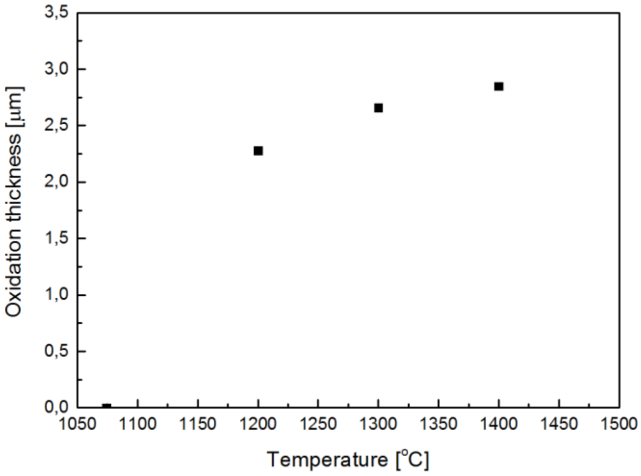

Figure 3.49. Relationship between oxidation thickness (t_{ox}) and temperature; note that t_{ox} was estimated from the EPMA results for SiHfBCN1 oxidized at 1200-1400 °C. The expressed temperature dependence of the t_{ox} values representing the oxidation thickness of SiHfBCN in this study is comparable to those of CVD Si_3N_4 and SiC ceramics[282].

The cross-sections of SiHfBCN1 exposed to oxidation conditions at 1200, 1300 and 1400 °C for 200 h were characterized using electron probe micro-analysis (EPMA); these instruments are used primarily for *in situ* non-destructive chemical analyses of oxidized samples. The contrast variation in the BSE image recorded at a temperature of 1200 °C (Figure 3.48a), indicates that a continuous oxidation scale is formed on the surface. However, the intrinsic pores located inside the matrix are clearly visible. The EPMA elemental analysis revealed that Si and Hf were present within the oxide scale, with silica being the major phase because the concentration of Si was much higher than that of Hf. It seems that the oxide scale is enriched in silica toward the top surface, whereas within the scale a composition consisting of hafnia dispersed within a silica matrix has been analyzed. The amount of boron present in the scale was not quantified in the characterization because of the low sensitivity of technique concerning light elements. However, considering the valuable data regarding the thermodynamic driving force for the formation of borosilicate above 1200 °C [160, 283], the oxide layer was likely composed of borosilicate/SiO_2 and HfO_2.

The EPMA analyses of the samples oxidized at 1300 °C indicated that a thicker oxide scale was formed at this temperature compared with that formed at 1200 °C (Figure 3.48b). Moreover, the oxide scale exhibited some cracking, though it remained adhered to the matrix. Thus, the oxide scales remained able to provide the underlying materials with diffusion-limiting oxidation protection. However, more pores were observed in the case of oxidation at 1300 °C, which are probably created during either the initial stage of the volatilization of B_2O_3 or the outward diffusion of CO and N_2 gas due to the oxidation of the SiHfBCN. The oxide scale that formed at 1400 °C appeared as a discontinuous layer with open pore channels (Figure 3.48c), which may have facilitated oxygen transport. Furthermore, the oxide scale appeared to penetrate from the surface into the inner pores, enabling greater oxygen permeation and confirming the higher weight gain observed at 1400 °C compared with the weight gain at 1200 and 1300 °C. The most intriguing finding of our study is that a uniform concentration of Hf was observed in the scale formed upon oxidation at 1200 °C, whereas a gradient distribution of Hf concentration from the surface to the underlying materials was observed in the scales exposed at 1300 and

1400 °C; the formation of this gradient might be related to higher depletion of other elements. Moreover, a decrease in the C content in the near-surface region resulted in HfO_2 particle coarsening in the SiO(C) at the internal surface compared with the bulk surfaces [284]. This finding may confirm the migration of m-HfO_2 to the surface that was observed in the SEM images (Figure 3.47).

A scale thickness of ~2-3 μm can be estimated based on the EPMA results. As shown in Figure 3.49, the thickness of oxide scale gradually increased as the temperature was increased from 1200 to 1400 °C, suggesting a passive oxidation and thus confirming the kinetic data obtained from recording the mass change of the samples as function of the exposition time.

In conclusion, the structure of the observed oxide scale that forms at 1200-1400 °C in oxidative conditions consists of: (i) a SiO_2-rich outer layer and (ii) a sub-layer consisting of HfO_2 embedded into SiO_2 (as for oxidation temperatures lower than 1400 °C); at 1400 °C, $HfSiO_4$ has been formed via the reaction of hafnia precipitations with the silica matrix, and is considered to contribute to an improvement of the oxidation resistance of SiHfBCN [2]. Thus, the results presented here indicate that SiHfBCN ceramics may be suitable materials to be used at high-temperatures and under oxidative and corrosive conditions.

3.4.2 Oxidation behavior of dense SiHfCN- and SiHfBCN-based UHTC-NCs

Although the amorphous ceramics exhibited good oxidation resistance, there was reasonable uncertainty about their oxidation rates because of the uncertainty in their geometric surface areas. Thus, they could not be compared with the oxidation rates determined for silicon-based ceramics. Therefore, investigations of the oxidation behavior of dense UHTC-NC ceramics are required to allow for a more accurate analysis of the oxidation rates of SiHf(B)CN-based ceramics.

3.4.2.1 Oxidation behavior

The oxidation behavior of SiHfBCN (SiHfBCN_06) and SiHfCN-based (SiHfCN_05) UHTC-NCs was evaluated via the TGA of small monolithic coupons by monitoring the mass changes of samples subjected to oxidizing environments at temperatures of up to 1500 °C.

The mass evolution of SiHfCN and SiHfBCN upon oxidation at 1400 and 1500 °C is depicted in Figure 3.51, which indicates remarkably higher oxidation resistance for SiHfBCN compared with its boron-free analog. During isothermal oxidation at 1400 °C, the weight of the SiHfCN sample initially increased linearly for a short time (approximately 1 h), indicating that the SiHfCN was oxidizing very rapidly. By comparison, the weight of the SiHfBCN did not increase significantly when subjected to continuous isothermal oxidation at a temperature of 1400 °C for up to 5 h. Moreover, photographs of the ceramic samples oxidized at 1400 °C show that spall-off from the parent matrix were observed in the SiHfCN (Figure 3.50). For the oxidation experiments at 1500 °C, the weight gain remained relatively low (< 1 wt %) for all investigated samples exposed to the oxidizing environment when the temperature was below 800 °C during the non-isothermal stage. However, the situation changed dramatically as the temperature was progressively increased. The SiHfCN sample exhibited a significant increase in weight change during the isothermal stage, with a high weight gain of approximately 10 wt % (approximately 110 wt %). By contrast, an extremely low weight gain observed in SiHfBCN at temperatures of up to 1500 °C, indicating that the protective oxide layer formed on the SiHfBCN at 1500 °C was very stable.

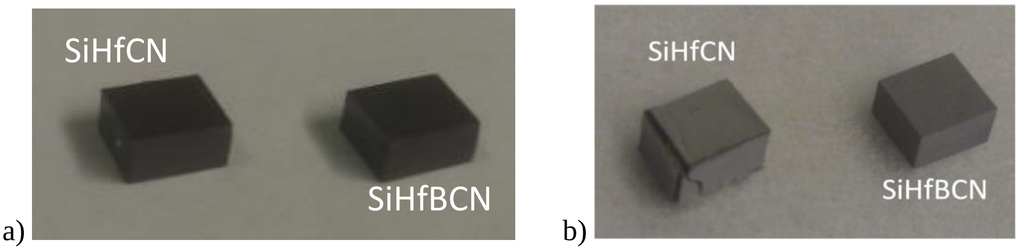

Figure 3.50. Photographs of the samples a) prior to oxidation and b) after oxidation. Spall-off from the parent matrix of the SiHfCN sample can be clearly observed.

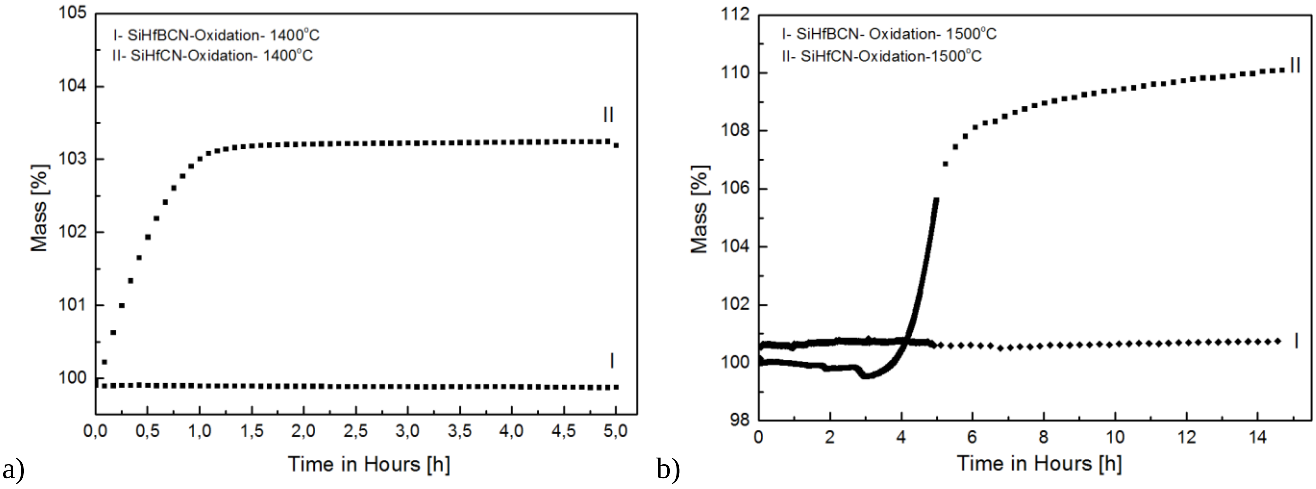

Figure 3.51. The oxidation behavior of dense SiHfCN and SiHfBCN at temperatures of 1400 (a) and 1500 °C (b), indicating remarkably high oxidation resistance for SiHfBCN compared with its boron-free analog.

Both samples were found to undergo parabolic oxidation, as revealed by the plots in Figure 3.51. Thus, the specific weight gain could be calculated from the weight gain per geometric surface area (Eq. 3.5). It should be noted that because the samples treated at 1500 °C had already oxidized during the non-isothermal stage, the net weight gain of the treated sample at T-1 was calculated by subtracting the initial weight from the final weight. Figure 3.52 plots the square of the specific weight gain as a function of the oxidation time in hours ($(\Delta m/S)^2$ *vs. t*). Obviously, SiHfCN differs fundamentally from SiHfBCN, as it exhibited significantly higher parabolic oxidation rates (though comparable to those reported for UHTCs such as HfB_2-20 vol% SiC). Moreover, it seems that there are two oxidation regimes for SiHfCN: in the short-term range, high rates were observed (28.2 and 4.7 $mg{\cdot}cm^{-2}{\cdot}h^{-1}$ for oxidation at 1400 and 1500 °C, respectively), whereas in the long-term range, i.e., for oxidation times longer than 3 h, significantly smaller values were recorded (0.4 and 2.1 $mg{\cdot}cm^{-2}{\cdot}h^{-1}$ for 1400 and 11500 °C, respectively). Similar oxidation behavior has also been observed for SiAlCN at temperatures of 1000–1400 °C. The short-term oxidation regime in SiHfCN likely corresponds to the oxidation of the HfC_xN_{1-x} phase and the generation of hafnia, whereas the behavior upon long-term exposure may be related to the formation of silica.

SiHfBCN was observed to exhibit excellent behavior upon oxidation at 1400 and 1500 °C. The determined parabolic oxidation rates (3.6×10^{-4} and 5.2×10^{-3} $mg \cdot cm^{-2} \cdot h^{-1}$ at 1400 and 1500 °C, respectively) were several orders of magnitude lower than those previously reported for UHTCs. Moreover, the parabolic oxidation rate of SiHfBCN at 1400 °C was one order of magnitude lower than that reported for CVD-SiC at the same temperature (i.e., 1.3×10^{-3} $mg \cdot cm^{-2} \cdot h^{-1}$) [150].

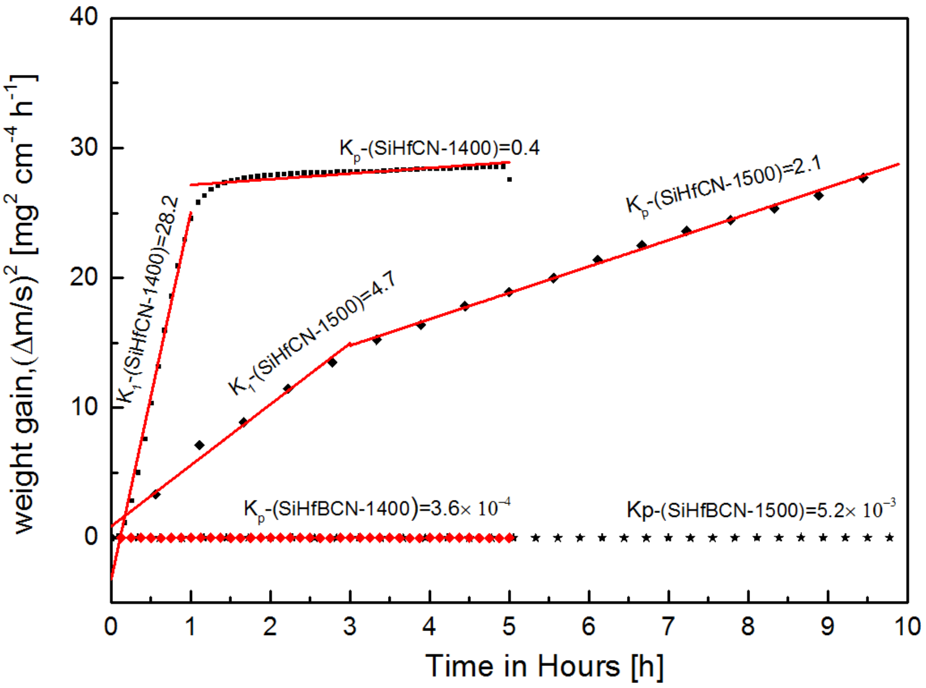

Figure 3.52. Parabolic plot of the surface specific mass gain as a function of the temperature for the oxidation of SiHfCN and SiHfBCN.

Table 3.18. Experimental values for the mass changes upon oxidation and parabolic oxidation rates of dense SiHfCN and SiHfBCN and a comparison with the corresponding values for Si-containing ceramics from the literature.

	Temperature [° C]	Isothermal time [min]	Weight change [mg cm^{-2}]	K$_p$ [mg^2 cm^{-4} h^{-1}]
SiHfCN-SPS	1400	300	5.2	28.2*/0.4**
	1500	600	5.3	4.7*/2.1**
SiHfBCN-SPS	1400	300	0.04	3.6×10^{-4}
	1500	600	0.16	5.2×10^{-3}
HfB2- 20vol% SiC [263]	1350	60	0.65 ± 0.03	0.42
	1500	60	1.60 ± 0.05	2.56

* Short-term value, ** long-term value.

3.4.2.2 Changes in phase and microstructure after oxidation treatment

The behavior observed in Figure 3.51 and Figure 3.52 can be associated with corresponding changes in the composition of the different systems undergoing oxidation. For this purpose, the surfaces of the products obtained from isothermal TGA tests were analyzed via XRD and SEM; the results are shown in Figure 3.53 and Figure 3.55. Clearly, oxidized products, likely HfO_2, cristobalite and $HfSiO_4$, were detected in the XRD analysis of the 1400 and 1500 °C samples. These findings are a consequence of SiC and HfC_xN_{1-x} reacting with O_2 to form SiO_2 (cristobalite) and m- or t-HfO_2. As the temperature progressively increased, $HfSiO_4$ formed from m-HfO_2 and SiO_2 [285]. Additionally, signals associated with the unreacted matrix materials HfC_xN_{1-x} and β-SiC were also observed, suggesting that the outermost oxidize layer may have protected the sublayer matrix against oxidation. Interestingly, the intensity of the peak corresponding to HfC_xN_{1-x} in the SiHfBCN pattern is much higher than that in the SiHfCN pattern, whereas the β-SiC peak exhibits the opposite behavior. This may be related to strong protection of the HfC_xN_{1-x} phase due to the presence of external glassy SiO_2 or borosilicate in the case of SiHfBCN. Furthermore, for the SiHfBCN ceramics, the intensity of the peak corresponding to $HfSiO_4$ is much stronger than that in the SiHfCN pattern, indicating that boron seems to facilitate the formation of $HfSiO_4$. It has been reported that Ti is able to catalyze the formation of $HfSiO_4$, thereby enhancing the stability of Hf-O-Si bonding compared with Ti-O-Si bonding in an archetypical zircon structure [286]; thus, a similar effect of boron on catalyzing the formation of $HfSiO_4$ could be assumed.

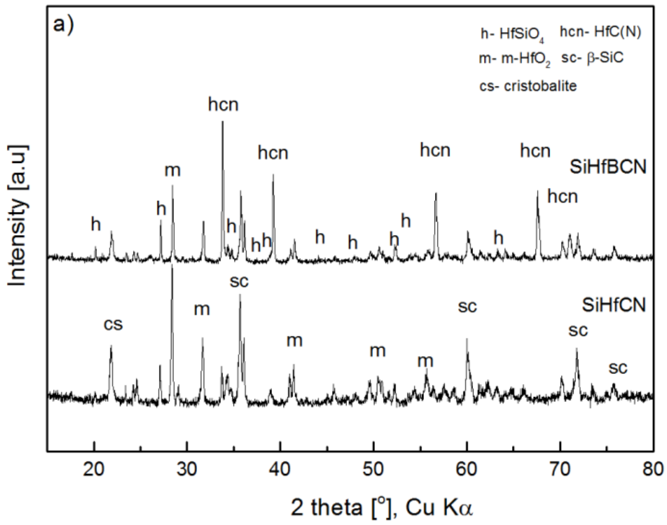

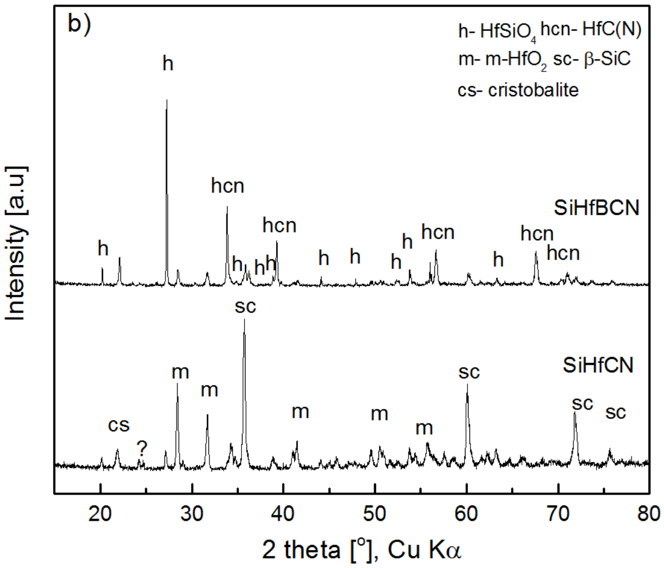

Figure 3.53. X-ray diffraction patterns of SiHfBCN- and SiHfCN-based dense ceramics oxidized in synthetic air for 5 h at (a) 1400 °C and (b) 1500 °C.

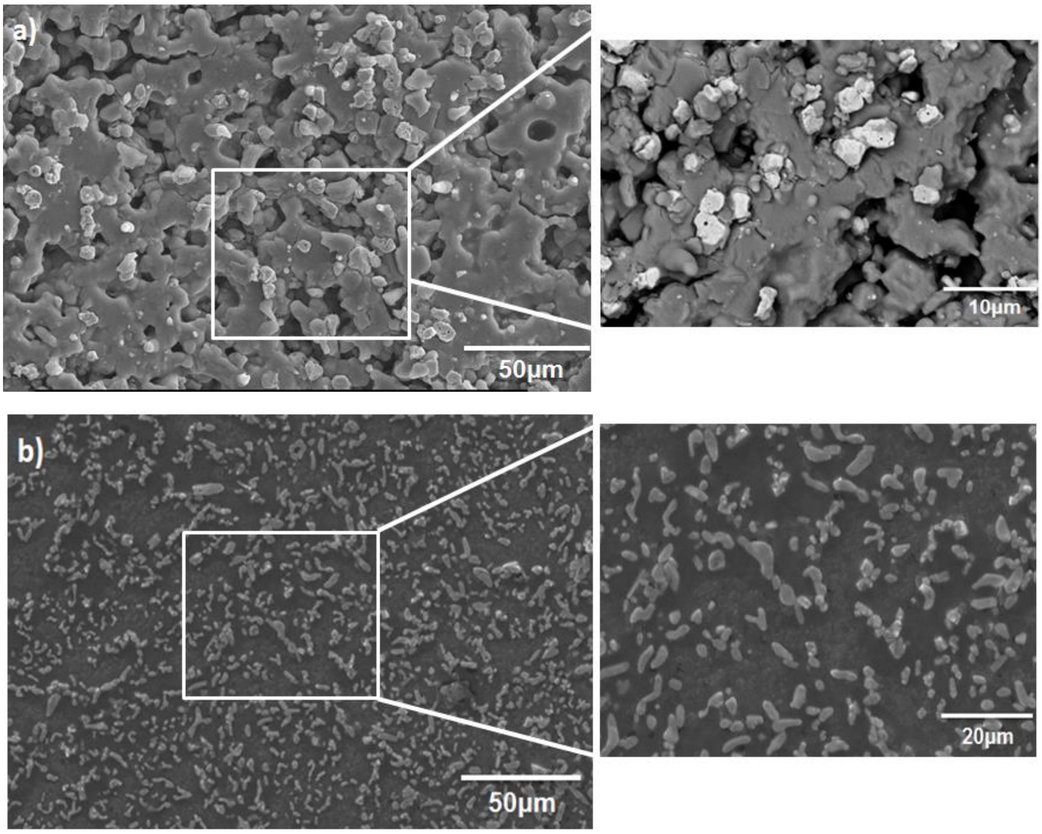

Figure 3.54. SEM micrographs of the surfaces of SiHfCN (a) and SiHfBCN (b) after oxidation at 1500 °C.

The micrograph in Figure 3.54 illustrates the oxidized surface of the SiHfCN and SiHfBCN after oxidation at 1500 °C. Clearly, a porous surface scale is observed in the oxidized SiHfCN sample; whereas the oxidized SiHfBCN sample exhibited a continuous, dense scale which provides obviously improved oxidation stability.

Furthermore, cross sections of the oxidized samples were analyzed via SEM and EDS, as shown in Figure 3.55. As revealed by the oxygen contents determined along the cross sections, the SiHfCN samples demonstrated lower oxidation resistance compared with their SiHfBCN counterparts. Thus, exposure to oxidative conditions resulted in deeper penetration of oxygen into the bulk SiHfCN compared with the SiHfBCN. Thus, the oxygen content was still as high as 4.6 wt % in the region located approximately 90 µm below the surface of the SiHfCN sample, whereas a similar oxygen content (4.1 wt %) had already been reached at approximately 10 µm below the surface of the SiHfBCN. Additionally, the cross-sectional SiHfBCN sample oxidized at 1500 °C was also assessed using EDS (Figure 3.55c). The analysis revealed that the oxidized scale was enriched in silicon and oxygen, indicating that silica or silicate dominated in this layer and provided an excellent barrier against oxygen penetration. Accordingly, very little oxygen content was observed beneath this layer (approximately 1.4 wt %).

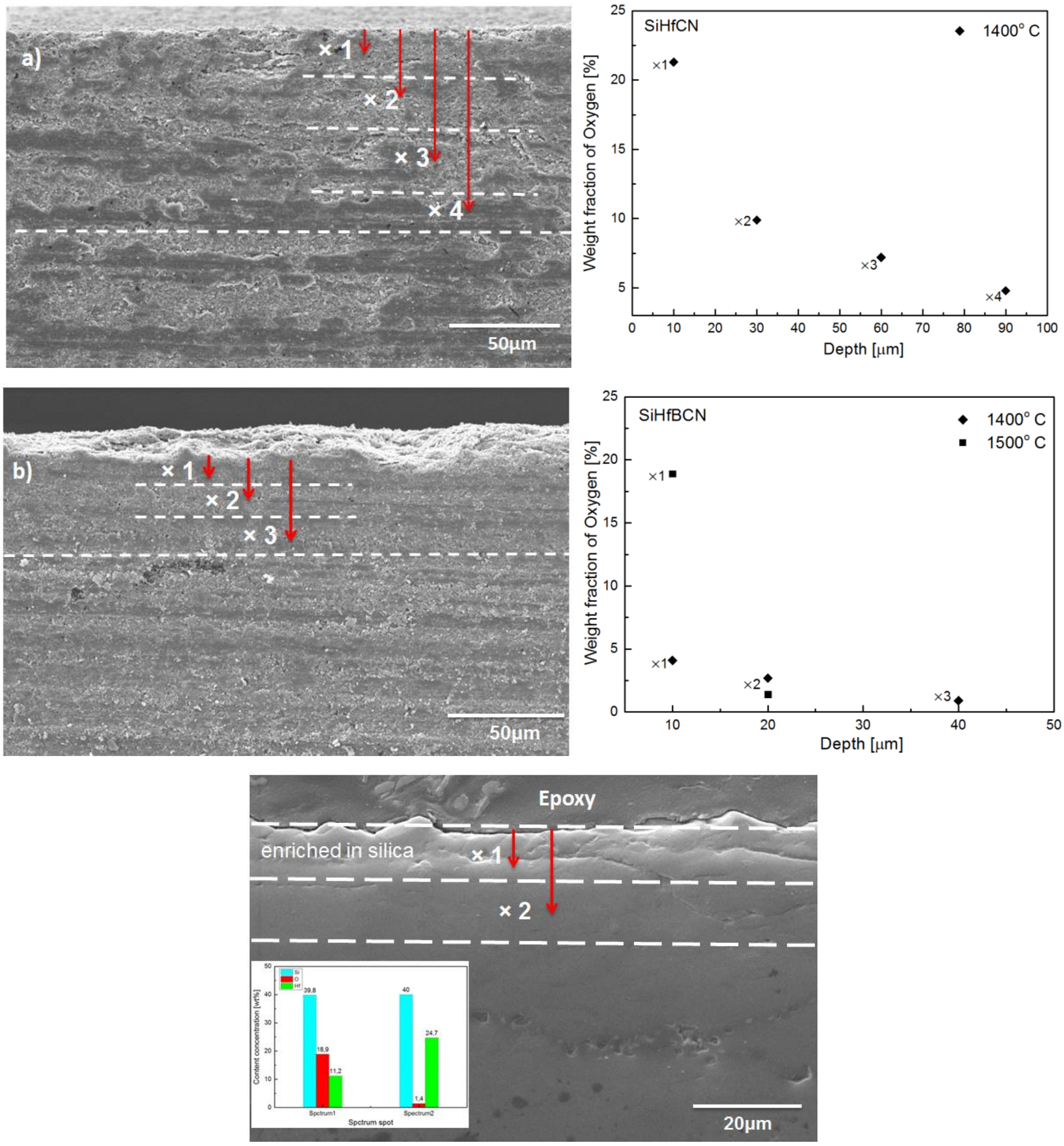

Figure 3.55. SEM micrographs of the cross sections and corresponding oxygen contents at various distances from the surface for a) SiHfCN oxidized at 1400 °C, b) SiHfBCN oxidized at 1400 °C, and c) SiHfBCN oxidized at 1400 and 1500 °C (sample oxidized at 1500 °C was embedded in epoxy and then polished).

A question still remains concerning the reason for the superior oxidation resistance of SiHfBCN compared with SiHfCN. First, let us consider the main reactions that are expected to describe the oxidation process, involving either a mass gain (reactions 3.10 - 3.15) or a mass loss (reactions 3.17 - 3.18):

HfC_xN_{1-x} (s) + (1+x) O_2 (g) = HfO_2 (s) + x CO (g) + ((1-x)/2) N_2 (g) (3.10)

BN (s) + 3/2 O_2 (g) = B_2O_3 (l) + N_2 (g) (3.11)

SiC (s) + 3/2 O_2 (g) = SiO_2 (s) + CO (g) (3.12)

Si_3N_4 (s) + 3 O_2 (g) = 3SiO_2 (s) + 2N_2 (g) (3.13)

2HfB_x (s) + (4+3x)/2 O_2 (g) = 2HfO_2 (s) + xB_2O_3 (g) (3.14)

$SiB_xC_yN_z$ (s) + (1+ ¾ x+ y/2) O_2 (g) = SiO_2 (s) + B_2O_3 (l) + CO(g) + N_2 (g) (3.15)

HfO_2 (s) + SiO_2 (s) = $HfSiO_4$ (s) (3.16)

B_2O_3(l) = B_2O_3(g) (3.17)

C (s) + O_2 (g) = CO (g) (3.18)

Plausible explanations can be summarized as follows:

i) For SiHfCN, considering that the oxidation rate of HfC_xN_{1-x} is significantly faster than that of Si-based ceramics, porous HfO_2 forms (at approximately 500 °C, reaction 3.10), which cannot protect the matrix, leading to the high weight gain during the initial oxidation stage (Figure 3.51). Moreover, the negative contribution is most likely related to the oxidation of free carbon (reaction 3.18). The additional amorphous (Si)BCN phase is related to the difference in composition between SiHfCN- and SiHfBCN-based SPS ceramics. By contrast, an additional B-containing phase is generated upon the oxidation of the liquid boria phase (B_2O_3, reactions 3.7 and 3.10), which could fill the pores of the HfO_2, forming a dense layer hindering further oxidation reactions at relatively low temperatures and leading to the observed stability in the weight gain of SiHfBCN at low temperatures (Figure 3.51).

ii) Because concrete advantages deriving from the presence of the SiC phase arise only at temperatures above 1400 °C, the kinetics may be parabolic because of the slower diffusion of oxygen through a silica layer once sufficient silica has formed, either during long-term oxidation at 1400 °C or at high temperatures (up to 1500 °C) (Figure 3.54) [10]. At 1500 °C, it is believed that sufficient silica (reaction 3.12) or borosilicate (reaction 3.15) from the oxidation of SiC and Si(B)CN, in combination with the $HfSiO_4$ (reaction 3.16) and HfO_2 products, will form an immiscible glass layer that will provide far more effective oxidation-protective capabilities because of its higher viscosity [83]. Therefore, the stability of the mass changes in SiHfBCN with increasing oxidation time is an indication of a very low rate of oxidation due to the formation of a dense layer of immiscible glass on the surface.

3.4.3 Summary

The high-temperature oxidation behavior of materials is of critical concern in evaluations of their performance in harsh environments. In this section, the oxidation behavior of amorphous ceramics derived from PDCs and dense UHTC-NC monoliths obtained via SPS was discussed.

i) The oxidation behavior of amorphous ceramic specimens was studied at temperatures of 1200 to 1400 °C. Measurements of the specific weight gain as a function of the isothermal oxidation time revealed that both powder and monolithic samples exhibited parabolic oxidation behavior and extremely low parabolic rates; the activation energy of 112.9 kJ mol^{-1} for SiHfBCN powder is within the range of values measured for oxygen diffusion through silica. Observations of the oxide scales that formed on the monoliths at different oxidation temperatures revealed that a continuous oxide scale consisting of borosilicate, silica (cristobalite), m- and t-HfO_2 forms at temperatures below 1300 °C, limiting the capacity for oxygen transport. At temperatures above 1300 °C, the oxide scale becomes a discontinuous layer consisting of silica, $HfSiO_4$ and m- and t-HfO_2, and large pores are formed in the matrix; thus, the higher weight gain observed at 1400 °C is attributed to these pores and the partial protection provided by the oxide layer. In summary, the formation of this unique oxide scale (borosilicate/silica, hafnon and hafnia) and good parabolic oxidation behavior strongly suggest that amorphous SiHf(B)CN ceramics can be considered as potential candidates for (ultra)-high-temperature applications.

ii) The oxidation behavior of SiHfCN was found to be comparable to that of other UHTCs. By contrast, SiHfBCN exhibited excellent oxidation behavior, with parabolic oxidation rates several orders of magnitude lower than those previously reported for UHTCs and even lower than values reported for SiC. The results presented in this work indicate that SiHfCN- and SiHfBCN-based UHTC-NCs can be considered to demonstrate great potential as candidates for high-temperature applications in harsh environments.

3.5 Hydrothermal corrosion behavior of C_f reinforced CMC composites

3.5.1 Introduction to the corrosion of CMCs

CMCs are candidates for various applications at high temperatures and in hostile environments. However, carbon fiber-reinforced CMCs suffer at high temperatures from oxidation issues [287]. Lamourourx *et al* devoted initial and intensive studies on the oxidation of carbon fiber-reinforced SiC composites [288, 289]. In order to improve their oxidation resistance, it has been suggested that, for instance, a multi-layered matrix design might be a suitable solution. Furthermore, when exposed to combustion environments, the long term durability of CMCs requires the use of environmental barrier coatings (EBCs) to prevent severe degradation reactions of the CMCs with the combustion products (e.g. steam or salts). Silicon-based matrix materials (such as SiC) are prone to strong decomposition in combustion environments, as $Si(OH)_4$ is generated and released from the reaction between the silica-based passivation layer and water vapor. SiC-based CMCs coated with barium strontium aluminosilicate (BSAS) [290] or with other oxide-based materials with low vapor pressure at high temperatures (e.g. ZrO_2, HfO_2, rare earth silicates) [291],[292] have been shown to effectively protect the CMCs from hot corrosion.

The hot corrosion behavior of CMCs was investigated within the context of their use in turbine engines. Thus, Cheng *et al* [21, 293, 294] described the high temperature degradation mechanisms of C_f/SiC composites in complex salt-vapor environments (i.e., O_2 / H_2O / Na_2SO_4 or Ar / Na_2SO_4). However, few studies concerning the corrosion behavior of ceramic fibers or CMCs under hydrothermal conditions have been reported [295], [296], and consequently only scarce information is present in the literature with respect to their behavior.

The purpose of the present study in Section 3.5.2 is to assess and discuss for the first time their corrosion behavior of fabricating C_f/SiCN and C_f/SiHfBCN CMCs via the PIP technique under subcritical hydrothermal conditions. A comparison between the corrosion behavior of C_f/SiCN and C_f/SiHfBCN CMCs is discussed in detail, indicating that the incorporation of Hf and B into SiCN has a significant effect on their performance under hydrothermal conditions. The presented results might be of great relevance within the context of the development of CMCs suitable for petrochemical applications, which are characterized by moderate temperatures (several hundreds of °C) and high hydrothermal pressure [297].

3.5.2 Hydrothermal corrosion behavior of C_f/SiCN and C_f/SiHfBCN CMCS

The C_f/SiCN and C_f/SiHfBCN CMCs were studied with respect to their behavior in hydrothermal conditions. In the case of C_f/SiCN, the relationship between the weight change rate and S/V ratio for the specimen corroded at 250 °C is shown in Figure 3.56 (a). At S/V values larger than 0.4, the CMC samples exhibited mass gain upon exposition to hydrothermal conditions; whereas at S/V ratios in the range of 0.4 and 0.2, the sample showed mass loss upon corrosion. Interestingly, the C_f/SiHfBCN composites presented only mass gain under similar conditions, indicating an improved performance of SiHfBCN. For significantly lower S/V ratios, i.e. less than 0.075, C_f/SiHfBCN showed mass loss upon corrosion.

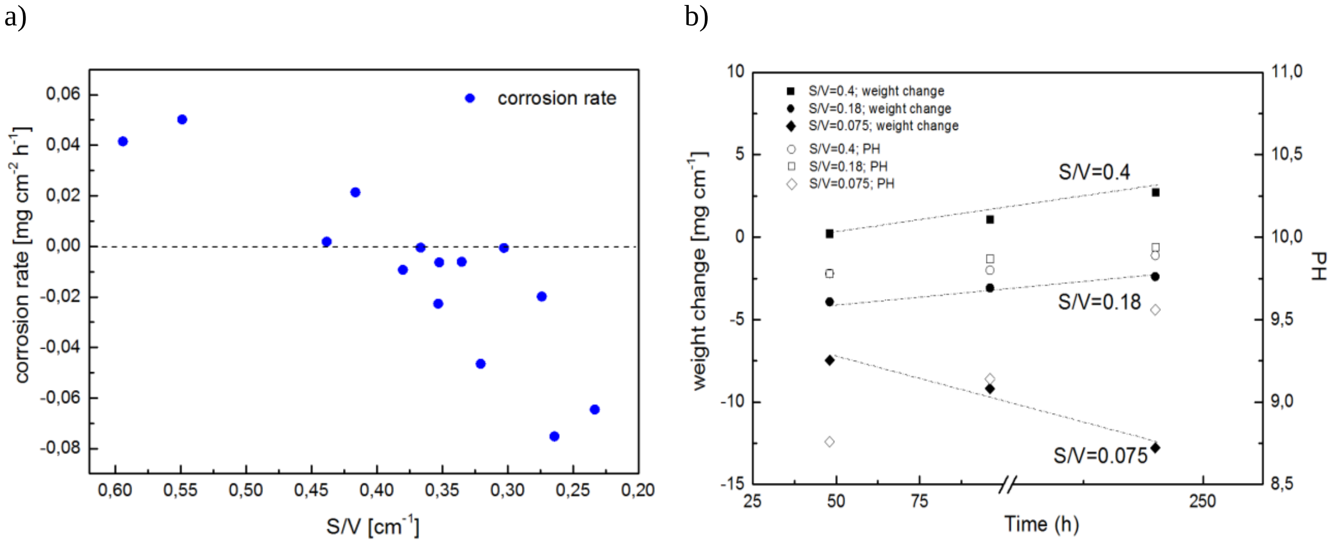

Figure 3.56. (a) Influence of the S/V ratio on the corrosion behavior of C_f/SiCN (250 °C) - the corrosion rate (mg cm^{-2} h^{-1}) for Cf/SiCN in (a) has been estimated from the time-dependent evolution of the surface specific weight of the specimens (48, 96 and 240 h); (b) Mass change of C_f/SiHfBCN as a function of the soaking time (250 °C; as for three S/V values, i.e. 0.4, 0.18 and 0.075).

Different reports have been done on the corrosion behavior of monolithic SiC and Si_3N_4 ceramics in various hydrothermal conditions (e.g. subcritical hydrothermal conditions [182, 296, 298], acid and basic environments [185], [299]) and revealed that their stability is mainly controlled by the grain boundaries or the grain-boundary phase [182]. Under hydrothermal corrosion, Si-based ceramic materials such as SiC, Si_3N_4 or SiOC exhibit active corrosion behavior, as the solubility of the passivation scale SiO_2 is significant in subcritical hydrothermal conditions [184]. For instance, studies related to the corrosion behavior of hot-pressed Si_3N_4 and reaction-sintered SiC at temperatures below 800 °C always showed active corrosion [183]. Despite the corrosion rates of SiOC-based ceramic materials being remarkably lower than those of typical SiC and Si_3N_4 ceramics, they also exhibited mass loss upon corrosion [4]. Therefore, it is concluded that active corrosion is a typical behavior of Si-based ceramics upon exposition to a hydrothermal environment.

In all experiments, the pH value of the corrosion medium after corrosion was found to be higher than 8.5 for both C_f/SiCN and C_f/SiHfBCN (Table 3.19). This obviously has correlations with the hydrolysis reactions of the Si-N and Hf-N bonds which lead to the formation of silica and hafnia and the release of ammonia.

Table 3.19. Evolution of the pH value of the corrosion medium with the corrosion temperature (150, 200 and 250 °C) and time (48, 96 and 240 h).

Temperature	C_f/SiCN			C_f/SiHfBCN		
[°C]	48h	96h	240h	48h	96h	240h
150	9.25	9.32	9.44	8.85	8.98	9.06
200	9.38	9.48	9.60	9.15	9.26	9.35
250	9.58	9.68	9.74	8.76	9.14	9.56

The hydrothermal corrosion of SiC and Si_3N_4 in the temperature range addressed within the present study (i.e. 200 - 250 °C) occurs according to the following reactions[183] ,

$$SiC + 2\,H_2O = SiO_2 + CH_4 \tag{3.19}$$

$$Si_3N_4 + 6\,H_2O = SiO_2 + 4NH_3 \tag{3.20}$$

Whereas the hydrothermal corrosion of SiCN can be written as follows (equation not balanced):

$$Si_xC_yN_z + H_2O = x\,SiO_2 + y\,CH_4 + z\,NH_3 \tag{3.21}$$

The processes occurring upon hydrothermal corrosion of SiHfBCN are obviously more complex. As shown in the XRD figures (Figure 3.57), the CMC samples show very broad reflections indicating that no crystallization occurs in SiHfBCN during corrosion. The same behavior has been reported in the case of Si-Ti-C-O (Tyranno) fibers treated under hydrothermal corrosion, i.e. the amorphous structure remained and no crystalline TiO_2 was observed after corrosion at temperatures lower than 500 °C [295].

Thus, we propose the following process to describe the hydrothermal corrosion of SiHfBCN, during which silica and hafnia are generated as passivation products, and methane and ammonia are released (equation not balanced):

$$SiHf_xB_yC_zN_w + H_2O = SiO_2 + x\,HfO_2 + y\,BCN + (z-y)\,CH_4 + (w-y)\,NH_3 \tag{3.22}$$

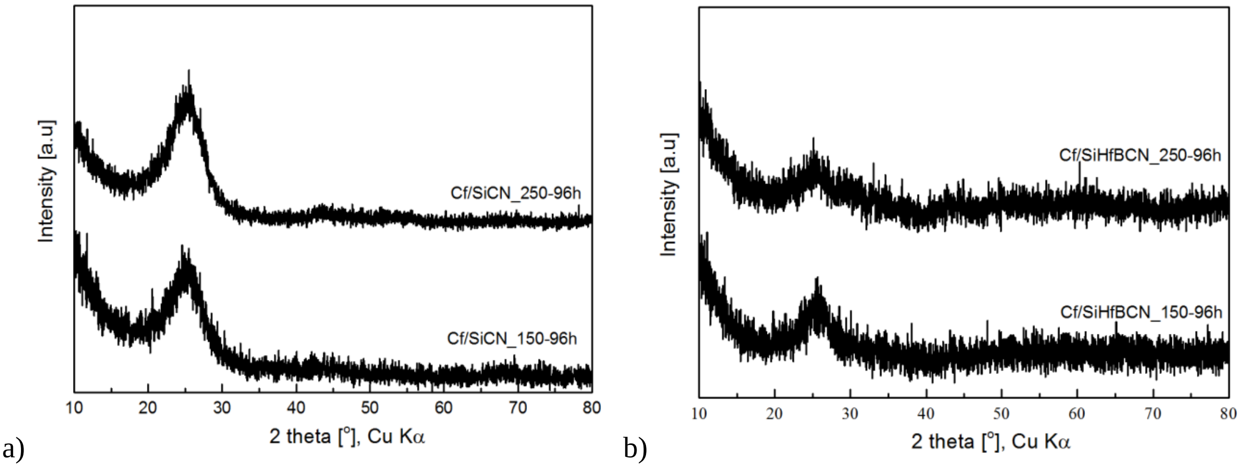

Figure 3.57. XRD patterns of C_f/SiCN (a) and C_f/SiHfBCN (b) ceramic composites after hydrothermal corrosion for 96 h at 150 °C and 250 °C.

Figure 3.58 shows the mass loss of C_f/SiCN and C_f/SiHfBCN CMCs during the hydrothermal corrosion tests at a S/V ratio of 0.075 as a function of the soaking time. The weight loss of C_f/SiHfBCN is lower than that of C_f/SiCN under the same corrosion conditions, revealing that the incorporation of Hf and B into the SiCN matrix contributes to the improvement of its corrosion resistance.

All samples showed active corrosion at a S/V ratio of 0.075. The strongest corrosive attack occurred under short time exposition (up to 48 h), particularly at a high temperature (250 °C).

Considering the chemical and phase compositions of the two samples, we assume that their corrosion occurs as follows:

a) In a first step, Si-N/Si-C as well as Hf-N/Hf-C (for SiHfBCN) bonds are hydrolytically attacked by water upon formation of silica (for both SiCN and SiHfBCN) and hafnia (for SiHfBCN) as well as releasing methane and ammonia (see reaction (3.22)). This process is in good agreement with the evolution of the pH value of the corrosion medium which was found to increase as the corrosion temperature and time increase (due to ammonia release) as shown in Table 3.19.

b) In a second step, silica dissolution (cf. (3.23)) occurs in addition to the hydrolytic corrosion of the samples and is thought to determine the corrosion rates.

$$SiO_2 + H_2O \underset{K_2}{\overset{K_1}{\rightleftharpoons}} Si(OH)_4 \tag{3.23}$$

Within this context, we assume that the dissolution of the silica determines the corrosion behavior of the investigated CMC samples, which means that the rate of silica dissolution (K_1) is significantly faster than formation of silica (K_2). However, as the amount of the released $Si(OH)_4$ increases, the rate of K_1 might decrease (if the solubility product of $Si(OH)_4$ in water is exceeded under the used conditions). This obviously will lead to a decrease of the rate of active corrosion of the investigated samples (see Figure 3.58). A similar behavior was observed in the case of a SiOC-based material [4].

It has been reported that small amounts of aluminum present within SiCN can remarkably improve its oxidation/corrosion resistance, due to the incorporation of Al within the silica passivation scale, which significantly suppresses the oxygen diffusion [300].

We consider a similar effect occurring in the case of Hf- and B-modified SiCN. Thus, the incorporation of Hf within the silica scale, which is generated as an intermediary during the hydrothermal corrosion, might significantly change its dissolution behavior/rate.

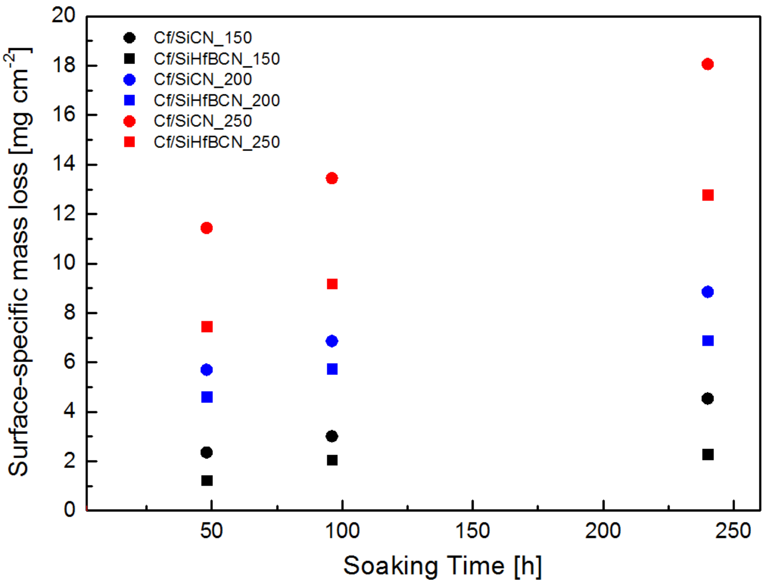

Figure 3.58. Dependence of the weight loss on the hydrothermal corrosion time at different temperatures.

The corrosion rates of the investigated CMCs were derived from the relationship between the surface specific mass loss (mg·cm^{-2}) and the soaking time (Figure 3.58 and Table 3.20). At 150 °C, a corrosion rate of 4.6×10^{-3} mg·cm^{-2}·h^{-1} for C_f/SiHfBCN was recorded, which is one order of magnitude lower than that of C_f/SiCN (1.1×10^{-2} mg·cm^{-2}·h^{-1}). With the corrosion temperature increasing, the corrosion rates of C_f/SiCN and C_f/SiHfBCN rise; thus, the values upon corrosion at 250 °C are 3.4×10^{-2} and 2.7×10^{-2} mg·cm^{-2}·h^{-1}, respectively.

A comparison of the corrosion rates of our samples with those determined for other ceramics is difficult to undertake because of the lack of standard procedures in the assessment and comparison of ceramic materials concerning their corrosion behavior [301]. Furthermore, it is difficult to unify the corrosion kinetics in various conditions of corrosion: For instance, the ratio of the volume of the medium solution to the specimen surface is not always defined. However, as the mechanism of Si-based materials underlying corrosion under hydrothermal conditions is the most comparable [184], the collected kinetics data may be compared to those reported in the literature. For instance, corrosion rates of 111 mg·cm^{-2}·h^{-1} were reported for SiC ceramics [302], being 2 orders of magnitude higher than those of C_f/SiCN (3.4×10^{-2} mg·cm^{-2}·h^{-1} at 250 °C) or C_f/SiHfBCN (2.7×10^{-2} mg·cm^{-2}·h^{-1} at 250 °C). This indicates that our investigated materials exhibit improved corrosion resistance under hydrothermal conditions.

The activation energies of the corrosion were obtained from the evolution of the corrosion rate with the temperature, as given in Table 3.20. It was found that the E_a of C_f/SiHfBCN (32.4kJ mol^{-1}) is slightly higher than that of C_f/SiCN (20.4 kJ mol^{-1})

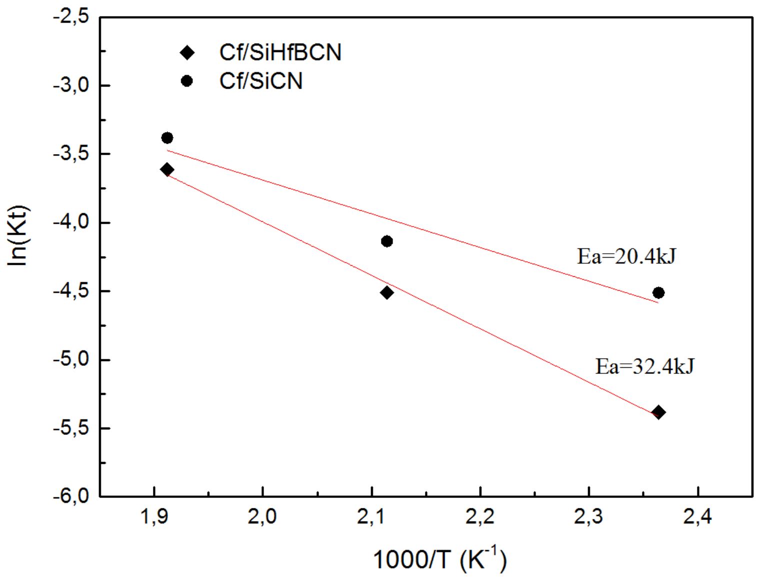

Figure 3.59. Arrhenius plot of the degradation of C_f/SiCN and C_f/SiHfBCN.

Table 3.20. Corrosion rates and activation energies of C_f/SiCN and C_f/SiHfBCN.

Temperature [°C]	Corrosion rate [$mg\cdot cm^{-2}\cdot h^{-1}$]		Activation energy [$kJ\ mol^{-1}$]	
	C_f/SiCN	C_f/SiHfBCN	C_f/SiCN	C_f/SiHfBCN
150	1.1×10^{-2}	4.6×10^{-3}	20.4±4.9	32.4±2.3
200	1.6×10^{-2}	1.1×10^{-2}		
250	3.4×10^{-2}	2.7×10^{-2}		

The activation energies for the corrosion process of the evaluated samples were found to be close to those of silica glass (40 kJ mol^{-1} at T < 500 °C [303]), indicating that their corrosion relies on a similar mechanism. As the solubility of hafnia in water [304], [4] is much lower than that of silica, it is concluded that the solubility of SiO_2 determines the corrosion of our CMCs under hydrothermal conditions.

The solubility of the water vapor in silica has been determined for oxygen and water vapor by Norton [305], demonstrating that the increased oxidation rate of silica in water vapor is three orders of magnitude higher than oxygen. That is attributed to a much greater solubility of silica in water vapor.

The corroded CMCs were investigated by means of SEM in order to understand the effect of the hydrothermal conditions on their microstructures (see Figure 3.60). As shown in Figure 3.60a (C_f/SiCN, 150 °C) and Figure 3.60c (C_f/SiCN, 250 °C), there is a significant effect of the corrosion temperature on the interface between the carbon fibers and the SiCN matrix. Thus, there is a pronounced spallation between the carbon fibers and the matrix in C_f/SiCN, which is additionally accentuated by increasing the corrosion temperature. This is considered to be due to the weak interface between C_f and SiCN (as demonstrated by the bending strength and fracture behavior of C_f/SiCN). However, no significant spallation was observed in C_f/SiHfBCN; this is consequently an effect of the tight interface between the fibers and the SiHfBCN matrix, which clearly contributes to the improved corrosion behavior of C_f/SiHfBCN CMCs as compared to that of C_f/SiCN.

Thus, the improvement in the corrosion performance of C_f/SiHfBCN is considered to rely on a synergistic effect of two parameters: i) improved corrosion kinetics due to the incorporation of Hf and B into SiCN and ii) a tight C_f/matrix interface which additionally suppresses the corrosion.

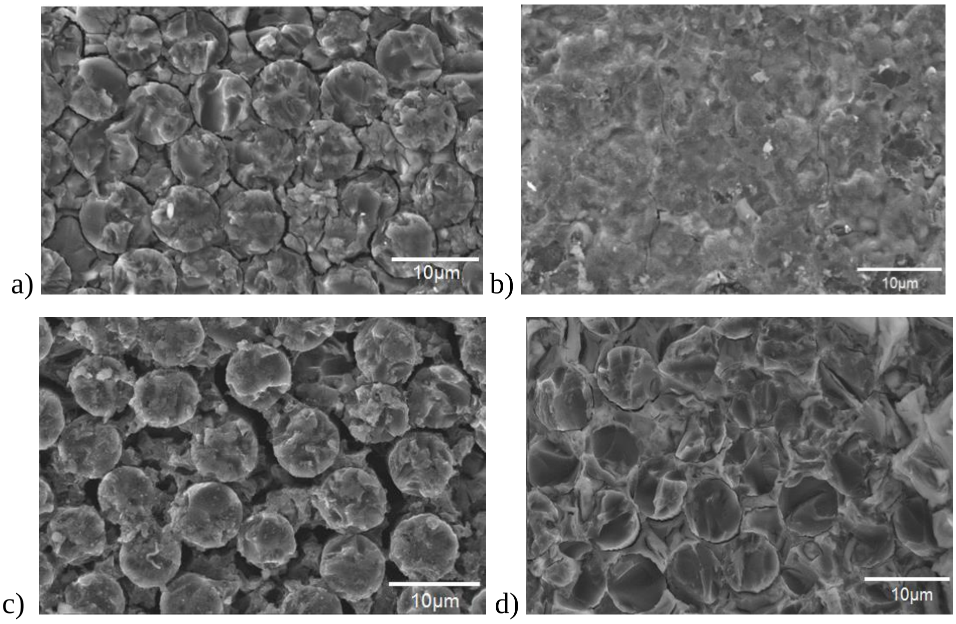

Figure 3.60. Microstructures of the CMCs upon hydrothermal corrosion at 150 and 250 °C: C_f/SiCN (a and c, respectively) and C_f/SiHfBCN (b and d, respectively).

3.5.3 Summary

Within this work, the hydrothermal corrosion of the prepared CMCs revealed that C_f/SiHfBCN CMCs exhibited better resistance than Cf/SiCN due to the improved kinetics after Hf and B incorporation. Additionally, a tight C_f/matrix interface (which is rather disadvantageous for the appropriate mechanical behavior) was found to be of additional benefit for an improved corrosion behavior in C_f/SiHfBCN.

3.6 Ablation behavior of C_f/SiHfBCN

The motivation of the study presented here was to combine these refractory materials to develop a composite with a mixed matrix (C_f/SiHfBCN) that would exhibit good ablation resistance. Therefore, it was necessary to investigate the fundamental ablation properties and mechanisms of carbon-fiber-reinforced SiHfBCN composites. The present section is mainly focused on the microstructural evolution of C_f/SiHfBCN composites exposed to laser ablation.

3.6.1 Thermodynamic analysis of C_f/SiHfBCN at ultra-high temperatures (~ 3000 °C)

The powder scraped from the tested surfaces and ablation pits were tested via X-ray diffraction analysis (Figure 3.61). The composites exhibited an amorphous nature before ablation. After ablation testing, the oxide product m-HfO_2 is believed to have formed; this product may have been generated from the HfB_2 and HfC_xN_{1-x} that were also observed in the XRD results. Moreover, the SiC phase was still present, although no SiO_2 could be detected.

The temperature for ablation testing can be estimated according to melting point of residual product, i.e., 3890 °C for HfC, 3827 °C for C, 3380 °C for HfB_2, 2987 °C for SiC and 2810°C for HfO_2, thus the temperature where the residual products located is below 2800 °C. The result is consistent with the work of M. Su *et al* [306], they has simulated the temperature distribution on the ablated surface using ANSYS 10.0 with a finite element analysis (FEA), proposing the surface temperature ranges at between 7000 °C and 2800 °C from the spot center to the edge when the diameter of the laser spot is 3 mm after ablated for 0.5 second.

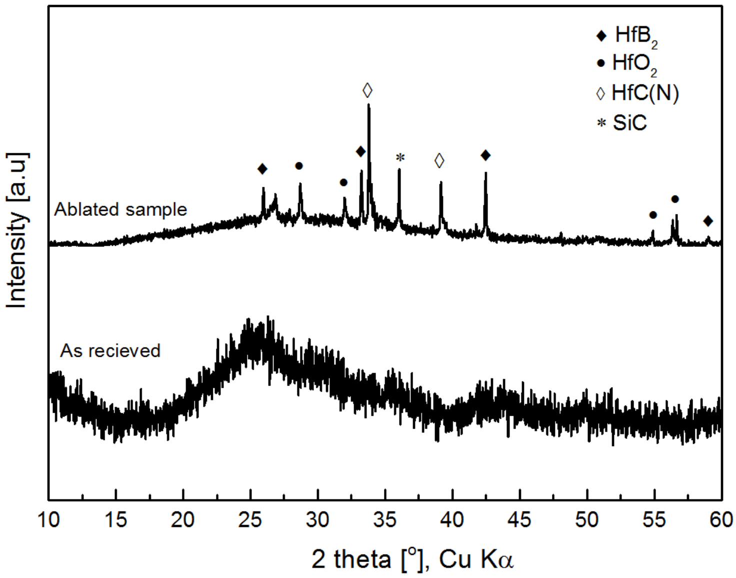

Figure 3.61. XRD analysis of C_f/SiHfBCN ceramic composites before and after ablation testing.

Accordingly, we conclude that the ablation of C_f/SiHfBCN in the temperature range addressed in the present study (~ 3000 °C) might proceed in accordance with the following reactions:

$C(s) = C\ (g)$ (1)
$C(s) + O_2\ (g) = CO_2\ (g)$ (2)
$C(s) + O_2\ (g) = CO\ (g)$ (3)
$SiC\ (s) = Si\ (g) + C\ (s)$ (4)
$SiC\ (s) + O_2\ (g) = SiO\ (g) + CO\ (g)$ (5)
$SiC\ (s) + 3/2\ O_2\ (g) = SiO_2\ (l) + CO\ (g)$ (6)
$BN\ (s) + 3/4\ O_2\ (g) = 1/2\ B_2O_3\ (g) + 1/2\ N_2\ (g)$ (7)
$HfC\ (s) + 2O_2\ (g) = HfO_2\ (s) + CO_2\ (g)$ (8)
$HfC\ (s) + 3/2\ O_2\ (g) = HfO_2\ (s) + CO\ (g)$ (9)
$HfB_2\ (s) + 5/2\ O_2\ (g) = HfO_2\ (s) + B_2O_3\ (g)$ (10)
$xSiO_2\ (l) + zHfO_2\ (s) = Si_xO_yHf_z\ (l)$ (11)

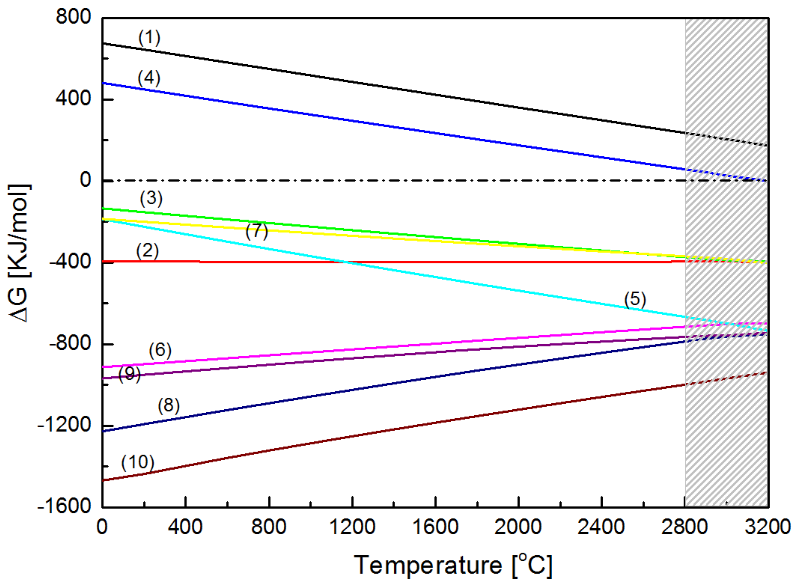

Figure 3.62. The changes in the Gibbs free energy during ablation associated with reactions (1)-(12), as calculated using Factsage. The gray shaded area represents the temperature range of the ablation experiments.

The values of the changes in the standard Gibbs free energy associated with the above reactions (ΔG_0) at various temperatures (room temperature to 3200 °C) were calculated using the Factsage software, and the results are shown in Figure 3.62. Any reaction for which the value of ΔG_0 is negative within the temperature range of interest could occur during ablation. Therefore, all of the listed reactions could have occurred above 3000 °C except for reactions (1) and (4), which require higher temperatures; in other words, they are regarded as potential reactions when the temperature is above 3000 °C. Note that reaction (11) could not be calculated because it involves the nonstoichiometric compound $Si_xO_yHf_z$. For the Hf-containing phase, HfO_2 (s) might be the main product after oxidation that is able to survive because of its very high melting point (see reactions (8)-(10)). The oxidation of the silicon-based and B-containing phases occurs in reactions (5)-(7) and (10), leading to the formation of a gas phase, i.e., B_2O_3 (g) and SiO (g), that would be emitted during the ablation process. Furthermore, it has been proven that the evaporation of SiO (g) and B_2O_3 (g) is beneficial for lowering the temperature of ablation surfaces [199], which, in turn, could improve the ablation properties of the C_f/SiHfBCN composite.

3.6.2 Microstructures of C_f/SiHfBCN ceramic composites after ablation testing

Figure 3.63 shows the morphology of the C_f/SiHfBCN composites sample after the laser ablation experiment. After ablation at such extremely high temperatures, a distinct pit (i.e., Circle 1) is clearly observed at the center of the ablation laser's target area. Based on the difference in ablation morphology, the ablated surface can be classified into three different regions: i) a visible pit located at the ablation center, named region A. Moreover, the diameter of Circle 1 is about 2.22, 2.29 and 2.38 mm corresponding to the laser ablation time of 0.2, 0.5 and 1 second respectively; ii) a transition zone with a shallow ablation step, named region B, where with the diameter of 3 mm (circle 2) is the location of the laser spot; and iii) an ablation fringe covered by a white glass layer, named region C. Furthermore, the diameter and the depth of the ablation pit increased with the prolonging testing time.

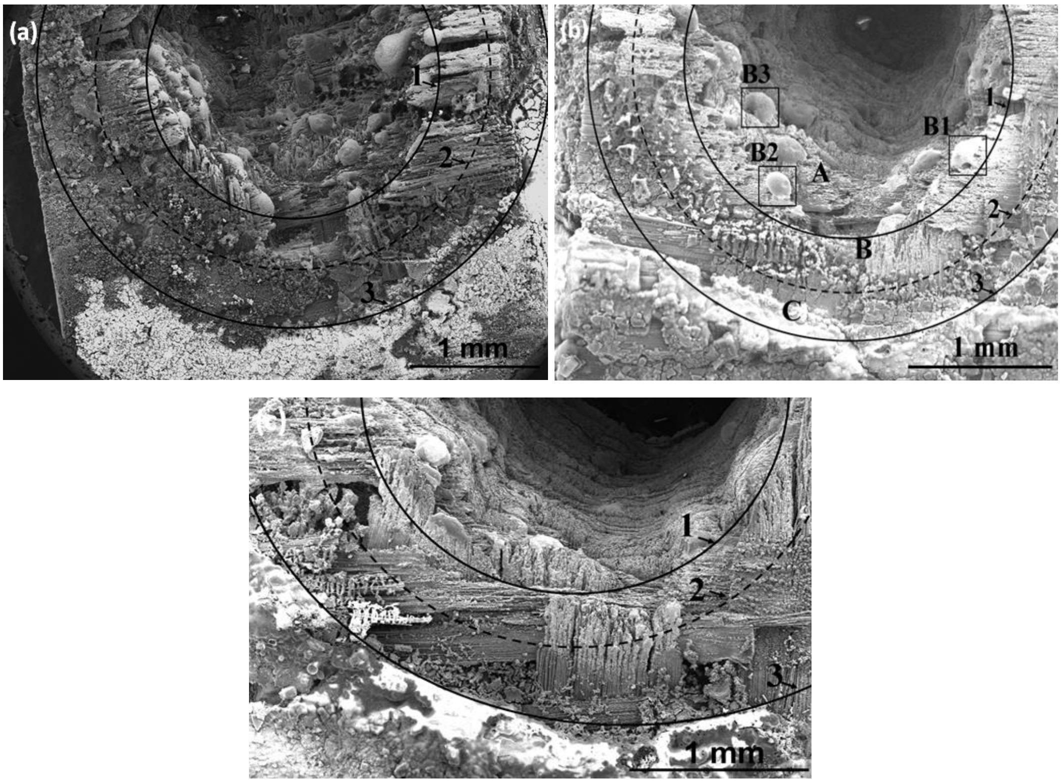

Figure 3.63. Macroscopic photograph of the ablation morphology of C_f/SiHfBCN after ablated by a 1000w laser beam for (a) 0.2 second; (b) 0.5 second and (c) 1 second.

In region A, bubble-shaped structures are typically observed, representing three different structural morphologies, as shown in Figure 3.64. The three types of bubble structures are labeled B1, B2 and B3, respectively. It was found that these bubbles adhere to the wall of the ablation pit, encapsulating the ends of the carbon fibers. As indicated in Figure 3.64a, B1 consists of a visibly cracked white scale, with no glassy phase; moreover, the EDS analysis revealed that the main elements composing the surface are C, Hf and O, indicating the presence of HfO_2. The surface of the B2 structure consists of Si, C, O and Hf, as detected with the assistance of EDS analysis; the magnified image (Figure 3.64b) shows that this surface is formed of nano-spherical grains, probably derived from flowing SiO_2 and HfO_2. The ablation center cooled within a very short time, meaning that some gaseous products (e.g., SiO and HfO) could not escape from the ablation pit and could thus be deposited as spherical particles. In contrast to the morphologies of B1 and B2, the B3 bubble morphology possesses a networked structure, as observed in the magnified image shown in Figure 3.64c; the EDS analysis of the B3 surface revealed the presence of Si, C, O and Hf, and because this continuous layer appears to be connected via glassy adhesion, we can assume it to be a glassy scale consisting of melted $SiC_xO_yHf_Z$.

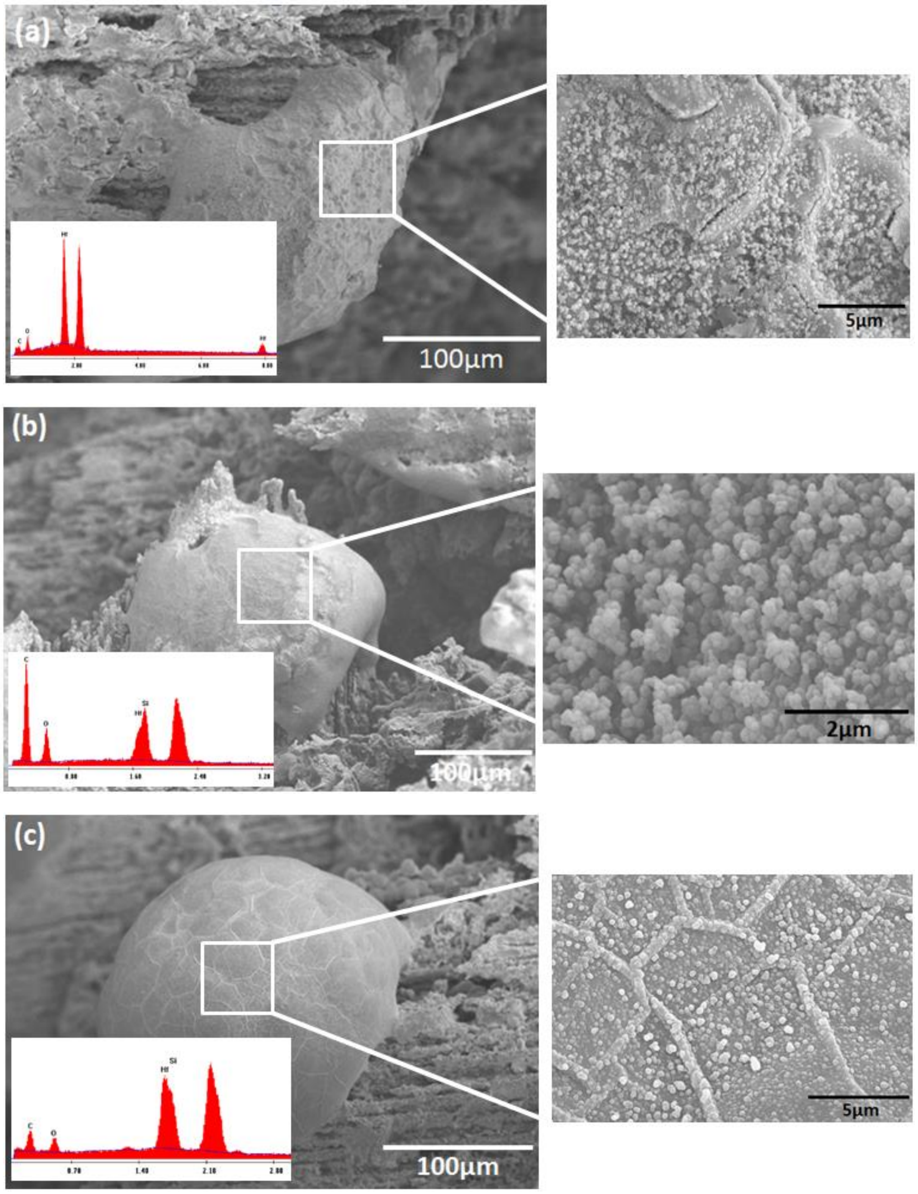

Figure 3.64. Morphologies of C_f/SiHfBCN ablated by a 1000w laser beam for 0.5 s: three types of bubble-shaped structures in the central region (region A), namely, (a) B1, (b) B2, and (c) B3.

In addition to these bubble-shaped structures, additional interesting morphologies related to the carbon fibers were observed. As indicated in Figure 3.65a, a discontinuous layer corresponding to HfC_xO_y formed on the residual matrix. Figure 3.65b and c show the eroded carbon fibers exposed after ablation in region A. In the case of C_f/SiC CMCs, because the SiC matrix and its oxidation products have boiling points lower than the flame temperature, they sublimate under ablation; thus, needle-like carbon fibers are observed after ablation [197, 307]. By contrast, the morphology of the carbon fibers in the ablated C_f/SiHfBCN material was completely different, indicating that the fibers retained their original shapes within the attached matrix. This was likely a result of the HfO_2 melting from the Hf-containing SiHfBCN, with a very high melting point (2758 °C) and high viscosity; it was difficult for this melted material to be blown away, and thus, it remained on the surfaces of the carbon fibers [197].

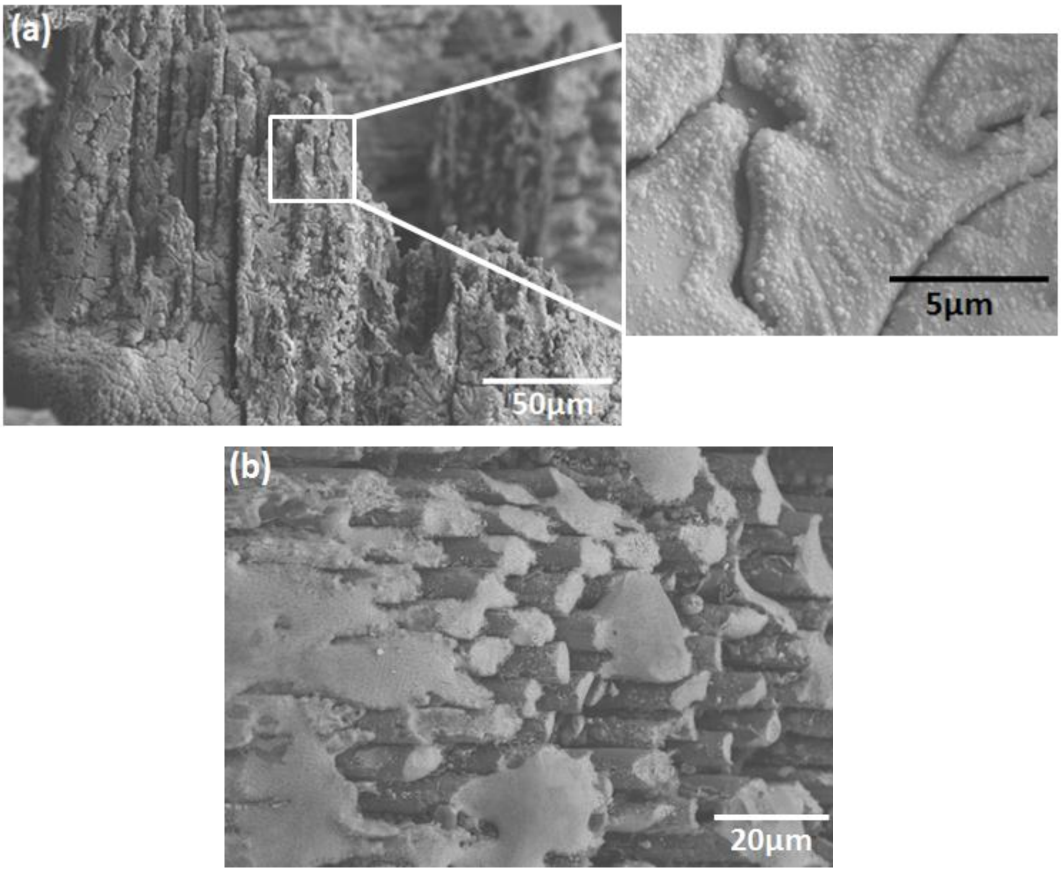

Figure 3.65. Morphologies of C_f/SiHfBCN ablated by a 1000w laser beam for 0.5 s in the central region: (a) HfO_2 covering the ends of the fibers and (b) the erosion of carbon fibers.

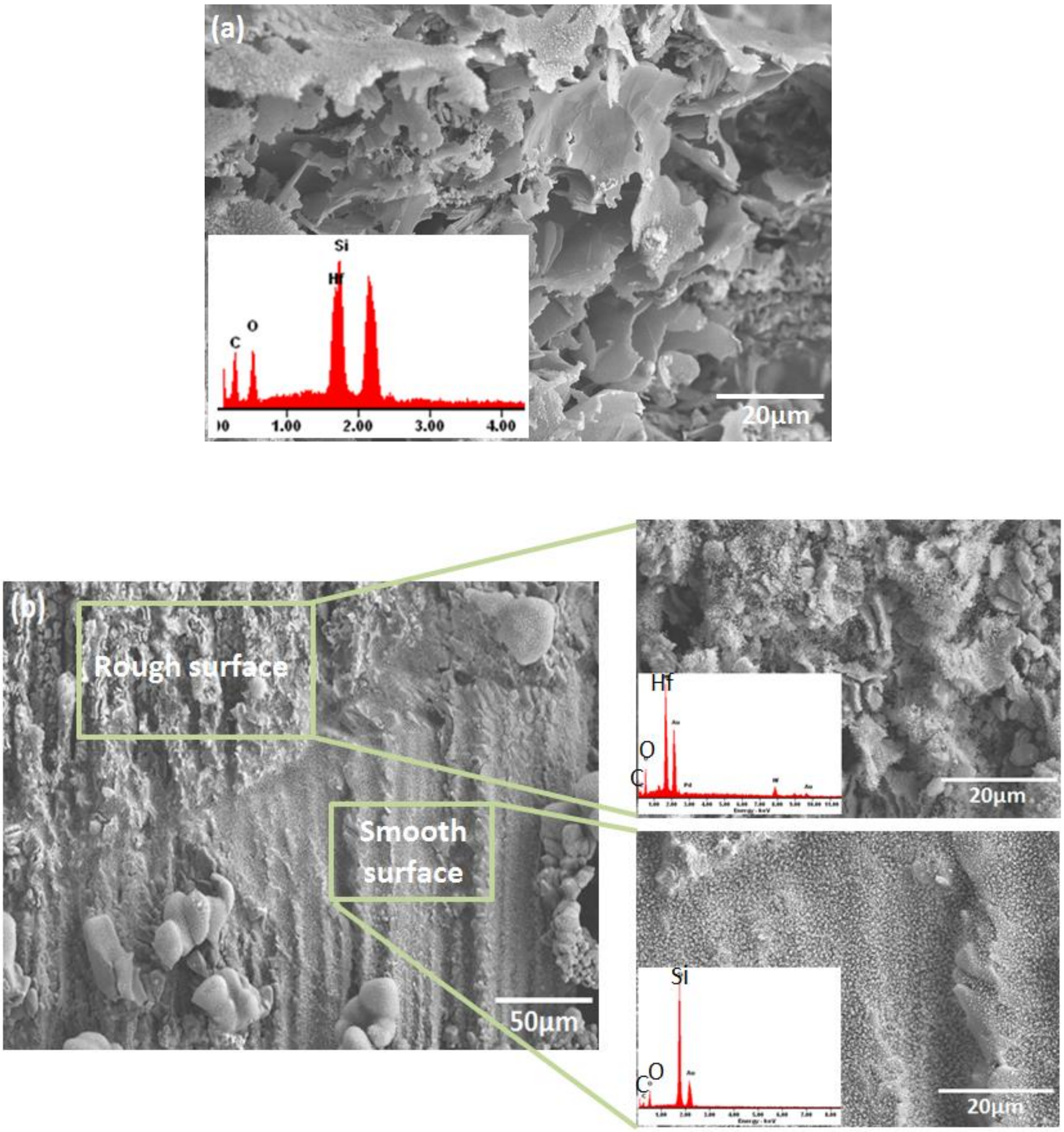

Figure 3.66. Morphologies of ablated samples for 0.5s in the transition region (region B): (a) a sheet structure and (b) rough and smooth zones.

Figure 3.66 shows SEM images of the morphology of the ablated surface in the transition region. A sheet-like morphology could be observed, as shown in Figure 3.66a. EDS analysis indicated that these sheet structures contain Si, Hf, C and O elements, suggesting the deposition of SiHfCO sheets in zone B. Furthermore, because the morphology changes significantly along the direction of the temperature gradient, it can be divided into two sub-zones: a rough zone nearer to the ablation center and a smooth zone farther from the center (Figure 3.66b). EDS analysis revealed that the main elements composing the smooth zone are Si, C and O, whereas the rough zone consists of C, Hf and O. The temperature increased from the smooth zone to the rough zone; accordingly, the viscosity of the SiO_2 decreased and the volatilization rate of the gas-phase SiO simultaneously increased, allowing SiO_2 to flow into the adjacent region. However, the disappearance of the SiO_2 allowed the HfC to be exposed to the laser and the air. Thus, HfC grains could grow and be subsequently oxidized. At relatively high temperatures, the amounts of HfO_2 and HfC present would remain constant. As a consequence, only Hf, C, and O were observed in the rough zone, whereas Si was observed in the smooth zone instead of Hf.

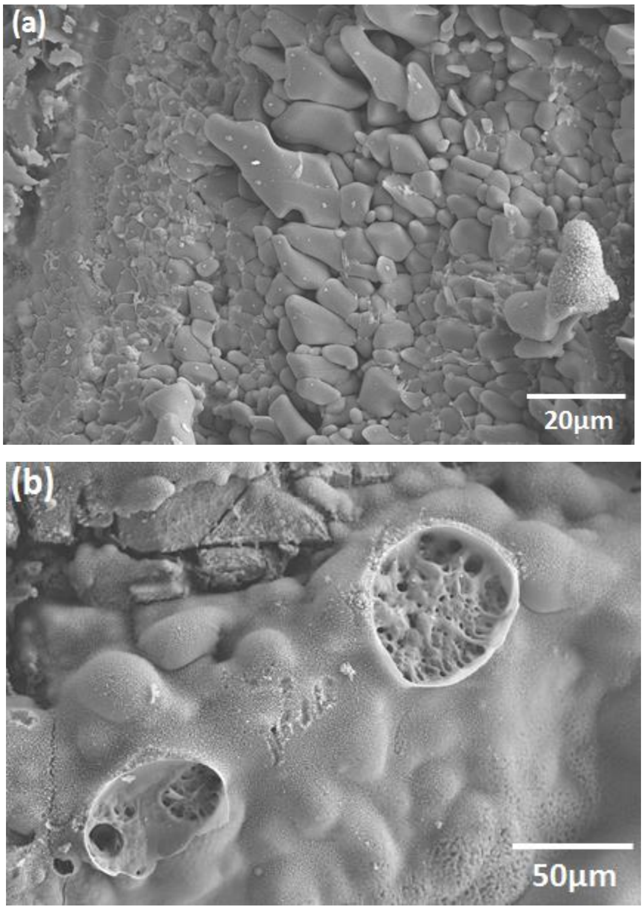

Figure 3.67. Morphologies of the ablation samples for 0.5s in the fringe region (region C): (a) the SiC grains and (b) the SiO_2 glass layer.

In the fringe region, region C, both grain (Figure 3.67a) and bubble (Figure 3.67b) morphologies were observed. Interestingly, the grains in the fringe region corresponding to SiC grew larger than those in the adjacent region. This observation is consistent with reports of increasing grain size with increasing temperature [308]. Continuous bubbling with a glass layer, identified as SiO_2 glass, was indicated. Because the temperature was not sufficiently high for SiO_2 evaporation in this region, the liquid SiO_2 formed a dense layer on the ablated surface. Furthermore, most of the bubbles identified as SiO (g) and B_2O_3 (g) might have been retained because of the presence of high-viscosity SiO_2 in this fringe region.

3.6.3 Ablation mechanism of C_f/SiHfBCN ceramic composites

Because the heat flow of a laser follows a Gaussian distribution, the ablation mechanism for C_f/SiHfBCN can be understood based on the differences in the observed surface morphologies and microstructures.

During the initial stage, when the surface temperature of the specimen is relatively low, the situation is similar to that in the ablation fringe region. In this stage, the oxidation of the SiHfBCN matrix is the primary ablation mechanism. From 500 °C to 1500 °C, silicon-based ceramics oxidize into SiO_2, which is expected to significantly protect the matrix below from oxidation because of its outstanding oxygen isolation ability below 1500 °C [309]. The ablation product SiO_2 melts and flows into the adjacent region. Solid products such as silica, borosilicate, and porous hafnium oxide and volatile products such as SiO (g) and B_2O_3 (g) could also be formed at this stage. Pores or bubbles would remain in the SiO_2 glass layer because of the emission of gaseous products. Because the oxidation temperature of HfC is lower than that of SiC, the SiC content is higher than the HfC content in the outer ablation surface. Once the HfC is oxidized, the rest will be protected by flowing SiO_2. Thus, the presence of HfC or HfO_2 is barely detectable in the fringe region. However, the surface temperature of the central region increases more rapidly than that of the fringe region because of the Gaussian nature of the beam. Thus, chemical oxidation occurs together with erosion in the central region. Considering the complexity of the ablation reaction, the suggested mechanism can be summarized as follows (Figure 3.68):

i) In the central region (i.e., inside Circle 1), evaporated SiO (g) and B_2O_3 (g) flow into adjacent regions, and the outer surface becomes depleted of these materials due to the strong flow, generating more HfO_2. Furthermore, a newly condensed liquid layer of SiO_2(l) forms beneath the eroded layer as a result of the re-oxidization of the SiO (g) that was released from inside the bulk because of the higher partial pressure of oxygen and the lower viscosity of SiO_2 [12, 310]. Then, this liquid will also tend to flow into adjacent areas, sealing the pores of the matrix and the porous HfO_2. Additionally, the SiO_2 (l) dissolves part of the HfO_2 (s) to form a hafnium-containing silicate liquid, $Si_xO_yHf_z$ (l) (see Figure 3.64c), as described by reaction (12). These refractory phases protect the carbon from being directly eroded, and the $Si_xO_yHf_z$ provides the fibers with better protection from oxidation than do the pure SiO_2 (l) and porous HfO_2, although the HfO_2 (s) does provide a framework for supporting the liquid $Si_xO_yHf_z$. However, with further denudation, the carbon fibers begin to be eroded via decomposition or sublimation (Figure 3.65b and c) when the refractory oxide (e.g., HfO_2 and $Si_xO_yHf_z$) reaches its limit.

ii) In the transition region (i.e., between Circle 1 and Circle 2), relatively low temperatures are produced compared with the central region. However, gas vapors originating from the central region imposes additional pressure on this region; thus, the laser ablation in this region is affected by the physical and chemical erosion processes occurring in the central region (i.e., the erosion of the fibers, matrix and oxidation products). Therefore, sheets of carbon peel off from the eroded fibers, revealing hafnium oxycarbide and SiC particles.

iii) The fringe region (i.e., between Circle 2 and Circle 3) experiences the lowest ablation temperature compared with the other two regions; thus, a SiO_2 glass layer forms, with bubbles corresponding to SiO (g) and B_2O_3 (g).

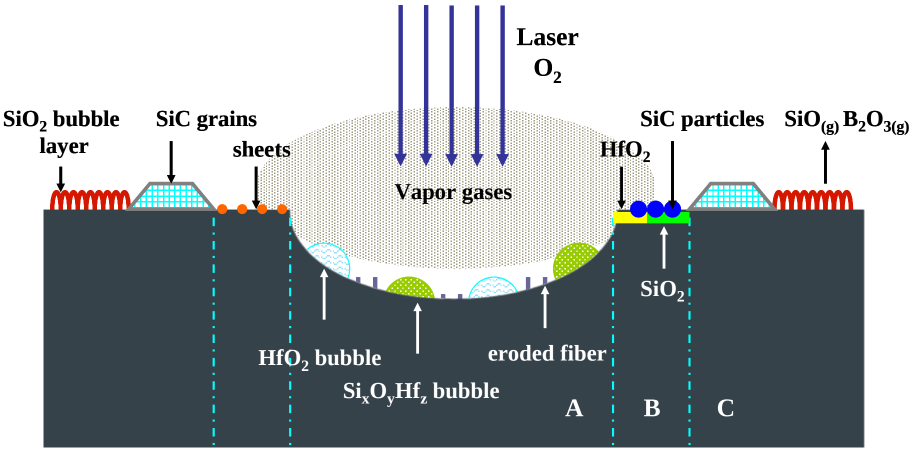

A: center region; B: transition region; C: fringe region

Figure 3.68. Schematic representation of the ablation mechanism for C_f/SiHfBCN composites.

3.6.4 Summary

The ablation behavior of C_f/SiHfBCN ceramic composites was investigated by means of a laser ablation test with duration of 1 s. A thermodynamic analysis based on ΔG calculations indicated the formation of SiO_2, HfO_2 and $Si_xO_yHf_z$ as ablation products. Furthermore, the formation of gas phases, such as SiO (g) and B_2O_3 (g), allows for heat transfer, thus lowering the temperature of the ablation surface. The microstructures of ablated CMCs revealed various ablation processes contributing to the formation of three distinct ablation regions: i) central region: oxidation and erosion of carbon fibers and the SiHfBCN matrix, accompanied by the formation of HfO_2 and $Si_xO_yHf_z$ and the evaporation of SiO (g) and B_2O_3 (g), which then flow into adjacent regions; ii) transition region: carbon and hafnium oxycarbide and SiC particles peeling off from the eroded fibers and oxide products blown away by gas vapors; iii) fringe region: high-viscosity liquid SiO_2 forming a bubbled glass layer.

4. CONCLUSION

In the research reported in this thesis, novel amorphous Hf-containing ceramics were synthesized from SSPs, followed by inorganic conversion through thermal pyrolysis (up to 1100 °C) and subsequent transformation into Hf-containing UHTC-NCs with promising compositions upon sintering at high temperatures. The Hf-containing SSPs could be shaped into dense ceramic monoliths via PLS and SPS. The results demonstrated that dense amorphous SiHfBCN ceramic monoliths could be achieved upon annealing in nitrogen at 1300 °C. Dense Hf-containing ceramic nanocomposites were also successfully obtained via SPS techniques at a high temperature (~1950 °C), a very fast heating rate (~450 °C/min) and a high pressure (≥100 MPa). Furthermore, SiHfBCN-based ceramic matrix composites reinforced with carbon fibers, namely, C_f/SiHfBCN composites, were fabricated by the PIP process, suggesting that the novel SiHfBCN SSPs could be utilized for the preparation of CMC materials. The behavior of these Hf-containing UHTC materials was investigated with regard to their potential application in harsh environments. The results indicated that Hf-containing ceramics and ceramic composites may serve as potential candidates for UHTC-NC materials to be used under extreme conditions (oxidation, hydrothermal corrosion and ablation). The following discussion summarizes the results of this dissertation.

In the context of the synthesis of Hf-containing UHTC-NCs, the structural characterization of Hf-containing SSPs and the mechanisms of the conversion from polymer to ceramic and high-temperature decomposition and crystallization were discussed. The synthesis of SiHfCN started with a commercial precursor, HTT1800 polysilazane, which was reacted with $Hf(N(Et)_2)_4$ through a substitution reaction between Si-H/N-H and ≡Hf-N-$(Et)_2$. A decrease in N-H/Si-H groups was observed by means of FT-IR and NMR spectroscopy, indicating the formation of the SiHfCN SSPs through Hf-N-Si linkages. An additional hydroboration reaction between the $BH_3{\cdot}SMe_2$ and vinyl groups of HTT1800 led to the formation of the SiHfBCN SSPs. Furthermore, a ^{29}Si NMR study of SiHfBCN cross-linked at 200 °C revealed that the chemical shifts of all signals were shifted towards lower field as compared with those of SiCN-based materials, confirming the formation of Hf-N-Si. An investigation of the inorganic conversion of SiHfCN and SiHfBCN suggested similar structural development, indicating that the evolution of structure predominantly occurs between 400 and 800 °C. Hydrocoupling, transamination and hydrosilylation reactions, among others, cause the polymers to develop into amorphous ceramics that consist of tetrahedral by coordinated Si-atoms (i.e., SiC_4, $SiCN_3$ and SiN_4), HfC_xN_{1-x}, segregated carbon, and additional BC_xN_{3-x} (only for SiHfBCN). Interestingly, the presence of Hf and B within the molecular structure of the single-source precursor leads to low-temperature phase separation, as indicated by the analyzed SiC_4 units formed at 800 °C, which is not common in B- and Hf-free SiCN ceramics at the same temperature. Furthermore, Hf and B seem to facilitate crystallization upon annealing at higher temperatures and thus allow for the preparation of UHTC-NCs with phase compositions suitable for applications at ultra-high temperatures and under harsh conditions. In the case of SiHfCN, $HfC_{0.56}N_{0.44}$ and β-SiC nanocomposites are generated upon annealing at 1500 °C in both argon and nitrogen. Moreover, the annealing atmosphere was found to affect the crystallization behavior found in SiHfBCN annealed at 1700 °C, with HfB_2, $HfC_{0.78}N_{0.22}$, and β-SiC nanocomposites forming upon annealing in argon and $HfN_{0.52}C_{0.48}$, Si_3N_4, SiBCN, and C nanocomposites forming upon annealing in nitrogen. These results demonstrate that the conversion of single-phase SiHfCN and SiHfBCN into UHTC-NCs is thermodynamically controlled. Additionally, the incorporation of Hf and B into SiCN results in outstanding high temperature stability with respect to decomposition: the mass losses of SiHfBCN annealed at 1700 °C in nitrogen were found to be below 5 wt%, representing a significant improvement compared with SiCN annealed under identical conditions, which exhibited a mass loss of approximately 30%.

We developed several types and classes of (ultra)-high-temperature materials, such as dense amorphous ceramic monoliths, dense UHTC-NC ceramic monoliths and CMCs derived from SiHfBCN SSPs. The parameters were optimized for the preparation of dense amorphous ceramic monoliths, motivated by the fact that the SiHfBCN1 sample (low Hf content) with the lowest porosity (5.9 %) was achieved upon annealing in nitrogen at 1300 °C. Dense SiHfCN- and SiHfBCN-based UHTC-NCs were successfully prepared by means of a rapid sintering procedure (i.e., a high heating rate of ~450 °C/min) at a high pressure ($\geq$100 MPa). Both materials exhibited fine microstructures, with grains sizes well below 200 nm for the HfC_xN_{1-x} phase and below 100 nm for SiC and Si_3N_4. Both prepared types of UHTC-NCs exhibited superior mechanical properties compared with other polymer-derived ceramics as a result of their phase compositions and fine microstructures. Moreover, C_f/SiHfBCN and C_f/SiCN were fabricated using the polymer (SiHfBCN and SiCN) infiltration pyrolysis (PIP) approach. Their open porosity could be controlled below 10 vol% by means of an 8-cycle fabrication procedure. The interface between C_f and SiHfBCN was found to be stronger than that between C_f and SiCN, resulting in brittle fracture behavior rather than the fiber pull-out mechanism observed in C_f/SiCN. Accordingly, to provide a weak interface, pyrolytic carbon was deposited via CVI prior to the infiltration of polymer precursors, leading to the formation of C_f/SiC/SiHfBCN and C_f/SiC/SiCN via combination of CVI and PIP-techniques. These CMCs exhibited improved mechanical properties compared with C_f/SiHfBCN and C_f/SiCN.

The subsequent studies of the presented research addressed the behavior of PDCs, UHTC-NCs, and CMCs in harsh environments (oxidative, corrosive and ablative conditions). The oxidation behavior of amorphous SiCN, SiHfCN and SiHfBCN ceramic powders was investigated via TGA, and the results revealed that all samples obeyed parabolic kinetics. A comparison of the oxidation kinetics based on the $(\Delta m/(S_{BET}\times m))^2$ *vs.* T relation indicated that SiCN demonstrates the best oxidation resistance and that SiHfBCN exhibits significantly improved oxidation kinetics compared with SiHfCN. The oxidation behavior of dense amorphous SiHfBCN ceramic monoliths (modified with 10 vol% and 30 vol% hafnium complexes, namely, SiHfBCN1 and SiHfBCN2) was also investigated with regard to their oxidation kinetics and the microstructural evolution of their oxidic scales at 1200-1400 °C. The parabolic rate of SiHfBCN1 was found to be lower than that of SiHfBCN2 at 1200 and 1300 °C, whereas that of SiHfBCN2 was shown to be slightly lower than that of SiHfBCN1 at 1400 °C. This may be a consequence of the differences in porosity, boria evaporation and outward diffusion of other gases (e.g., CO and N_2) between the two compositions. XRD, SEM and EPMA investigations suggested that a continuous oxidation layer consisting of hafnia and borosilicate or silica forms on these materials at 1200 °C, which then becomes a discontinuous layer with a composition of silica, hafnia and $HfSiO_4$ as the temperature increases (> 1300 °C). Accordingly, the wide range of E_a values (174 ± 57.7 and 139.7 ± 39 KJ mol^{-1} for SiHfBCN1 and SiHfBCN2, respectively) derived from the parabolic kinetic analyses may be the result of a wide variety of oxygen-controlling mechanisms, including inward oxygen transport into the complex oxide scale (borosilicate or silica, hafnia, and hafnium silicate) and the outward transport of gases produced via the oxidation reaction. However, the oxidation rates of amorphous ceramic monoliths were rather uncertain because of the uncertainty in the value of geometric surface area. Thus, the oxidation behavior of dense UHTC-NCs prepared via SPS was also investigated and compared. The oxidation behavior of SiHfCN was found to be comparable to that of other UHTCs. By contrast, SiHfBCN exhibits outstanding oxidation resistance at temperatures of up to 1500 °C (with a weight gain of 0.16 $mg \cdot cm^{-2}$), and moreover, the parabolic rate of SiHfBCN (3.6×10^{-4} $mg \cdot cm^{-2} \cdot h^{-1}$) was shown to be 3-4 orders of magnitude lower than that of SiHfCN (0.4 $mg \cdot cm^{-2} \cdot h^{-1}$) and even lower than the values reported for SiC ceramics.

Furthermore, the C_f/SiHfBCN CMCs exhibited enhanced hydrothermal corrosion resistance than C_f/SiCN because of their improved corrosion kinetics due to Hf and B incorporation. Additionally, a tight C_f/matrix interface (which is rather disadvantageous with respect to mechanical behavior) was found to be of further benefit in improving the corrosion behavior of C_f/SiHfBCN. The ablation behavior of C_f/SiHfBCN ceramic composites was investigated in a laser ablation test. A model of the morphology of the prepared CMCs after ablation was developed based on our observations. Various ablation processes were considered to contribute to the formation of three distinct ablation regions: i) central region: oxidation and erosion of carbon fibers and SiHfBCN matrix, accompanied by the formation of HfO_2 and $Si_xO_yHf_z$ and the evaporation of SiO (g) and B_2O_3 (g), which then flow into adjacent regions; ii) transition region: sheets of carbon peeling off from the eroded fibers, which are then blown away by gas vapors; iii) fringe region: high-viscosity liquid SiO_2 forming a layer of glass with bubbles containing B_2O_3 and SiO gases.

5. OUTLOOK

This thesis presents a systematic study of the synthesis and characterization of Hf-containing UHTC-NCs formed form SSPs. Furthermore, it also presents an investigation of the properties of novel Hf-containing ceramic monoliths (i.e., amorphous ceramics and UHTC-NC monoliths) and CMCs subjected to harsh environments. The oxidation behavior, hydrothermal corrosion and ablation behavior of these novel materials can provide guidance for future studies. However, supplementary work will be necessary to better understand the performance of Hf-containing SiHf(B)CN and UHTC-NC materials under harsh conditions in more detail.

Future work can build on the results of this dissertation. A number of examples are provided below:

- The oxidation kinetics must be standardized to determine the thickness of the oxide scale in such a way that it can be compared with the data determined based on the specific weight gain (weight gain per specific surface area).
- UHTC-NCs derived from SiHfBCN have demonstrated excellent oxidation resistance according to in situ TGA. However, there is a limit on how long a TGA device can operate in long-term oxidation tests. Accordingly, an *ex situ* oxidation experiment performed by means of a furnace test will be needed to confirm the oxidation behavior determined via in situ TGA. Additionally, the results indicate that the prepared UHTC-NCs can withstand oxidation at 1500 °C. Moreover, it has been discovered that the precipitation of $HfSiO_4$ into SiO_2 is beneficial for increasing the viscosity of SiO_2 and the melting temperature; therefore, higher operating temperatures ($\geq$1500 °C) should be tested.
- The oxidation behavior of SiHfCN-based amorphous and UHTC-NCs was found to be improved significantly by the addition of boron. However, because of the low sensitivity of most techniques to light elements, a detailed and quantitative understanding of the presence of B_2O_3 in the glasses layer and the porous HfO_2 formed upon the oxidation of SiHfBCN-based UHTC-NCs is still lacking. This issue should be further investigated by applying advanced techniques (i.e., X-ray photoelectron spectroscopy (XPS) and secondary ion mass spectrometry (SIMS)).
- Alternatively, as suggested in previous literature, the adhesion of the oxide layer could be modified through doping with higher valence ions (e.g., Cr^{5+} and Ta^{5+}) to allow for the substitution of cation (e.g., Ta) on the Hf site in HfO_2, reducing the concentration of oxygen vacancies in the HfO_2. The resultant lower concentration of oxygen vacancies can lower the oxidation rate of Hf-containing UHTC-NCs. This procedure potentially indicates a route for synthesizing novel Hf-containing UHTC-NCs with excellent oxidation and corrosion resistance.
- If the investigated materials (e.g., dense amorphous SiHfBCN-based ceramic monoliths, UHTC-NCs, and CMCs) are to be considered for structural applications, their thermal shock resistance must be investigated in future work. However, prior to this investigation, their coefficients of thermal expansion should be also studied.
- The prepared C_f/SiC-SiCN and C_f/SiC-SiHfBCN CMCs exhibited good mechanical properties at room temperature. Furthermore, good oxidation resistance of the SiCN and SiHfBCN matrices was analyzed.

Thus, these CMCs might be interesting to consider them for application in turbine engines in steam gas environments.

6. REFERENCE

[1] Ionescu E, Papendorf B, Kleebe HJ, Poli F, Muller K, Riedel R. Polymer-Derived Silicon Oxycarbide/Hafnia Ceramic Nanocomposites. Part I: Phase and Microstructure Evolution During the Ceramization Process. J Am Ceram Soc. 2010;93(6):1774-1782.
[2] Ionescu E, Papendorf B, Kleebe HJ, Riedel R. Polymer-Derived Silicon Oxycarbide/Hafnia Ceramic Nanocomposites. Part II: Stability Toward Decomposition and Microstructure Evolution at T≥1000° C. J Am Ceram Soc. 2010;93(6):1783-1789.
[3] Ionescu E, Linck C, Fasel C, Muller M, Kleebe HJ, Riedel R. Polymer-Derived SiOC/ZrO2 Ceramic Nanocomposites with Excellent High-Temperature Stability. J Am Ceram Soc. 2010;93(1):241-250.
[4] Linck C, Ionescu E, Papendorf B, Galuskova D, Galusek D, Sajgalik P, et al. Corrosion behavior of silicon oxycarbide-based ceramic nanocomposites under hydrothermal conditions. Int J Mater Res. 2012;103(1):31-39.
[5] Kaur S, Riedel R, Ionescu E. Pressureless fabrication of dense monolithic SiC ceramics from a polycarbosilane. J Eur Ceram Soc. 2014;34(15):3571-3578.
[6] Iwamoto Y, Kikuta K, Hirano S. Synthesis of poly-titanosilazanes and conversion into Si3N4-TiN ceramics. J Ceram Soc Jpn. 2000;108(4):350-356.
[7] Ionescu E, Francis A, Riedel R. Dispersion assessment and studies on AC percolative conductivity in polymer-derived Si-C-N/CNT ceramic nanocomposites. J Mater Sci. 2009;44(8):2055-2062.
[8] Wang YG, An LN, Fan Y, Zhang LG, Burton S, Gan ZH. Oxidation of polymer-derived SiAlCN ceramics. J Am Ceram Soc. 2005;88(11):3075-3080.
[9] Riedel R, Kienzle A, Dressler W, Ruwisch L, Bill J, Aldinger F. A silicoboron carbonitride ceramic stable to 2,000 degrees C. Nature. 1996;382(6594):796-798.
[10] Wuchina E, Opila E, Opeka M, Fahrenholtz W, Talmy I. UHTCs: ultra-high temperature ceramic materials for extreme environment applications. Electrochem Soc Interface. 2007;16(4):30.
[11] Carney CM. Oxidation resistance of hafnium diboride-silicon carbide from 1400 to 2000 °C. J Mater Sci. 2009;44(20):5673-5681.
[12] Opeka MM, Talmy IG, Zaykoski JA. Oxidation-based materials selection for 2000 °C+ hypersonic aerosurfaces: Theoretical considerations and historical experience. J Mater Sci. 2004;39(19):5887-5904.
[13] Wuchina E, Opeka M, Causey S, Buesking K, Spain J, Cull A, et al. Designing for ultrahigh-temperature applications: The mechanical and thermal properties of HfB2, HfCx , HfNx and α Hf(N). J Mater Sci. 2004;39(19):5939-5949.
[14] Roy R, Roy R. Diphasic xerogels: I. Ceramic-metal composites. Mater Res Bull. 1984;19(2):169-177.
[15] Gleiter H. Nanocrystalline materials. progress in Materials Science. 1989;33(4):223-315.
[16] Newnham RE, Skinner DP, Cross LE. Connectivity and piezoelectric-pyroelectric composites. Mater Res Bull. 1978;13(5):525-536.
[17] Komarneni S. Nanocomposites. J Mater Chem. 1992;2(12):1219-1230.
[18] Spear KE, Visco S, Wuchina EJ, Wachsman ED. High temperature materials. Electrochem Soc Interface. 2006:49.
[19] Brewer L. Thermodynamic Properties of the Oxides and their Vaporization Processes. Chem Rev. 1953;52(1):1-75.
[20] Wuchina EJ, Opeka MM, Nswccd WB. The oxidation behavior of HfC, HfN, and HfB2. High Temperature Corrosion and Materials Chemistry III: Proceedings of the International Symposium, vol. 2001: The Electrochemical Society; 2001. p. 136.
[21] Cheng L, Xu Y, Zhang L, Luan X. Corrosion of a 3D-C/SiC composite in salt vapor environments. Carbon. 2002;40(6):877-882.
[22] Jacobson NS, Morscher GN, Bryant DR, Tressler RE. High-Temperature Oxidation of Boron Nitride: II, Boron Nitride Layers in Composites. J Am Ceram Soc. 1999;82(6):1473-1482.
[23] Koh Y-H, Lee S-Y, Kim H-E. Oxidation Behavior of Titanium Boride at Elevated Temperatures. J Am Ceram Soc. 2001;84(1):239-241.
[24] Mitsuo A, Uchida S, Nihira N, Iwaki M. Improvement of high-temperature oxidation resistance of titanium nitride and titanium carbide films by aluminum ion implantation. Surf Coat Tech. 1998;103–104(0):98-103.
[25] Monteverde F, Bellosi A. Oxidation behavior of titanium carbonitride based materials. Corros Sci. 2002;44(9):1967-1982.
[26] Dokumaci E, Özkan I, Özyigit MB, Önay B. Effect of boronizing on the oxidation of niobium. Int J Refract Met H. 2013;41(0):276-281.

[27] Shi L, Gu Y, Chen L, Yang Z, Ma J, Qian Y. Synthesis and oxidation behavior of nanocrystalline niobium carbide. Solid State Ionics. 2005;176(7–8):841-843.
[28] Kaufman L, Clougherty EV. Investigation of boride compounds for very high temperature applications. DTIC Document; 1963.
[29] Clougherty EV, Kalish D, Peters ET. Research and development of refractory oxidation resistant diborides. DTIC Document; 1968.
[30] Hinze J, Tripp W, Graham H. The High-Temperature Oxidation Behavior of a HfB2+ 20 vol% SiC Composite. J Electrochem Soc. 1975;122(9):1249-1254.
[31] Talmy IG, Zaykoski JA, Opeka MM, Dallek S. Oxidation of ZrB2 ceramics modified with SiC and group IV–VI transition metal diborides. Elec Chem Soc Proc, vol. 122001. p. 144-158.
[32] Chantrell P, Popper P. Inorganic polymers and ceramics. Special Ceramics. 1965:67.
[33] Production of shaped articles of homogeneous mixtures of silicon carbide and nitride. US Patent 3,853,567; 1974.
[34] Yajima S, Okamura K, Hayashi J, Omori M. Synthesis of continuous SiC fibers with high tensile strength. J Am Ceram Soc. 1976;59(7-8):324-327.
[35] Yajima S, Hasegawa Y, Okamura K, Matsuzawa T. Development of high tensile strength silicon carbide fibre using an organosilicon polymer precursor. Nature. 1978;273:525 - 527.
[36] Hemley RJ, Crabtree GW, Buchanan MV. Materials in extreme environments. Physics today. 2009;62(11):32-37.
[37] Powell CA, Morreale BD. Materials challenges in advanced coal conversion technologies. Mrs Bulletin. 2008;33(04):309-315.
[38] Dimiduk DM, Woodward C, LeSar R, Uchic MD. Scale-Free Intermittent Flow in Crystal Plasticity. Science. 2006;312(5777):1188-1190.
[39] Niihara K. New design concept of structural ceramics—ceramic nanocomposites. Nippon seramikkusu kyokai gakujutsu ronbunshi. 1991;99(10):974-982.
[40] Bhaduri S, Bhaduri S. Recent developments in ceramic nanocomposites. JOM. 1998;50(1):44-51.
[41] Niihara K, Hirai T. Chemical vapour-deposited silicon nitride. J Mater Sci. 1976;11(4):593-603.
[42] Niihara K, Hirai T. Chemical vapour-deposited silicon nitride. J Mater Sci. 1977;12(6):1243-1252.
[43] http://www.sanken.osaka-u.ac.jp/labs/scm/about_resE.html.
[44] Roy R. Ceramics by the solution-sol-gel route. Science. 1987;238(4834):1664-1669.
[45] Matsuda A, Kotani Y, Kogure T, Tatsumisago M, Minami T. Transparent anatase nanocomposite films by the sol–gel process at low temperatures. J Am Ceram Soc. 2000;83(1):229-231.
[46] Komarneni S, Roy R, Selvaraj U, Malla PB, Breval E. Nanocomposite aerogels: The SiO2–Al2O3 system. J Mater Res. 1993;8(12):3163-3167.
[47] Osterholtz FD, Pohl ER. Kinetics of the hydrolysis and condensation of organofunctional alkoxysilanes: a review. J Adhes Sci Technol. 1992;6(1):127-149.
[48] Xiao TD, Gonsalves KE, Strutt PR. Synthesis of aluminum nitride/boron nitride composite materials. J Am Ceram Soc. 1993;76(4):987-992.
[49] Negita K. Effective sintering aids for silicon carbide ceramics: reactivities of silicon carbide with various additives. J Am Ceram Soc. 1986;69(12):308-310.
[50] Ziegler G, Heinrich J, Wötting G. Relationships between processing, microstructure and properties of dense and reaction-bonded silicon nitride. J Mater Sci. 1987;22(9):3041-3086.
[51] Miele P, Bernard S, Cornu D, Toury B. Recent developments in Polymer-Derived ceramic fibers (PDCFs): Preparation, properties and applications–A review. Soft Mater. 2007;4(2-4):249-286.
[52] Torrey JD, Bordia RK. Mechanical properties of polymer-derived ceramic composite coatings on steel. J Eur Ceram Soc. 2008;28(1):253-257.
[53] Jones R, Szweda A, Petrak D. Polymer derived ceramic matrix composites. Compos Part A-Appl S. 1999;30(4):569-575.
[54] Fritz G, Raabe B. Bildung siliciumorganischer verbindungen. V. Die thermische zersetzung von Si (CH3) 4 und Si (C2H5) 4. Z Anorg Allg Chem. 1956;286(3-4):149-167.
[55] Colombo P, Mera G, Riedel R, Soraru GD. Polymer-Derived Ceramics: 40 Years of Research and Innovation in Advanced Ceramics. J Am Ceram Soc. 2010;93(7):1805-1837.
[56] Czekaj CL, Hackney ML, Hurley WJ, Interrante LV, Sigel GA, Schields PJ, et al. Preparation of silicon carbide/aluminum nitride ceramics using organometallic precursors. J Am Ceram Soc. 1990;73(2):352-357.

[57] Paine R, Janik J, Fan M. Some recent developments in precursor routes to ceramic nanocomposites. Polyhedron. 1994;13(8):1225-1232.

[58] Seyferth D, Bryson N, Workman DP, Sobon CA. Preceramic Polymers as “Reagents” in the Preparation of Ceramics. J Am Ceram Soc. 1991;74(10):2687-2689.

[59] Seyferth D, Lang H, Sobon CA, Borm J, Tracy HJ, Bryson N. Chemical modification of preceramic polymers: Their reactions with transition metal complexes and transition metal powders. J Inorg Organomet P. 1992;2(1):59-77.

[60] Greil P. Active-Filler-Controlled Pyrolysis of Preceramic Polymers. J Am Ceram Soc. 1995;78(4):835-848.

[61] Cordelair J, Greil P. Electrical Characterization of Polymethylsiloxane/MoSi2-Derived Composite Ceramics. J Am Ceram Soc. 2001;84(10):2256-2259.

[62] Hauser R, Francis A, Theismann R, Riedel R. Processing and magnetic properties of metal-containing SiCN ceramic micro- and nano-composites. J Mater Sci. 2008;43(12):4042-4049.

[63] Interrante LV, Schmidt WR, Marchetti PS, Maciel GE. Preparation of Non-Oxide Ceramics by Pyrolysis of Organometallic Precursors. MRS Online Proceedings Library. 1992;271:739.

[64] Schmidt WR, Hurley WJ, Sukumar V, Doremus RH, Interrante LV. Polymer-Derived Si3N4/BN Composites. MRS Online Proceedings Library. 1989;171:79.

[65] Su K, Remsen EE, Zank GA, Sneddon LG. Synthesis, characterization, and ceramic conversion reactions of borazine-modified hydridopolysilazanes: new polymeric precursors to silicon nitride carbide boride (SiNCB) ceramic composites. Chem Mater. 1993;5(4):547-556.

[66] Babonneau F, Sorarú GD, Thorne KJ, Mackenzie JD. Chemical Characterization of Si-Al-C-O Precursor and Its Pyrolysis. J Am Ceram Soc. 1991;74(7):1725-1728.

[67] Babonneau F, Sorarù GD. Synthesis and characterization of Si-Zr-C-O ceramics from polymer precursors. J Eur Ceram Soc. 1991;8(1):29-34.

[68] Ishikawa T, Kajii S, Matsunaga K, Hogami T, Kohtoku Y, Nagasawa T. A Tough, Thermally Conductive Silicon Carbide Composite with High Strength up to 1600°C in Air. Science. 1998;282(5392):1295-1297.

[69] Ishikawa T, Kohtoku Y, Kumagawa K. Production mechanism of polyzirconocarbo- silane using zirconium(IV)acetylacetonate and its conversion of the polymer into inorganic materials. J Mater Sci. 1998;33(1):161-166.

[70] Yamamura T, Ishikawa. A new type of ceramic matrix composite using Si-Ti-CO fiber. 13th Annual Conference on Composites and Advanced Ceramic Materials, Part 1 of 2: Ceramic Engineering and Science Proceedings, Volume 10: John Wiley & Sons; 2009. p. 736.

[71] Mishra R, Tiwari RK, Saxena AK. Synthesis of Fe–SiC Nanowires via Precursor Route. J Inorg Organomet Polym. 2009;19(2):223-227.

[72] Iwamoto Y, Kikuta K-I, Hirano S-I. Synthesis of poly-titanosilazanes and conversion into Si3N4-TiN ceramics. J Ceram Soc Jpn. 2000;108(4):350-356.

[73] Papendorf B, Nonnenmacher K, Ionescu E, Kleebe HJ, Riedel R. Strong Influence of Polymer Architecture on the Microstructural Evolution of Hafnium-Alkoxide-Modified Silazanes upon Ceramization. Small. 2011;7(7):970-978.

[74] Ionescu E, Kleebe HJ, Riedel R. Silicon-containing polymer-derived ceramic nanocomposites (PDC-NCs): preparative approaches and properties. Chem Soc Rev. 2012;41(15):5032-5052.

[75] Widgeon S, Mera G, Gao Y, Stoyanov E, Sen S, Navrotsky A, et al. Nanostructure and Energetics of Carbon-Rich SiCN Ceramics Derived from Polysilylcarbodiimides: Role of the Nanodomain Interfaces. Chem Mater. 2012;24(6):1181-1191.

[76] Glatz G, Schmalz T, Kraus T, Haarmann F, Motz G, Kempe R. Copper-Containing SiCN Precursor Ceramics (Cu@SiCN) as Selective Hydrocarbon Oxidation Catalysts Using Air as an Oxidant. Chem-Eur J. 2010;16(14):4231-4238.

[77] Zaheer M, Motz G, Kempe R. The generation of palladium silicide nanoalloy particles in a SiCN matrix and their catalytic applications. J Mater Chem. 2011;21(46):18825-18831.

[78] Lengauer W. Transition Metal Carbides, Nitrides, and Carbonitrides. Handbook of Ceramic Hard Materials: Wiley-VCH Verlag GmbH; 2008. p. 202-252.

[79] Córdoba JM, Sayagués MJ, Alcalá MD, Gotor FJ. Monophasic Nanostructured Powders of Niobium, Tantalum, and Hafnium Carbonitrides Synthesized by a Mechanically Induced Self-Propagating Reaction. J Am Ceram Soc. 2007;90(2):381-387.

[80] Sacks MD, Wang C-A, Yang Z, Jain A. Carbothermal reduction synthesis of nanocrystalline zirconium carbide and hafnium carbide powders using solution-derived precursors. J Mater Sci. 2004;39(19):6057-6066.

[81] Sarkar S, Miller A, Mueller J. Solubility of oxygen in ZrC. J Am Ceram Soc. 1972;55(12):628-630.
[82] Lengauer W, Binder S, Aigner K, Ettmayer P, Guillou A, Debuigne J, et al. Solid state properties of group IVb carbonitrides. J Alloy Compd. 1995;217(1):137-147.
[83] Opeka MM, Talmy IG, Wuchina EJ, Zaykoski JA, Causey SJ. Mechanical, Thermal, and Oxidation Properties of Refractory Hafnium and zirconium Compounds. J Eur Ceram Soc. 1999;19(13–14):2405-2414.
[84] Kral C, Lengauer W, Rafaja D, Ettmayer P. Critical review on the elastic properties of transition metal carbides, nitrides and carbonitrides. J Alloy Compd. 1998;265(1–2):215-233.
[85] Telle R, Sigl LS, Takagi K. Boride-Based Hard Materials. Handbook of Ceramic Hard Materials: Wiley-VCH Verlag GmbH; 2008. p. 802-945.
[86] Fahrenholtz WG, Hilmas GE, Talmy IG, Zaykoski JA. Refractory diborides of zirconium and hafnium. J Am Ceram Soc. 2007;90(5):1347-1364.
[87] Post B, Glaser FW, Moskowitz D. Transition metal diborides. Acta Metallurgica. 1954;2(1):20-25.
[88] Goldstein A, Geffen Y, Goldenberg A. Boron Carbide–Zirconium Boride In Situ Composites by the Reactive Pressureless Sintering of Boron Carbide–Zirconia Mixtures. J Am Ceram Soc. 2001;84(3):642-644.
[89] Das S, Das SK, Ramachandrarao P. Sintering studies on ultrafine ZrB2 powder produced by a self-propagating high-temperature synthesis process. J Mater Res. 2000;15(11):2499-2504.
[90] Chamberlain AL, Fahrenholtz WG, Hilmas GE. Reactive hot pressing of zirconium diboride. J Eur Ceram Soc. 2009;29(16):3401-3408.
[91] Segal D. Chemical routes for the preparation of powders. The Physics and Chemistry of Carbides, Nitrides and Borides: Springer; 1990. p. 3-11.
[92] Chen L, Gu Y, Shi L, Yang Z, Ma J, Qian Y. Synthesis and oxidation of nanocrystalline HfB2. J Alloy Compd. 2004;368(1–2):353-356.
[93] Chen L, Gu Y, Yang Z, Shi L, Ma J, Qian Y. Preparation and some properties of nanocrystalline ZrB2 powders. Scripta Mater. 2004;50(7):959-961.
[94] Su K, Sneddon LG. A polymer precursor route to metal borides. Chem Mater. 1993;5(11):1659-1668.
[95] Su K, Sneddon LG. Polymer-precursor routes to metal borides: synthesis of titanium boride (TiB2) and zirconium boride (ZrB2). Chem Mater. 1991;3(1):10-12.
[96] Lönnberg B. Thermal expansion studies on the group IV–VII transition metal diborides. Journal of the Less Common Metals. 1988;141(1):145-156.
[97] Monteverde F. Progress in the fabrication of ultra-high-temperature ceramics:“in situ” synthesis, microstructure and properties of a reactive hot-pressed HfB2/SiC composite. Compos Sci Technol. 2005;65(11):1869-1879.
[98] Monteverde F, Bellosi A. Microstructure and Properties of an HfB2-SiC Composite for Ultra High Temperature Applications. Adv Eng Mater. 2004;6(5):331-336.
[99] Sciti D, Guicciardi S, Bellosi A, Pezzotti G. Properties of a Pressureless-Sintered ZrB2-MoSi2 Ceramic Composite. J Am Ceram Soc. 2006;89(7):2320-2322.
[100] Chamberlain AL, Fahrenholtz WG, Hilmas GE, Ellerby DT. High-Strength Zirconium Diboride-Based Ceramics. J Am Ceram Soc. 2004;87(6):1170-1172.
[101] Colombo P, Sglavo V, Pippel E, Woltersdorf J. Joining of reaction-bonded silicon carbide using a preceramic polymer. J Mater Sci. 1998;33(9):2405-2412.
[102] Haug R, Weinmann M, Bill J, Aldinger F. Plastic forming of preceramic polymers. J Eur Ceram Soc. 1999;19(1):1-6.
[103] Konetschny C, Galusek D, Reschke S, Fasel C, Riedel R. Dense silicon carbonitride ceramics by pyrolysis of cross-linked and warm pressed polysilazane powders. J Eur Ceram Soc. 1999;19(16):2789-2796.
[104] Riedel R, Passing G, Schönfelder H, Brook R. Synthesis of dense silicon-based ceramics at low temperatures. Nature. 1992;355(6362):714-717.
[105] Seitz J, Bill J. Production of compact polysilazane-derived Si/C/N-ceramics by plastic forming. J Mater Sci Lett. 1996;15(5):391-393.
[106] Wan J, Gasch M, Mukherjee A. Silicon carbonitride ceramics produced by pyrolysis of polymer ceramic precursor. J Mater Res. 2000;15(08):1657-1660.
[107] Shah SR, Raj R. Mechanical properties of a fully dense polymer derived ceramic made by a novel pressure casting process. Acta Mater. 2002;50(16):4093-4103.
[108] Moysan C, Riedel R, Harshe R, Rouxel T, Augereau F. Mechanical characterization of a polysiloxane-derived SiOC glass. J Eur Ceram Soc. 2007;27(1):397-403.

[109] Harshe R, Balan C, Riedel R. Amorphous Si (Al) OC ceramic from polysiloxanes: bulk ceramic processing, crystallization behavior and applications. J Eur Ceram Soc. 2004;24(12):3471-3482.

[110] Gao Y, Mera G, Nguyen H, Morita K, Kleebe H-J, Riedel R. Processing route dramatically influencing the nanostructure of carbon-rich SiCN and SiBCN polymer-derived ceramics. Part I: Low temperature thermal transformation. J Eur Ceram Soc. 2012;32(9):1857-1866.

[111] Kalish D, Clougherty EV, Kreder K. Strength, Fracture Mode, and Thermal Stress Resistance of HfB2 and ZrB2. J Am Ceram Soc. 1969;52(1):30-36.

[112] Medri V, Monteverde F, Balbo A, Bellosi A. Comparison of ZrB2-ZrC-SiC Composites Fabricated by Spark Plasma Sintering and Hot-Pressing. Adv Eng Mater. 2005;7(3):159-163.

[113] Sciti D, Silvestroni L, Bellosi A. Fabrication and properties of HfB2–MoSi2 composites produced by hot pressing and spark plasma sintering. J Mater Res. 2006;21(06):1460-1466.

[114] Monteverde F. Ultra-high temperature HfB2/SiC ceramics consolidated by hot-pressing and spark plasma sintering. J Alloy Compd. 2007;428(1):197-205.

[115] Liu JX, Huang X, Zhang GJ. Pressureless Sintering of Hafnium Carbide–Silicon Carbide Ceramics. J Am Ceram Soc. 2013;96(6):1751-1756.

[116] Krenkel W. Ceramic matrix composites: fiber reinforced ceramics and their applications: John Wiley & Sons; 2008.

[117] Curtin WA. Theory of Mechanical Properties of Ceramic-Matrix Composites. J Am Ceram Soc. 1991;74(11):2837-2845.

[118] Krenkel W. Carbon Fiber Reinforced CMC for High-Performance Structures. Int J Appl Ceram Tec. 2004;1(2):188-200.

[119] Naslain R, Langlais F, Fedou R. The CVI-processing of ceramic matrix composites. Journal de Physique Colloques. 1989;50(C5).

[120] Naslain R. Design, preparation and properties of non-oxide CMCs for application in engines and nuclear reactors: an overview. Compos Sci Technol. 2004;64(2):155-170.

[121] Ly H, Taylor R, Day R. Carbon fibre-reinforced CMCs by PCS infiltration. J Mater Sci. 2001;36(16):4027-4035.

[122] Ziegler G, Richter I, Suttor D. Fiber-reinforced composites with polymer-derived matrix: processing, matrix formation and properties. Compos Part A-Appl S. 1999;30(4):411-417.

[123] Lee SH, Weinmann M, Aldinger F. Processing and properties of C/Si-B-C-N fiber-reinforced ceramic matrix composites prepared by precursor impregnation and pyrolysis. Acta Mater. 2008;56(7):1529-1538.

[124] Raffray AR, Jones R, Aiello G, Billone M, Giancarli L, Golfier H, et al. Design and material issues for high performance SiCf/SiC-based fusion power cores. Fusion Eng Des. 2001;55(1):55-95.

[125] Yoshida K, Imai M, Yano T. Improvement of the mechanical properties of hot-pressed silicon-carbide-fiber-reinforced silicon carbide composites by polycarbosilane impregnation. Compos Sci Technol. 2001;61(9):1323-1329.

[126] Klatt E, Frass A, Frieß M, Koch D, Voggenreiter H. Mechanical and microstructural characterisation of SiC-and SiBNC-fibre reinforced CMCs manufactured via PIP method before and after exposure to air. J Eur Ceram Soc. 2012;32(14):3861-3874.

[127] Motz G, Schmidt S, Beyer S. The PIP-Process: Precursor Properties and Applications. Ceramic Matrix Composites: Fiber Reinforced Ceramics and their Applications. 2008:165-186.

[128] Zhu Y, Huang Z, Dong S, Yuan M, Jiang D. Fabricating 2.5D SiCf/SiC Composite Using Polycarbosilane/SiC/Al Mixture for Matrix Derivation. J Am Ceram Soc. 2007;90(3):969-972.

[129] Rak ZS. A process for Cf/SiC composites using liquid polymer infiltration. J Am Ceram Soc. 2001;84(10):2235-2239.

[130] Nannetti C, Riccardi B, Ortona A, La Barbera A, Scafè E, Vekinis G. Development of 2D and 3D Hi-Nicalon fibres/SiC matrix composites manufactured by a combined CVI-PIP route. J Nucl Mater. 2002;307:1196-1199.

[131] Yamada R, Taguchi T, Igawa N. Mechanical and thermal properties of 2D and 3D SiC/SiC composites. J Nucl Mater. 2000;283:574-578.

[132] Ortona A, Donato A, Filacchioni G, De Angelis U, La Barbera A, Nannetti CA, et al. SiC–SiCf CMC manufacturing by hybrid CVI-PIP techniques: process optimisation. Fusion Eng Des. 2000;51-52(0):159-163.

[133] Hillig WB. Making ceramic composites by melt infitration. Am Ceram Soc Bull. 1994;73(4):56-62.

[134] Shimada S, Inagaki M, Matsui K. Oxidation Kinetics of Hafnium Carbide in the Temperature Range of 480° to 600°C. J Am Ceram Soc. 1992;75(10):2671-2678.

[135] Shimada S, Nakajima K, Inagaki M. Oxidation of Single Crystals of Hafnium Carbide in a Temperature Range of 600° to 900°C. J Am Ceram Soc. 1997;80(7):1749-1756.

[136] Bargeron CB, Benson RC, Jette AN, Phillips TE. Oxidation of Hafnium Carbide in the Temperature Range 1400° to 2060°C. J Am Ceram Soc. 1993;76(4):1040-1046.

[137] Berkowitz-Mattuck JB. High-Temperature Oxidation III. Zirconium and Hafnium Diborides. J Electrochem Soc. 1966;113(9):908-914.

[138] Parthasarathy TA, Rapp RA, Opeka M, Kerans RJ. A model for the oxidation of ZrB2, HfB2 and TiB2. Acta Mater. 2007;55(17):5999-6010.

[139] Parthasarathy TA, Rapp RA, Opeka M, Kerans RJ. Effects of Phase Change and Oxygen Permeability in Oxide Scales on Oxidation Kinetics of ZrB2 and HfB2. J Am Ceram Soc. 2009;92(5):1079-1086.

[140] Tripp W, Graham H. Thermogravi metric Study of the Oxidation of ZrB2 in the Temperature Range of 800° to 1500° C. J Electrochem Soc. 1971;118(7):1195-1199.

[141] Opila EJ, Jacobson NS. Oxidation and Corrosion of Ceramics. Ceramics Science and Technology: Wiley-VCH Verlag GmbH & Co. KGaA; 2013. p. 1-93.

[142] Riedel R, Ruswisch LM, An L, Raj R. Amorphous Silicoboron Carbonitride Ceramic with Very High Viscosity at Temperatures above 1500°C. J Am Ceram Soc. 1998;81(12):3341-3344.

[143] Raj R, An LN, Shah S, Riedel R, Fasel C, Kleebe HJ. Oxidation kinetics of an amorphous silicon carbonitride ceramic. J Am Ceram Soc. 2001;84(8):1803-1810.

[144] Bharadwaj L, Fan Y, Zhang LG, Jiang DP, An LN. Oxidation behavior of a fully dense polymer-derived amorphous silicon carbonitride ceramic. J Am Ceram Soc. 2004;87(3):483-486.

[145] Wang Y, Li H, Zhang L, Cheng L. Oxidation behavior of polymer derived SiCO powders. Ceram Int. 2009;35(3):1129-1132.

[146] Wang YG, Fan Y, Zhang LG, Zhang WG, An LA. Polymer-derived SiAlCN ceramics resist oxidation at 1400°C. Scripta Mater. 2006;55(4):295-297.

[147] Cinibulk MK, Parthasarathy TA. Characterization of Oxidized Polymer-Derived SiBCN Fibers. J Am Ceram Soc. 2001;84(10):2197-2202.

[148] Butchereit E, Nickel KG, Müller A. Precursor-Derived Si-B-C-N Ceramics: Oxidation Kinetics. J Am Ceram Soc. 2001;84(10):2184-2188.

[149] Müller A, Gerstel P, Butchereit E, Nickel KG, Aldinger F. Si/B/C/N/Al precursor-derived ceramics: Synthesis, high temperature behaviour and oxidation resistance. J Eur Ceram Soc. 2004;24(12):3409-3417.

[150] Jacobson NS. Corrosion of Silicon-Based Ceramics in Combustion Environments. J Am Ceram Soc. 1993;76(1):3-28.

[151] Ralf Riedel AK, Wolfgang Dressler, Lutz Ruwisch, Joachim Bill, Fritz Aldinger. A silicoboron carbonitride ceramic stable to 2,000 ^{O}C. Nature. 1996;382(6594):796-798.

[152] Baldus P, Jansen M, Sporn D. Ceramic fibers for matrix composites in high-temperature engine applications. Science. 1999;285(5428):699-703.

[153] Butchereit E, Nickel KG. Comparison of the oxidation kinetics of boron free and boron containing precursor derived ceramics. High Temperature Corrosion and Materials Chemistry III: Proceedings of the International Symposium, vol. 2001: The Electrochemical Society; 2001. p. 112.

[154] Vaughn WL, Maahs HG. Active-to-Passive Transition in the Oxidation of Silicon Carbide and Silicon Nitride in Air. J Am Ceram Soc. 1990;73(6):1540-1543.

[155] Balat MJ. Determination of the active-to-passive transition in the oxidation of silicon carbide in standard and microwave-excited air. J Eur Ceram Soc. 1996;16(1):55-62.

[156] Opila EJ, Smialek JL, Robinson RC, Fox DS, Jacobson NS. SiC Recession Caused by SiO2 Scale Volatility under Combustion Conditions: II, Thermodynamics and Gaseous-Diffusion Model. J Am Ceram Soc. 1999;82(7):1826-1834.

[157] Tripp W, Davis H, Graham H. Effect of an SiC Addition on the Oxidation of ZrB 2. 1973.

[158] Rezaie A, Fahrenholtz WG, Hilmas GE. Evolution of structure during the oxidation of zirconium diboride–silicon carbide in air up to 1500°C. J Eur Ceram Soc. 2007;27(6):2495-2501.

[159] Han W-B, Hu P, Zhang X-H, Han J-C, Meng S-H. High-Temperature Oxidation at 1900°C of ZrB2–xSiC Ultrahigh-Temperature Ceramic Composites. J Am Ceram Soc. 2008;91(10):3328-3334.

[160] Monteverde F, Bellosi A. Oxidation of ZrB2-based ceramics in dry air. J Electrochem Soc. 2003;150(11):B552-B559.

[161] Carney CM. Oxidation resistance of hafnium diboride—silicon carbide from 1400 to 2000 °C. J Mater Sci. 2009;44(20):5673-5681.

[162] Hu P, Guolin W, Wang Z. Oxidation mechanism and resistance of ZrB2–SiC composites. Corros Sci. 2009;51(11):2724-2732.

[163] Guo W-M, Zhang G-J. Oxidation resistance and strength retention of ZrB2–SiC ceramics. J Eur Ceram Soc. 2010;30(11):2387-2395.

[164] Levine SR, Opila EJ, Halbig MC, Kiser JD, Singh M, Salem JA. Evaluation of ultra-high temperature ceramics foraeropropulsion use. J Eur Ceram Soc. 2002;22(14-15):2757-2767.

[165] Opila EJ, Halbig MC. Oxidation of Zrb2-Sic. 25th Annual Conference on Composites, Advanced Ceramics, Materials, and Structures: A: Ceramic Engineering and Science Proceedings: John Wiley & Sons, Inc.; 2008. p. 221-228.

[166] Fahrenholtz WG. Thermodynamic Analysis of ZrB2–SiC Oxidation: Formation of a SiC-Depleted Region. J Am Ceram Soc. 2007;90(1):143-148.

[167] Han J, Hu P, Zhang X, Meng S. Oxidation behavior of zirconium diboride–silicon carbide at 1800°C. Scripta Mater. 2007;57(9):825-828.

[168] Talmy IG, Zaykoski JA, Opeka MM. High-Temperature Chemistry and Oxidation of ZrB2 Ceramics Containing SiC, Si3N4, Ta5Si3, and TaSi2. J Am Ceram Soc. 2008;91(7):2250-2257.

[169] Peng F, Speyer RF. Oxidation Resistance of Fully Dense ZrB2 with SiC, TaB2, and TaSi2 Additives. J Am Ceram Soc. 2008;91(5):1489-1494.

[170] Opila E, Levine S, Lorincz J. Oxidation of ZrB2- and HfB2-based ultra-high temperature ceramics: Effect of Ta additions. J Mater Sci. 2004;39(19):5969-5977.

[171] Levine SR, Opila EJ. Tantalum addition to zirconium diboride for improved oxidation resistance. 2003.

[172] Jacobson NS. Corrosion of Silicon-Based Ceramics in Combustion Environments. J Am Ceram Soc. 1993;76(1):3-28.

[173] Wang Y, Fei W, An L. Oxidation/Corrosion of Polymer-Derived SiAlCN Ceramics in Water Vapor. J Am Ceram Soc. 2006;89(3):1079-1082.

[174] Singhal SC. Effect of Water Vapor on the Oxidation of Hot-Pressed Silicon Nitride and Silicon Carbide. J Am Ceram Soc. 1976;59(1-2):81-82.

[175] Fox DS, Opila EJ, Nguyen QN, Humphrey DL, Lewton SM. Paralinear Oxidation of Silicon Nitride in a Water-Vapor/Oxygen Environment. J Am Ceram Soc. 2003;86(8):1256-1261.

[176] Opila EJ. Oxidation Kinetics of Chemically Vapor-Deposited Silicon Carbide in Wet Oxygen. J Am Ceram Soc. 1994;77(3):730-736.

[177] Opila EJ. Variation of the Oxidation Rate of Silicon Carbide with Water-Vapor Pressure. J Am Ceram Soc. 1999;82(3):625-636.

[178] Opila EJ, Hann RE. Paralinear Oxidation of CVD SiC in Water Vapor. J Am Ceram Soc. 1997;80(1):197-205.

[179] Robinson RC, Smialek JL. SiC Recession Caused by SiO2 Scale Volatility under Combustion Conditions: I, Experimental Results and Empirical Model. J Am Ceram Soc. 1999;82(7):1817-1825.

[180] Opila EJ, Fox DS, Jacobson NS. Mass Spectrometric Identification of Si-O-H(g) Species from the Reaction of Silica with Water Vapor at Atmospheric Pressure. J Am Ceram Soc. 1997;80(4):1009-1012.

[181] Wang Y, Fei W, Fan Y, Zhang L, Zhang W, An L. Silicoaluminum carbonitride ceramic resist to oxidation/corrosion in water vapor. J Mater Res. 2006;21(07):1625-1628.

[182] Oda K, Yoshio T, Miyamoto Y, Koizumi M. Hydrothermal Corrosion of Pure, Hot Isostatically Pressed Silicon Nitride. J Am Ceram Soc. 1993;76(5):1365-1368.

[183] Sōmiya S. Hydrothermal corrosion of nitride and carbide of silicon. Mater Chem Phys. 2001;67(1-3):157-164.

[184] Herrmann M. Corrosion of Silicon Nitride Materials in Aqueous Solutions. J Am Ceram Soc. 2013;96(10):3009-3022.

[185] Herrmann M, Schilm J, Michael G, Meinhardt J, Flegler R. Corrosion of silicon nitride materials in acidic and basic solutions and under hydrothermal conditions. J Eur Ceram Soc. 2003;23(4):585-594.

[186] Herrmann M, Klemm H, Schubert C. Silicon nitride based hard materials. Handbook of Ceramic Hard Materials. 2000:749-801.

[187] Williams S, Curry DM. Thermal protection materials: thermophysical property data. NASA STI/Recon Technical Report N. 1992;93:18765.

[188] Anselmi-Tamburini U, Kodera Y, Gasch M, Unuvar C, Munir ZA, Ohyanagi M, et al. Synthesis and characterization of dense ultra-high temperature thermal protection materials produced by field activation through spark plasma sintering (SPS): I. Hafnium Diboride. J Mater Sci. 2006;41(10):3097-3104.

[189] Upadhya K, Yang J-M, Hoffman WP. Materials for ultrahigh temperature structural applications. Am Ceram Soc Bull. 1997;76(12):51-56.

[190] Bongiorno A, Först CJ, Kalia RK, Li J, Marschall J, Nakano A, et al. A Perspective on Modeling Materials in Extreme Environments: Oxidation of Ultrahigh-Temperature Ceramics. MRS Bulletin. 2006;31(05):410-418.

[191] Monteverde F, Savino R. Stability of ultra-high-temperature ZrB2-SiC ceramics under simulated atmospheric re-entry conditions. J Eur Ceram Soc. 2007;27(16):4797-4805.

[192] Zhang X, Hu P, Han J, Meng S. Ablation behavior of ZrB2–SiC ultra high temperature ceramics under simulated atmospheric re-entry conditions. Compos Sci Technol. 2008;68(7-8):1718-1726.

[193] Tang S, Deng J, Wang S, Liu W, Yang K. Ablation behaviors of ultra-high temperature ceramic composites. Mat Sci Eng A. 2007;465(1-2):1-7.

[194] Fang D, Chen Z, Song Y, Sun Z. Morphology and microstructure of 2.5 dimension C/SiC composites ablated by oxyacetylene torch. Ceram Int. 2009;35(3):1249-1253.

[195] Zhou S, Li W, Hu P, Hong C, Weng L. Ablation behavior of ZrB2-SiC-ZrO2 ceramic composites by means of the oxyacetylene torch. Corros Sci. 2009;51(9):2071-2079.

[196] Xuetao S, Kezhi L, Hejun L, Hongying D, Weifeng C, Fengtao L. Microstructure and ablation properties of zirconium carbide doped carbon/carbon composites. Carbon. 2010;48(2):344-351.

[197] Zhao D, Zhang C, Hu H, Zhang Y. Ablation behavior and mechanism of 3D C/ZrC composite in oxyacetylene torch environment. Compos Sci Technol. 2011;71(11):1392-1396.

[198] Xie J, Li K, Li H, Fu Q, Guo L. Ablation behavior and mechanism of C/C-ZrC-SiC composites under an oxyacetylene torch at 3000°C. Ceram Int. 2013;39(4):4171-4178.

[199] Tang S, Deng J, Wang S, Liu W. Comparison of thermal and ablation behaviors of C/SiC composites and C/ZrB2–SiC composites. Corros Sci. 2009;51(1):54-61.

[200] Monteverde F, Savino R, Fumo MDS, Di Maso A. Plasma wind tunnel testing of ultra-high temperature ZrB2–SiC composites under hypersonic re-entry conditions. J Eur Ceram Soc. 2010;30(11):2313-2321.

[201] Savino R, De Stefano Fumo M, Silvestroni L, Sciti D. Arc-jet testing on HfB2 and HfC-based ultra-high temperature ceramic materials. J Eur Ceram Soc. 2008;28(9):1899-1907.

[202] Zhang X, Weng L, Han J, Meng S, Han W. Preparation and Thermal Ablation Behavior of HfB2–SiC-Based Ultra-High-Temperature Ceramics Under Severe Heat Conditions. Int J Appl Ceram Tec. 2009;6(2):134-144.

[203] Savino R, De Stefano Fumo M, Paterna D, Di Maso A, Monteverde F. Arc-jet testing of ultra-high-temperature-ceramics. Aerosp Sci Technol. 2010;14(3):178-187.

[204] Tong Y, Bai S, Zhang H, Ye Y. Laser ablation behavior and mechanism of C/SiC composite. Ceram Int. 2013;39(6):6813-6820.

[205] Tang S, Deng J, Wang S, Liu W, Yang K. Ablation behaviors of ultra-high temperature ceramic composites. Mat Sci Eng A. 2007;465(1):1-7.

[206] Paul A, Venugopal S, Binner JGP, Vaidhyanathan B, Heaton ACJ, Brown PM. UHTC–carbon fibre composites: Preparation, oxyacetylene torch testing and characterisation. J Eur Ceram Soc. 2013;33(2):423-432.

[207] Traßl S, Suttor D, Motz G, Rössler E, Ziegler G. Structural characterisation of silicon carbonitride ceramics derived from polymeric precursors. J Eur Ceram Soc. 2000;20(2):215-225.

[208] Muller A, Gerstel P, Weinmann M, Bill J, Aldinger F. Si-B-C-N ceramic precursors derived from dichlorodivinylsilane and chlorotrivinylsilane. 1. Precursor synthesis. Chem Mater. 2002;14(8):3398-3405.

[209] Bill J, Seitz J, Thurn G, Durr J, Canel J, Janos BZ, et al. Structure analysis and properties of Si-C-N ceramics derived from polysilazanes. Phys Status Solidi A. 1998;166(1):269-296.

[210] Kroke E, Li YL, Konetschny C, Lecomte E, Fasel C, Riedel R. Silazane derived ceramics and related materials. Mat Sci Eng R. 2000;26(4-6):97-199.

[211] Li YL, Kroke E, Riedel R, Fasel C, Gervais C, Babonneau F. Thermal cross-linking and pyrolytic conversion of poly(ureamethylvinyl)silazanes to silicon-based ceramics. Appl Organomet Chem. 2001;15(10):820-832.

[212] Ionescu E, Papendorf B, Kleebe HJ, Breitzke H, Nonnenmacher K, Buntkowsky G, et al. Phase separation of a hafnium alkoxide-modified polysilazane upon polymer-to-ceramic transformation-A case study. J Eur Ceram Soc. 2012;32(9):1873-1881.

[213] Tsetsgee O. Solid-state NMR studies on precursor derived Si-BCN and BCN ceramics. 2009.

[214] Mera G, Navrotsky A, Sen S, Kleebe HJ, Riedel R. Polymer-derived SiCN and SiOC ceramics - structure and energetics at the nanoscale. J Mater Chem A. 2013;1(12):3826-3836.

[215] Ziegler G, Kleebe HJ, Motz G, Muller H, Trassl S, Weibelzahl W. Synthesis, microstructure and properties of SiCN ceramics prepared from tailored polymers. Mater Chem Phys. 1999;61(1):55-63.
[216] Haluschka C, Kleebe HJ, Franke R, Riedel R. Silicon carbonitride ceramics derived from polysilazanes Part I. Investigation of compositional and structural properties. J Eur Ceram Soc. 2000;20(9):1355-1364.
[217] Kleebe HJ, Stormer H, Trassl S, Ziegler G. Thermal stability of SiCN ceramics studied by spectroscopy and electron microscopy. Appl Organomet Chem. 2001;15(10):858-866.
[218] Trassl S, Kleebe HJ, Stormer H, Motz G, Rossler E, Ziegler G. Characterization of the free-carbon phase in Si-C-N ceramics: Part II, comparison of different polysilazane precursors. J Am Ceram Soc. 2002;85(5):1268-1274.
[219] Gerardin C, Taulelle F, Bahloul D. Pyrolysis chemistry of polysilazane precursors to silicon carbonitride. J Mater Chem. 1997;7(1):117-126.
[220] Sauter D, Weinmann M, Berger F, Lamparter P, Muller K, Aldinger F. X-ray and neutron scattering and solid state NMR investigations on precursor-derived B-C-N ceramics using isotopic substitution. Chem Mater. 2002;14(7):2859-2870.
[221] Widgeon S, Mera G, Gao Y, Sen S, Navrotsky A, Riedel R. Effect of Precursor on Speciation and Nanostructure of SiBCN Polymer-Derived Ceramics. J Am Ceram Soc. 2013;96(5):1651-1659.
[222] Trassl S, Motz G, Rössler E, Ziegler G. Characterisation of the free-carbon phase in precursor-derived SiCN ceramics. J Non-Cryst Solids. 2001;293:261-267.
[223] Trassl S, Motz G, Rössler E, Ziegler G. Characterization of the Free-Carbon Phase in Precursor-Derived Si-C-N Ceramics: I, Spectroscopic Methods. J Am Ceram Soc. 2002;85(1):239-244.
[224] Rahaman MN. Sintering of ceramics: CRC press Boca Raton:; 2008.
[225] Bellosi A, Monteverde F, Sciti D. Fast Densification of Ultra-High-Temperature Ceramics by Spark Plasma Sintering. Int J Appl Ceram Tec. 2006;3(1):32-40.
[226] Yang Z-H, Jia D-C, Zhou Y, Zhang J-X. Processing and characterization of SiB0.5C1.5N0.5 produced by mechanical alloying and subsequent spark plasma sintering. Mat Sci Eng A. 2008;488(1-2):241-246.
[227] Ang C, Seeber A, Williams T, Cheng Y-B. SPS densification and microstructure of ZrB2 composites derived from sol–gel ZrC coating. J Eur Ceram Soc. 2014;34(12):2875-2883.
[228] Ghaffari SA, Faghihi-Sani MA, Golestani-Fard F, Mandal H. Spark plasma sintering of TaC-HfC UHTC via disilicides sintering aids. J Eur Ceram Soc. 2013;33(8):1479-1484.
[229] Orrù R, Cao G. Comparison of Reactive and Non-Reactive Spark Plasma Sintering Routes for the Fabrication of Monolithic and Composite Ultra High Temperature Ceramics (UHTC) Materials. Materials. 2013;6(5):1566-1583.
[230] Licheri R, Orru R, Musa C, Locci AM, Cao G. Spark plasma sintering of UHTC powders obtained by self-propagating high-temperature synthesis. J Mater Sci. 2008;43(19):6406-6413.
[231] Shen Z, Johnsson M, Zhao Z, Nygren M. Spark Plasma Sintering of Alumina. J Am Ceram Soc. 2002;85(8):1921-1927.
[232] Omori M. Sintering, consolidation, reaction and crystal growth by the spark plasma system (SPS). Mat Sci Eng A. 2000;287(2):183-188.
[233] Munir ZA, Anselmi-Tamburini U, Ohyanagi M. The effect of electric field and pressure on the synthesis and consolidation of materials: A review of the spark plasma sintering method. J Mater Sci. 2006;41(3):763-777.
[234] Olevsky EA, Kandukuri S, Froyen L. Consolidation enhancement in spark-plasma sintering: Impact of high heating rates. J Appl Phys. 2007;102(114913):1-11.
[235] Li D, Li W, Fasel C, Shen J, Riedel R. Sinterability of the oxynitride LaTiO2N with perovskite-type structure. J Alloy Compd. 2014;586(0):567-573.
[236] D. Li J-FH, J.-Z. Zhang, J. Ma, Z. Shen. Densification as an exothermic process revealed by rapid high temperature consolidation of BaTiO3 nanopowder. Advances in Applied Ceramics. 2014;113(4):251-256.
[237] Tavakoli AH, Gerstel P, Golczewski JA, Bill J. Kinetic effect of boron on the crystallization of Si3N4 in Si–B–C–N polymer-derived ceramics. J Mater Res. 2011;26(04):600-608.
[238] Liao SC, Mayo WE, Pae KD. Theory of high pressure/low temperature sintering of bulk nanocrystalline TiO2. Acta Mater. 1997;45(10):4027-4040.
[239] Grasso S, Sakka Y, Maizza G, Hu C. Pressure Effect on the Homogeneity of Spark Plasma-Sintered Tungsten Carbide Powder. J Am Ceram Soc. 2009;92(10):2418-2421.
[240] Larouche N, Stansfield BL. Classifying nanostructured carbons using graphitic indices derived from Raman spectra. Carbon. 2010;48(3):620-629.

[241] Oliver WC, Pharr GM. An improved technique for determining hardness and elastic modulus using load and displacement sensing indentation experiments. J Mater Res. 1992;7(06):1564-1583.

[242] Monteverde F, Bellosi A, Scatteia L. Processing and properties of ultra-high temperature ceramics for space applications. Materials Science and Engineering: A. 2008;485(1–2):415-421.

[243] Li W, Wang T. Elasticity, stability, and ideal strength of β-SiC in plane-wave-based ab initio calculations. Phys Rev B. 1999;59(6):3993-4001.

[244] Greil P, Vogli E, Fey T, Bezold A, Popovska N, Gerhard H, et al. Effect of microstructure on the fracture behavior of biomorphous silicon carbide ceramics. J Eur Ceram Soc. 2002;22(14-15):2697-2707.

[245] Nishimura T, Haug R, Bill J, Thurn G, Aldinger F. Mechanical and thermal properties of Si–C–N material from polyvinylsilazane. J Mater Sci. 1998;33(21):5237-5241.

[246] Moraes KV, Interrante LV. Processing, Fracture Toughness, and Vickers Hardness of Allylhydridopolycarbosilane-Derived Silicon Carbide. J Am Ceram Soc. 2003;86(2):342-346.

[247] Martínez-Crespiera S, Ionescu E, Kleebe H-J, Riedel R. Pressureless synthesis of fully dense and crack-free SiOC bulk ceramics via photo-crosslinking and pyrolysis of a polysiloxane. J Eur Ceram Soc. 2011;31(5):913-919.

[248] Galusek D, Riley FL, Riedel R. Nanoindentation of a Polymer-Derived Amorphous Silicon Carbonitride Ceramic. J Am Ceram Soc. 2001;84(5):1164-1166.

[249] Janakiraman N, Aldinger F. Indentation analysis of elastic and plastic deformation of precursor-derived Si–C–N ceramics. J Eur Ceram Soc. 2010;30(3):775-785.

[250] Janakiraman N, Aldinger F. Fabrication and characterization of fully dense Si-C-N ceramics from a poly(ureamethylvinyl)silazane precursor. J Eur Ceram Soc. 2009;29(1):163-173.

[251] An L, Xu W, Rajagopalan S, Wang C, Wang H, Fan Y, et al. Carbon-Nanotube-Reinforced Polymer-Derived Ceramic Composites. Adv Mater. 2004;16(22):2036-2040.

[252] Bechelany MC, Proust V, Gervais C, Ghisleni R, Bernard S, Miele P. In situ controlled growth of titanium nitride in amorphous silicon nitride: A general route toward bulk nitride nanocomposites with very high hardness. Adv Mater. 2014;26(38):6548-6553.

[253] Bechelany MC, Salameh C, Viard A, Guichaoua L, Rossignol F, Chartier T, et al. Preparation of polymer-derived Si–B–C–N monoliths by spark plasma sintering technique. J Eur Ceram Soc. 2015;35(5):1361-1374.

[254] Yuan J, Hapis S, Breitzke H, Xu Y, Fasel C, Kleebe H-J, et al. Single-Source-Precursor Synthesis of Hafnium-Containing Ultrahigh-Temperature Ceramic Nanocomposites (UHTC-NCs). Inorg Chem. 2014;53(19):10443-10455.

[255] Naslain RR. The design of the fibre-matrix interfacial zone in ceramic matrix composites. Compos Part A-Appl S. 1998;29(9):1145-1155.

[256] Helmer T, Peterlik H, Kromp K. Coating of Carbon Fibers—The Strength of the Fibers. J Am Ceram Soc. 1995;78(1):133-136.

[257] Seifert HJ, Peng J, Lukas HL, Aldinger F. Phase equilibria and thermal analysis of Si-C-N ceramics. J Alloy Compd. 2001;320(2):251-261.

[258] Lee JS, Butt DP, Baney RH, Bowers CR, Tulenko JS. Synthesis and pyrolysis of novel polysilazane to SiBCN ceramic. J Non-Cryst Solids. 2005;351(37-39):2995-3005.

[259] Weinmann M, Schuhmacher J, Kummer H, Prinz S, Peng JQ, Seifert HJ, et al. Synthesis and thermal behavior of novel Si-B-C-N ceramic precursors. Chem Mater. 2000;12(3):623-632.

[260] Taylor KM. Boron nitride - metal carbide bodies and the manufacture thereof. vol. 2,888,355 USA1959. p. 4.

[261] Blum Y, Kleebe H-J. Chemical reactivities of hafnium and its derived boride, carbide and nitride compounds at relatively mild temperature. J Mater Sci. 2004;39(19):6023-6042.

[262] Ferreira EM, Moutinho MV, Stavale F, Lucchese M, Capaz RB, Achete C, et al. Evolution of the Raman spectra from single-, few-, and many-layer graphene with increasing disorder. Phys Rev B. 2010;82(12):125429.

[263] Monteverde F, Bellosi A. The resistance to oxidation of an HfB2/SiC composite. J Eur Ceram Soc. 2005;25(7):1025-1031.

[264] Pavese M, Fino P, Badini C, Ortona A, Marino G. HfB2/SiC as a protective coating for 2D Cf/SiC composites: Effect of high temperature oxidation on mechanical properties. Surf Coat Tech. 2008;202(10):2059-2067.

[265] Verdon C, Szwedek O, Jacques S, Allemand A, Le Petitcorps Y. Hafnium and silicon carbide multilayer coatings for the protection of carbon composites. Surf Coat Tech. 2013;230:124-129.

[266] Wang Y, Li H, Fu Q, Wu H, Yao D, Li H. SiC/HfC/SiC ablation resistant coating for carbon/carbon composites. Surf Coat Tech. 2012;206(19–20):3883-3887.

[267] Papendorf B, Ionescu E, Kleebe HJ, Linck C, Guillon O, Nonnenmacher K, et al. High-Temperature Creep Behavior of Dense SiOC-Based Ceramic Nanocomposites: Microstructural and Phase Composition Effects. J Am Ceram Soc. 2013;96(1):272-280.

[268] Quanli J, Haijun Z, Suping L, Xiaolin J. Effect of particle size on oxidation of silicon carbide powders. Ceram Int. 2007;33(2):309-313.

[269] Vaben R, Stöver D. Oxidation of ultrafine (Si-) SiC powders. J Mater Sci. 1994;29(14):3791-3796.

[270] Pieraggi B. Calculations of parabolic reaction rate constants. Oxid Met. 1987;27(3-4):177-185.

[271] Du H, Tressler RE, Spear KE, Pantano CG. Oxidation Studies of Crystalline CVD Silicon Nitride. J Electrochem Soc. 1989;136(5):1527-1536.

[272] Norton FJ. Permeation of gaseous oxygen through vitreous silica. 1961.

[273] Ramberg CE, Worrell WL. Oxygen Transport in Silica at High Temperatures: Implications of Oxidation Kinetics. J Am Ceram Soc. 2001;84(11):2607-2616.

[274] Shugart K, Liu S, Craven F, Opila E. Determination of Retained B2O3 Content in ZrB2-30 vol% SiC Oxide Scales. J Am Ceram Soc. 2015;98(1):287-295.

[275] Monteverde F, Bellosi A. Oxidation of ZrB(2)-based ceramics in dry air. J Electrochem Soc. 2003;150(11):B552-B559.

[276] HORTON RM. Oxidation kinetics of powdered silicon nitride. J Am Ceram Soc. 1969;52(3):121-124.

[277] Deal BE. The oxidation of silicon in dry oxygen, wet oxygen, and steam. J Electrochem Soc. 1963;110(6):527-533.

[278] Ogbuji LU, Opila EJ. A Comparison of the Oxidation Kinetics of SiC and Si3N4. J Electrochem Soc. 1995;142(3):925-930.

[279] Schlichting J. Oxygen transport through glass layers formed by a gel process. J Non-Cryst Solids. 1984;63(1):173-181.

[280] Rho H, Hecht NL, Graves GA. Oxidation behavior of hot isostatically pressed silicon nitride containing Y2O3. J Mater Sci. 2000;35(14):3631-3639.

[281] Vogel W. Glass Chemistry, 1994. Springer-Verlag Berlin Heidelberg.2:24-25.

[282] Fox DS. Oxidation Behavior of Chemically-Vapor-Deposited Silicon Carbide and Silicon Nitride from 1200° to 1600° C. J Am Ceram Soc. 1998;81(4):945-950.

[283] Sciti D, Brach M, Bellosi A. Long-term oxidation behavior and mechanical strength degradation of a pressurelessly sintered ZrB2–MoSi2 ceramic. Scripta Mater. 2005;53(11):1297-1302.

[284] Kleebe H-J, Nonnenmacher K, Ionescu E, Riedel R. Decomposition-Coarsening Model of SiOC/HfO2 Ceramic Nanocomposites Upon Isothermal Anneal at 1300°C. J Am Ceram Soc. 2012;95(7):2290-2297.

[285] Musa C, Licheri R, Orrù R, Cao G. Synthesis, Sintering, and Oxidative Behavior of HfB2–HfSi2 Ceramics. Ind Eng Chem Res. 2014;53(22):9101–9108.

[286] Hoppe EE, Cisneros-Morales MC, Aita CR. Ti-catalyzed HfSiO4 formation in HfTiO4 films on SiO2 studied by Z-contrast scanning electron microscopy. APL Materials. 2013;1(022108):1-7.

[287] Jacobson NS, Opila EJ, Lee KN. Oxidation and corrosion of ceramics and ceramic matrix composites. Current Opinion in Solid State and Materials Science. 2001;5(4):301-309.

[288] Lamouroux F, Camus G, Thebault J. Kinetics and mechanisms of oxidation of 2D woven C/SiC composites: I, experimental approach. J Am Ceram Soc. 1994;77(8):2049-2057.

[289] Lamouroux F, Naslain R, Jouin JM. Kinetics and mechanisms of oxidation of 2D woven C/SiC composites: II, Theoretical approach. J Am Ceram Soc. 1994;77(8):2058-2068.

[290] Eaton HE, Linsey GD. Accelerated oxidation of SiC CMC's by water vapor and protection via environmental barrier coating approach. J Eur Ceram Soc. 2002;22(14-15):2741-2747.

[291] Lee KN. Current status of environmental barrier coatings for Si-Based ceramics. Surf Coat Tech. 2000;133-134(0):1-7.

[292] Liu J, Zhang L, Hu F, Yang J, Cheng L, Wang Y. Polymer-derived yttrium silicate coatings on 2D C/SiC composites. J Eur Ceram Soc. 2013;33(2):433-439.

[293] Luan X, Cheng L, Yin X. Corrosion of a SiC-C/PyC/SiC composite by sodium sulfate vapor at high temperatures. Sci Eng Compos Mater. 2002;10(2):157-162.

[294] Luan X, Zhang J, Cheng L. Effects of water vapor on corrosion behaviors of C/SiC in oxidizing atmosphere containing Na2SO4 vapor. Compos Part B-Eng. 2012;43(8):2968-2972.

[295] Gogotsi YG, Yoshimura M. Low-Temperature Oxidation, Hydrothermal Corrosion, and Their Effects on Properties of SiC (Tyranno) Fibers. J Am Ceram Soc. 1995;78(6):1439-1450.

[296] Kraft T, Nickel KG, Gogotsi YG. Hydrothermal degradation of chemical vapour deposited SiC fibres. J Mater Sci. 1998;33(17):4357-4364.

[297] Rosso M. Ceramic and metal matrix composites: Routes and properties. J Mater Process Tech. 2006;175(1–3):364-375.

[298] Sato T, Murakami T, Endo T, Shimada M, Komeya K, Kameda T, et al. Corrosion of silicon nitride ceramics under hydrothermal conditions. J Mater Sci. 1991;26(7):1749-1754.

[299] Monteverde F, Mingazzini C, Giorgi M, Bellosi A. Corrosion of silicon nitride in sulphuric acid aqueous solution. Corros Sci. 2001;43(10):1851-1863.

[300] Wang Y, Fei W, An L. Oxidation/Corrosion of Polymer-Derived SiAlCN Ceramics in Water Vapor. J Am Ceram Soc. 2006;89(3):1079-1082.

[301] Nickel K, Gogotsi YG. Approaches to standardisation: High temperature oxidation and hydrothermal corrosion of silica forming ceramics. Key Eng Mat. 1995;113:15-32.

[302] Hirayama H, Kawakubo T, Goto A, Kaneko T. Corrosion behavior of silicon carbide in 290 C water. J Am Ceram Soc. 1989;72(11):2049-2053.

[303] Wakabayashi H, Tomozawa M. Diffusion of Water into Silica Glass at Low Temperature. J Am Ceram Soc. 1989;72(10):1850-1855.

[304] Rai D, Xia Y, Hess NJ, Strachan DM, McGrail BP. Hydroxo and chloro complexes/ion interactions of Hf4+ and the solubility product of HfO2 (am). J Solution Chem. 2001;30(11):949-967.

[305] Norton FJ. Permeation of Gaseous Oxygen through Vitreous Silica. Nature. 1961;191(4789):701-701.

[306] Su M, Cheng L, Luan X, Zhang L. Laser ablation behaviors of C/SiC composites in air. Acta Materiae Compositae Sinica. 2013;30(6):37-47.

[307] Chen Sa, Zhang C, Zhang Y, Zhao D, Hu H, Zhang Z. Mechanism of ablation of 3D C/ZrC–SiC composite under an oxyacetylene flame. Corros Sci. 2013;68:168-175.

[308] Brook R. Controlled grain growth. Treatise on materials science and technology. 1976;9:331-364.

[309] Ni C, Li K, Liu L, Li H, Fu Q, Guo L, et al. Ablation mechanism of SiC coated C/C composites at 0° angle in two flame conditions under an oxyacetylene flame. Corros Sci. 2014;84(0):1-10.

[310] Verdon C, Szwedek O, Allemand A, Jacques S, Le Petitcorps Y, David P. High temperature oxidation of two- and three-dimensional hafnium carbide and silicon carbide coatings. J Eur Ceram Soc. 2014;34(4):879-887.

LIST OF ABBREVIATIONS

ATR-FTIR	Attenuated total reflection-Fourier transform infrared spectroscopy
BET surface	Brunauer–Emmett–Teller surface
CMCs	Ceramic matrix composites
EA	Elemental analysis
EDX/EDS	Energy Dispersive X-ray Spectroscopy
E	Elastic modulus
E_a	Activation Energy
EGA	Evolved Gas Analyzer
FWMH	Full Width at Half Maximum
H	Hardness
MAS	Magic Angle Spinning
MS	Mass Spectrum
PAS	Pressure assisted sintering
PDCs	Polymer Derived Ceramics
PLS	Pressure-less sintering
SAED	Selected Area Electron Diffraction
SEM	Scanning Electron Microscopy
STA	Simultaneous Thermal Analysis
SSPs	Single-source-precursors
TEM	Transmision Electron Microscopy
TGA	Thermogravimetric Analysis
UHTC-NCs	Ultra-High Temperature Ceramic Nanocomposites
XRD	X-Ray Diffraction

CURRICULUM VITAE

PERSONAL STATUS

Name: Jia Yuan
Date of Birth: 17/08/1985
Citizenship: Chinese

EDUCATIONAL BACKGROUND

PhD: 11/2011-Present Disperse Feststoffe, TU Darmstadt, Deutschland
Project: Single-source precursor to synthesize Hf-containing SiHfBCN ceramic and ultra-high temperature ceramic nanocomposites (UHTC-NCs) and their behavior under harsh environment
Advisor: Prof. Ralf Riedel
MS: 2008-2011 Materials Science & Engineering, Donghua University, P.R. China
Thesis: Melt spinning process and characterization of copolymer precursors for SiBN(C) ceramic fiber
Advisor: Prof. Muhuo Yu
BS: 2004-2008 Chemical Science & Engineering, Wuhan Textile University, P.R. China
Thesis: Synthesis and Characterization of Imidazoline-based surfactants
Advisor: Prof. Minggui Xia

WORKING/RESEARCH EXPERIENCES

- **2012-2015 Doctoral program/Research Assistant, Technical University of Darmstadt**

- Designed and synthesized the precursor polymers with systematically varied compositions and structures, such as polysilazane, poly-hafnosilazanes (SiHfCN), poly-hafno(borosilazane) (SiHfBCN).
- Developed a novel processing technology that can make dense monoliths ultra-high temperature ceramic nanocomposites (UHTC-NCs). Synthesized a polymer-derived amorphous SiHf(B)CN and Hf-containing UHTC-NCs, which can withstand very high temperature with respect to decompositions and crystallizations.
- Developed a novel Hf-containing ceramic matrix composites reinforced by carbon fibers (C_f/SiHfBCN) with low-cost and simply way Polymer infiltration pyrolysis (PIP).
- Investigated their (i.e. amorphous ceramic monoliths SiHfBCN, dense crystallization Hf-containing UHTC-NCs, fibers reinforced ceramic composites.) behavior upon treating under harsh environments (i.e. oxidized gas, hydrothermal corrosion, erode conditions).

- **2008-2011 Research Assistant, Donghua University**

- Developed new precursor for ceramic fibers based on silicon-based molecular structure, optimized viscosity of polymer precursor for subsequent melt-spinning by tailored synthesis parameters (molecular ratio, polymerization temperature and time etc.)
- Explored the possibility from lab-scale to large-scale for synthesis of polymer precursor, optimized melt-spinning techniques to achieve green fibers with highly flexible tensile strength.
- Addressed the pyrolysis process that induced conversion from green fibers to amorphous ceramic fibers

with dense and crack free.

PUBLICATIONS

- **Journal Papers:**

1. **Yuan J**, Hapis S, Breitzke H, Xu Y, Fasel C, Kleebe H-J, R Riedel, E Ionescu. Single-source precursor Synthesis of Hafnium-Containing Ultra-high-Temperature Ceramic Nanocomposites (UHTC-NCs). Inorg Chem. 2014; 53(19):10443-10455.
2. **J Yuan**, XG Luan, R Riedel, E Ionescu. Preparation and hydrothermal corrosion behavior of Cf/SiCN and C_f/SiHfBCN ceramic matrix composites. J Eur Ceram Soc. 2015; 35(12):3329-3337.
3. **J Yuan**, KQ Han, X Zhao, YQ Peng, HM Yu. Melt spinning process and characterization of precursors for SiBN(C) ceramic fiber [J].China Synthetic Fiber Industry, 2011, 34(3).
4. Xi Zhao, **Jia Yuan**, Shutong Li, Muhuo Yu. A novel precursor route for the production of Si-B-N ceramic fibers. Material Letters. 2011, 65(17-18) 2717-2720.
5. YQ Peng, KQ Han, X Zhao, **J Yuan**, MH Yu. Research progress in new high temperature resistant nitride ceramic fiber [J].China Synthetic Fiber Industry, 2011, 34(4).

- **Conference Presentations:**

1. J.Yuan, QB Wen, R.Riedel, E. Ionescu. Single source precursor Synthesis and Properties of Ultra-high-Temperature Ceramic Nanocomposites (UHTC-NCs) Presentation in “**8th International Symposium on Nitrides (ISNT)**”, Wildbad Kreuth, Germany, from 31.08.2014 to 05.09.2014.
2. Yuan J, Hapis S, Breitzke H, Xu Y, Fasel C, Kleebe H-J, R Riedel, E Ionescu. Single-source precursor Synthesis of Hafnium-Containing Ultra-high-Temperature Ceramic Nanocomposites (UHTC-NCs), Presentation in “**Materials Science Engineering (MSE 2014)** ”, Darmstadt, Germany, from 23 - 25 September 2014
3. J Yuan, XG Luan, E Ionescu, R Riedel, Synthesis of Polymer-Derived C_f/SiC, C_f/SiCN and Cf/SiHfBCN Ceramic Matrix Composites and Their Corrosion Behavior in Hydrothermal Conditions, Poster in **“8th International Conference on High Temperature Ceramic Matrix Composites”**, Xi an, Shangxi, China, September 22-26, 2013.

M. Eng. JIA YUAN
Nieder-Ramstädter.str.11
64283 Darmstadt

Eidesstattliche Erklärung

Hiermit erkläre ich an Eides statt, dass ich die vorliegende Dissertation selbstständig und nur mit den angegebenen Hilfsmitteln angefertigt habe. Von mir wurde weder an der Technischen Universität Darmstadt noch einer anderen Hochschule ein Promotionsversuch unternommen.

Darmstadt, den 25.08.2015